CRANFIELD UNIVERSITY

JIAJUN ZHANG

STUDY OF THE MECHANISM OF THERMOCATALYTIC DECOMPOSITION OF ANISOLE FOR PRODUCING AROMATIC-RICH FUEL ADDITIVES

SCHOOL OF WATER, ENERGY, AND ENVIRONMENT
FULL TIME PHD IN ENERGY AND POWER

PhD thesis
Academic Year: 2014 – 2017

Supervisor:
Dr. Beatriz Fidalgo
Professor Dekui Shen (external)
Dr. Stuart Wagland

May 2017

CRANFIELD UNIVERSITY

SCHOOL OF WATER, ENERGY, AND ENVIRONMENT
FULL TIME PHD IN ENERGY AND POWER

PhD thesis

Academic Year 2014 - 2017

Jiajun Zhang

STUDY OF THE MECHANISM OF THERMOCATALYTIC DECOMPOSITION OF ANISOLE FOR PRODUCING AROMATIC-RICH FUEL ADDITIVES

Supervisor:
Dr. Beatriz Fidalgo
Professor Dekui Shen (external)
Dr. Stuart Wagland

May 2017

This thesis is submitted in partial fulfilment of the requirements for the degree of PhD

ABSTRACT

In the context of the bio-based economy, lignin is a major source of aromatic compounds. Fast pyrolysis of lignin with catalytic reforming of the liquid fraction provides an efficient approach for producing aromatic hydrocarbons (AHs) as fuel additives. Methoxy compounds abundantly exist in the primary liquid products from fast pyrolysis of lignin, which further convert into phenolic and aromatic compounds via secondary pyrolysis and the upgrading reactions. This thesis focuses on the decomposition mechanism of the methoxyl group, using anisole as a model compound.

Methyl transfer (transmethylation) as the primary reaction of the thermal decomposition of anisole, led to the prominent production of phenolic compounds (Phs). Plausible mechanisms for both non-catalytic and catalytic transmethylation were proposed, based on the analyses of the active sites on anisole and phenol by the means of DFT modelling. The intrinsic transfer orientation preferences onto relevant compounds were then predicted by corresponding reaction energy barriers. Experiments investigated the decomposition of anisole in a fluidized bed reactor over no catalysts and a series of HZSM-5 zeolite catalysts with different Si/Al atomic ratios. Study on transmethylation illustrated how the acid catalysts promoted the preferential formation of Phs.

Deoxygenation reaction of the Phs as second stage reaction at higher temperatures produced AHs. Metal loaded acid (Bi-functional) catalysts designed by multiscale modelling were used in the investigation. Novel mechanism of anisole decomposition over bi-functional catalyst was proposed with the illustration of each role for metal and acid site in the catalysis. DFT modelling also predicted the reaction energy barriers of deoxygenation for various Phs to exhibit the metals effect in promoting the reactions. Experiments of anisole decomposition over the designed single and bi-metal based bi-functional catalysts revealed the distinct characteristics of each metal loading and their synergistic effect in promoting the BTX production.

Keywords:

Lignin; Transmethylation; Deoxygenation; DFT; Bifunctional Catalyst

ACKNOWLEDGEMENTS

First and foremost, I would like sincerely thank my primary supervisor Dr. Beatriz Fidalgo for her excellent guidance, constant feedback, huge encouragement and support on both my research and thesis writing during my PhD at Cranfield University.

I would like to deeply thank my external supervisor Prof. Dekui Shen for his immense guidance and encouragement on my research and life, and the generous support during my exchange period at Southeast University.

I am also grateful to the rest of my review panel members: Prof. Stephen James, Professor Gary Leeke, and Dr. Stuart Wagland, for their insightful comments and encouragement in every annual review meeting.

I would like to acknowledge the financial support from the FP7 Marie Curie iComFluid (project reference: 312261), the National Natural Science Foundation of China (project references: 51476034 and 51628601), and the Natural Science Foundation of Jiangsu Province (project reference: BK20161423) to the research of this thesis.

I would like to specially thank Prof. Sai Gu at University of Surrey, Prof. Rui Xiao and Dr. Huiyang Zhang at Southeast University, Prof. Xuefeng Guo and Prof. Zhaoxu Chen at Nanjing University, and Dr. Athanasios Kolios at Cranfield University for their valuable advice on the research project. Special thanks also to Dr. Anqing Zheng at Guangzhou Institute of Energy Conversion, Chinese Academy of Sciences and Dr. Aiqun Xu at Southeast University for their guidance on XPS and TEM tests, and Dr. Jinghui Zhang at Southeast University for his help in computational platform establishment.

I would express my faithful appreciation to my colleagues Chrysi Karagiannaki, Ebuwa Osagie, Ali S. Al-Turaihi, Khalid Alshamary, Dr. Bing Xia, Yufei Lin, Peter Xia, Xin Chen, Dr. Nan Yu at Cranfield University, and Mengmeng Zhou, Dr. Shuai Zhang, Dr. Jun Hu, Shiliang Wu, Dr. Jun Xie, Dr. Maiomiao Niu, Dr. Qing Dong, Lijun Heng, Dr.Shanshan Shao, Xing Chen, Jimin Zeng, Dewang Zeng, Zhanghong Wang, Chongbo Cheng, Guofu Liu, Pengfei Li, Jing Zhao, Shuheng Yao, Wei Jin, Pengfei He, Nana Liu, Lanqing Zhang, Jiao Zhou, Jinzhi Wang, Wenwen Cai, Wenjie Zhang, and Ming Li at Southeast University. I am so lucky to meet them every one in the past years, and they are unfailing source of friendship, good advice and collaboration, making my work and life pleasant.

Lastly, I would like to thank everyone else who once gave me advice and guidance for the PhD research and life in the past three years. Thank you!

Jiajun Zhang
Cranfield University
May 2017

I dedicate this thesis to

my parents, Genguang Zhang and Ping Zhang, as well as all my families

for their unconditional love and encouragement.

I love you

TABLE OF CONTENTS

LIST OF FIGURES

LIST OF TABLES

LIST OF EQUATIONS

LIST OF ABBREVIATIONS

AHs	Aromatic Hydrocarbons
BSSE	Basis Set Superposition Error
BTX	Benzene-Toluene-Xylene
CFP	Catalytic Fast Pyrolysis
Cr	Cresol Isomers
CVFF	Consistent-Valence Forcefield
DFT	Density Functional Theory
DNP	Double Numerical Plus Polarization
DOS	Density of States
EDS	Energy Dispersive X-Ray Spectroscopy
FID	Flame Ionization Detector
FTIR	Fourier Transform Infrared Spectroscopy
FTT	Fast Fourier Transform
GC	Gas Chromatography
GGA	Generalized Gradient Approximation
HDO	Hydrodeoxygenation
HEM	Half Empirical Method
HZ	HZSM-5
ICP	Inductively Coupled Plasma
LDA	Local Density Approximation
LHV	Lower Heating Value

m-	Meta-
MA	Methyl Anisole Isomers
MS	Mass Spectrometry
NMR	Nuclear Magnetic Resonance
NIST	National Institute of Standards and Technology
o-	Ortho-
p-	Para-
PDOS	Partial Density of States
Phs	Phenolic Compounds
SAED	Selected Area Electron Diffraction
SCF	Self-Consistent Field
SEM	Scanning Electron Microscope
TEM	Transmission Electron Microscopy
TG	Thermogravimetry
TPD	Temperature Programmed Desorption
TPR	Temperature Programmed Reduction
TS	Transition State
Xol	Xylenol Isomers
XPS	X-ray Photoelectron Spectroscopy
XRD	X-Ray Diffraction
XRF	X-Ray Fluorescence

1 Introduction

This chapter starts with a brief introduction to bioenergy and its role in renewable energy. The motivation, aim and objectives, novelty elements of the research, and the structure of this thesis are then introduced in sequence. The chapter ends up with a list of publications, submitted manuscripts, and conference presentations produced from the research project of PhD.

1.1 Research background

Increasing concern about climate change and unsustainable fossil fuel resources are attracting more and more attention to renewable clean energy (Ruddy et al., 2014). Renewable energy includes many different types such as solar energy, hydropower, tidal power, wind energy, geothermal power and bioenergy (Demirbaş, 2001). Bioenergy plays an important role in the renewable energy sector because of its production from abundant source of renewable carbon and its potential low cost (Isahak et al., 2012; Smets et al., 2014).

1.1.1 Biomass and bioenergy

Biomass, which normally refers to wood and wood wastes, agricultural wastes and wastes from aquatic plants (Demirbaş, 2001; Liu et al., 2014), is regarded as the most ideal carbon resource for the production of renewable heat & power, fuels and chemicals without hazardous effects to the environment (He, Sun and Han, 2013). The energy contained in biomass (bioenergy) comes from the carbon in the atmosphere rather than the carbon from deep underground, and the utilization of bioenergy is establishing a green “above ground” carbon cycle, as shown in **Fig. 1-1**. Therefore, it has the potential to be sustainable and completely environmental friendly, and plays a unique role in the consolidation of the bio-economy.

It is projected that the production of bioenergy from biomass would increase in the next thirty years irrespective of the fluctuation of fossil oil price (Liu et al., 2014).

Fig. 1-1 Bioenergy as a promising renewable energy (Mu et al., 2013)

1.1.2 Ways to obtain bioenergy

There are different ways to derive bioenergy from the biomass, and roughly divided into two categories: biochemical conversion and thermochemical conversion (Leibbrandt, Knoetze and Görgens, 2011; Liu et al., 2014). Some widely-acknowledged technologies that are applicable to bioenergy are anaerobic digestion, saccharification, esterification, hydrolysis, liquefaction, torrefaction, pyrolysis, gasification, and combustion.

Pyrolysis is a technology that has been applied for thousands year in charcoal production (Bridgwater and Cottam, 1992; Bridgwater and Peacocke, 2000), and it is a typical thermochemical decomposition process in the absence of oxygen; pyrolysis of biomass mainly produces bio-oil, char and non-condensable gas (CO, CO_2 etc.); proportions of the products vary depending on the operating conditions, raw material and process configuration. Pyrolysis targets bio-oil as the desired product, and its yield normally ranges from 30-45 wt.% in a conventional pyrolysis process (Watkinson, 2014). Fast pyrolysis emerges in late 1970s, which usually runs at moderate temperature (400-700˚C), high heating rate (over 500˚C/s) and short vapour residence time (2s), which favours the

production of high yield of bio-oil (75-80 wt.% for dry feed basis woody biomass) (Bridgwater, 2012; Carlson, Vispute and Huber, 2008).

Among the all the conversion techniques, fast pyrolysis shows good potential to be integrated in biorefining as it has distinct advantages. First, the configuration for the reaction is simpler than most of other processes, which may save substantial capital costs; second, liquid fuel and chemicals can be produced efficiently. Third, the process time is shorter than most of other conversions. Finally, compared to combustion, there are less undesirable emissions from the pyrolysis process itself (Anex et al., 2010; Zhou et al., 2011).

Nevertheless, as an emerging technology, fast pyrolysis of biomass is still undergoing R&D stage, and currently is hard to be widely scaled up in industries because of several critical bottlenecks, such as higher production costs compared to fossil fuels, instability, difference in bio-oil quality, and the lack of uniform standards in its use and sales. Nowadays, intensive investigations have focused on the systemic development of fast pyrolysis in terms of efficient reactor development, process parameters optimization, liquid products upgrading, and the impact of biofuels to engine performance, etc. (Chiaramonti et al., 2003; Zhai, Liu and Han, 2005). For example, the bio-oil produced from fast pyrolysis usually contains large proportion of oxygen, which results in instability, low calorific value (lower heating value (LHV) is only 40–45% of hydrocarbon fuels in the same mass), and high acidity (Lyu, Wu and Zhang, 2015). Therefore, deoxygenation processes are always required to obtain resemble fossil-based fuels products. One of the latest advances in fast pyrolysis include the catalytic upgrading of the bio-oil as part of the process, either as in-situ catalytic fast pyrolysis (CFP) or ex-situ catalytic reforming of the primary bio-oil (Liu et al., 2014; Yildiz et al., 2014).

There are good reasons to believe that pyrolysis bio-oil will become a reliable substituted energy in near future if the bottlenecks could be properly addressed.

1.1.3 Lignin resources

Lignin is one of the three main components in lignocellulosic biomass (constituting 15-35% of dry biomass), and it is a major and the most abundant

aromatic-rich bio-resource (Liu, Jiang and Yu, 2015). The paper industry is currently the main producer of lignin, which is extracted to avoid a yellowish-brown look in the paper product and is normally discarded as a residue in the black liquor fraction. It is estimated that approximately 70 million tons of lignin is extracted annually mainly from the pulp and paper industry (Boerjan, Ralph and Baucher, 2003; Lancefield and Westwood, 2015; Liu, Jiang and Yu, 2015). Currently, the most common usage of both black liquor and extracted industrial lignin is directly burning (accounting for about 95% of the total lignin market) to produce heat and power in the paper process itself (Liu, Jiang and Yu, 2015; Steven Mufson, 2009). The process can hardly make the most use of lignin and may produce pollutants (i.e. organic pollutants due to incomplete combustion, particulate matters etc.). Given its high composition in aromatic compounds, the high-value usage of lignin as a platform chemical in biorefining has drawn increasing attention in recent years (Van den Bosch et al., 2015; Cornella and Martin, 2014; He, Zhao and Lercher, 2012; He, Sun and Han, 2013; Saidi et al., 2014; Zhang et al., 2013).

1.1.4 Fast pyrolysis of lignin

Fast pyrolysis of lignin has been intensively investigated since late 2000s, and it is accepted as a feasible and viable route to convert lignin into value added fuel additives (Bridgwater, 2012; Bridgwater and Peacocke, 2000; Jung et al., 2015). However, as aforementioned, the primary bio-oil produced from fast pyrolysis of lignin cannot be directly used in fuel applications. This is because of its inadequate properties, such as acidity, low calorific value, and low stability, which are a consequence of its high oxygen content in composition. The bio-oil derived from primary fast pyrolysis of lignin mainly consists of compounds such as Phs, aldehydes, and ketones which are lower reforming active compounds (Mu et al., 2013; Shen et al., 2010) (see **Fig. 1-2**). The effective removal of the oxygen by catalytic reforming is therefore crucial for increasing the amount of aromatic hydrocarbons (AHs) in composition, making the bio-oil compatible with the existing fossil fuel infrastructure and widening its use (Liu et al., 2014; Zhang et al., 2013). Zeolites with dispersed Brønsted acid sites, such as HZSM-5 (HZ), as

well as modified zeolites, have been proven as suitable catalysts for this deoxygenation process (Mukarakate et al., 2014, 2015; Vichaphund et al., 2014; Yildiz et al., 2013).

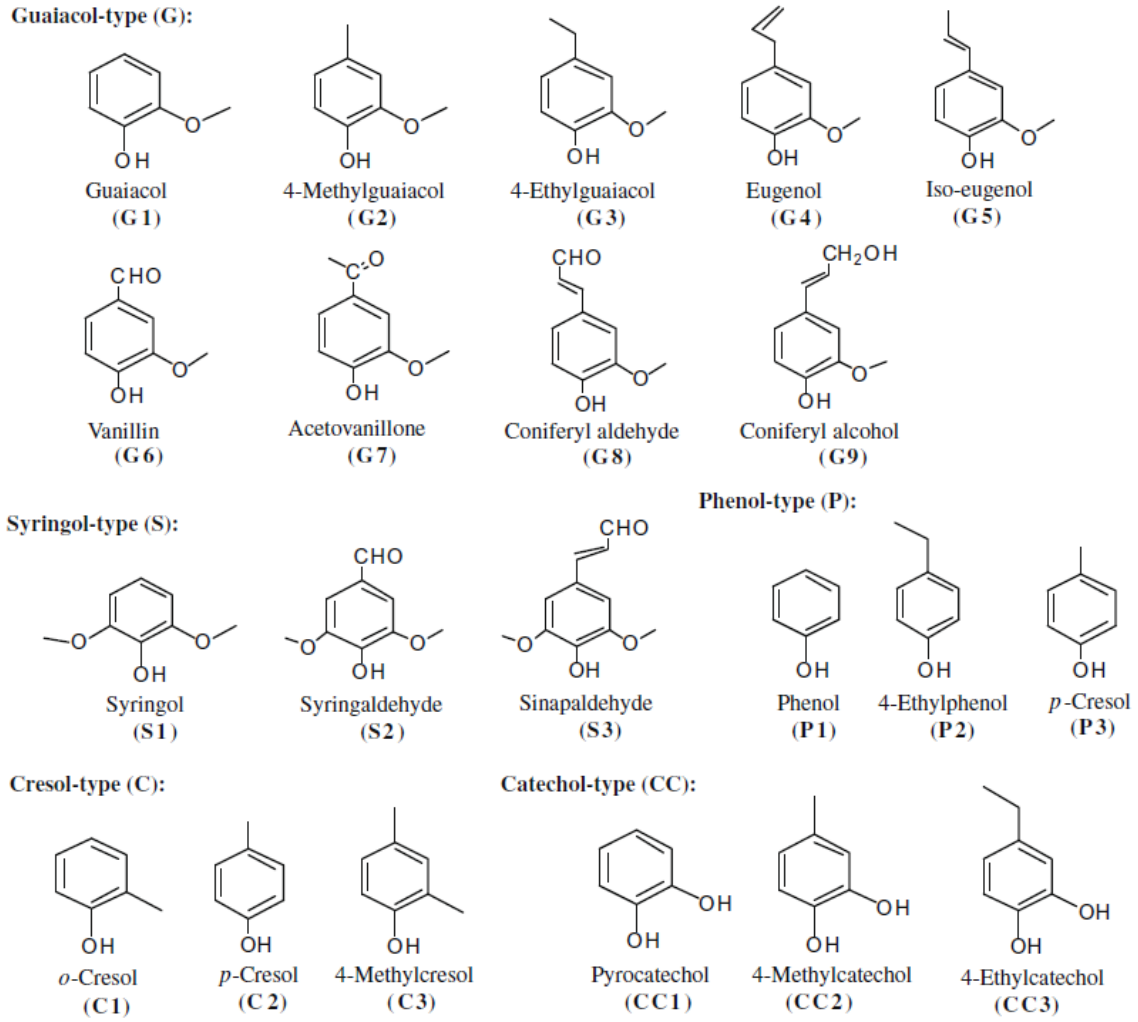

Fig. 1-2 Typical compounds in lignin-derived primary bio-oils (Shen et al., 2010)

Fast pyrolysis of lignin coupled with catalytic reforming of the bio-oil precursors vapours to produce AHs is a promising approach to realise effective utilisation of lignin (Alonso, Bond and Dumesic, 2010), and this process has been intensively studied in the literature (Adam et al., 2006; Adjaye and Bakhshi, 1995; Chantal et al., 1984; Gayubo et al., 2004; Samolada et al., 2000; Shen et al., 2010). It has been found that oxygen containing aromatic compounds in lignin derived bio-oil affect more significantly the reforming performance of catalysts than oxygen containing aliphatic compounds such as methanol, ethanol, acetic acid etc.

(Xiong et al., 2010). Due to the complex composition of the primary liquid products, especially the presence of oxygen containing aromatic compounds derived from the fast pyrolysis of lignin, further studies on the reactions occurring to each type compound and oxygen functionality are essential to accurately understand and control the fast pyrolysis of lignin with catalytic reforming.

Methoxyl group is an oxygen containing functional group which abundantly exists in the components present in the primary bio-oil obtained from the fast pyrolysis of lignin, such as anisole, guaiacol, syringol and their derivatives (Shen et al., 2010) as shown in **Fig. 1-2**. Methoxyl group further decomposes either in-situ in fast pyrolysis reactions or ex-situ in downstream catalytic reforming stages to give rise to phenolic compounds (Phs) and AHs compounds. Understanding the reactivity of the methoxyl group is important to properly assess the catalytic reforming process of these lignin-derived aromatic compounds, and is essential to tailor the compound distribution in the final liquid product.

1.1.5 Anisole as model compound

In this thesis, anisole has been selected as model for the compounds having the methoxyl group functionality contained in the primary bio-oil fraction. Anisole (or methoxybenzene) is an prototype model compound to investigate the reactivity of methoxyl-based lignin-derived compounds (Hurff and Klein, 1983), because:

- the structure of anisole is relatively simple, and the pyrolysis products can be analysed more conveniently and are more reliable compared to other model compounds (i.e. guaiacol, syringol).
- methoxy group is the unique functional group in the anisole molecule, which allows the investigation to focus on the transformation of this functional group without the interaction with or impact of other functional groups.
- anisole is in the liquid phase at room temperature so that is readily fed continually in experiments.

1.2 Thesis aim and objectives

The research of this thesis is within the scope of catalytic reforming of bio-oi (vapour) derived from lignin fast pyrolysis. The aim of this work is to investigate

the reaction mechanism of the decomposition of anisole at different stages, and to address the effect of catalysts during the processes. The major work is to carry out experiments and modelling investigations regarding the decomposition of anisole over different catalysts and the relative samples characterization. A “top to bottom” idea penetrates throughout the whole research; theoretical modelling work would provide reference to reaction mechanism resolution and predictions for catalyst performance in both chemical absorption process and elemental reactions, and experimental investigation would then be implemented with the guidance of modelling results. The specific objectives set for the thesis are:

- To investigate the reaction process of non-catalytic and catalytic thermal decomposition of anisole;
- To investigate the mechanism of transmethylation in thermal decomposition of anisole over acid solid catalyst;
- To investigate the mechanism of deoxygenation in thermal decomposition of anisole over metal modified acid solid (bi-functional) catalyst;
- To evaluate different metal effects on the catalytic deoxygenation in thermal decomposition of anisole;
- To establish methodology for the design and evaluation of bi-functional catalysts used for catalytic reforming of lignin-derived aromatic compounds.

1.3 Novelty elements

The following implementations and outputs from the PhD project contribute to current knowledge:

- Comprehensive comparison of transmethylation reactions between non-catalytic and catalytic anisole decomposition across the reaction mechanism and products distribution in a large temperature range.
- Proposed novel mechanism supported by theoretical and experimental results for the deoxygenation reaction of anisole decomposition over base

metal/acid-solid bi-functional catalyst, and explanation of the role of each function during the catalytic process.

- Adopted bi-metal loading catalyst for the deoxygenation in anisole decomposition, including the evaluation of the effects of each loading metal.
- Resolved in-situ hydrogen supply mechanism for the deoxygenation reaction in the decomposition of anisole, and evaluated the potential of in-situ hydrogen supply during the reactions over different catalysts.
- Taking the lead in using DFT modelling on reactions analyses of the decomposition of anisole, and established systematic method with multi-approaches to investigate reactions.

1.4 Structure of the thesis

This thesis consists of five result chapters and appendix, in addition to the chapters of introduction, literature review, methodology and conclusion:

- Chapter 1 primarily provides the background and context of the PhD project and summarizes the aim, objectives and novelty elements of the thesis.
- Chapter 2 constitutes a literature review mainly on the state-of-the-art research on the decomposition of anisole, emphasizing the application of catalysts, investigations on reaction pathways and mechanisms of respect transmethylation and deoxygenation, and the method development regarding the chemical reaction investigation of anisole decomposition. Besides, the gaps in knowledge and research interests are identified.
- Chapter 3 describes both experimental and modelling methodology used in the investigations, comprising specific parameters and models adopted for the modelling investigation, the design details of fluidized bed reactor, material applied in the experiments, and characterization and quantification techniques.
- Chapter 4 includes the investigation of DFT modelling on the mechanism of transmethylation as a primary reaction of the non-catalytic and catalytic

decomposition of anisole. The effects of acid catalyst on transmethylation reaction are identified. Various acceptor compounds such as phenol, benzene, toluene, anisole, cresol, xylenol and tri-methyl phenol are investigated in the transmethylation reaction, and the transfer orientation preference on relevant molecules is also evaluated.

- Chapter 5 focuses on the modelling investigation of deoxygenation mechanism for Phs (intermediate compounds during the catalytic decomposition of anisole) over bi-functional catalyst. The adsorption energy of reactant module onto various transition metals is calculated, and the adsorption capacity onto bi-functional catalyst is predicted by molecular modelling. Additionally, the interactions between reactant anisole and bi-metal surface are investigated. Finally, the deoxygenation mechanism of Phs over bi-functional catalyst is investigated and related reactions are modelled.

- Chapter 6 describes the experimental investigation of transmethylation mechanism in both non-catalytic and catalytic decomposition of anisole. The distribution of products in the liquid fraction, with focus on the Phs, is evaluated to explain the catalytic activity of the HZ zeolite on the transmethylation process compared to the non-catalytic reaction. The effects of temperature and Si/Al ratio of HZ on yields and distribution of the products are also investigated in detail.

- Chapter 7 exhibits the experimental investigation on the catalytic deoxygenation of anisole over single metal loaded HZ. The effects of temperature, type of metal, and metal loading ratio on the deoxygenation behaviour in anisole decomposition are investigated. Various catalyst characterizations are applied to both fresh and spent catalysts to establish the reaction pathways over various bi-function catalysts.

- Chapter 8 describes the experimental investigation of deoxygenation reaction in anisole decomposition over bi-metal loading HZ catalyst, with the focus on the effect of temperature, metal composition, and metal loading ratio. The synergistic effect between two metal loadings is illustrated.

- Chapter 9 draws the main conclusions from the research project. This final chapter includes an outlook to future research work.

1.5 Publications

This thesis has resulted in 5 papers; one has been already published, one has been submitted, and three are under preparation. In addition, 3 communications have been accepted in international conferences. Details are listed below.

Published:

[1] **Jiajun Zhang**, Beatriz Fidalgo, Dekui Shen, Rui Xiao, Sai Gu. (2016) 'Mechanism of transmethylation in anisole decomposition over HZSM-5: Experimental study', Journal of Analytical and Applied Pyrolysis, 122, pp. 323–331.

Submitted to journal "Chinese Journal of Catalysis":

[1] **Jiajun Zhang**, Beatriz Fidalgo, Athanasios Kolios, Dekui Shen, Sai Gu. Mechanism of transmethylation in anisole decomposition over HZSM-5: Density Functional Theory (DFT) modelling

Manuscripts in preparation:

[1] **Jiajun Zhang**, Beatriz Fidalgo, Athanasios Kolios, Dekui Shen, Sai Gu. Mechanism of deoxygenation in anisole decomposition over HZSM-5: Density Functional Theory (DFT) modelling

[2] **Jiajun Zhang**, Beatriz Fidalgo, Athanasios Kolios, Dekui Shen, Sai Gu. Mechanism of deoxygenation in anisole decomposition over single metal loaded HZSM-5: Experimental study

[3] **Jiajun Zhang**, Beatriz Fidalgo, Athanasios Kolios, Dekui Shen, Sai Gu. Mechanism of deoxygenation in anisole decomposition over bi-metal loaded HZSM-5

Conference (oral presentations):

[1] **"International Bioenergy Conference 2017", Manchester, UK. March 22nd to 23rd, 2017**

Jiajun Zhang, Beatriz Fidalgo, Dekui Shen, Rui Xiao, Sai Gu, Abstract: Mechanism of catalytic hydrodeoxygenation for Phs over metal loaded HZSM-5 – A Density Functional Theory (DFT) study

[2] **"AIChE annual meeting 2016", San Francisco, US. November 13th to 18th, 2016**

Jiajun Zhang, Beatriz, Fidalgo, Dekui Shen, Abstract: Study of transmethylation as primary step on the decomposition of methoxy-rich lignin model compound over zeolite catalyst.

[3] **"Engineering Thermophysics Annual Conference", Maanshan, China. October 21st to 23rd, 2016**

Jiajun Zhang, Mengmeng Zhou, Dekui Shen, Rui Xiao, Paper: Mechanism study of transmethylation in anisole catalytic pyrolysis.

Besides, I have contributed as second author to another publication not directly related to my PhD topic:

[1] Shuheng Yao, **Jiajun Zhang**, Dekui Shen, Rui Xiao, Sai Gu, Ming Zhao, Junyu Liang. (2016) 'Removal of Pb(II) from water by the activated carbon modified by nitric acid under microwave heating', Journal of Colloid and Interface Science, 463, pp. 118–127.

2 Literature review

This chapter provides a critical review of the published scientific literature on the topic of anisole decomposition. Anisole is usually used a model compound of compounds containing the methoxyl group functionality (Hurff and Klein, 1983). The review focuses on the application of catalysts, reaction pathways and mechanism and the development of research methods, with the aim to point out the knowledge gaps and the research interests in this area.

2.1 Anisole decomposition

The interest in investigating the decomposition of anisole (methoxybenzene) has its origin in the thermal decomposition of low-rank coals during the 1940s, and continues focusing on the reaction kinetics and pathways between the 1970s to 1980s (Hurff and Klein, 1983; Kislitsyn, Savinykh and Latyshev, 1972; Mackie, Doolan and Nelson, 1989). Renovated attention on the catalytic decomposition of anisole as a model compound of lignin has developed in the last decade, with the increasing research interests in resourceful use of lignocellulosic biomass to address challenges on energy crisis and climate change (González-Borja and Resasco, 2011; Li et al., 2014a; Pichaikaran and Arumugam, 2016; Runnebaum et al., 2011b; Xiong et al., 2010; Zhu et al., 2011; Zhu, Mallinson and Resasco, 2010). Current research on the anisole decomposition focuses on the reaction mechanisms in order to completely understand the interface interactions between reactants and catalytic active sites, and orientation control to the catalytic process towards desirable products (Rahzani et al., 2017; Tan et al., 2017; Zhang et al., 2016).

2.1.1 Non-catalytic decomposition of anisole

Many studies have been implemented in early stage regarding the non-catalytic decomposition of anisole to investigate the products distribution, mechanisms, and even kinetic parameters of the reactions (Lin and Lin, 1986; Mackie, Doolan and Nelson, 1989), and there are also several recent investigations on non-catalytic decomposition implemented with novel methods for pyrolysis (Li et al., 2014a; Taghvaei et al., 2014). Mackie et al. (Mackie, Doolan and Nelson, 1989)

carried out experiments on non-catalytic anisole decomposition at the temperature range between 570°C to 730°C, and they found the primary liquid products at 570°C were phenol and cresols, and the gaseous products consisted of methane, ethane and CO. While at 650°C, the liquid products consisted of benzene, methylcyclopentadiene, benzaldehyde, toluene, benzofuran, dibenzofuran, and naphthalene, and ethane and trace of ethylene were detected as gaseous products. Several studies have suggested that the reaction mechanism of non-catalytic anisole decomposition is based on radical reactions, and the methyl radical transfer played important role in these processes. The decomposition starts by the rupture of the CH_3-O bond and followed by further decomposition of phenoxy radicals to cyclopentadienyl radical and CO, as shown in Reaction 1 and Reaction 2 respectively (Lin and Lin, 1986; Mackie, Doolan and Nelson, 1989). In a similar investigation, Li et al (Li et al., 2014a) considered that the cyclopentadienyl can then either add a hydrogen atom to generate cyclopentadiene or continue the decomposition into acetylene and propargyl radical, as shown Reaction 3 and Reaction 4.

$$C_6H_5OCH_3 \rightarrow C_6H_5O^{\cdot} + CH_3^{\cdot} \quad (1)$$

$$C_6H_5O^{\cdot} \rightarrow C_5H_5^{\cdot} + CO \quad (2)$$

$$C_5H_5^{\cdot} + H^{\cdot} \rightarrow C_5H_6 \quad (3)$$

$$C_5H_5^{\cdot} \rightarrow C_3H_3^{\cdot} + C_2H_2 \quad (4)$$

Mulcahy et al (Mulcahy et al., 1967) firstly investigated the potential hydrogen source for the formation of molecules of phenolic compounds (Phs), and concluded that the hydrogen atoms were produced by abstraction reactions from anisole and used in the formation of Phs and methane, as shown in reaction (5) and (6). Moreover, the formed anisyl radical could subsequently decompose to benzaldehyde and produce hydrogen radical, as shown in reaction (7)

$$C_6H_5O^{\cdot} + C_6H_5OCH_3 \rightarrow C_6H_5OH + C_6H_5OCH_2^{\cdot} \quad (5)$$

$$CH_3^{\cdot} + C_6H_5OCH_3 \rightarrow C_6H_5OCH_2^{\cdot} + CH_4 \quad (6)$$

$$C_6H_5OCH_2^{\cdot} \rightarrow C_6H_5CHO + H^{\cdot} \quad (7)$$

It has been observed that cresols are usually the main products during the non-catalytic decomposition of anisole, and their formation is considered to be due to the isomerization of anisole, which has been termed as transmethylation in modern research (Meng et al., 2015; Prasomsri et al., 2011). The methyl radical transfer was identified firstly by Mulcahy and Williams (Mulcahy et al., 1967; Mulcahy and Williams, 1965) by proposing the reaction (8), and was accepted and confirmed by other studies (Lin and Lin, 1986; Mackie, Doolan and Nelson, 1989).

$$C_6H_5O^{\cdot} + CH_3^{\cdot} \rightarrow \text{ortho-}C_6H_4(OH)CH_3 + \text{para-}C_6H_4(OH)CH_3 \quad (8)$$

Aromatic hydrocarbons (AHs; including benzene, toluene, xylene etc.) are often the desirable products in thermal decomposition of anisole. However, they are normally produced to little extent at moderate temperature range (below 700°C) due to the recalcitrant bond of Aryl-O (also known as C_{sp^2}-O bond) (Li et al., 2014a; Mackie, Doolan and Nelson, 1989). Although, some authors have reported that the benzene formation is based on recombination reaction with two propargyl radicals (Dagaut, 1998; Miller and Melius, 1992), this pathway has not been observed in the experimental studies for the non-catalytic decomposition of anisole, instead propyne can be formed by the propargyl radicals and hydrogen (Li et al., 2014a; Scheer et al., 2010). Indeed, more literature agreed that benzene formation during anisole decomposition is likely to occur through bicyclic intermediate and ring expansion of methylcyclopentadiene (1-, 2-, and 5-methylcyclopentadiene) by abstracting two hydrogen atoms as shown in reaction (9) (Dubnikova and Lifshitz, 2002; Lamprecht, Atakan and Kohse-Höinghaus, 2000; Lifshitz et al., 2005). This mechanism has been experimentally demonstrated by Lin et al (Li et al., 2014a)

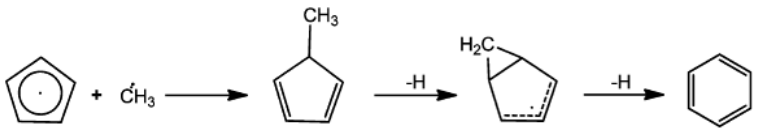

(9)

On the contrary to the transmethylation reactions during the non-catalytic decomposition of anisole, the mechanism of the deoxygenation reactions has been less reported in literature as they are not the significant reactions in the non-

catalytic decomposition of anisole. It is also found that the starting point of temperature for non-catalytic decomposition of anisole has been inconsistently reported (Li et al., 2014a; Mackie, Doolan and Nelson, 1989; Scheer et al., 2010; Wu, Fu and Lu, 2013), and most of previous studies have mainly focused on the radical interaction within a narrow temperature range (500°C or less) without considering the evolution of the product profile at a wider temperature change.

2.1.2 Decomposition of anisole over zeolite catalysts

The application of lignin fast pyrolysis in fuel additives compounds production is limited by the low selectivity to desirable aromatic hydrocarbons (AHs). Numerous studies have demonstrated that acid solid catalysts, especially acid zeolites catalysts, favour the upgrading of lignin derived bio-oil into targeted products, in either in-situ or ex-situ fast pyrolysis; this is because zeolite catalysts present large specific surface area, great stability during reactions and dispersed acid sites (Adjaye and Bakhshi, 1995; Chantal, Kaliaguine and Grandmaison, 1985; Gayubo et al., 2004; Horne and Williams, 1996; Li et al., 2012; Ma, Troussard and van Bokhoven, 2012). Therefore, a number of investigation specially focused on the catalytic decomposition of anisole over sole zeolites catalysts (Adjaye and Bakhshi, 1995; Prasomsri et al., 2011; Thilakaratne, Tessonnier and Brown, 2016; Zhu, Mallinson and Resasco, 2010).

Thilakaratne et al. explored the sequence decomposition of anisole over ZSM-5 zeolite in ammonia form at 600°C. They reported very high AHs yield of 58.4% without any yield of phenolic products, and the selectivity of BTX for 69.8% (Thilakaratne, Tessonnier and Brown, 2016). However, they did not explore the products profile of catalytic decomposition of anisole at other temperatures. Zhu et al. (Zhu, Mallinson and Resasco, 2010) studied the influence of operating condition on the decomposition of anisole over HZSM-5 (HZ), including temperature ranging from 200°C to 550°C, space times (weight of catalyst (g)/feeding mass flowrate (g/h), W/F) from 0.2 to 1.0 h, the addition of hydrogen in carrier gas, and the addition of water in feeding. The conversion of anisole and grouped liquid products obtained from their study are shown in **Fig. 2-1** and **Fig. 2-2** respectively. During the first 0.5 h of reaction, Zhu et al. observed a quick

increase in conversion with temperature, the conversion of anisole being 100% at 500°C. At these conditions, phenol (Ph) and cresol isomers (Cr) were the main liquid products, with the presence of xylenol isomers (Xol) and methyl-anisole isomers (MA). The authors also highlighted the presence of other minor products including AHs, dimethyl-anisole isomers, trimethyl-phenol isomers, and heavy products such as naphthalene and methylated naphthalene. Similar products profiles were obtained by other studies based on HZ (Chantal, Kaliaguine and Grandmaison, 1985; Horne and Williams, 1996). Zhu et al. (Zhu, Mallinson and Resasco, 2010) also demonstrated that W/F had similar effect as temperature on anisole conversion and products distribution, and the presence of hydrogen in the carrier gas stream did not exhibit much effect on the conversion of anisole or products distribution because of the absence of a metal function in the catalyst; however, the addition of water dramatically improved the conversion of anisole and the yield of Ph while decrease the yield of MA, as shown in **Fig. 2-3** and **Fig. 2-4**. The authors addressed that the positive effect of water was reversible and was not related to catalyst deactivation.

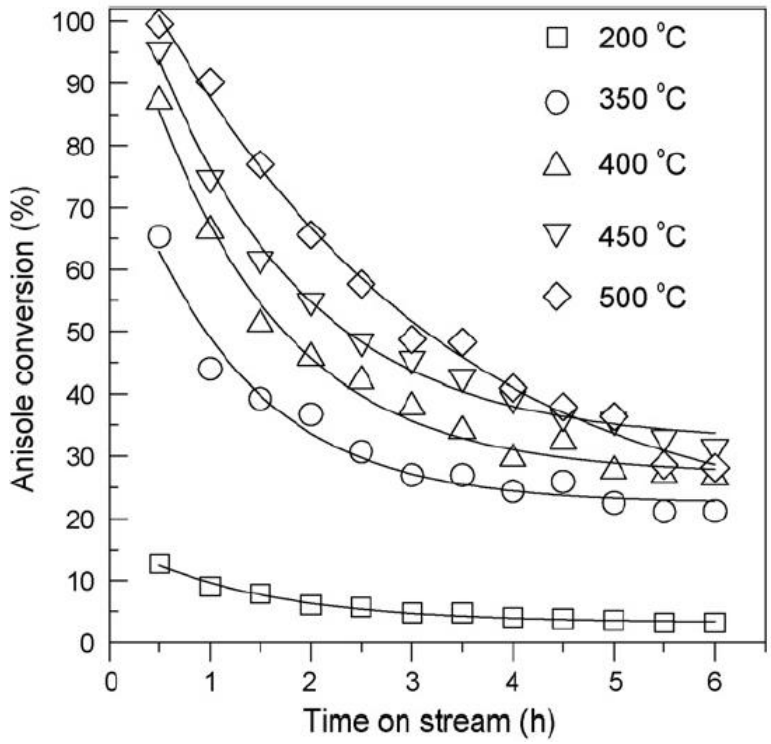

Fig. 2-1 Anisole conversion as a function of time on stream (TOS) over HZ at various temperatures. Space time (W/F) = 0.5 h (Zhu, Mallinson and Resasco, 2010)

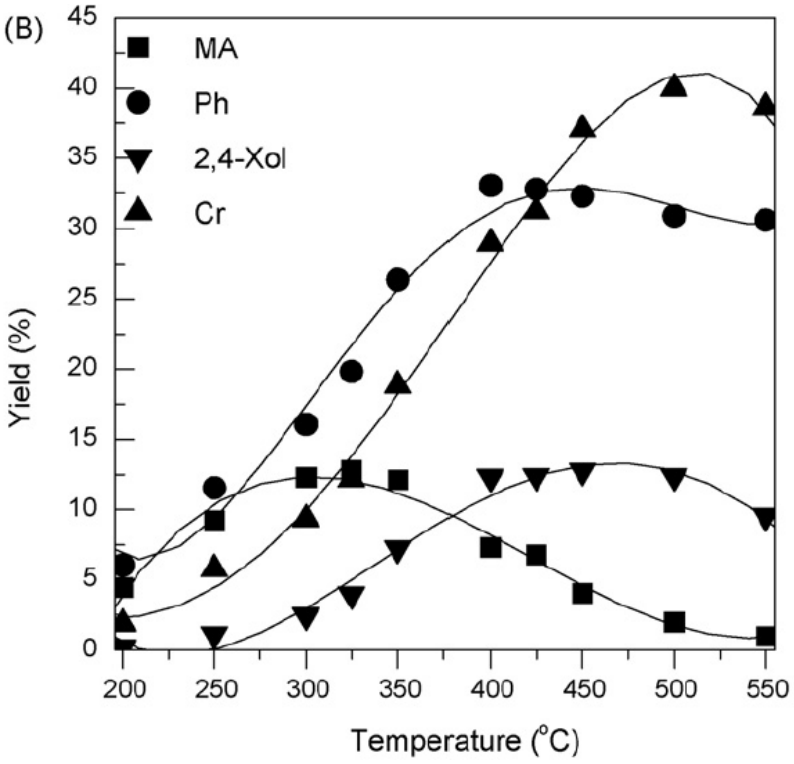

Fig. 2-2 Effect of reaction temperature on major product yields over HZ. W/F = 0.5h, TOS = 0.5h (Zhu, Mallinson and Resasco, 2010)

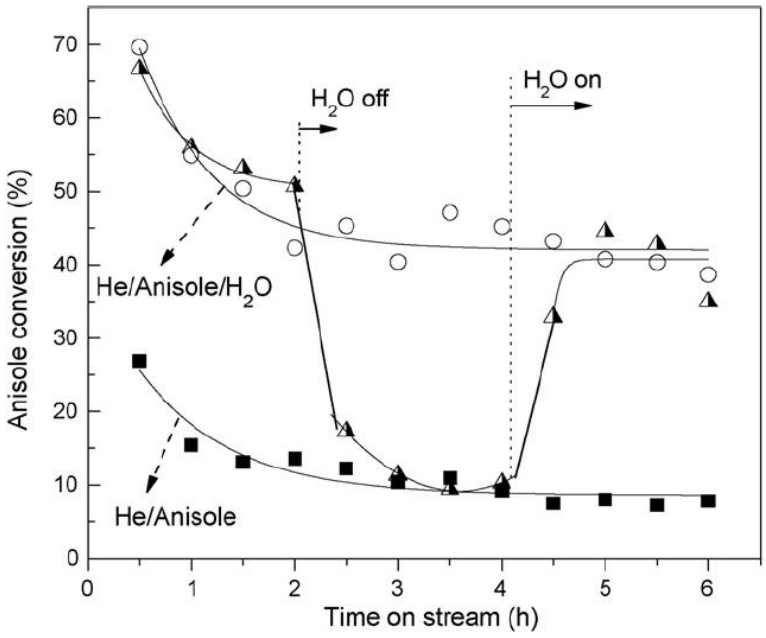

Fig. 2-3 Effect of water addition on anisole conversion over HZ. Reaction conditions: W/F = 0.083 h, 400°C. Full symbols: no water; open symbols: continuous water addition; half-full symbol: water addition on–off–on (Zhu, Mallinson and Resasco, 2010)

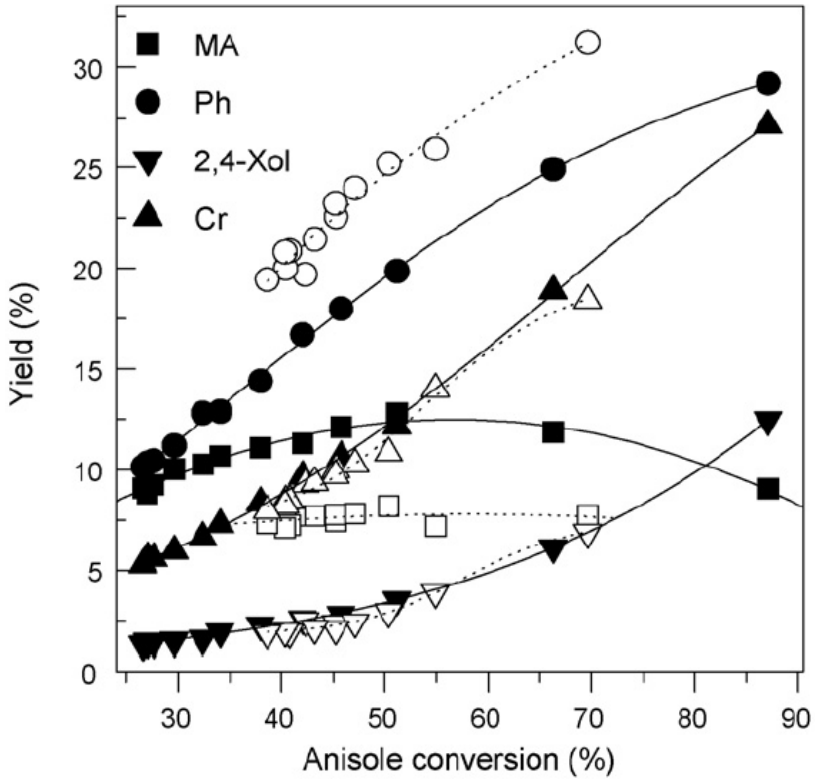

Fig. 2-4 Effect of water addition on major product yields as a function of anisole conversion over HZ. Reaction conditions: W/F = 0.083h with water added and W/F = 0.5 h without water condition. The variable conversion data was obtained at varying time on stream. Full symbols: no water; open symbols: with water addition. (Zhu, Mallinson and Resasco, 2010)

Prasomsri et al. (Prasomsri et al., 2011) reported the anisole decomposition over HY zeolite at 400°C. The research compared co-feeding anisole and hydrocarbon mixtures (i.e. propylene, n-decane, benzene, or tetralin) as potential hydrogen donors. They argued that the conversion of anisole and products distribution based on HY zeolite were like those obtained over HZ zeolite at the same temperature, although no AHs were obtained. The study reported that tetralin had the most positive effect on improving the conversion of anisole from 84 wt.% to 100 wt.%, and simultaneously reducing coke formation from 11.8 wt.% to 6.0 wt.%. However, the co-feeding of anisole and tetralin yielded less phenol and cresols. On the other hand, the positive effect of co-feeding on the decomposition of anisole was not demonstrated at other temperatures.

The literature review in this section has shown the limited research dedicated to investigate anisole decomposition over sole zeolite catalyst, carried out in addition at a narrow temperature range below 600°C. To the best of knowledge, the performance of catalysts and product distribution of anisole decomposition over sole zeolite catalysts at temperatures higher than 600°C have not been investigated. Reported research suggests the positive effect of zeolite on anisole decomposition, and HZ is described as one of the best zeolite catalysts to achieve high conversion and selectivity to AHs, due to its unique structure and content of acid sites (Guisnet and Gilson, 2002; Ivanova et al., 2007; Thilakaratne, Tessonnier and Brown, 2016). Nevertheless, existing research lacks comparison with non-catalytic decomposition of anisole to assess to what extent the presence of zeolite catalyst affects the decomposition of anisole.

2.1.3 Decomposition of anisole over metal based solid catalysts

Metal based (loaded) solid catalysts are one type of the most promising catalysts used in lignin fast pyrolysis and the upgrading of its derived bio-oil to produce AHs. These catalysts consist of active metals dispersed on a solid support. Transition metals have been observed to be highly active cataysts for product reforming. Various supports have also been studied including inert metal oxides (i.e. SiO2, Al_2O_3 etc.), acid zeolite (i.e. HBeta, HZ etc.) and even carbon nanofibers (Mu et al., 2013), with zeolite being the most widely used support (González-Borja and Resasco, 2011; Runnebaum et al., 2012; Xiong et al., 2010; Zhu et al., 2011).

Noble metals have been widely used in the investigation of lignin derived bio-oil upgrading and catalytic reforming of representative model compounds. Runnebaum et al. (Runnebaum et al., 2011b, 2011a, 2012) investigated the anisole decomposition over Pt/Al_2O_3 with hydrogen supply at 300°C and 140kPa, and reported that Phs were the most abundant products. Zhu et al (Zhu et al., 2011) used Pt/HBeta catalyst in anisole decomposition at 400°C and atmospheric pressure with a H_2/anisole ratio of 50; the major products are shown in **Table 2-1**.

Table 2-1 Major product distributions for complete conversion of anisole over HBeta and complete deoxygenation of anisole over Pt/SiO2 and Pt/HBeta catalysts (Source: (Zhu et al., 2011)).

Catalyst	HBeta	1%Pt/SiO_2	1%Pt/Beta	1%Pt/Beta
W/F(h)	0.5	4	0.33	1.5
Major product yield (mol $_{carbon}$%)				
Phenol	39.5	0.2	0.1	0.7
Cresols	33.5	0	0.2	0.6
Xylenols	24.2	0	0	0.3
C_{1-2}	0.2	15.4	6.0	4.2
C_3	0.2	0	0.4	0.7
C_{4-9}	0.2	14.1	1.6	1.5
Benzene	0.1	69.2	51.2	40.2
Toluene	0.1	0.8	27.6	31.8
Xylenes	0.3	0	10.6	14.4
C_9+aromatics	0.3	0	1.7	3.4

They reported a BTX yield of 89.4 wt.% over 1%Pt/HBeta with only trace of Phs, and the BTX yield was dramatically improved compared to that for sole HBeta. Zhu et al. also studied the effect of the support by comparing HBeta and SiO_2 performance, and found that the use of an acid support leads to higher yields of methyl containing AHs (toluene and xylenes). They pointed out that acidic function of the catalyst (i.e. the support HBeta) catalysed the methyl transfer reaction, while the metal function (i.e. the Pt active sites) accelerated both methyl transfer and deoxygenation reactions, and the metal favoured the cleaning of adjacent acid sites by hydrogenation of the precursors of coke (Zhu et al., 2011).

Other research on the use of noble metals for the catalytic decomposition of anisole can be found in literature. In general, Pt has been the most commonly

investigated metal catalyst with other noble metals rarely reported in the literature, and its performance has been found to highly depend on the selected support, and operating conditions such as temperature and hydrogen flow. González-Borja and Resasco (González-Borja and Resasco, 2011) used monolithic Pt-Sn bi-metal catalysts in anisole decomposition at 400°C and atmospheric pressure, and obtained almost 60 mol% of BTX, which mainly consisted of benzene. Ruthenium supported mesoporous aluminosilicate showed poor performance on anisole decomposition with less than 10% conversion in the temperature range of 300 to 400°C (Pichaikaran and Arumugam, 2016). Tan et al (Tan et al., 2017) found that Pt showed high selectivity (80%) of benzene when it was loaded on Fe_2O_3 but a high selectivity (93%) of phenol over SiO_2 in the decomposition of anisole both at 100°C under H_2 flow and atmospheric pressure; nevertheless, low conversion of less than 15% were obtained in both cases.

Regardless the increasing interest of using base metals in catalytic fast pyrolysis of lignin and other model compounds (Barta et al., 2010; Horáček et al., 2012; Jongerius et al., 2012; Klein, Saha and Abu-Omar, 2015; Mukundan et al., 2015; Shu et al., 2017; Song et al., 2013b; Toledano et al., 2013), anisole decomposition over base metal based catalysts have been rarely reported. Khromova et al. (Khromova et al., 2014) and Smirnov et al.(Smirnov et al., 2014) reported the anisole decomposition over Ni-Cu/SiO_2 (loading of Ni ranged in 15~85%, and loading of Cu ranged in 75~5%), and evaluated the effect of varied Ni/Cu ratios at 280°C and a hydrogen pressure of 6000 kpa. They obtained BTX yields lower than 10% and the dominant products were cyclohexane, methoxy-cyclohexane, and cyclohexanol. Their results show the obvious occurrence of the hydrogenation of the benzene ring during the reaction at the studied operation conditions. Pichaikaran and Arumugam (Pichaikaran and Arumugam, 2016) reported the yield of deoxygenated products was 34.9% over 7.0 wt.% Ni/mesoporous aluminosilicate at 450°C and H_2 flow rate of 50 mL/min. Xiong et al. (Xiong et al., 2010) evaluated the catalytic performance of Ni-Cu-Zn/Al_2O_3 in the electrochemical catalytic reforming of anisole for gas production at 700°C with a current of 4A. They found a good selectivity of 88.7% in hydrogen production with an anisole conversion of 98.3% in the experiments.

The information inferred from the literature review points that metal based solid catalysts promote the deoxygenation reactions in the decomposition of anisole, and noble metals (especially Pt) exhibit good catalytic performance. However, the application of noble metals is limited by their high costs. In comparison, the base metals are preferred in terms of lower cost but they have been investigated in the decomposition of anisole to a much lesser extent. The gaps in knowledge have been identified after the literature review:

- Few base metals have been applied directly to catalyse the decomposition of anisole, and there are no widely accepted evaluation criteria for the base transition metals applied to the reaction.
- Despite it is commonly acknowledge that acid sites play an important role in the decomposition reactions, limited literature reporting the use of bi-functional catalyst (i.e. consisting of a base metal and acid solid support) in the decomposition of anisole is available.

2.2 Reaction pathways and mechanism for anisole decomposition

The decomposition of anisole is commonly recognized to consist of two steps: transmethylation (methyl transfer) and deoxygenation (Li et al., 2017a; Zhang et al., 2016; Zhu, Mallinson and Resasco, 2010). Transmethylation is an isomerization reaction which involves the intramolecular (or intermolecular) transfer of a methyl group cleavage. In the case of the anisole decomposition at relatively low temperatures (below 500°C at atmosphere pressure), transmethylation is considered to be primary reaction aiding the subsequent formation of AHs (Cornella, Gómez-Bengoa and Martin, 2013; Mackie, Doolan and Nelson, 1989; Meng et al., 2015; Prasomsri et al., 2011; Wang et al., 2014), and the most dominant products from this stage are methyl-containing Phs, benzaldehyde, and olefins. Further decomposition of the Phs at higher temperature undergoes deoxygenation process and gives rise to AHs and even naphthenic hydrocarbons. The detailed pathways and mechanisms regarding these two reaction steps in anisole decomposition are reviewed in this section.

2.2.1 Transmethylation stage in the decomposition of anisole

Reaction pathways and detailed mechanism for non-catalytic transmethylation of anisole is reviewed in Section 2.1.1. It has been stated that it is widely accepted that the non-catalytic decomposition primarily consists of free radical reactions, and the transmethylation is regarded as an isomerization based on methyl free radical transfer intramolecularly and intermolecularly. Catalytic transmethylation over acid sites has been largely reported in phenol alkylation in the presence of methanol (Bhattacharyya et al., 2003; Bregolato et al., 2007; Sad, Padró and Apesteguía, 2008, 2010; Wang et al., 2004; Xu, Yan and Xu, 1999). However, catalytic transmethylation in anisole decomposition has been less investigated, and available literature focused on the general study of pathways and kinetic parameters for the transmethylation reactions, with no details on catalysis mechanisms despite their importance to understand the entire catalytic process (Ballarini et al., 2007).

Several authors have described the transmethylation in the decomposition of anisole over acid sites consisting of isomerization, dealkylation, and intermolecular methyl transfer, as depicted in **Fig. 2-5** (Sad, Padró and Apesteguía, 2010; Zhu, Mallinson and Resasco, 2010).

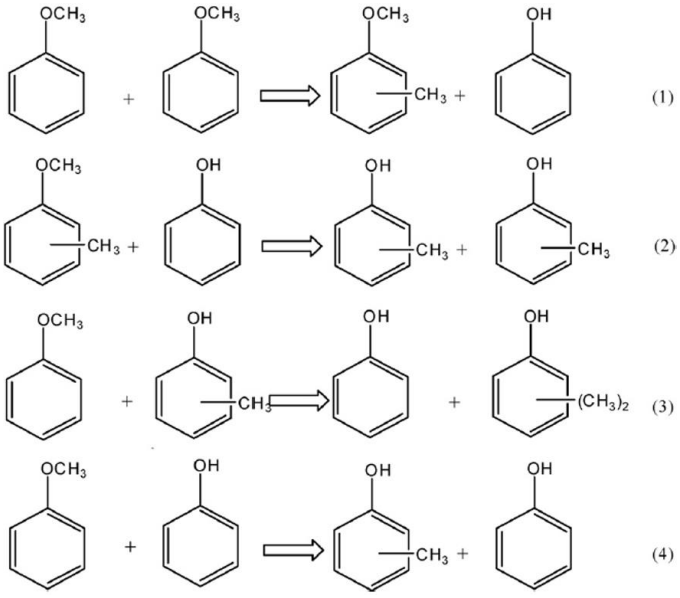

Fig. 2-5 Major reaction pathways of transmethylation in anisole conversion over HZ, T = 400°C. (Zhu, Mallinson and Resasco, 2010)

Regarding the position preference of transmethylation, Zhu et al. (Zhu, Mallinson and Resasco, 2010) argued that, using HZ as catalyst, the meta position was thermodynamically most favourable, while the ortho position was kinetically favoured and para position was the preferred by the shape selectivity of HZ. Thilakaratne (Thilakaratne, Tessonnier and Brown, 2016) reported the similar reaction pathways.

Even though the reaction pathway for the catalytic transmethylation is analogous to the non-catalytic reaction, the reaction mechanism for the former does not consist of free radical transfer. It has been reported that transmethylation in anisole decomposition over acid zeolite catalyst is largely influenced by Brønsted acid sites (Meng et al., 2015; Sad, Padró and Apesteguía, 2008, 2010). However, the precise mechanism for transmethylation in the anisole decomposition over acid sites is still unclear and rarely reported. Different, and sometimes inconsistent, reaction pathways and mechanisms have been proposed for explaining the same chemical process in previous studies. Thilakaratne et al. (Thilakaratne, Tessonnier and Brown, 2016) proposed the transmethylation mechanism based on the formation of a methenium ion during anisole decomposition on the Brønsted acid site as shown in **Fig. 2-6**; a phenol molecular is generated while giving a methylene radical, which constitutes the methenium ion together with the proton on the acid site, and the following transmethylation is based on the electrophilic attack of the methenium ion to adjacent molecules. However, the active group in the reaction is more likely to be the methylene radical but without much engagement of proton. There has been other study suggesting the formation of a methyl carbocation directly by the methyl group in the anisole molecule, and argued Si/Al ratio had significant effect on transmethylation (Meng et al., 2015). However, further evidence to prove the proposed mechanism regarding the transmethylation, or to evaluate the reactions based on the mechanism were not provided in the literature.

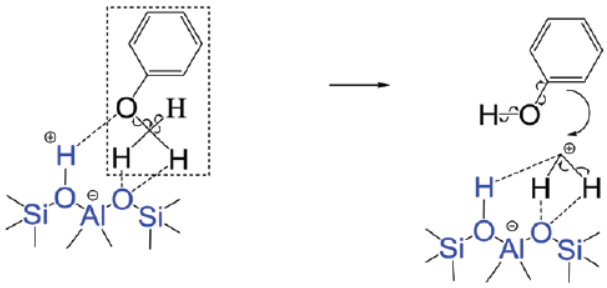

Fig. 2-6 Proposed mechanism for conversion of anisole over zeolites at 600 °C
(Thilakaratne, Tessonnier and Brown, 2016)

Nuclear magnetic resonance (NMR) tests has been used to detect possible carbon cations generated during reactions (Munson, Xu and Haw, 1993; Xu, Zhang and Munson, 1994); however, the application of NMR to track any evidence of the cation generated during the decomposition of anisole over acid catalyst has not been reported. Furthermore, no reaction network describing the comprehensive process of catalytic transmethylation in anisole decomposition has been published, and less details description are found in the literature on the interaction between molecular with acid site covering each step of transmethylation.

2.2.2 Deoxygenation stage in the decomposition of anisole

Deoxygenation during the decomposition of anisole has been largely investigated, and the reactions normally lead to AHs (AH) or cycloalkanes (Ghampson et al., 2017; González-Borja and Resasco, 2011; Khromova et al., 2014; Pichaikaran and Arumugam, 2016; Smirnov et al., 2014; Zhu et al., 2011). The reaction pathways and the mechanism of deoxygenation in non-catalytic decomposition of anisole is reviewed in Section 2.1.1. The non-catalytic deoxygenation is likely to happen through the formation of CO, and the formation of benzene is due to the expansion of methylcyclopentadiene. Nevertheless, it is worth noting that deoxygenation does not play an important role in the reaction when no catalyst is present as AHs were scarcely produced. In contrast, investigations of the deoxygenation in catalytic decomposition of anisole over catalysts (i.e. acid solid catalysts, metal/inert solid catalyst or metal/acid catalysts) are more intensively reported in the literature.

As mentioned in Sections 2.1.2 and 2.2.1, sole acid solid catalyst is found to be more active on the transmethylation reaction than the deoxygenation reaction, and it merely exhibits activity in deoxygenation at high temperatures (above 500°C at atmosphere pressure). On the other hand, transition metals loaded on inert solid support or acid solid catalyst have been widely applied in the deoxygenation reactions as described in Section 2.1.3. Most investigations with metal based catalysts consider the addition of hydrogen to the reaction favouring the occurrence of hydrogenation or hydrogenolysis along with deoxygenation, which is normally termed as hydrodeoxygenation (HDO) (Ghampson et al., 2017; Jin et al., 2014; Khromova et al., 2014; Song et al., 2013a; Takagi, 1967; Zhu et al., 2011). As explained in Section 2.2.1, Phs are the main products from transmethylation and considered as the precursors for AHs from deoxygenation reactions.

HDO over metal based inert solid (i.e. supports such as SiO_2, Al_2O_3 etc.) have been broadly investigated. Two parallel pathways have been reported for the HDO of Phs in the decomposition of anisole over metal/inert solid catalysts, leading to different products: (1) direct HDO giving rise to the formation of AHs and water; and (2) hydrogenation of the phenolic ring followed by deoxygenation, forming cyclohexene and its derivatives, and subsequent re-hydrogenation of the double bond of the cyclohexene to form cyclohexane and its derivatives (Odebunmi, 1983). The nature of the catalyst is considered to determine the reaction pathway (Ferrari et al., 2001; Gevert, Otterstedt and Massoth, 1987; Kallury, 1985; Laurent and Delmon, 1994; Odebunmi, 1983; Romero, Richard and Brunet, 2010; Viljava, 2000; Weigold, 1982). Zhu et al (Zhu et al., 2011) reported that direct HDO dominated the reaction of Phs over Pt/SiO_2 catalyst, even though cyclohexane and other aliphatic hydrocarbons were obtained when the W/F was higher than 1.0. A more comprehensive reaction network showing the occurrence of parallel reactions was proposed by Runnebaum et al. (Runnebaum et al., 2011b, 2011a) in the investigation of the decomposition of anisole over Pt/Al_2O_3 as shown in **Fig. 2-7**.

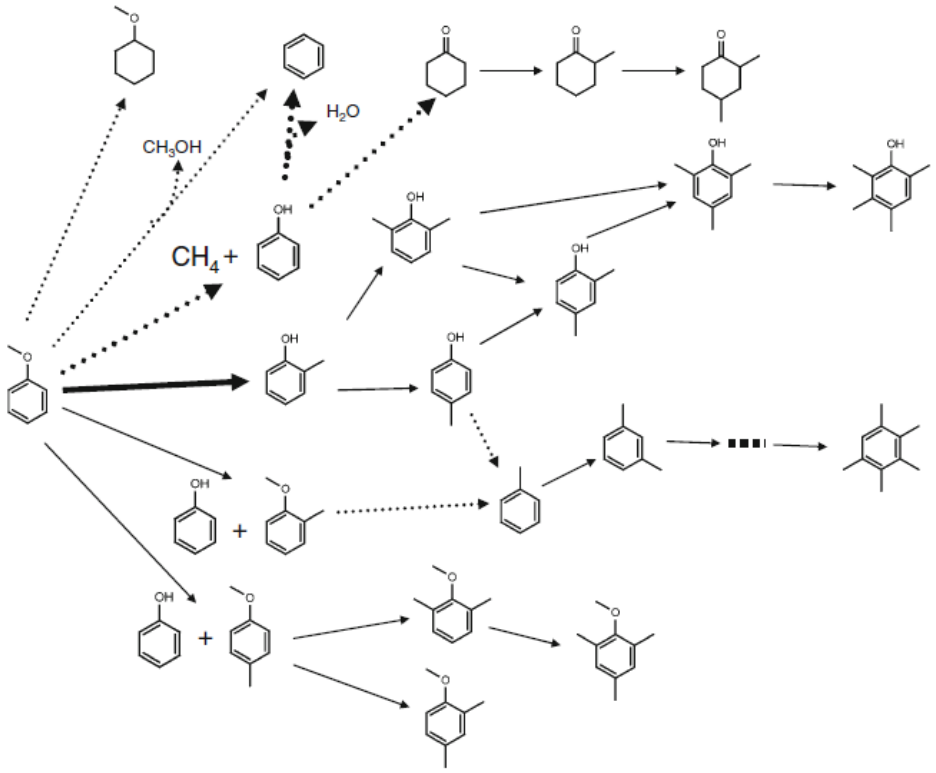

Fig. 2-7 Reaction network for the decomposition of anisole with hydrogen catalysed by Pt/Al_2O_3 at 300°C. Hydrogenation/HDO reactions are represented by dotted lines and methyl group transfer reactions by solid lines. H_2 as a reactant is omitted for simplicity. Bold arrows show the reactions that are kinetically most significant with the width of the arrow denoting a rough measure of rate (the wider the arrow, the faster the reaction). Source: (Runnebaum et al., 2011b)

The reaction pathways are broadly consistent with the investigation of Zhu et al., including the presence of traces of cyclohexanone and its derivatives in the products. Analogous reaction pathways have also been proposed by other researchers (González-Borja and Resasco, 2011; Runnebaum et al., 2012). Ghampson et al (Ghampson et al., 2017) reported the dominating role of direct HDO in the experiments of anisole decomposition over $Re\text{-}MoO_x/TiO_2$ and $Re\text{-}VO_x/TiO_2$; the authors pointed out that the combination of reduced Re and oxidation states of Mo and V showed distinct effect of on the production of AHs. Large yields of benzene and methoxy-cyclohexane over base metal catalysts such as $Ni/Cu/SiO_2$ has been observed (Khromova et al., 2014; Smirnov et al., 2014), pointing that the presence of the sole function of base metal results in less

control of the inhibition of the ring saturation and the formation of naphthenic hydrocarbon.

Compared to sole metal function, the HDO reaction pathways in anisole decomposition over bi-functional catalysts (i.e. metal loaded acid solid catalysts) have been reported to less extent. Existing literature states different reaction pathways when the acid function is added to the catalyst; Zhu et al (Zhu et al., 2011) reported that Pt/HBeta was a more effective catalyst for HDO in anisole decomposition compared to Pt/SiO2, without any cyclohexane or its derivatives being produced. Pichaikaran and Arumugam (Pichaikaran and Arumugam, 2016) also showed that the Ni-Ru/mesoporous aluminosilicate (Al-SBA-15) catalyst led to a conversion route of direct HDO without any cyclohexane production. These results point to the inhibiting effect of the Brønsted acid sites on the hydrogenation of the ring. This hypothesis is further confirmed by the experimental investigation with ^{13}C labelled anisole decomposition over sole acid catalyst (Thilakaratne, Tessonnier and Brown, 2016). They observed that the benzene ring remained intact throughout deoxygenation reactions. The potential function of Brønsted acid in blocking the hydrogenation of the ring has not been explicitly reported in literature. However, it is very important in mechanism investigation as it implies that the HDO may have different mechanism in the presence of bi-functional catalysts compared to sole metal catalysts.

Despite of the reaction pathways for HDO in the catalytic decomposition of anisole have been thoroughly discussed, less works has focused on the mechanism for the reactions, especially in terms of direct HDO.

González-Borja and Resasco (González-Borja and Resasco, 2011) studied the direct HDO over bimetal catalyst supported on inert solid and proposed that Phs might experience both direct C-O celeavage through hydrogenolysis and partial hydrogenation of the aromatic ring. However, Zhu et al. (Zhu et al., 2011) argued that a direct hydrogenolysis of the $C_{aromatic}$-OH bond was not likely to occur due to its stronger bond strength than that of the $C_{aliphatic}$-OH bond. More examples of HDO over sole metal catalysts occurring through partial hydrogenation of the phenolic ring near the $C_{aromatic}$-OH bond, and resulting in the formation of benzene

and water after dehydration, have been reported for the deoxygenation of phenol on $CoMo/Al_2O_3$ catalyst (Massoth et al., 2006) and HDO of Phs on Rh catalysts (Takagi, 1967). Nevertheless, the existing investigations do not provide sufficient information on the reaction details to support their proposed mechanisms. Recent modelling investigations based on Density Functional Theory (DFT) studies have provided more detailes on the mechanism of HDO in the anisole decomposition over sole metal catalysts (Réocreux et al., 2016; Tan et al., 2017). The DFT studies suggest that dehydrogenation reaction happens first to the methyl group, and it facilitates the breaking of C_{alkyl}-O bond with the formation of a surface phenoxy, which then undergoes either direct hydrogenation to produce phenol or further cleavage of C_{aryl}-O bond to form surface phenyl that finally leads to benzene through hydrogenation under the function of the metal oxophilicity. The DFT prediction provides a novel mechanism for HDO, which could explain the unexpected selectivities of benzene and phenol in anisole decomposition over noble metal surface. However, the proposed mechanism is similar to the radical reaction with anisyl radical formed in the abstraction reactions in the non-catalytic decomposition of anisole (Reaction (5)- (7) in Section 2.1.1) with the only diffrence of the radical state remaining on the metal surface rather than being transferried to the benzaldehyde.

In the case of deoxygenation over bi-functional metal/acid support catalysts, it has been reported that Brønsted acid sites show synergistic effect in enhancing the HDO rate, and that the metal loading may improve the rate of methyl transfer, also mainly catalysed by Brønsted acid sites (Zhu et al., 2011); however, the mechanism is still not clear and has been rarely reported. Specifically, research on detailed interactions between reactants and catalyst surface, the role of metal and acid catalytic sites in the deoxygenation reactions during anisole decomposition, and their combined effect on the reaction mechanism have not been reported in the literature.

On the other hand, most of the research work about deoxygenation stage in the catalytic anisole decomposition considers the external supply of hydrogen to the reaction atmosphere. The use of hydrogen not only increases the cost and risk

of the process, but also an excessive hydrogen supply normally leads to aromatic ring saturation with high selectivity towards cyclohexane and cyclohexanol (Khromova et al., 2014). There is an increasing interest in using alternative hydrogen sources, such as hydrogen rich AH mixtures (propylene, n-decane, benzene, or tetralin) (Prasomsri et al., 2011). Nevertheless, there is a lack of investigations that evaluate the ability of in-situ hydrogen supply during the reaction of anisole decomposition; even though the methyl group in the anisole molecule is a hydrogen rich group itself. Previous studies have suggested that the formation of carbonaceous deposit in anisole decomposition is related to the strong polycondensation of oxygenated compounds and the coke formation on the catalysts (Adjaye and Bakhshi, 1995; Zhu, Mallinson and Resasco, 2010). Thus, it can be hypothesised that the polycondensation can be a potential hydrogen source for the HDO reactions.

2.3 Research methods for the investigation of anisole decomposition reaction

Experiments and modelling are two main research methods applied in the investigation of heterogeneous reactions in the literature. The state-of-art of these two methods for their application in the decomposition of anisole is reviewed in this section.

2.3.1 Experimental methods

The most widely used reactors for the study of thermal decomposition of anisole are fixed bed reactor, fluidized bed reactor and autoclave reactor (Ardiyanti et al., 2012; Bridgwater, 2012; Bridgwater and Peacocke, 2000; Horáček et al., 2012; Pichaikaran and Arumugam, 2016; Thilakaratne, Tessonnier and Brown, 2016; Zhang et al., 2016; Zhu et al., 2011). Fixed bed is normally a cylindrical and horizontal tube with stationary packed bed during the reaction. It has the features of well understanding, simple construction, and being widely used in multi-phase reactions (Eigenberger and Ruppel, 2012). Fluidized bed achieves a good mixing of reactant and the bed material through fluidization, which refers to the particles in the reactor suspended due to fluid introduction from the bottom of reactor (Richardson, Backhurst and J Harker, 2002). A.V.Bridgwater (Bridgwater, 2012)

pointed out that the main advantages of bubbling fluidized bed are good temperature control and efficient heat and mass transfer for the reactions. It is also the most intensively applied and investigated reactor for the thermal conversion of various compounds currently. Autoclaves are batch-reactors without continue feeding and commonly used with high pressures for the reaction (Ardiyanti et al., 2012; Jin et al., 2014).

Beside the most common reactors, other reactors have been developed in past decades for reaction investigation. A tubular hyperthermal pulsed nozzle reactor was developed by Chen (Chen, 1994) as shown in **Fig. 2-8**, where reactants experiences high temperature in very short residence time in dozens of microseconds, so that primary products from thermal reactions can be captured while decreasing secondary reactions. This kind of reactor has been used in the mechanism investigation of the non-catalytic decomposition of anisole and to describe the aromatic growth (Friderichsen et al., 2001; Scheer et al., 2010).

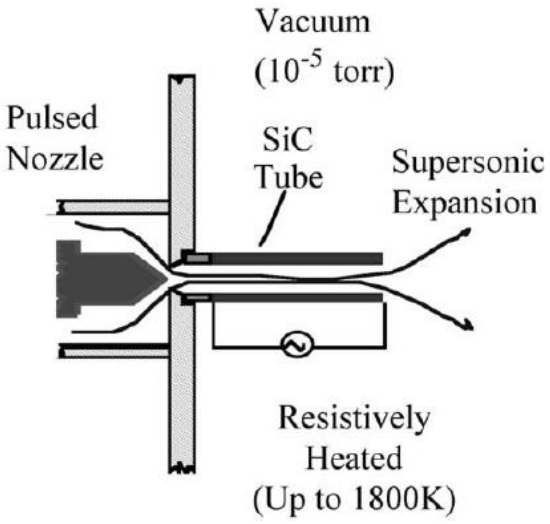

Fig. 2-8 Schematic diagram of hyperthermal nozzle (Friderichsen et al., 2001)

Other reactors such as single-pulse shock tube, dielectric barrier discharge plasma have also been used for the decomposition of anisole and related molecules (Lifshitz et al., 2005; Taghvaei et al., 2014). However, these reactors are mainly designed to investigate free radical reactions i.e. the non-catalytic decomposition of anisole, but less benefit the mechanism research of catalytic reactions. Xiong et al (Xiong et al., 2010) developed the method of

electrochemical catalytic reforming with the reactor equipped with Ni-Cr wire, which is adopted for heating and synchronously providing electrons to the catalyst bed, and it was reported that the reactor could promote the catalytic reforming performance of anisole over NiCuZn-Al_2O_3 catalyst by improving the conversion and hydrogen yield. There have been more reactors and methods used for catalytic fast pyrolysis like microwave reactor, entrained flow reactors, vacuum reactors, and plasma reactors etc., but they are rarely used as reactors for the mechanism research in the literature.

Apart from the development of various reactor configurations, experimental research regarding catalytic reaction pathways and mechanism has also benefit from the advanced characterization techniques in material science. For gaseous products, gas chromatography (GC) coupled with flame ionization detector (FID) has been widely used for the species detection. Regarding liquid products, GC-FID or GC-Mass Spectrometry (MS) provide highly accurate quantitative information of the existing species (Barry and Grob, 2004; Budiman, Nuryatini and Zuas, 2015). In addition, Nuclear Magnetic Resonance (NMR) has been used in quantifying the species in liquid and solid samples (Wei et al., 2014). For solid sample characterization i.e. catalyst or carbonaceous deposit, many techniques employing X ray are commonly used: X-Ray Diffraction (XRD) is used to detect the atomic and molecular structure of a crystal; X-ray Photoelectron Spectroscopy (XPS) is used to detect surface elements including their valences (Albers et al., 1998; Cheng et al., 2017; J.F.Watts and J.Wolstenholme, 2003; Liu et al., 2007); X-Ray Fluorescence (XRF) and energy-dispersive X-Ray Spectroscopy (EDS) are used to quantify the surface elemental analysis (Beckhoff et al., 2006; Corbari et al., 2008). Inductively Coupled Plasma (ICP)-MS has also been used for quantifying elements of solid samples (Tessonnier et al., 2006). The appearance of the solid surface can be observed using Scanning Electron Microscope (SEM) with up to micrometre level resolution, and Transmission Electron Microscopy (TEM) can provide higher resolution images up to 10nm (Gayubo et al., 2010; Shu et al., 2017). For acid catalyst, the type, amount and acidity are normally determined quantitively by Pyridine-Fourier Transform Infrared Spectroscopy (FTIR) or qualitatively by NH_3-temperature

programmed desorption (TPD). Textural properties including the specific surface area, pore volume, and mean pore size are commonly determined by BET analyses (Brunauer, Emmett and Teller, 1938). In the case of the catalysts with metal loading, the specific reduction temperatures for the metals can be determined by H_2-Temperature Programmed Reduction (TPR) (Ciambelli et al., 1995; Nie et al., 2012). On the other hand, the quantitative analysis of carbonaceous deposits is most frequently carried out by Thermogravimetry (TG). More advanced technique like Terahertz Spectroscopy has been developed and allows the characterization of electron distribution of the carbonaceous deposit (Parrott et al., 2009).

2.3.2 Computational methods

First-principle methods and molecular modelling are the two most frequently adopted computational methods for investigating reactions and surface chemistry (Broclawik et al., 2006; Hensley, Wang and McEwen, 2014a; Hernández et al., 2012; Kalita and Deka, 2009; Mo et al., 2013; Rimarcík et al., 2008; Yang et al., 2011). First-principle methods are in quantum scale and resolve reactions based on the calculations at the electron level (the minimum scale that calculation can currently reach). Molecular modelling is a larger scale computational method at the atom level. The method regards atoms as “balls” without electrons, and treats atomic interactions with developed forcefields. In this thesis, the first-principle method is used to predict the reactions and molecule properties; its fundamental theory is consequently reviewed in detail in this section.

2.3.2.1 First-principle methods

The basic concepts of various first-principle methods which have been reported in the literature and the state-of-art of the common DFT software applied in this thesis is reviewed below.

- Wave function

It is considered that most of reactions and compound properties are governed by the electron behaviour, because all chemical bonds are described by quantum mechanics (Marx and Hutter, 2000). Classical mechanics normally describes the

state of particle with its position and momentum, but it is difficult to be applied to describe electrons. According to the “Uncertainty Principle” proposed by Werner Heisenberg (Heisenberg, 1927), the specific position and momentum of an electron can hardly be measured at the same time. From the view point of quantum mechanics, electrons also behave like wave that is subject to the fluctuation rule, which can be depicted by matter wave in De Broglie hypothesis (Broglie, 1924). The concept of wave function for electrons was first proposed by Erwin Schrödinger in 1926 to describe all the states of electrons with Schrödinger equation (Schrödinger, 1926): ψ(x,y,z,t), where x, y, z refer to the space coordinate of one electron at the time t. However, Schrödinger did not establish a proper physical meaning for the wave function. Wave function was later interpreted as by Born (Max Born, 1954): the appearance probability of an electron in a unit region is proportional to the square of the wave function absolute value, $|\psi(x,y,z,t)|^2$. This interpretation proposes an understandable meaning to the wave function by linking it with the probability wave, so that the wave function is also termed as “probability amplitude”.

- Rationale of first-principle methods

Schrödinger equation provides an accurate method to determine properties of electrons. First-principle methods refer to the calculation based on the fundamental physical laws of electrons behaviour without any free parameters, by solving the Schrödinger equations. Most first principle methods convert the interaction between electrons into effective potentials, so that a set of one-electron Schrödinger-like equations are yielded which are constructed mainly by the wave functions, as shown in **Eq. 2-1** (Segall et al., 2002).

$$H\psi_n = \left(-\frac{\hbar^2}{2m}\Delta^2 + V_{ext} + V_{eff}\right)\psi_n = \epsilon_i\psi_n \qquad \textbf{Eq. 2-1}$$

where H is the Hamiltonian Operator that acts on the wave function ψ_n; and the operator involves three sub-operators: “$-\hbar^2\cdot\Delta^2/2m$” is kinetic-energy operator ($\hbar$ is reduced Planck constant: $h/2\pi=6.582*10^{-16}$ eV·s, Δ^2 is the Laplacian, m is the particle's "reduced mass"); V_{ext} is the external potential (Coulomb potential) of the

nuclei; V_{eff} is the effective potential (electron-electron Coulomb interaction). ψ_n are the n one-electron wave functions. ϵ_i is the total energy eigenvalue of an electron.

Many attempts have been made then to simplify the problem and find a solution to the equations to determine the wave functions of electrons (Szabo and Ostlund N, 1989). Nowadays, first-principle methods can be divided into three categories: ab Initio method, half empirical method (HEM) and Density Functional Theory (DFT) method.

Ab Initio method is to expand wave functions of electrons in a system to electron orbital wave functions, and atomic orbital wave function is a combination of some certain functions. These functions are solved in Schrödinger Equations like **Eq. 2-1**. Hartree approach and Hartree-Fock approach are two most widely used ab initio methods (Szabo and Ostlund N, 1989). It worth noting that all the ab initio methods focus on solving N wave functions that have in all 3N variables (N denotes to the number of electrons, and 3 coordinates for one electron), therefore it requires incredibly huge amount of computation capacity even if for a system with only several atoms. Despite pseudopotential has been developed by Hans G. A. Hellmann in 1934 to replace the complicated effects of the core electrons[1], it does not make the computation for wave functions much efficiently (Hellmann, 1999). Hemi empirical method (HEM) was later introduced to simplify the computation of Schrödinger Equations using empirical parameters. All above methods have inherent approximation in practical calculations and sometimes give rise to poor results because of the less consideration of exchange and correlation potential of the electrons.

- Density functional theory

DFT takes a radically different approach compared to the foregoing wave function methods, and targets electron density instead of wave function as the study

[1] It is the valence electrons that mainly influence the compound properties by electrons migration and binding, therefore non-valence electrons and nuclei are categorized to be a group termed “core”, and the rest part comprising only valence electrons is another group; this term is involved in the effective potential of Schrödinger equation.

object. The electron density is just a function of three variables, so that the computation is significantly simplified and faster compared to Ab Initio and HEM (Segall et al., 2002). The concepts of conventional first-principle methods (ab initio and HEM) and DFT method are shown in **Fig. 2-9**.

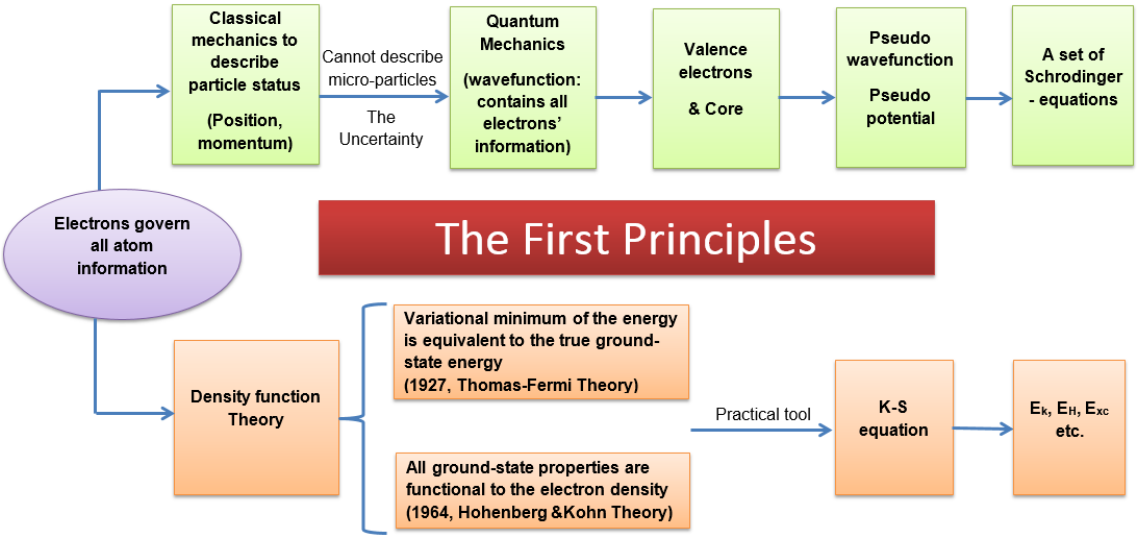

Fig. 2-9 Rationale of first-principle methods

Density functional theory is based on a theorem by Hohenberg and Kohn, later generalized by Levy, which states that all properties of a system are functions of the charge density ρ(r), and that ground-state contains complete information about system (Fermi, 1927; Hohenberg and Kohn, 1964; Levy, 1979; Thomas, 1927), as shown in **Fig. 2-9**.

According to DFT, the energy of a system is written as function of the electron density (Calais, 1993):

$$E = E[\rho(r)] = \int drV_{ext}(r)\rho(r) + F[\rho(r)] \qquad \textbf{Eq. 2-2}$$

The functionals are completed constructed by the function of electron density, however, what the functional exactly is and how to find it were not given in the method initially (Segall et al., 2002). A practical tool for DFT method was established in 1965 when Kohn–Sham (K-S) equation defined the F[ρ(r)] function as shown in **Eq. 2-3**, and substituted the operator in the Schrödinger equations to form K-S equation as shown in **Eq. 2-4**. Equations **Eq. 2-3** and **Eq. 2-4** are

Schrödinger equations of a fictitious system, i.e. the Kohn–Sham system, considering non-interacting electrons with an effective potential (Kohn and Sham, 1965).

$$E = E[\rho(r)] = V_k[\rho(r)] + \int drV_{ext}(r)\rho(r) + V_H(r) + \frac{\sigma E_{xc}[\rho(r)]}{\sigma\rho(r)} \qquad \textbf{Eq. 2-3}$$

$$H\psi_i = (E[\rho(r)])\psi_i = \epsilon_i\psi_i \qquad \textbf{Eq. 2-4}$$

where V_K is the functional for electron kinetic energy; $\int drV_{ext}(r)\rho(r)$ is the functional for external potential; V_H is the functional for Hartree Coulomb potential, excluding the exchange and correlation effects; and the last term contains E_{xc} includes all many-body contributions to the total energy, mainly the exchange and correlation energies. It should be notice that ψ_i in **Eq. 2-4** is no longer the real wave function of a molecule, but is an auxiliary quantity simply to make the math work with this method.

In practice, the real density ρ(r) is determined by a self-consistent-field (SCF) calculation as shown in **Fig. 2-10**. During the SCF calculation, solutions for ψ_i are found for a fixed E[ρ(r)], and then the latter is updated. The procedure is repeated until self-consistency is achieved. The SCF procedures have been adopted by most DFT calculation packages i.e. GAUSSIAN, CASTEP, DMOL3, VASP etc. At the beginning of the calculation, initial electron density $\rho(r)_i$ is constructed by the wave function of molecular orbitals Ψ_i, as shown in **Eq. 2-5**, and the wave function of molecule orbitals are normally expanded from those of atomic orbitals.

There are different methods to obtain the wave function of molecule orbitals from the atomic orbitals. Gaussian functions (Andzelm, Wimmer and Dennis R. Salahub, 1989) are used in the GAUSSIAN package; plane waves (Ashcroft and N D Mermin, 1976; Payne et al., 1992) are used in the packages of CASTEP and VASP; and numerical orbital basis sets (Delley, 1990) are used in Dmol^3 package. Among them, numerical orbital basis sets save huge computational resources because it is a linear combination of atomic orbitals.

$$\rho(r)_i = \sum_i |\psi_i|^2 \qquad \textbf{Eq. 2-5}$$

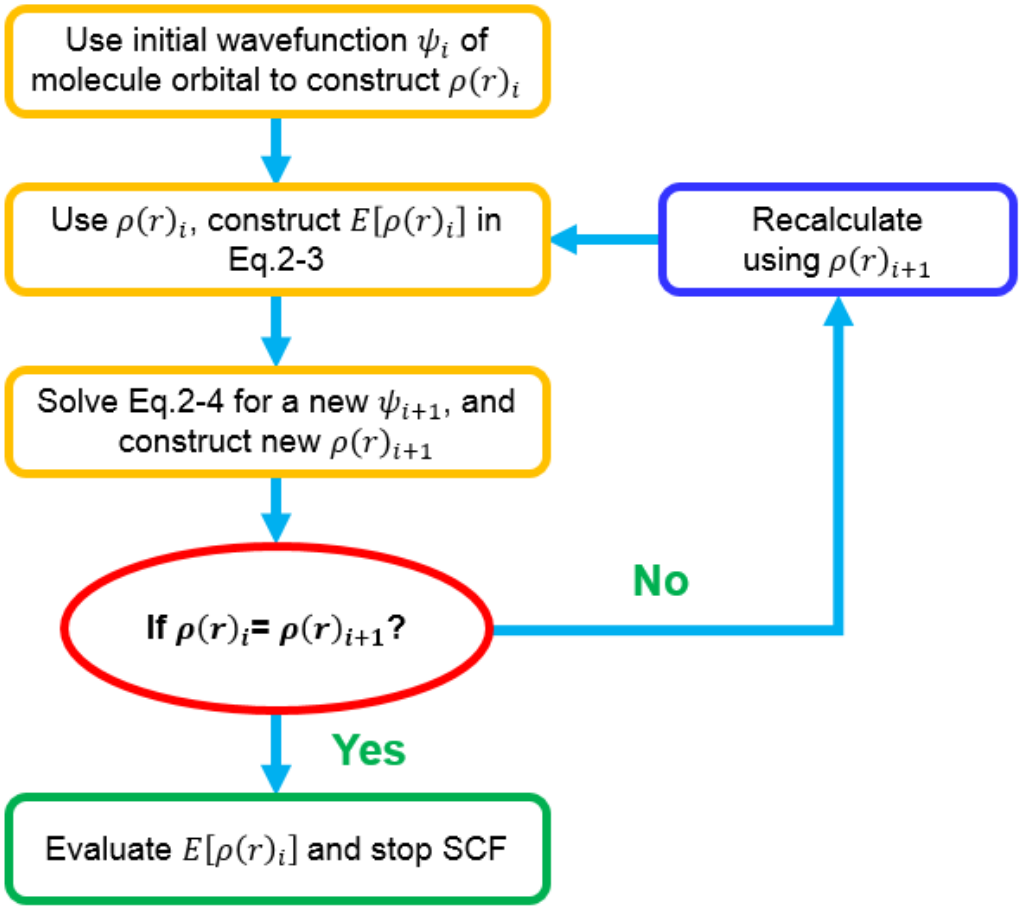

Fig. 2-10 SCF calculation procedures

The kinetic energy V_K, external potential $\int drV_{ext}(r)\rho(r)$ and Hartree Coulomb potential V_H in **Eq. 2-3** can all be determined accurately by the function of electron density ρ(r), and the nuclei and non-valence electrons can normally be treated as cores with pseudopotential to simplify the calculation. However, exchange and correlation potential (the last term in **Eq. 2-3**) can hardly be determined exactly under K-S method (Kohn and Sham, 1965).

State-of-art development regarding DFT is mainly on the construction of accurate functional for exchange and correlation potential. Although as yet no functionals have been able to provide an absolutely accurate solution for it, some approximations that can provide acceptable prediction have been proposed and widely adopted in DFT packages such as Local Density Approximation (LDA)

(Ceperley and Alder, 1980) and Generalized Gradient Approximation (GGA) (Perdew et al., 1992). It remains a great chanllenge in DFT to find an accurate and universally-applicable functional for E_{xc} (Segall et al., 2002).

2.3.2.2 DFT in the investigation of anisole decomposition

DFT has been widely used in the investigation of various reactions (Abdullah, Bakar and BhatiaHATIA, 2004; Broclawik et al., 2006; Huang et al., 2015; Sukrat et al., 2012), however its application on the decomposition of anisole is limited and only a few references are found in literature: two recent articles adopting DFT modelling in the anisole decomposition over metal/SiO_2 catalysts has been found (Réocreux et al., 2016; Tan et al., 2017); the details of these works on the mechanism investigation have been reviewed in Sections 2.1.3 and 2.2.2. On the other hand, literature reporting the adsorption process of Phs onto metals surface and the catalytic hydrogenation mechanism of Phs in aqueous phase is more extensive (Hensley, Wang and McEwen, 2014b; Honkela, Björk and Persson, 2012; Johnston et al., 2010).

2.3.3 Advantages and limitations of experimental and DFT modelling methods

Reactions in which tracking of every change from reactants to products is difficult can be considered as "black boxes". Experiments are “bottom-to-top” approaches that target at linking outcomes from the reaction to changes happening inside the “black box” through the determination and analyses of intermediate and product compounds, as well as catalysts. Experiments provide the most direct and convincing evidence to gain understanding about a macroscopic principle between a variable and a chemical reaction by keeping other variables constant. Despite experimental results being highly valuable to understand the overall reaction and products distribution at a macroscopic level, they present limitations in unravelling the specific reaction mechanism, because it is hard to identify each elemental reaction by the analyses of products, even if using isotope labelling reactants in the experiments. Reaction pathways can be proposed from analyses of experimental products, but they are normally based on inference. Reaction mechanisms are even more difficult to be obtained from sole experimental work.

Even though techniques which allow observing what occurs inside the "black box" during the reactions have been developed, such as on-line characterization of radicals and ions formed during the reactions (Munson, Xu and Haw, 1993; Xu, Zhang and Munson, 1994); these techniques have not been widely established because of their high cost, and transition states of reactions are still hard to capture experimentally because they are extremely unstable (Baraban et al., 2015).

DFT modelling provides a revolutionary approach to the study of chemical reactions by means of a “top-to-bottom” calculation based on electron interactions independent from the complex effects from operational parameters. Compared to experimental approach, the modelling can provide intrinsic information of diffusion, adsorption, reaction and desorption, independently of the very short life span of the transition states, radicals and ions existing in the process. DFT modelling has been widely used as a systematic, reliable and low cost approach to explain molecule properties and mechanisms in many reactions (Gao et al., 2014; Geng, Zhang and Yu, 2012; Huang et al., 2014, 2015; Li et al., 2014b).

Nevertheless, because the DFT modelling calculates the interactions of electrons, the size of model is significantly limited by the computation power and normally hard to 1:1 fit the real reaction system. In fact, this limitation may cause deviation between the modelling and experimental results. Besides, as mentioned in Section 2.3.2.1, the exchange-correlation term for DFT modelling cannot be determined accurately using existing functionals. This is another factor that currently limits the first principle modeling to be a completely independent method able to replace the experiment method.

All in all, a combination of experimental and modelling methods seems to be an efficient way for investigating most chemical reactions. Experiments may provide reliable evidence of the products from a reaction carried out under particular set of operating conditions, while first principle modelling enables to reveal how it happens at an atomic level.

2.4 Gaps in knowledge and research interest areas

Based on the literature review, gaps in knowledge and research interest areas in the study of decomposition of anisole have been identified:

- Detailed product evolution profiles of non-catalytic and catalytic anisole decomposition over acid catalyst against a wider temperature range (e.g. from 200°C to 800°C) need to be established. Further investigation to stablish the effects of acid catalyst on the product distribution is also required.
- A clear reaction mechanism of the catalytic transmethylation of anisole is not reported in the literature, especially regarding the interactions between reactant molecule and the acid sites. DFT modelling can be used to explore the reactivity of each atom in the reactant molecule and predict the most possible and favourable products.
- Base metals are of great interests as catalysts for deoxygenation reactions, but their application in the decomposition of anisole is rarely reported in the literature. Besides, no criteria for metal screening are available.
- Deoxygenation in anisole decomposition over bi-functional catalysts (i.e. base metal site and acid solid support) has been rarely investigated. Furthermore, bi-metal loaded acid solid catalysts are of great interest to be applied to bio-oil upgrading, but their effects on the decomposition of model compounds such as anisole are unclear and not comprehensively reported in the literature.
- The potential of in-situ hydrogen supply during the decomposition of anisole to the deoxygenation reaction has been rarely investigated, despite it is known that hydrogen is abundantly produced during the carbonaceous deposit formation.
- Research opportunities also exist in the DFT investigation of the mechanism of deoxygenation in catalytic anisole decomposition, especially over bi-functional catalyst and including the contribution from both the acid and metal sites to the decomposition of anisole.

2.5 Summary

The investigation of anisole decomposition started in the 1940s, and it is widely accepted that the overall reaction consists of transmethylation and deoxygenation stages. Current investigation on anisole decomposition has mainly focused on the catalyst performance to achieve the targeted conversion of anisole into the desired products (i.e. phenolics or oxygen free compounds). Efforts have also been made to clarify the reaction pathways and mechanism in the decomposition of anisole. Experimental method is a conventional method widely reported in literature for the study of anisole decomposition, while DFT modelling method is a promising method for studying reactions but rarely applied to anisole decomposition. Both methods have advantages and limitations, and are undergoing development. A combination of experiment and DFT modelling is a reliable approach to obtain comprehensive understanding of the reaction of anisole decomposition. Gaps in knowledge identified based on the literature review are related to the application of various catalysts, the role of different active sites of the catalysts in the decomposition of anisole, and relevant catalysis mechanisms

3 Methodology

This chapter describes detailed methodology for the investigation in this thesis, including parameters for modelling with DFT and Monte Carlo Method, and procedures for reactor design and experiments. The aim is of this chapter is to illustrate the reliability of the investigation and make the investigation in this thesis repeatable to other researchers.

3.1 Density Functional Theory (DFT) modelling

For the modelling work (Chapters 4 and 5), the first-principle density functional theory plus dispersion (DFT-D) calculations were implemented in the DMol^3 module available in Materials Studio 2016 from BIOVIA (Delley, 1990, 2000).

The double numerical plus polarization (DNP) basis set was used to calculate the valence orbital of all the atoms, including a polarization p-function on all hydrogen atoms. The numerical basis sets in DMol^3 minimize or even eliminate basis set superposition error (BSSE), in contrast to Gaussian basis sets, in which BSSE can be a serious problem (Elanany et al., 2004; Kalita and Deka, 2009). Calculations used the generalized gradient corrected approximation (GGA) (Perdew, Burke and Ernzerhof, 1996) treated by the Perdew−Burke−Ernzerhof exchange-correlation potential with long-range dispersion correction via Grimme's scheme (Grimme, 2006). The self-consistent field (SCF) procedure was used with a convergence threshold of 10^{-6} au on the energy and electron density. Geometry optimizations were performed with a convergence threshold of 0.002 Ha/Å on the gradient, 0.005 Å on displacements, and 10^{-5} Ha on the energy. The real-space global cut-off radius was set to 5 Å. In this study, no symmetry constraints were used for any cluster models. The transition state was completely determined by the LST/QST method, and confirmed by the unique imaginary frequency. Milliken charges were assigned to each bond to address the bond order, and Hirshfeld charges were assigned to each atom for the function selected as the Fukui field (Hirshfeld, 1977). Radical Fukui analysis was applied to the phenol molecule to establish its reactivity to free radical attack in non-catalytic reactions. Electrophilic Fukui analysis was applied to anisole and

phenol molecules to determine their reactivity to carbocation attack in catalytic reactions. The same computation condition was applied for both catalytic and non-catalytic modellings; in the case of catalytic modelling, mainly Brønsted acid site was considered. The initial configuration of the ZSM-5 catalysts was obtained from the siliceous ZSM-5 crystal, and an 8T model derived from MFI structure was used to simulate the performance of a Brønsted acid site on HZSM-5 (HZ) (Huang et al., 2014, 2015). The energy barrier for transmethylation reaction was determined by the difference between the transition state and reactant energies. The relative energy of the transition state and product were defined as the energy difference with the reactant respectively. The adsorption energy was determined by the energy difference of the system before and after the adsorption process. All the energies were calculated at 0K in the DFT investigation.

3.2 Molecular modelling

The molecular modelling with Metropolis Monte Carlo method (Metropolis et al., 1953) were performed to investigate the isothermals and adsorption capacity of selected metal loaded HZ catalyst in the Sorption module available in Materials Studio 2016 from BIOVIA (Chapter 5).

The adsorbent model was built based on a unit of imported periodic MFI zeolite (from the Database of Zeolite Structures of Structure Commission of the International Zeolite Association) without symmetry. The sorbate structure was treated as rigid, and only rigid body translations and reorientations were incorporated in the modelling. The Si/Al ratio (23, 47, 95) of the HZ catalyst was tuned by replacing (respective 4, 2, 1) Si atoms with Al atoms randomly, keeping the limitation of no more than one Al atom being bonded to the same oxygen atom; the catalyst models were denoted as HZ(23), HZ(47) and HZ(95). The loading of protons was implemented with the task of Locate, the number of protons was equivalent to the number of Al atoms. The charges of +2.4, +1.4, -1.2, and +1 were assigned to Si, Al, O and H respectively. The consistent-valence forcefield (cvff) was assigned in the modelling. The Ewan electrostatic summation method was used (Ewald, 1921), and was atom based for Van Der Waals summation. Temperature was in automated control with 40 cycles, and the frame

with the lowest energy was returned. The maximum loading steps were 10^5, and the production steps were 10^7. The computation quality was ultra-fine.

The models of metal loaded HZ(23) (metal/HZ(23)) were built with the task of Locate by introducing 4 metal atoms in the HZ(23), and the procedures and computational parameters were the same as the loading of protons described above.

The adsorption modelling was implemented based on the task of Adsorption Isotherm by introducing anisole molecule into the models of both HZ with various Si/Al ratios and metals/HZ(23), within the pressure range of 101.33 kpa and 1013 kpa. COMPASS was assigned to the forcefield, and charges were assigned by forcefield. Ewald& Group was set as the electrostatic summation method, where the interactions between charge groups were calculated using a group-based sum, and all other interactions were calculated using an Ewald sum. The Van Der Waals summation method was set to atom based. Sample interval was 25, grid interval was set as 0.25Å, and resolution was set as Fine. The equilibration steps were 10^5, and the production steps were 10^6, and the fugacity step was 9. Isotherms for HZ with different SI/Al ratios were investigated at temperatures of 25°C, 200°C, 400°C, 600°C, and isotherms for metal/HZ(23) were investigated at temperatures of 25°C, 200°C, 400°C, 600°C and 800°C. The computation quality was ultra-fine.

3.3 Experimental work

3.3.1 Description of reactor and experiment setup

Experiments were carried out in a bench-scale fluidized bed. The dimensions of the reactor were designed considering the ratios of packed height to reactor height and packed height to width, with referring to the published reports as shown in **Table 3-1**. The detailed reactor configuration is shown in **Fig. 3-1**. The designed fluidized reactor (Φ32*600mm) has a side feeding tube, where a polytetrafluoroethylene tube is inserted in till the main reactor for the feeding of reactant during the experiments. The inlet for carrier gas is at the bottom of the

reactor and the side outlet is on the top. There are two holes on the top of the reactor that are used for fixation of thermocouples.

Table 3-1 Dimensions of literature reported bubbling fluidized bed reactors

Inner Diameter (cm)	Height (cm)	Packing height (cm)	Packed height/height	Packed height/width	Height /width	Reference
60.00	100.00	54.00	0.54	0.90	1.67	(Gera et al., 1998)
4.00	26.00	8.00	0.31	2.00	6.50	(Papadikis, Gu and Bridgwater, 2009)
3.81	34.00	5.50	0.16	1.44	8.92	(Xue et al., 2012)
5.20	57.00	24.42	0.43	4.70	10.96	(Paasikallio et al., 2013)
11.00	900.00	-	-	-	81.82	(Hua, Wang and Li, 2014)
4.92	60.96	5.77	0.09	1.17	12.39	(Karanjkar et al., 2014)
7.21	95.00	5.75	0.06	0.80	13.18	(Mellin, Yang and Yu, 2015)
3.20	60.00	6.00	0.10	1.88	18.75	Designed dimensions

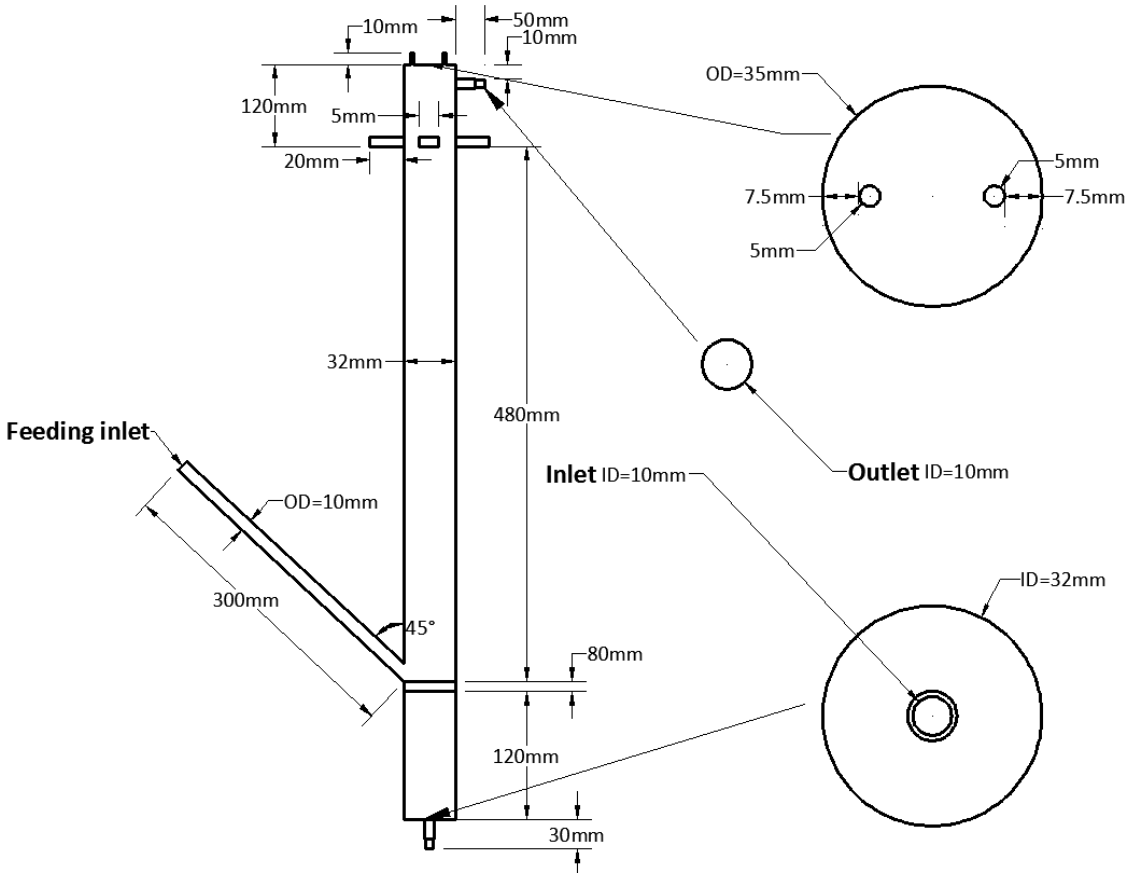

Fig. 3-1 Dimensions of the designed fluidized bed reactor

The entire setup of experimental system is shown in **Fig. 3-2**, and the designed key operational parameters are shown in **Table 3-2**.

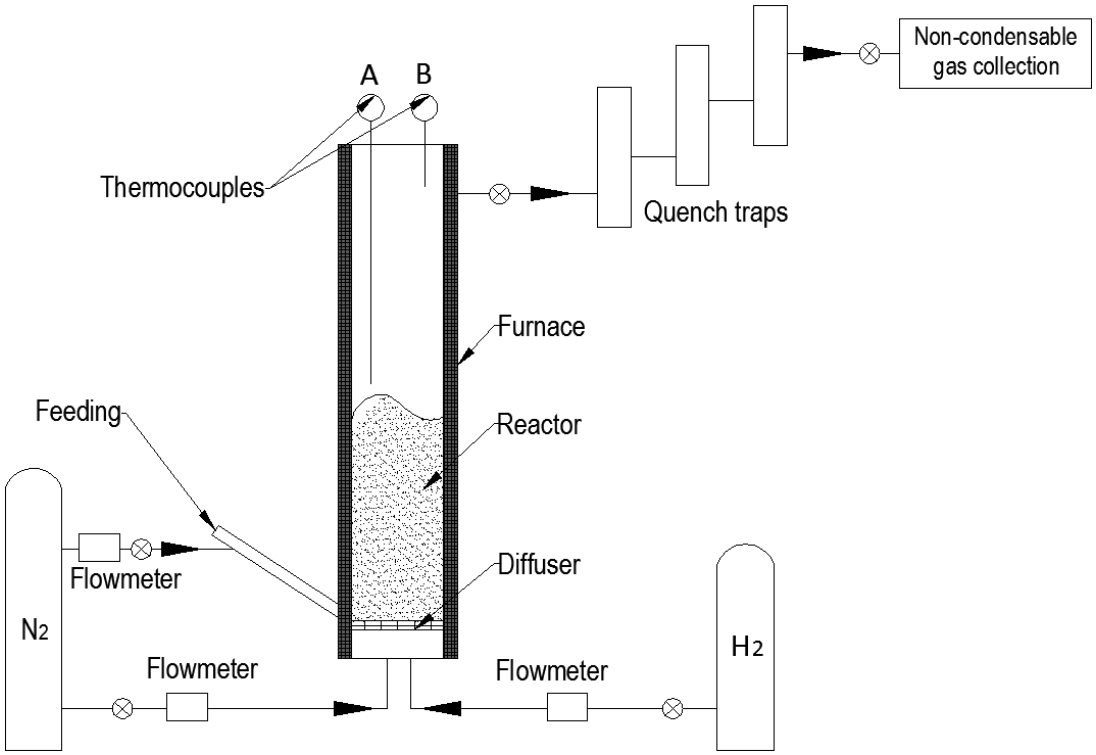

Fig. 3-2 Schematic for the experiment setup

Table 3-2. Designed key operational conditions

Weight hourly space velocity (WHSV)	$1h^{-1}$
Feeding rate	0.83g/min
Bed packing mass	50g
Operation temperature range	200°C-800°C
Operation pressure	Atmospheric pressure (atm)
Feeding time	10min

WHSV of feeding is defined in **Eq. 3-1** (Karanjkar et al., 2014):

$$WHSV(h^{-1}) = \frac{feeding\ mass\ flow\ rate\ (g \cdot h^{-1})}{weight\ of\ catalyst\ (g)} \qquad \textbf{Eq. 3-1}$$

The system consists of a fluidized reactor which is equipped with two thermocouples, quench traps, nitrogen supply, hydrogen supply and liquid reactant feeding system. Flowmeter and valve are equipped to each gas circuit.

Nitrogen was used as the carrier gas for fluidization and feeding flow. Hydrogen supply was used only for the reduction of metal based catalysts, and was turned off during the experiments of anisole decomposition. Thermocouple A was used to measure the reaction temperature and provide feedback to furnace controller, and thermocouple B was used to measure the temperature around outlet area. The outlet of reactor was connected to a three-stage quench trap for the liquid products collection. Non-condensable gaseous products were collected in gas bags at the end of the system.

3.3.2 Assessment of bed material size and carrier gas flowrate

The particle size of the bed material and the practical flowrate of carrier gas were adjusted by cold state tests, which were performed in a quartz tube that had the same dimensions as the actual experimental reactor.

Two types of silica sand particles with the diameters of respective 60-80 mesh (~0.2mm) and 40-60 mesh (~0.3mm) were used in the tests with the carrier gas flow rate at 360L/h (**Fig. 3-3**). Based on the observation of fluidization status, particles within 60-80 mesh showed better fluidization (higher bed extension and more uniform fluidization at same flowrate) so that was selected for the experiments.

Fig. 3-3 Fluidization of silica sand particles (~0.2mm and ~0.3mm) at the carrier gas flowrate of 360L/h

The minimum fluidisation velocity (V_{mf}) based on 0.2mm particles for both HZ and silica sand were calculated by means of **Eq. 3-2** (Fogler, 1981).

$$V_{mf} = \frac{(\psi d_p)^2}{150\mu}[g(\rho_c - \rho_g)]\frac{\varepsilon_{mf}^3}{1-\varepsilon_{mf}} \qquad \textbf{Eq. 3-2}$$

where V_{mf} is the minimum fluidisation velocity (m/s), ψ is the particle sphericity (1 was adopted in the calculation for an ideal sphericity), d_p is the particle diameter (m), μ is the gas viscosity (kg/m·s), g is gravitational acceleration 9.81m/s^2, ρ_c and ρ_g are the densities of particle and gas respectively (kg/m^3), and ε_{mf} is porosity at the minimum fluidisation velocity.

The minimum fluidisation flowrate (U_{mf}) was 77 L/h for zeolite catalyst and 180 L/h for silica sand. The detailed calculations of V_{mf} and U_{mf} for the packing of both silica sand and HZ are shown in Appendix **A1** and **A2** respectively.

The silica sand particle within 60-80 mesh was then tested with a range of carrier gas flowrates between 100L/h to 400L/h as shown in **Fig. 3-4**, to determine the flowrate of carrier gas for experiments.

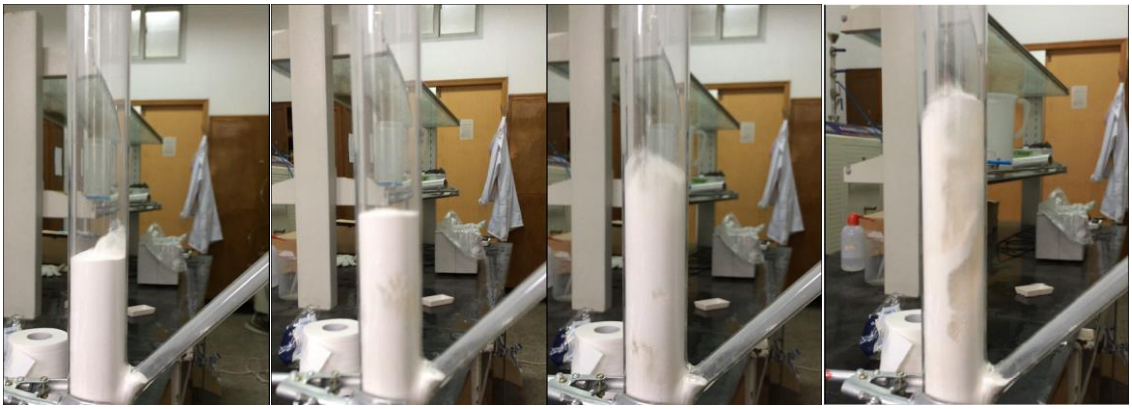

Fig. 3-4. Cold state tests of silica sand particle (~0.2mm) with different gas flowrates (selected presenting: 100L/h,200L/h,300L/h and 400L/h)

The test results indicate that a proper fluidization (roughly 2-3 times static bed height) for the packing of silica sand (~0.2mm) can be achieved when the flowrate is above 350L/h, roughly equivalent to 2 times of calculated minimum fluidization flowrate ($2U_{mf}$). Therefore, $2U_{mf}$ was selected as the flowrate of the carrier gas for the fluidization of both silica sand ($2U_{mf}$ = 360L/h) and HZ catalyst ($2U_{mf}$=154L/h), to keep the fluidization consistent in all the experiments.

Considering the volume expansion of the carrier gas when it enters the reactor during the experiments, the operational flow rates of carrier gas at the different reaction temperatures were determined by means of the ideal gas equation and considering the inlet flow rate at room temperature (~25°C). Values are shown in **Table 3-3**.

Table 3-3. Operational carrier gas flow rates at different reaction temperatures considering inlet flow rates at room temperature (~25°C)

Inlet flowrate of main carrier gas for fluidization (for silica sand; 60-80 mesh)										
Temperature(°C)	25	300	350	400	500	550	600	650	700	800
Inlet flowrate at RT (L/h; 2*U_{mf})	360.0	187.3	172.2	159.5	138.8	130.4	122.9	116.3	110.3	100.0
Inlet flowrate of main carrier gas for fluidization (for HZ and metal/HZ(25); 60-80 mesh)										
Temperature(°C)	25	300	350	400	500	550	600	650	700	800
Inlet flowrate at RT (L/h; 2*U_{mf})	154.0	80.2	73.8	68.3	59.5	55.9	52.7	49.8	47.2	42.8
Inlet flowrate of the side carrier gas for anisole feeding (for all the experiments)										
Temperature(°C)	25	300	350	400	500	550	600	650	700	800
Inlet flowrate at RT (L/h)	20.0	10.4	9.6	8.9	7.7	7.2	6.8	6.5	6.1	5.6

Based on above analyses, different flowrates of carrier gas (at room temperature) were applied to the experiments with different operating temperatures to obtain the same inside flowrate for fluidization.

3.3.3 Materials

Anisole used in experiments was supplied by Aladdin Reagents Co., Ltd. The silica sand used as inert material of the fluidised bed was purchased from Kermel Laboratory Equipment Co., Ltd, China. The HZ zeolite catalyst with different Si/Al atomic ratios in composition (i.e. 25, 50, 80, and 200) was provided by Nankai University Catalyst Co., Ltd, China. Chemicals of nickel nitrite hexahydrate ($Ni(NO_3)_2 \cdot 6H_2O$), cobalt nitrite hexahydrate ($Co(NO_3)_2 \cdot 6H_2O$), ammonium molybdate tetrahydrate ($(NH_4)_6Mo_7O_{24}.4H_2O$), copper nitrate trihydrate ($Cu(NO_3)_2 \cdot 3H_2O$), iron nitrate nonahydrate ($Fe(NO_3)_3 \cdot 9H_2O$) and citric acid were used in wet impregnation of metal loading and supplied by Aladdin Reagents Co., Ltd. The chemicals used for calibration in GC-MS were supplied by Aladdin

Reagents Co., Ltd. All the chemicals mentioned in this thesis are of analytical purity. The gas of nitrogen, hydrogen and all the standard gaseous species used for calibration in GC-FID were supplied by Nanjing Shangyuan industrial gas plant. All the gas was supplied with the purity of 99.999%.

3.3.4 Catalyst preparation and synthesis

Before being used in the experiments, the catalyst samples of HZ catalyst were calcined in a muffle furnace at 500°C for 3 h in air, and subsequently crushed and sieved to a particle size range between 60-80 mesh. The catalyst of sole HZ with the Si/Al ratios of 25, 50, 80 and 200 are denoted as HZ(25), HZ(50), HZ(80) and HZ(200) respectively.

Single metal/HZ(25) catalysts were synthesized by wetness impregnation of the support (HZ(25)) with aqueous solutions of the metal precursor, i.e. $Ni(NO_3)_2 \cdot 6H_2O$, $Co(NO_3)_2 \cdot 6H_2O$, $(NH4)_6Mo_7O_{24}.4H_2O$ and $Cu(NO_3)_2 \cdot 3H_2O$ depending on the active metal (see Appendix **A3** for full details). The impregnation mixtures were stirred with a magnetic stirrer for 24h at room temperature (~25°C). Water was removed by evaporation at 80°C and dried at 110°C for 12h, followed by a calcination in a muffle furnace at 500°C for 6h in air. The calcined catalyst precursors were subsequently crushed and sieved to a particle size range between 60-80 mesh. The catalyst was reduced in-situ with 25 vol.% H_2/N_2 (total flow rate of 500 mL/min) at different temperatures corresponding to each metal loading for 2h before the experiments. Reduction temperatures were established from H_2-TPR analyses. Samples impregnated with Ni (loading ratios of 0.5, 1 and 5 wt.%), Co (loading ratio of 1 wt.%), Mo (loading ratios 0.5, 1 and 5 wt.%) and Cu (loading ratio of 1 wt.%) were denoted as x%M/HZ(25), where M is the active metal (M = Ni, Cu, Mo or Co) and x is the loading ratio (x= 0.5, 1, or 5).

Bi-metal/HZ(25) catalysts were prepared by a co-impregnation method with the aqueous solutions of two metal precursors for the bi-metal loading of Ni-Mo, Ni-Fe and Mo-Fe respectively. The concentration of each metal solution used as precursor is shown in Appendix **A3**. It is worth mentioning that citric acid (~20g) was used for dissolving the precursors of Mo-Fe due to its ability to ligate the

metals and inhibit precipitate formation (Whiffen, Smith and Straus, 2012). Impregnation, drying, calcination, and reduction were performed at the same conditions as those detailed above for single metal based catalysts except the reduction temperatures. The temperatures for bi-metals reduction were obtained referring to the literature; the catalyst of Ni-Fe/HZ(25) was reduced at 600°C (Nie et al., 2014; Yang et al., 2016), and Ni-Mo/HZ(25) and Mo-Fe/HZ(25) were reduced at 800°C (Özdemir, Yeniova and Alibeyli, 2014; Rensel et al., 2013; Smirnov et al., 2016). Fresh catalyst samples impregnated with the bi-metals of Ni-Mo (loading ratios of 0.5 wt.% - 1 wt.%, 1 wt.% - 1 wt.%, 1 wt.% - 0.5 wt.%), Ni-Fe (loading ration of 1 wt.% - 1wt.%) and Mo-Fe (loading ratio of 1 wt.% - 1 wt.%) were denoted as x%M-y%N/HZ(25), where M (= Ni or Mo) and N (= Mo or Fe) are the active metals, x is the loading ratio of M, and y is the loading ratio of N.

3.3.5 Catalyst characterization techniques

3.3.5.1 Pyridine-FTIR

Qualitative and quantitative determination of the Brønsted and Lewis acid sites on the calcined HZ zeolites were performed by infrared study of the pyridine absorbed on the surface samples with a PerkinElmer Frontier Pyridine - Fourier Transform Infrared Spectroscopy (FTIR) Spectrometer. Samples were pre-treated under high vacuum for 2 h prior to the FTIR study. The measurements were performed by saturation of all acid sites in the samples by exposure to pyridine vapours at room temperature (~25°C) for 30 min followed by outgassing at temperatures of 150°C and 350°C respectively.

3.3.5.2 H_2-TPR

H_2-TPR (Temperature Programmed Reduction) analyses were performed on the calcined single-metal based catalysts (metal oxide/HZ(25)) in order to determine the reduction temperature for the metal active site. About 100 mg of the sample was loaded in a U-shaped quartz tube and flushed in a 20ml/min Ar stream at 400°C for 40min. The temperature was then decreased to room temperature (~25°C) under inert conditions. The sample was reduced in with a mixture stream of 10 vol.% H_2/Ar (total flow rate of 20 mL/min) with the temperature rise to 800°C

at a heating rate of 10°C/min. The output signal was detected with a thermal conductive detector (TCD).

3.3.5.3 TEM-EDS

Both fresh (reduced) and spent metal-based HZ(25) catalysts were analyzed with TEM-EDS, and the specimens were prepared by ultrasonic dispersion of catalyst samples in ethanol before dropping the suspension to a copper/nickel grid. The morphology of metal active sites and carbonaceous deposit on the zeolite support were characterized by Transmission Electron Microscope (TEM) using Tecnai G2 T20 from FEI Ltd. Images of the microstructure and the relevant selected area electron diffraction (SAED) patterns of the specimens were acquired. Energy Dispersive Spectrometer (EDS) tests were performed using Genesis 2000 from EDAX Ltd. to determine the existing elements on the sample surface.

3.3.5.4 XPS

X-ray photoelectron spectroscopy (XPS) tests were carried out to evaluate the surface composition of the fresh catalyst samples and the composition of carbonaceous deposits on the spend catalyst. The tests were performed based on an XPS analyser (ESCALAB 250Xi, Thermo Fisher Scientific Inc.) with an Al Kα X-ray source (10 mA, 20 kV), under the conditions of 20 and 100 eV pass energy for the survey spectra and the single element spectra (Ni, Co, Mo, Cu, C), respectively. Peaks were identified by referring to the database from American National Institute of Standards and Technology (NIST).

3.3.5.5 TG

Thermogravimetry (TG) analyses were used to determine the amount of carbonaceous deposits present in the spent catalyst. Tests were carried out in a SETSYS-1750 CS Evolution TG Instrument. Around 15 mg of sample was charge in the pan and heated from room temperature (~25°C) up to 900°C at a heating rate of 20 °C/min and under an air flow rate of 20 mL/min. The sample was kept at 900°C for 15 min to ensure total burn-out of the carbonaceous deposits.

3.3.6 Experimental procedure

Non-catalytic and catalytic anisole decomposition experiments were carried out in the bench scale fluidised bed reactor described in Section 3.3.1, every set of experiment carried out in this thesis is listed in **Table 3-4**. In all cases nitrogen was used as fluidising gas.

Table 3-4 Set of experiment

Set of experiment	Catalyst	Temperature (°C)
T1	none (silica sand)	200
T2	HZ(25)	200
T3	none (silica sand)	300
T4	HZ(25)	300
T5	HZ(25)	350
T6	none (silica sand)	400
T7	HZ(25)	400
T8	HZ(50)	400
T9	HZ(80)	400
T10	HZ(200)	400
T11	none (silica sand)	500
T12	HZ(25)	500
T13	none (silica sand)	550
T14	none (silica sand)	600
T15	HZ(25)	600
T16	none (silica sand)	650
T17	none (silica sand)	700
T18	HZ(25)	700
T19	none (silica sand)	800

T20	HZ(25)	800
D1	1%Ni/HZ(25)	400
D2	1%Ni/HZ(25)	500
D3	1%Ni/HZ(25)	600
D4	0.5%Ni/HZ(25)	500
D5	5%Ni/HZ(25)	500
D6	1%Co/HZ(25)	500
D7	1%Mo/HZ(25)	500
D8	0.5%Mo/HZ(25)	500
D9	5%Mo/HZ(25)	500
D10	1%Cu/HZ(25)	500
D11	1%Ni-1%Mo/HZ(25)	400
D12	1%Ni-1%Mo/HZ(25)	500
D13	1%Ni-1%Mo/HZ(25)	600
D14	1%Ni-0.5%Mo/HZ(25)	500
D15	0.5%Ni-1%Mo/HZ(25)	500
D16	1%Ni-1%Fe/HZ(25)	500
D17	1%Mo-1%Fe/HZ(25)	500

Notes: T for experiments of transmethylation, and D for experiments of deoxygenation.

Non-catalytic experiments were performed at temperatures between 200°C to 800°C. 50 g of silica sand (SiO_2) was placed inside the reactor and fluidised by a N_2 flow rate of 360 L/h (see Section 3.3.2). The amount of sand was adjusted by preliminary experiments to ensure adequate contact between the anisole and bed material. The reactor was heated up to the operating temperature in an inert atmosphere. A total amount of 8.3 g of liquid anisole was placed in a syringe pump at the beginning of the experiment and pumped into the reactor at a constant flow rate of 50 g/h once the operating temperature was achieved.

Feeding time was 10 min. The nitrogen stream was kept flowing for an additional 5 min after end of the feeding to ensure all the vapour of products were blown out from the reactor and collected.

Catalytic decomposition experiments over sole HZ catalysts were carried out in a temperature range between 200°C and 800°C, at increasing intervals of 100°C. In addition, the effect of the catalyst acidity on the anisole conversion was investigated at 400°C by testing HZ with different Si/Al atomic ratios in composition, i.e. HZ(25), HZ(50), HZ(80), and HZ(200). 50 g of the fresh pre-calcined HZ catalyst was placed inside the reactor. The reactor was then heated up to the operating temperature, and the catalyst sample was fluidised by a N_2 flow rate of 154 L/h as depicted in **Table 3-3**. Anisole feeding rate and feeding time were the same as those for the non-catalytic experiments.

Anisole decomposition experiments over single metal based catalyst of 1%Ni/HZ(25) were performed at 400, 500 and 600°C. In order to investigate the effect of the metal type on the anisole decomposition, experiments were carried out over 1%Ni/HZ(25), 1%Co/HZ(25), 1%Mo/HZ(25) and 1%Cu/HZ(25) at 500°C. The effect of metal loadings were investigated by the experiments with 0.5%Ni/HZ(25), 1%Ni/HZ(25), 5%Ni/HZ(25), 0.5%Mo/HZ(25) 1%Mo/HZ(25) and 5%Mo/HZ(25) at 500°C.

The catalytic decomposition experiments of anisole over bi-metal based catalyst of 1%Ni-1%Mo/HZ(25) were implemented at temperatures of 400°C, 500°C and 600°C. The effect of type of bi-metal active sites were investigated by experiments carried out over 1%Ni-1%Mo/HZ(25), 1%Ni-1%Fe/HZ(25), 1%Mo-1%Fe/HZ(25) at 500°C. The effect of bi-metal loadings were investigated by the experiments carried out over 1%Ni-1%Mo/HZ(25), 1%Ni-0.5%Mo/HZ(25) and 0.5%Ni-1%Mo/HZ(25) at 500°C.

For all metal based experiments, 50g of fresh catalyst was in-situ reduced as depicted in Section 3.3.4 and fluidised during each experiment by a N_2 flow rate of 154 L/h depicted in **Table 3-3**. Anisole feeding rate and feeding time were the same as those for the non-catalytic experiments.

3.3.7 Liquid products collection and characterization

For all the experiments, the outflow product gas stream was passed through a three-stage ethanol filled quench trap to collect the liquid product as shown in Appendix **A4**. 30ml ethanol was filled in each trap as the solution for liquid products, and the trap tubes were submerged in an ethanol bath at temperature below -30°C. The collected liquid product was then recovered from the tubes and diluted to a constant volume of 150 mL in a graduated cylinder.

About 1 mL liquid solution sample was extracted using a syringe equipped with a solid filter head, and stored a screw-thread vial for further analyses. The liquid product was analysed by GC-MS in an Agilent 7890A/5975C equipped with a capillary column DB-5ms (30 m x 250 μm x 0.25 μm). The injector temperature was kept at 270°C. The column was programmed from 40°C (held 3 min) to 180°C (held 2min) with a heating rate of 5°C/min, and finally to 280°C (held 2 min) with the heating rate of 10°C/min. Entire running time for each GC-MS test was 45min. The mass spectra were operated in electron ionization (EI) mode at 70 eV, and were obtained from m/z 35-550. The compounds present in the liquid product were quantified by total ion and were identified based on the database of NIST library (calibrated with an external standard). All detected compounds (peak threshold value: 18) were utilised for the external calibration. Yield of each liquid product compound was determined as a percentage of the initial weight of the anisole sample (as shown in **Eq. 3-3**), and selectivity of each liquid product was determined as percentage of the total liquid fraction (as shown in **Eq. 3-4**). The conversion of anisole was defined as 100 minus the percent of anisole in products.

Liquid product yield (Karanjkar et al., 2014):

$$Y_l = \frac{mass\ of\ \ product}{mass\ of\ reactant} \times 100\% \qquad \textbf{Eq. 3-3}$$

Liquid product selectivity (Karanjkar et al., 2014):

$$S_l = \frac{yield\ of\ product}{yield\ of\ total\ liquid\ fraction} \times 100\% \qquad \textbf{Eq. 3-4}$$

3.3.8 Gaseous products collection and quantification

Non-condensable gaseous products were collected in gas bags throughout the experiment duration. Gas samples were only collected in the metal based catalytic decomposition experiments (from D1 To D17). The composition of gaseous products was analysed by GC-FID, and the yield of the gaseous fraction (Y_g) was determined as a percentage of the initial weight of the anisole sample, based on the balance of nitrogen between the inlet and the collected amount, as shown in **Eq. 3-5**.

$$Y_g = \left(\frac{V_{N_2} \times C_g}{C_{N_2}} \times \frac{M}{V_m}\right) / M_a \qquad \textbf{Eq. 3-5}$$

where y_g is the yield of one compound in gaseous products (wt.%), V_{N2} is the total inlet nitrogen volume at room temperature (~25°C) (L), C_g is the concentration of one compound in gas bag (vol. %), C_{N2} is the concentration of nitrogen in gas bag (vol. %), M is the molar mass of the gas compound (g/mol), V_m is the molar volume of the gas compound at room temperature (~25°C) (L/mol), and M_a is the mass of the reactant anisole (8.3g). The concentration of each compound in the gas bag was obtained by the analysis in GC-FID with external calibration.

3.3.9 Solid products collection and quantification

As mention in Section 3.3.5.5, the yield of carbonaceous deposit on the spent catalyst samples was analysed by TG, and given as a percentage of the initial weight of the anisole sample.

In the case of the experiments carried out over silica sand and sole HZ catalyst (T1 To T20), the amount of carbonaceous deposit on the catalyst was determined by mass difference of the sample before and after the TG analysis, and the yield of the solid fraction (Y_s) was determined as a percentage of the initial weight of the anisole sample.

In the case of the experiments performed over the metal-based catalysts (D1 To D17), the yield of carbonaceous deposit was determined by means of **Eq. 3-6** to **Eq. 3-9**, considering the metals oxidization during the TG analyses.

$$Y_s = \frac{(M_s + M_m) \times m_c}{m_{s+m} \times M_a} \quad \textbf{Eq. 3-6}$$

$$m_c = m_{s+m+c} - m_{s+m} \quad \textbf{Eq. 3-7}$$

$$m_{s+m} = m_{s+m+o} \times \left(1 - \frac{M_{O_2}}{M_{s+m+o}}\right) \quad \textbf{Eq. 3-8}$$

$$M_{O_2} = M_{s+m+o} - (M_s + M_m) \quad \textbf{Eq. 3-9}$$

where Y_s is the yield of carbonaceous deposit during on experiment (wt.%); M_s is the mass of HZ(25) support of the catalyst (g); M_m is the mass of metal loading of the catalyst (g); m_c is the mass of carbonaceous deposit on the sample before the TG analysis (g), which is determined by **Eq. 3-7**; m_{s+m} is the mass of the support and metal of the sample in the TG analysis (g), which is supposed to be constant throughout the test and calculated by means of **Eq. 3-8**; M_a is the mass of reactant anisole (8.3g); m_{s+m+c} is total mass of the sample before TG test, which consists of the mass of support, metal and carbonaceous deposit; m_{s+m+o} is total mass of the sample after TG test, which consists of the mass of support and metal oxides; M_{O2} is the estimated gained mass of oxygen content if entire spent catalyst underwent such TG analysis, and it is calculated based on different metal oxides by **Eq. 3-9**; and M_{s+m+o} is the estimated mass of total catalyst if entire spent catalyst underwent such TG analysis.

In the calculation, metals of Ni, Co, Mo, Cu and Fe were assumed to convert to NiO, CoO, MoO_3, CuO and Fe_3O_4 respectively after the TG analyses.

3.3.10 Repeatability and experimental error

The repeatability of the experiments was evaluated primarily for the fraction of liquid and solid quantification by performing three times the experiment T16, and two times the experiments of T7, T15, D1 and D15 respectively.

The absolute peak areas of each compound in the liquid fraction based on GC-MS analyses for in experiment T16 are shown in **Table 3-5**, and the relative error of the peak area was calculated by using **Eq. 3-10**, and shown in **Table 3-6**. The deviations of each compound yield in the liquid fraction and solid yield are shown

in **Table 3-7** to **Table 3-11** for experiments of T16, T7, T15, D1 and D15 respectively.

$$Relative\ error = 100\% \times \frac{(eigenvalue\ value - average\ value)}{average\ value} \quad \textbf{Eq. 3-10}$$

Table 3-5. Absolute peak area of each liquid product compound in the experiment T16

Peak	substance	Triplicated tests comparison		
		T16(1)	T16(2)	T16(3)
		peak area	peak area	peak area
1	Benzene	2.89E+08	2.97E+08	3.10E+08
2	Toluene	1.30E+08	1.29E+08	1.41E+08
3	Ethylbenzene	2.61E+07	2.53E+07	2.69E+07
4	Styrene	2.61E+07	2.52E+07	2.85E+07
5	Anisole	2.03E+07	1.92E+07	2.10E+07
6	Phenol	1.17E+09	1.13E+09	1.14E+09
7	Benzofuran	2.48E+08	2.44E+08	2.76E+08
8	Phenol, 2-methyl-	9.99E+07	9.62E+07	9.94E+07
9	Phenol, 4-methyl-	1.30E+08	1.22E+08	1.14E+08
10	Naphthalene	1.45E+07	1.41E+07	1.58E+07
11	Benzoin ethyl ether	1.74E+08	1.73E+08	1.71E+08

Table 3-6. Relative error of the peak area for liquid products in the experiment T16

substance	Relative deviation (%)		
	T16(1)	T16 (2)	T16 (3)
	peak area	peak area	peak area
Benzene	-3.16	-0.48	3.64
Toluene	-2.39	-3.50	5.88
Ethylbenzene	-0.08	-3.02	3.09
Styrene	-1.87	-5.25	7.13
Anisole	0.72	-4.89	4.16
Phenol	1.75	-1.23	-0.52
Benzofuran	-3.06	-4.84	7.90
Phenol, 2-methyl-	1.43	-2.36	0.93
Phenol, 4-methyl-	6.37	0.03	-6.40
Naphthalene	-1.94	-4.76	6.69
Benzoin ethyl ether	0.75	0.24	-0.99

Table 3-7. Deviation of the yield for liquid products in experiment T16

Substance	T16 (1)	T16 (2)	T16 (3)	STDEV.S
Benzene	4.44	4.57	4.75	0.16
Toluene	1.83	1.81	1.99	0.10
Ethylbenzene	0.48	0.46	0.49	0.01
Styrene	0.35	0.34	0.38	0.02
Anisole	0.23	0.22	0.24	0.01
Phenol	24.77	24.04	24.21	0.38
Benzofuran	3.96	3.89	4.41	0.28
Phenol, 2-methyl-	1.53	1.47	1.52	0.03
Phenol, 4-methyl-	2.01	1.89	1.77	0.12
Naphthalene	0.14	0.14	0.15	0.01
Benzoin ethyl ether	1.69	1.68	1.66	0.01
overall	41.43	40.50	41.58	0.58

Table 3-8 Deviation of the yield for liquid and solid products in experiment T7

substances	T7 (1)	T7 (2)	STDEV.S
Benzene	0.31	0.35	0.03
Toluene	1.06	0.99	0.05
p-Xylene	0.53	0.51	0.01
Anisole	0.59	0.52	0.05
Phenol	28.57	27.93	0.45
Phenol, 2-methyl-	11.79	11.29	0.36
Phenol, 4-methyl-	12.61	13.02	0.29
Phenol, 2,6-dimethyl-	4.18	3.98	0.14
Phenol, 3,5-dimethyl-	2.80	3.16	0.25
Phenol, 2,4-dimethyl-	3.39	3.15	0.17
Phenol, 3,4-dimethyl-	1.75	2.12	0.26
Phenol, 2,3-dimethyl-	1.64	1.46	0.13
Phenol, 2,4,6-trimethyl-	2.08	1.95	0.09
Phenol, 2,3,6-trimethyl-	1.23	1.15	0.06
Overall	72.53	71.58	0.67
carbonaceous deposit	27.00	34.50	5.31

Table 3-9 Deviation of the yield for liquid and solid products in experiment T15

substances	T15 (1)	T15 (2)	STDEV.S
Benzene	13.93	14.91	0.69
Toluene	11.10	10.16	0.66
p-Xylene	1.62	1.74	0.08
o-Xylene	0.64	0.55	0.07
Naphthalene	4.17	4.71	0.38
Naphthalene, 1-methyl-	1.45	1.75	0.21
Naphthalene, 2-methyl-	0.58	0.42	0.12
overall	33.49	34.24	0.53
carbonaceous deposit	46.21	55.32	6.44

Table 3-10 Deviation of the yield for liquid and solid products in experiment D1

substances	D1 (1)	D1 (2)	STDEV.S
Benzene	0.89	0.83	0.04
Toluene	1.58	1.46	0.09
p-Xylene	0.54	0.51	0.02
Anisole	9.98	9.10	0.62
Phenol	16.24	15.54	0.50
Phenol, 2-methyl-	5.29	5.61	0.23
Phenol, 4-methyl-	8.06	8.67	0.43
Phenol, 2,6-dimethyl-	1.92	2.13	0.14
Phenol, 3,5-dimethyl-	3.04	2.77	0.20
Phenol, 2,4-dimethyl-	1.29	1.18	0.08
Phenol, 3,4-dimethyl-	0.87	0.99	0.08
Phenol, 2,3-dimethyl-	0.00	0.09	0.06
Phenol, 2,4,6-trimethyl-	0.46	0.41	0.03
Phenol, 2,3,6-trimethyl-	0.38	0.35	0.02
naphthalene	0.67	0.56	0.08
Benzene, pentamethyl-	0.06	0.07	0.01
Phenol, tetramethyl-	0.27	0.24	0.03
Overall	51.56	50.51	0.74
carbonaceous deposit	45.23	51.02	4.10

Table 3-11 Deviation of the yield for liquid and solid products in experiment D15

substances	D15 (1)	D15 (2)	STDEV.S
Benzene	11.14	10.85	0.21
Toluene	11.93	11.32	0.44
p-Xylene	2.34	2.24	0.07
o-Xylene	0.59	0.58	0.00
Phenol	2.58	2.55	0.03
Phenol, 2-methyl-	0.81	0.80	0.01
Phenol, 4-methyl-	0.24	0.25	0.01
Naphthalene	1.87	1.81	0.04
Naphthalene, 1-methyl-	0.78	0.57	0.15
Naphthalene, 2-methyl-	0.36	0.28	0.06
Naphthalene, 2,7-dimethyl-	0.17	0.16	0.01
Phenanthrene	0.27	0.26	0.01
Phenanthrene, 2-methyl-	0.42	0.40	0.02
overall	33.53	32.07	1.03
carbonaceous deposit	66.72	60.73	4.23

The analyses result indicates that the deviation of liquid yield is within 1%, and the deviation of solid yield is within 6.5%, therefore the experimental results based on this system are regarded reliable.

4 DFT modelling study of transmethylation in the decomposition of anisole

Transmethylation reaction has been observed to be the primary reaction taking place in anisole decomposition, leading to the prominent production of phenolic compounds (Cornella, Gómez-Bengoa and Martin, 2013; Mackie, Doolan and Nelson, 1989; Meng et al., 2015; Prasomsri et al., 2011; Wang et al., 2014). The deoxygenation of the phenyl-oxygen bond follows the transmethylation reaction as the second stage in the decomposition of anisole. Although it is widely accepted that Brønsted acid sites play a dominant role in anisole decomposition (Meng et al., 2015; Sad, Padró and Apesteguía, 2008, 2010), the precise mechanism for transmethylation is still controversial.

The aim of this chapter is to investigate by means of DFT modelling the mechanism of transmethylation as a primary reaction of the non-catalytic and catalytic decomposition of anisole, and to identify the preferred positions for methyl group transfer on different molecules. Compounds such as phenol, benzene, toluene, anisole, cresol, xylenol and tri-methyl phenol were investigated. The transfer orientation preference of both the free radical and electrophilic substituents on relevant molecules was studied. In addition, various possible reaction pathways of the transmethylation reaction were evaluated to address energy barriers during formation of major product compounds.

4.1 Active sites in anisole and phenol molecules for the transmethylation reaction

The first step in the DFT investigation of transmethylation as the initial stage of the catalytic and non-catalytic decomposition of anisole is to determine the active sites in the reactant molecule. Reactions initiate at active sites where the electron density difference is large, which is indicative of weak bonds or high reactivity to other surrounding molecules. Thus, the active sites in the anisole molecule for the transmethylation reaction were identified by addressing the bond strength by means of the Mulliken bond order. **Fig. 4-1** shows the Mulliken bond order of the anisole molecule for the transmethylation reaction. An increasing bond order

corresponds to increasing bond strength. The ring C-C bonds exhibited the highest bond order values. The bond order of the link between the carbon from the ring and the oxygen, C_{SP}^2-O (Bond ID C5-O7), was lower; however, it was found not to be the weakest bond. This is because the delocalization of the lone electron pair from oxygen leads to the formation of π-P conjugation and reinforces the bond strength (Zhu et al., 2011). The weakest bond was observed for C_{SP}^3-O (Bond ID C8-O7). The results point to both the non-catalytic and catalytic thermal decomposition of anisole being likely to be initiated at this site (Li et al., 2014a).

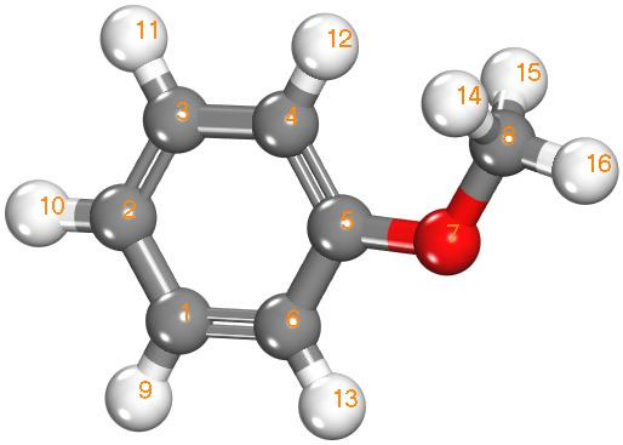

Bond ID	Mulliken Bond order
C8-O7	0.515
C5-O7	0.668
C8-H14	0.798
C8-H15	0.799
C6-H13	0.813
C4-H12	0.814
C3-H11	0.821
C1-H9	0.824
C2-H10	0.825
C8-H16	0.826
C4-C5	1.003
C3-C4	1.025
C5-C6	1.030
C1-C2	1.032
C1-C6	1.054
C2-C3	1.063

Fig. 4-1. Mulliken bond order of the anisole molecule for the transmethylation reaction. Atoms are coloured as follows: carbon atom (grey), hydrogen atom (white) and oxygen atom (red)

In the case of the catalytic decomposition of anisole over Brønsted acid sites, it has been largely recognized that the transmethylation reaction is induced by a proton that dissociates from the acid site and launches an electrophilic attack on the reactant (Haw et al., 1989; Meng et al., 2015; Munson, Xu and Haw, 1993; Richardson et al., 1990; Teng Xu, Jinhua Zhang, 1994). For that reason, the reactivity of each atom in the anisole molecule to an electrophilic attack was evaluated by conducting an electrophilic Fukui analysis (Fukui (-)). The results are shown in **Fig. 4-2**. A higher Fukui index relates to a higher affinity with an electrophilic attack. The results reveal that the oxygen atom (O7) is the most vulnerable under an electrophilic attack, followed by the para-carbon atom (C2).

It is worth pointing out that the oxygen atom is part of the weakest bond (C_{SP}^3-O, Bond ID C8-O7), and it is reasonable to infer that the electrophilic attack may have a significant effect on the cleavage of C_{SP}^3-O which leads to the catalytic decomposition of anisole. As a result of catalytic anisole decomposition, a methyl carbocation group and phenol molecule can be produced. It is hypothesized that the methyl carbocation can launch another electrophilic attack on the phenol molecule. Consequently, cresol can be produced by a cation substitution between the methyl carbocation group and the hydrogen on the phenol ring. To investigate this hypothesis, an electrophilic Fukui analysis was carried out for the atoms in the phenol molecule, and the vulnerable positions to the electrophilic attack launched by the methyl carbocation were identified. Results shown in **Fig.4-3** exhibit that the carbon atoms at the ortho-position (C4) and para-position (C2) of the phenol molecule presented relatively high reactivity to the electrophilic attack. This result indicates that these positions are prone to exchange linked hydrogen atoms under the attack of the methyl carbocation group, and produce o-cresol and p-cresol respectively. In fact the formation of these two products has been observed experimentally (Zhang et al., 2016), and will be further discussed in Chapter 6.

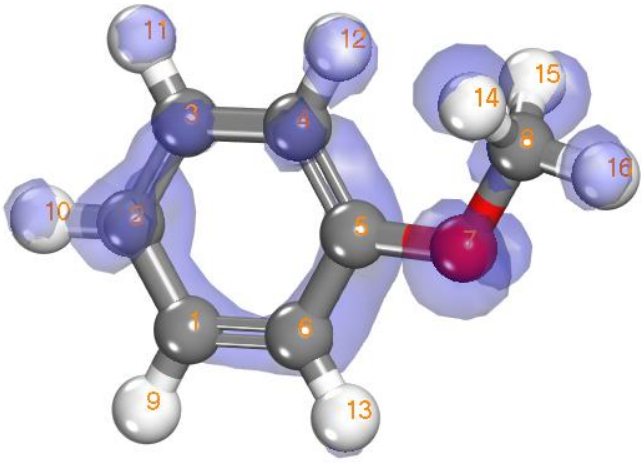

Atom	Fukui (-) index
O7	0.129
C2	0.125
C6	0.086
C5	0.075
C4	0.072
C3	0.071
C1	0.061
H10	0.057
H11	0.046
H13	0.046
H9	0.044
H12	0.040
H15	0.038
H14	0.037
H16	0.036
C8	0.035

Fig. 4-2. Fukui indices of anisole atoms under electrophilic attack (Fukui (-)). Isovalue 0.035. Atoms are coloured as follows: carbon atom (grey), hydrogen atom (white) and oxygen atom (red)

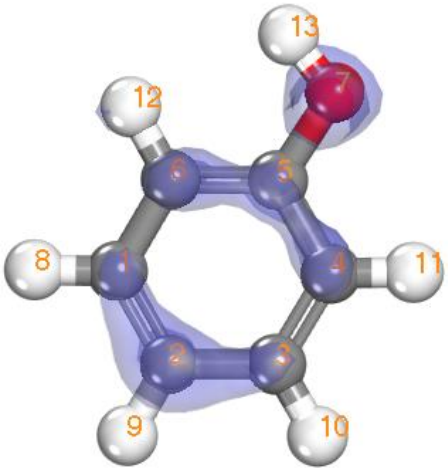

Atom	Fukui (-) index
O7	0.152
C2	0.136
C4	0.089
C5	0.089
C6	0.083
C1	0.073
C3	0.068
H9	0.061
H13	0.055
H11	0.050
H8	0.049
H10	0.048
H12	0.048

Fig.4-3. Fukui indices for (a) electrophilic attack on phenol molecule (Fukui (-)), Isovalue 0.035. Atoms are coloured as follows: carbon atom (grey), and hydrogen atom (white) and oxygen atom (red)

In the case of the non-catalytic decomposition of anisole, the weak bond between the methyl group and benzene ring (C_{SP}^3-O bond ID C8-O7) in the anisole molecule is activated and cleaved when the temperature increases. The molecule is subsequently cracked into free radicals, with a methyl radical being formed (Li et al., 2014a). As it will be discussed in Chapter 6; the formation of cresols at temperatures lower than 650°C during the non-catalytic decomposition of anisole is preferential (Zhang et al., 2016). It is then hypothesized that substitution reactions to other molecules present in the media, such as phenol and benzene, can occur under the methyl free radical attack to form cresol and toluene. The hypothesis was tested by performing a Fukui analysis for radical attack (Fukui (0)) in the phenol molecule. As can be seen in **Fig.4-4**, the atoms C4, C2 and O7 in the phenol molecule were identified as active sites ready to accept methyl radicals as they showed the strongest reactivity indices towards the free radical attack during non-catalytic transmethylation. In other words, the free radical substitutions are more likely to occur at the ortho-position and para-position of the phenol molecule (Zhang et al., 2016). It should be noticed that due to there is no obvious intermediate compound existing in the non-catalytic transmethylation reactions, they are more likely to occur as one step reactions, as shown in **Fig.4-5**.

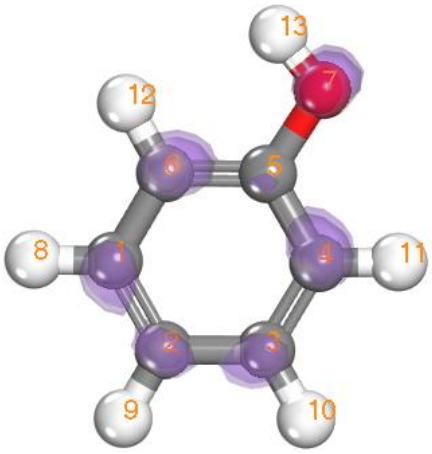

Atom	Fukui (0) index
C4	0.105
O7	0.103
C2	0.102
C6	0.100
C1	0.099
C3	0.095
C5	0.073
H8	0.057
H10	0.056
H11	0.056
H9	0.055
H12	0.055
H13	0.044

Fig.4-4. Fukui indices for radical attack on phenol molecule (Fukui (0)), Isovalue 0.035. Atoms are coloured as follows: carbon atom (grey), and hydrogen atom (white) and oxygen atom (red)

4.2 Mechanism for catalytic transmethylation of anisole

Based on above discussion, the transmethylation mechanism is proposed to proceed through carbocation transfers in the case of catalytic decomposition, as shown in **Fig.4-6**. The most likely transfers of the methyl carbocation to ortho- and para-positions occur by carbocation substitution.

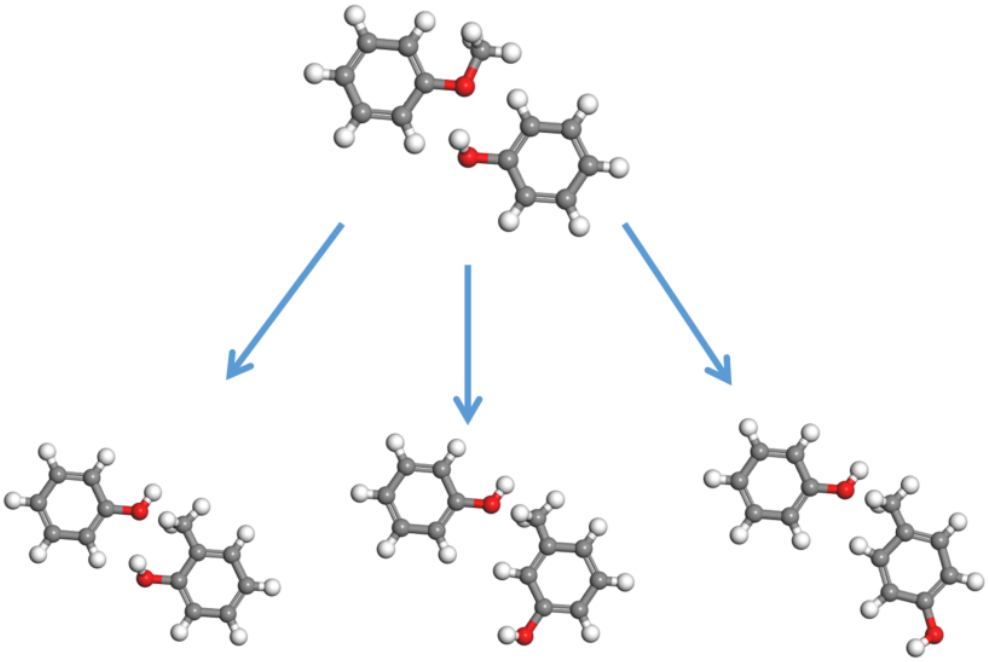

Fig.4-5. Free radical mechanism of non-catalytic transmethylation

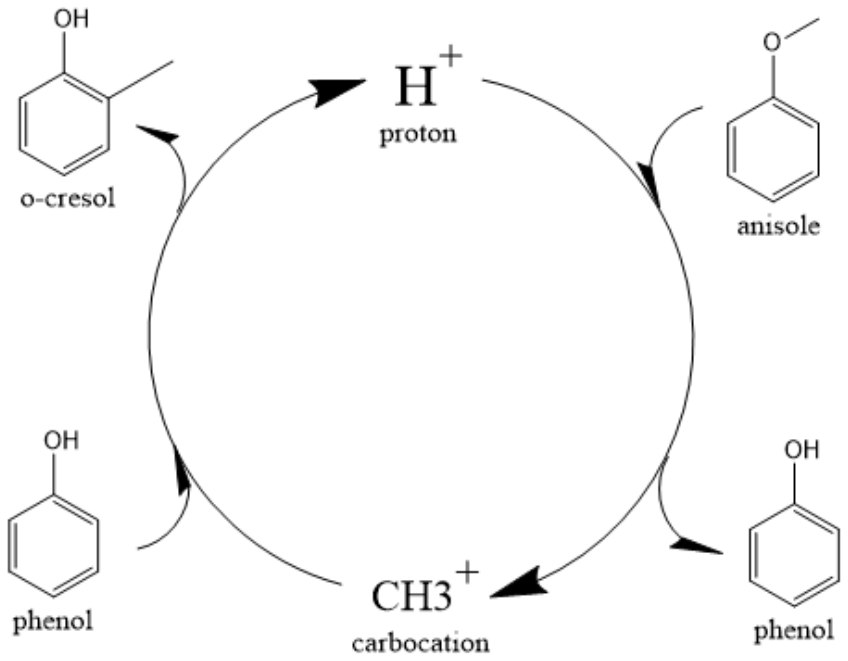

Fig.4-6. Dual electrophilic attack mechanism of catalytic transmethylation

The catalytic process of transmethylation can be divided into two steps. The first step consists of the methyl group cleavage in the anisole molecule; an initial electrophilic attack is launched by the proton dissociated from the catalyst acid site to the O atom, and the methyl carbocation is released. A second electrophilic attack is launched by the methyl carbocation group; the group substitutes the hydrogen atom at the o- and p-positions on the phenol ring. The displaced free proton simultaneously interacts with the catalyst to recover the Brønsted acid site and maintain the catalytic activity throughout the reaction. Although not included in **Fig.4-6**, it is worth noting that the methyl carbocation can be transferred not only to phenol but also to other compounds such as benzene, toluene, and non-decomposed anisole present in the reaction media. All the transmethylation processes are initiated from methyl cleavage.

Transition state compounds normally exist for a very short time due to instability; however, the methyl carbocation attached to the active site during the transmethylation process is a relatively stable structure with zero valency. Consequently, it can be considered as an intermediate compound, rather than a transition state compound, therefore it is possible to build reaction models for the

methyl carbocation cleavage and the carbocation substitution reactions separately.

The mechanism described in **Fig.4-6** shows the role of the acid catalyst in providing an alternative reaction pathway compared to that observed for the non-catalytic reaction. As explained above, the transmethylation in non-catalytic decomposition of anisole proceeds as a free radical reaction, without the participation of any carbocations (Zhu, Mallinson and Resasco, 2010), as shown in **Fig.4-5**. The use of Brønsted acid catalyst replaces the one-step reaction of direct methyl free radical transfer observed for the non-catalytic reaction by a two-step process. The catalysis mechanism also shows constant maintenance of acid sites in the catalyst by proton recovery throughout the reaction. Further reaction modelling was carried out considering the mechanism proposed here.

4.3 Modelling of non-catalytic and catalytic transmethylation of anisole to phenol and other acceptor molecules

The transmethylation reactions with a phenol molecule in the non-catalytic and catalytic decomposition of anisole were modelled. Both non-catalytic and catalytic transmethylation models were built by locating equidistantly the reactant molecules (about 3Å) to minimize any possible position-related errors. The catalytic transmethylation was modelled based on the dual electrophilic attack mechanism proposed in **Fig.4-6**, considering the system containing methyl carbocation on the acid site as the intermediate compound (see **Fig.4-7**). The modelling was implemented in two stages: methyl carbocation cleavage from anisole over the catalyst active site, and transfer of the carbocation to the surrounding molecules. The transition states for both stages are denoted as TS1 and TS2 respectively. The non-catalytic transmethylation model was built according to the free radical mechanism, and the transition state of the reaction is denoted as TS. The unique imaginary frequency of each transition state is shown in Appendix **A5**. The cleavage energy of the carbocation from the anisole molecule (for TS1) and the energy barriers for the methyl carbocation transfer to ortho-, meta-, and para-positions of phenol (for TS2) during the catalytic transmethylation of anisole to form cresol via phenol, as predicted by the model,

are shown in **Fig.4-8**. The transition state (TS) and corresponding energy barriers for the non-catalytic transmethylation of anisole to n-cresol are shown for comparison.

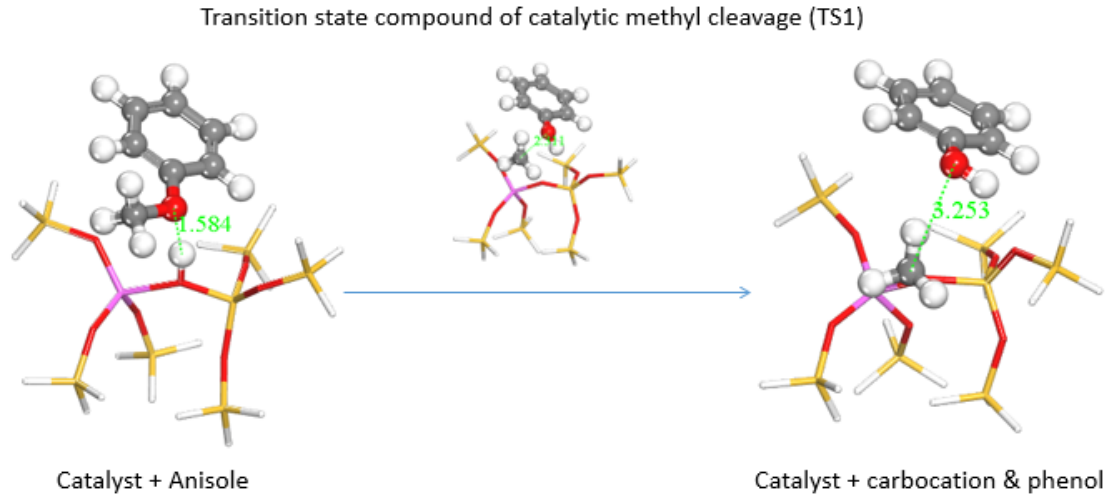

(a)

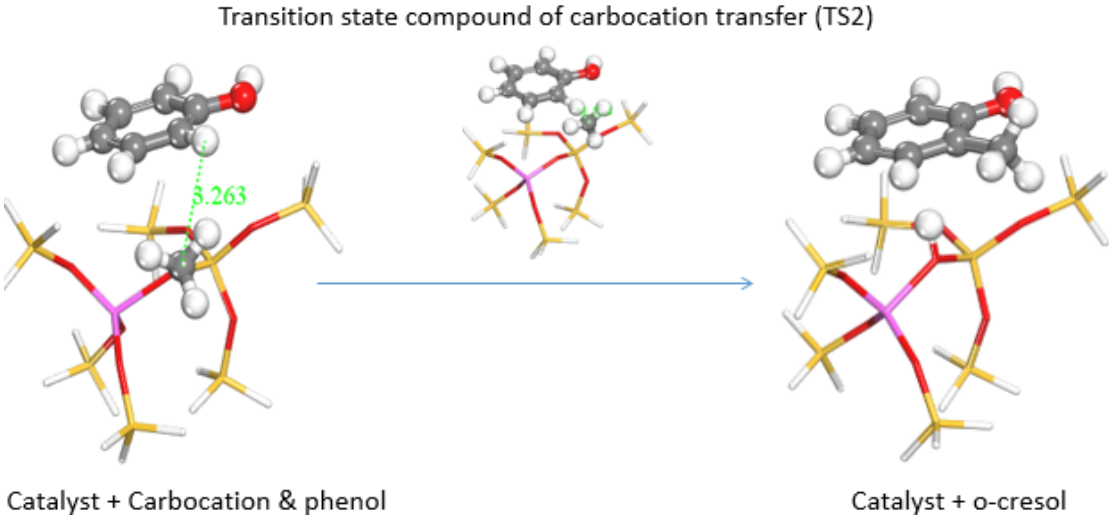

(b)

Fig.4-7. (a) C_{SP}^3-O bond (C8-O7) cleavage and carbocation formation; (b) Methyl carbocation transfer to ortho-position of phenol (transfers to meta- and para-positions are not shown here). Atoms are coloured as follows: carbon atom (grey), hydrogen atom (light grey), oxygen atom (red), silica atom (yellow) and aluminium atom (pink).

As can be seen in **Fig.4-8**, the transmethylation to the ortho-position of phenol presented a lower energy barrier than the meta-position and para-position transfers both in non-catalytic and catalytic decomposition. This result indicates that ortho-position transmethylation is more likely to occur to the phenol molecule,

which would be further illustrated by the experimental observations detailed in Chapter 6. In short, experiments showed that o-cresol was formed at a lower temperature (550˚C) than p-cresol (600˚C) in non-catalytic anisole decomposition, and most multi-methyl phenolic compounds presented the ortho-position occupied by a methyl group in the catalytic anisole decomposition (Zhang et al., 2016). In addition, the model pointed to the highest energy barrier for the meta-position transfer. This is in agreement with experimental results, which exhibited no evidence of m-cresol formation (Zhang et al., 2016).

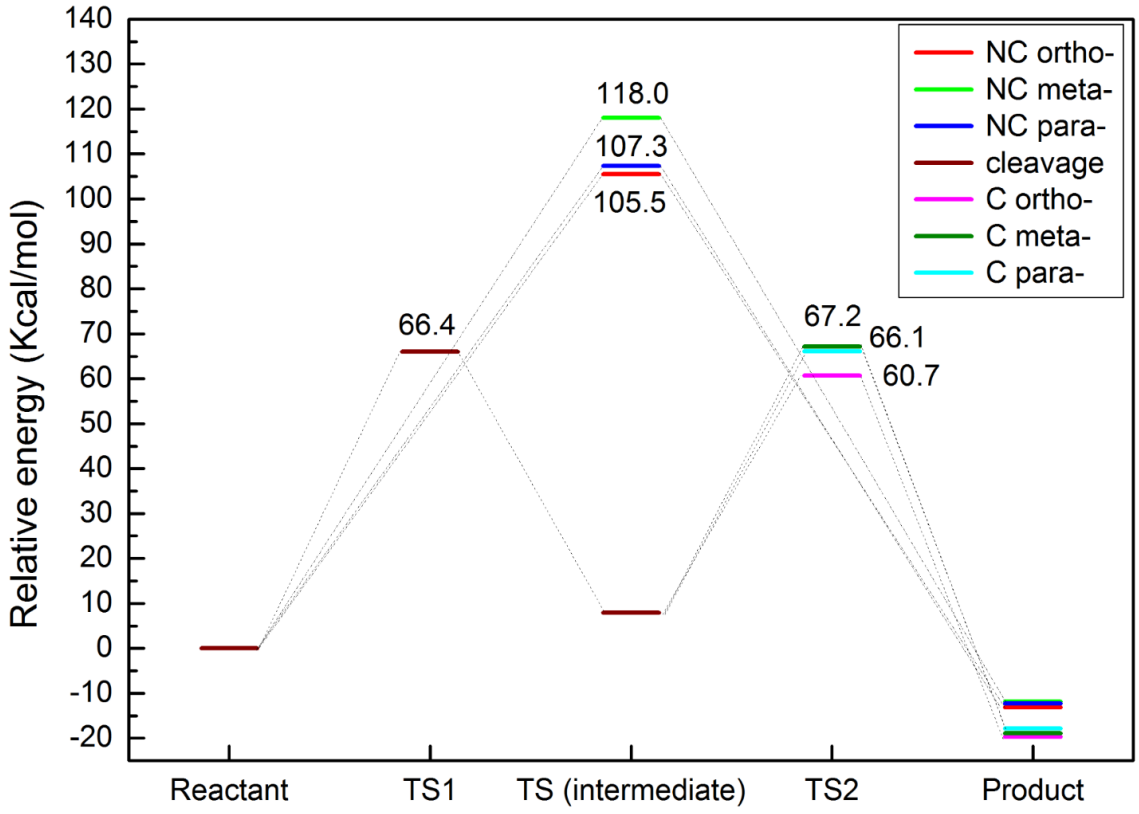

Fig.4-8. Energy barriers for transmethylation reactions of anisole to cresol (via phenol). (C denotes to catalytic transmethylation; NC denotes to non-catalytic transmethylation)

The model also predicted that the energy barrier for the methyl cleavage in the presence of the catalyst was 66.4 kcal/mol, which was much lower than the energy barrier values of the non-catalytic process. Moreover, compared to the non-catalytic process, the energy barrier for catalytic transmethylation to ortho-position decreased from 105.5 kcal/mol to 60.7 kcal/mol, and those for para- and meta-positions dropped from 107.3 kcal/mol to 66.1 kcal/mol and from 118.0

kcal/mol to 67.2 kcal/mol respectively. These results are further interpreted by experimental data, which showed that a lower temperature (approximately by 150˚C) was required to achieve the most Phs yield with the same anisole conversion during the catalytic decomposition of anisole compared to non-catalytic decomposition (see Chapter 6) (Zhang et al., 2016).

4.4 Transmethylation for different acceptors in the decomposition of anisole

The transmethylation process also gives rise to other methyl substituted compounds apart from cresol (Zhang et al., 2016). Therefore, transmethylation reactions with other acceptor molecules were modelled to assess the reactivity of these intermediate compounds, and the selectivity of the resulting products. The formation of toluene, methyl anisole, xylene, xylenol, and trimethyl-phenol due to the addition of a methyl group to benzene, anisole, toluene, cresol and xylenol respectively were also modelled. The energy barriers for the different reactions pathways in non-catalytic and catalytic decomposition of anisole are shown in **Table 4-1**.

In the case of non-catalytic decomposition, the energy barriers of transmethylation changed significantly, depending on the acceptor molecules. This is related to the fact that the substituents on the molecule affect the charge distribution in the aromatic ring, giving rise to the site migration of substituted reactions (Lambert, 1958). Anisole, toluene and phenolic compounds showed energy barrier values between 105.7 and 121.1 kcal/mol in the non-catalytic transmethylation (**Table 4-1**), and the energy barrier for the methyl transfer to benzene in the non-catalytic reaction was the highest for 126.4 kcal/mol.

It is found the molecules containing branch chain substituents, especially oxygen-rich chains such as hydroxy and methoxy functional groups, more readily accept methyl radicals. The branch chains may have an impact on the π-bond of the benzene ring, making the ring more susceptible to methyl attack especially at the ortho- and para-positions, while the benzene ring without branch chains may have smaller electron density, so that is more stable to radical attack (Phuong, 1986).

Table 4-1. Energy barrier for the different reaction pathways of transmethylation in non-catalytic and catalytic decomposition of anisole

Reactant	Via	Product	Orientation	Relative Energy (kcal/mol)		
				Non-catalytic (TS)	Catalytic	
					Cleavage (TS1)	Methyl cation transfer (TS2)
Anisole	Phenol	Cresol	Ortho	105.5	66.4	60.7
			Meta	118.0		67.2
			Para	107.3		66.1
	o-Cresol	Xylenol	Ortho	107.2		60.4
			Meta	121.1		61.8
			Para	107.0		54.1
	2,4-Xylenol	2,4,6-Phenol	Ortho	114.3		60.4
	2,6-Xylenol	2,3,6-Phenol	Meta	110.0		59.9
	Benzene	Toluene	-	126.4		73.5
	Toluene	Xylene	Ortho	108.1		71.2
			Meta	112.2		68.3
			Para	109.5		70.8
	Anisole	Methyl-anisole	Ortho	106.9		63.3
			Meta	105.7		67.0
			Para	108.3		71.7

In the case of catalytic reactions, the presence of the acid catalyst decreased notably the energy barrier values, exhibiting a big influence on promoting transmethylation. The decreases in the energy barrier was observed range from 36.6 kcal/mol (transmethylation to para position of anisole) to 59.3 kcal/mol (transmethylation to meta position of o-cresol). The transmethylation to benzene

is found had the highest energy barrier for 73.5 kcal/mol, even though it has been diminished by roughly 53 kcal/mol compared to the non-catalytic process, this indicates the stability of the benzene ring to electrophilic attack compared to other branch chain contained compounds. In the case of the transmethylation to toluene, the model also predicted a decrease in the energy barrier value for each of the position transfers when using a catalyst (ranging between 68.3kcal/mol and 71.2kcal/mol), but the predicted energy barriers are higher than those for most oxygen contained compounds, regardless of the position transfer. It is also noted that transmethylation to anisole at the ortho-position to produce methyl-anisole exhibited a similar energy barrier value to other intermediate compounds (63.3 kcal/mol). This result suggests that the presence of sole methyl group attached to the aromatic ring has limited effect on the molecules to accept electrophilic substitution by methyl carbocation, this may attribute to the lower electronegativity of the methyl group than that of the oxygen contained functional groups (De Proft, Langenaeker and Geerlings, 1993). At a macroscopic level, it can be inferred that in the decomposition of anisole, majority of toluene and xylene are probably produced from the deoxygenation of cresols and xylenols, rather than from the transmethylation to benzene over the Brønsted acid sites.

Compared to AHs, methyl phenolic compounds, i.e. cresol and xylenol, are found to be prone to accept electrophilic substitution at all positions. Among all the evaluated compounds, these molecules accept methyl carbocation at the lowest energy barrier values. Transmethylation for cresol into xylenol presented energy barriers ranging from 54.1 kcal/mol (p-position transfer) to 61.8 kcal/mol (m-position transfer). Transmethylation to convert xylenol into 2,3,6-methyl phenol and 2,4,6-methyl phenol exhibited similar energy barriers at around 60 kcal/mol. These results well illustrate the experimental results during catalytic decomposition of anisole in which the abundant production of multi-methyl phenolic compounds and the typical position preference was observed (Zhang et al., 2016). The formation of these multi-methyl phenolic compounds from anisole depends on the initial formation of cresol.

4.5 Summary

This chapter presents the DFT modelling of the transmethylation as the primary reaction taking place in both non-catalytic and catalytic anisole decomposition. Molecule analysis revealed that the weakest bond in the anisole molecule was the C_{sp}^3-O bond, where the methyl radical cleavage readily happened, leading to the transmethylation process in non-catalytic transmethylation, which primarily took place with the methyl free radical transfer. In catalytic transmethylation, reactants interacted with the Brønsted acid sites present in the catalyst. Fukui analysis showed that the catalytic transmethylation was initiated by the Brønsted acid proton electrophilic attack at the oxygen atom of anisole, followed by a carbocation substitution. Ortho- and para-positions in the phenolic molecules were more reactive. A dual electrophilic attack mechanism was proposed for the catalytic transmethylation. Transmethylation reactions modelling, based on the proposed mechanism, proved that the Brønsted acid catalyst could significantly lower the reaction energy barrier for all reactant compounds investigated due to changes in the reaction pathways. Most of the energy barriers for the evaluated transmethylation reactions decreased more than 40 kcal/mol when considering the catalytic effect, the highest decrease being observed in the case of o-cresol (around 60 kcal/mol). Furthermore, both non-catalytic and catalytic transmethylation exhibited target molecule preference, depending on the original substituents of the acceptor, and transmethylation to most compounds showed preference for the ortho- and para-positions. Non-catalytic transmethylation to compounds with oxygen-rich substituents generally showed lower energy barriers. In the catalytic decomposition of anisole, the presence of oxygen-rich substituents also enhanced the reactivity of the ring, especially for phenolic compounds at the ortho- and para-positions. The lowest energy barrier was observed in the case of transmethylation towards the para-position of the cresol molecule (54.1 kcal/mol).

5 Multiscale modelling study of deoxygenation in the decomposition of anisole over metal-loaded zeolite catalyst

Deoxygenation is found to be the second stage following transmethylation in anisole decomposition process (Zhang et al., 2016). This chapter presents the modelling prediction on deoxygenation process in anisole catalytic decomposition over HZSM-5 (HZ) catalyst and metal loaded HZSM-5 (metal/HZ) zeolite catalyst with the aim of assessing the metal effects on the catalytic deoxygenation. A proper prediction in catalyst design could save huge costs and time for experiments. DFT modelling could also reveal insight of deoxygenation reaction mechanism on atomic level.

Multiscale modelling was used to design proper metal loaded catalyst for experiment use. At quantum scale, common transition metals were compared in terms of their adsorption energy when adsorbing an anisole molecule. A metal cluster model was used to investigate the adsorption process. A bi-metal crystal model was used to investigate the interaction between two metals and reactant molecules. At molecular modelling scale, the adsorption capacity of single metal loaded HZ (metal/HZ) was investigated by isotherms using the Monte Carlo method.

After analysing the performance of metals in the adsorption process, the mechanism of deoxygenation reaction over acid catalyst was investigated by a combination analyses of Fukui index and bond orders of relative molecules. In addition, a novel deoxygenation mechanism was proposed and compared with the reported mechanism.

The chapter ends up with the implementation of the modelling of the deoxygenation reactions over HZ and Ni, Co, Mo, Cu supported HZ catalysts. The modelling results revealed the metal performance in affecting the deoxygenation of related phenolic compounds (phenol, cresols, xylenols and trimethyl-phenols; Phs). It also illustrated the effect of side chain methyl group on deoxygenation reactions of various intermediates during anisole decomposition.

5.1 Anisole adsorption on clusters of transition metals

Adsorption usually happens as the first step of catalytic reactions and it consists of the link between the reactants and the catalyst active sites. In the case of heterogeneous catalysis, adsorption can determine the overall reaction rate in a big extent (Davis and Davis, 2003; Johnston et al., 2010; Peköz and Donadio, 2016). In catalytic reactions of anisole deoxygenation, the investigation of the reactant adsorption is essential to understand the entire catalytic process, besides, it has been reported that adsorption plays an important role in determining the selectivity to desired products (i.e. BTX) (Ghampson et al., 2017). Modelling of anisole adsorption onto metal loaded catalyst would provide a good prediction of the performance of metals as active sites, and aid the selection of metals for real operation.

Models of twelve common transition metals, i.e. Mn, Fe, Co, Ni, Cu, Zn, Ga, Mo, Ru, Rh, Pd, and Pt, were built and compared in terms of their performance in the adsorption of molecular anisole. All the models were based on four atomic clusters that are shown in **Fig. 5-1**. In the actual anisole conversion process, not only anisole can be the adsorbate, but also Phs and aromatic hydrocarbons (AHs) compounds formed during the reactions. In this model, the anisole molecule as the reactant was used as representative of those compounds.

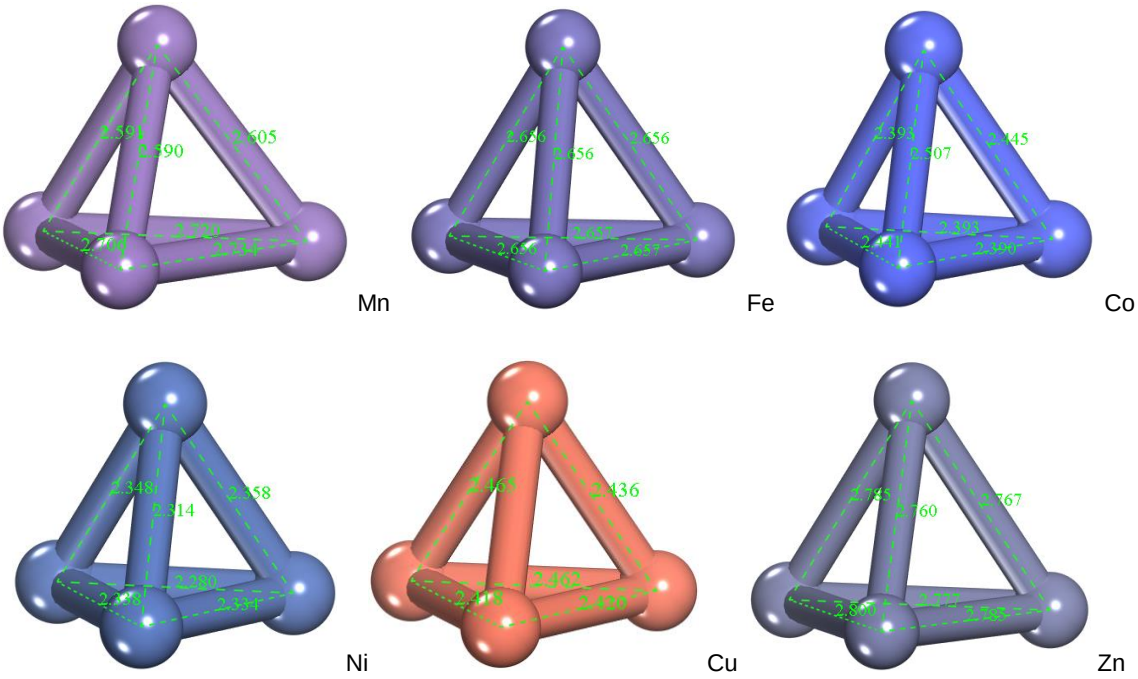

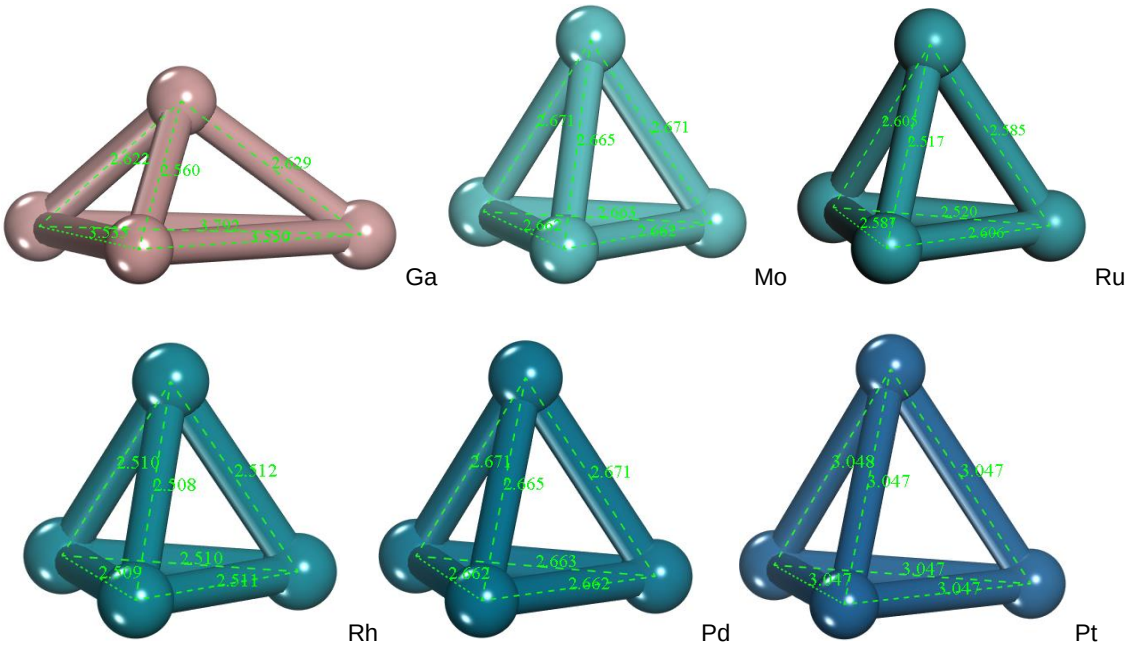

Fig. 5-1 Metal cluster models labelled with inner dimensions (Å)

Fig. 5-2 shows the values of the adsorption energy of anisole onto each single metal calculated through the modelling. Co, Mo, Ni and Cu exhibited the highest adsorption energy. This implies stronger bindings between the anisole molecule and these metal clusters than those shown by the other modelled metals. On the contrary, Fe, Ru and Zn showed the lowest adsorption energy, corresponding to weak bindings between the metals and the adsorbate.

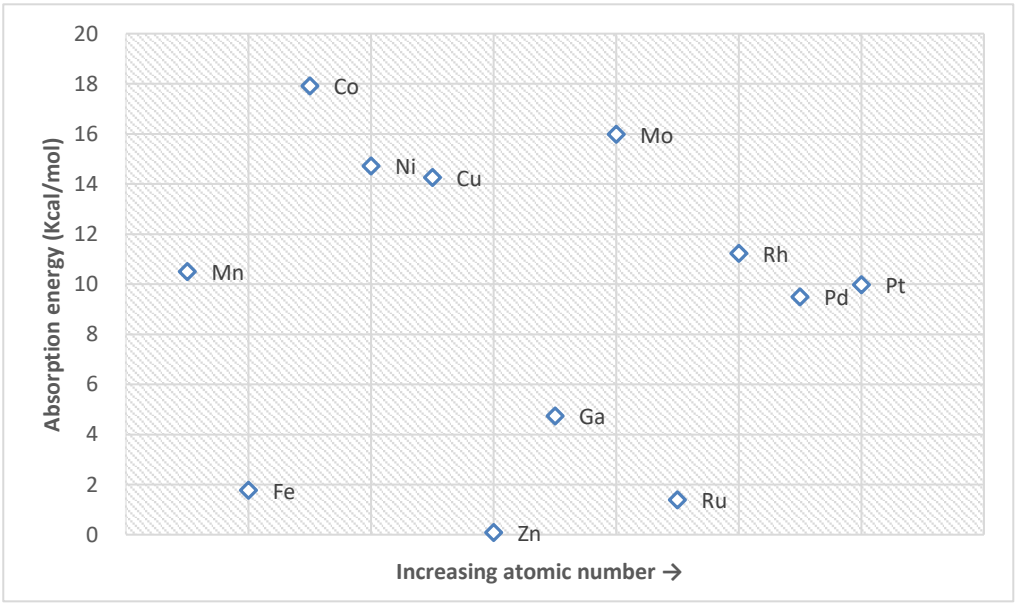

Fig. 5-2 Adsorption energy of common transition metals in adsorbing anisole

Ni, Co, Mo, Cu metals were used for further modelling investigation in Sections 5.2 and 5.5 because of the predicted large adsorption energy values.

5.2 Anisole adsorption on single metal loaded HZ zeolite

Adsorption capacity of a targeted reactant on an active site is an important indicator for catalyst design and synthesis (Corma et al., 1989). Adsorption capacity of anisole on HZ zeolite catalyst with different Si/Al ratios (23, 47 and 95, denoted as HZ(23), HZ(47), and HZ(95) respectively) was investigated by molecular modelling (Monte Carlo method) in a temperature range from 25°C to 600°C, and the isotherms for the adsorption of anisole were predicted (shown as symbols in the figures) in a pressure range from 101.3 kpa to 1013 kpa as shown in the **Fig. 5-3**. The isotherms were predicted using fitting curves (shown as lines in the figures) because Monte Carlo method is based on stochastic calculation that relies on probabilities (Rahmati and Modarress, 2009).

Regardless the Si/Al ratio of the zeolite, the average loading of anisole increased when pressure rose. For HZ(23), the loading became steady quite readily before 300kPa at 25°C, 200°C and 400°C. Regarding HZ(47) and HZ(95), the isotherms for 25°C and 400°C had no big difference compared to HZ(23), however, an obvious loading increase was observed for 200°C at high pressures, which is probably related to the less mesoporous intercrystalline voids in the structures of HZ(47) and HZ(95) (Gao et al., 2016; Liu et al., 2016; Zhao et al., 2014). For the isotherms at 600°C in all three cases, the average anisole loadings increased throughout the whole pressure range. The results exhibit that the increase in pressure promotes the anisole adsorption capability of HZ both at moderate and high temperatures (Rahmati and Modarress, 2009). On the contrary, increasing temperatures negatively affect the adsorption capacity of anisole on HZ. For the three types of zeolites, at atmospheric pressure (101 kpa) and lower tested temperatures (25°C and 200°C), the average loadings of anisole barely varied, with no less than 4 molecules per cell. However, it decreased to about 3.0 per cell when temperature raised up to 400°C, and dropped significantly to less than 0.5 per cell at 600°C. Analogue trends have been observed for all the pressures investigated. Higher temperatures relate to larger kinetic energy of the anisole

molecules, which would promote its desorption from the zeolite surface rather than adsorption onto it.

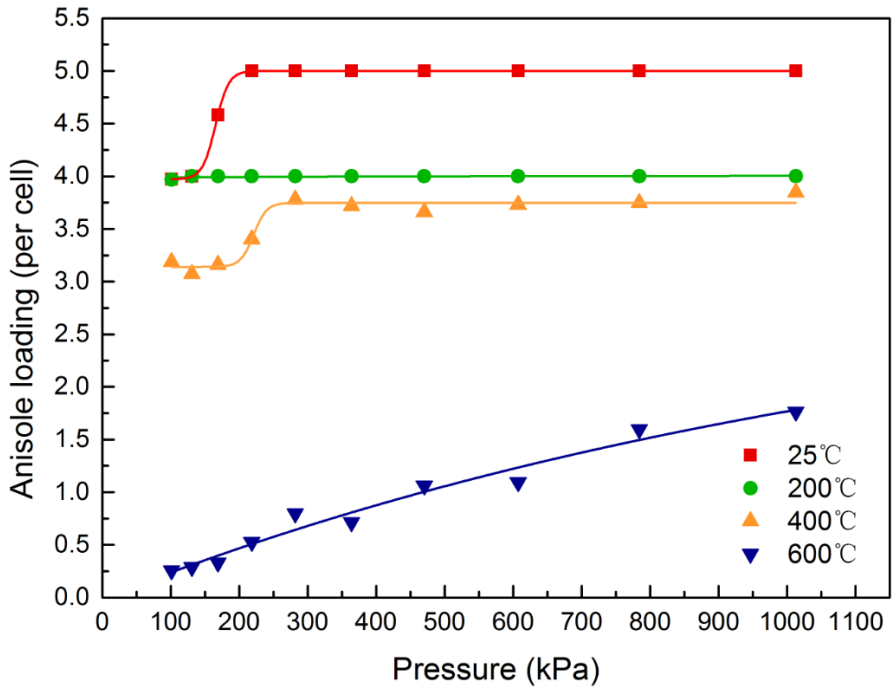

(a)

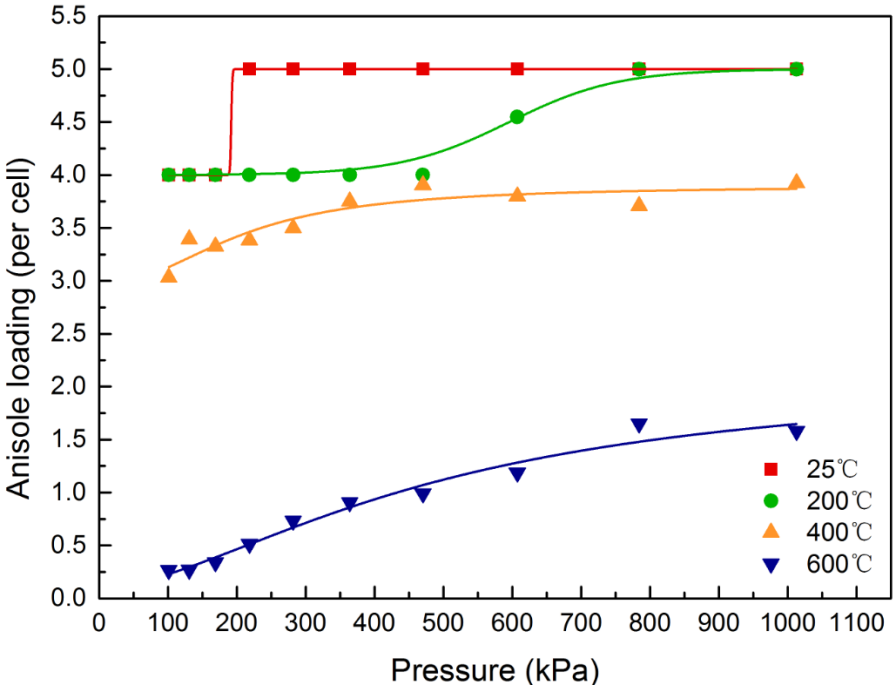

(b)

Fig. 5-3 Average loading of anisole onto HZ with different Si/Al ratios: (a) Si/Al = 23; (b) Si/Al = 47; and (c) Si/Al = 95 (solid symbol: predicted by the model; line: fitting curve)

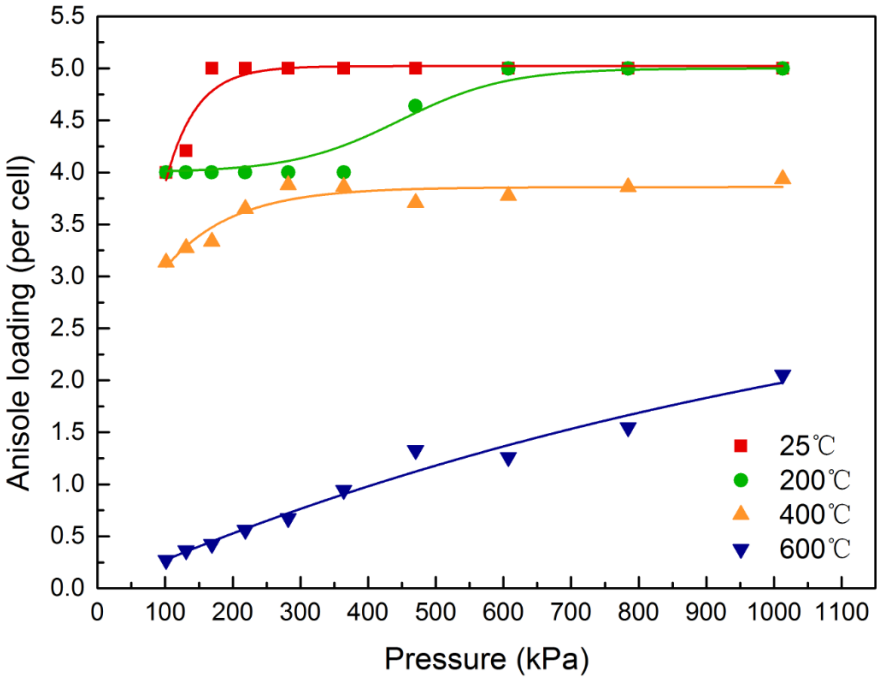

(c)

Fig. 5-3 Average loading of anisole onto HZ with different Si/Al ratios: (a) Si/Al = 23; (b) Si/Al = 47; and (c) Si/Al = 95 (solid symbol: predicted by the model; line: fitting curve)

The modelling predicted that the Si/Al ratio has influence on the HZ adsorption capability of anisole molecule at the relative low tested temperatures, particularly at 200°C. However, the adsorption capacity at higher temperatures (400°C and 600°C) does not show significant variations with the changes in the Si/Al ratio of the zeolite. The highest average loadings for HZ(23), HZ(47) and HZ(95) is 5.0 per cell obtained at low temperatures.

The adsorption isotherms for metal loaded zeolite catalysts were modelled in a larger temperature range from 25°C to 800°C. The adsorption performance of Ni, Co, Mo and Cu loaded HZ(23) (denoted as Ni/HZ(23), Co/HZ(23), Mo/HZ(23), and Cu/HZ(23) respectively) was compared (as shown in **Fig. 5-4**).

Temperature rise would also decrease the anisole adsorption capacity of the metal based catalysts. Compared to sole zeolite catalysts, metal loading showed negative influence on the adsorption capacity of anisole under 400°C, especially at the upper end of the evaluated pressure range, nevertheless, the promotion of

adsorption capacity by the metal was observed at higher temperatures above 400°C. The average anisole loading at 600ºC was significantly enhanced to the values like those obtained at lower temperatures in the case of Ni, Co and Mo, but the loading of Cu only showed limited promotion of adsorption capacity at only 400°C and 600°C compared to the isotherms for HZ(23).

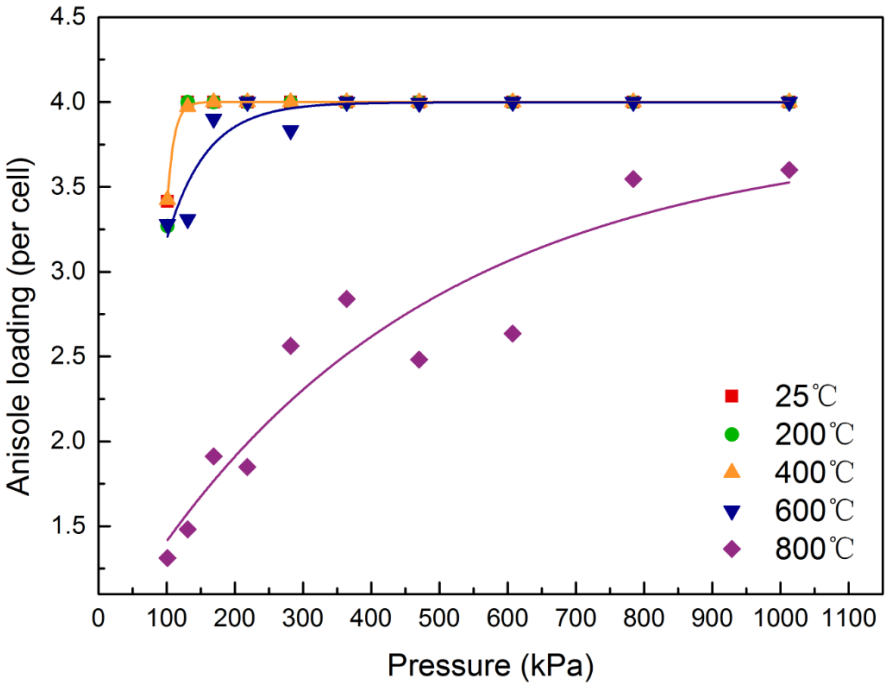

(a)

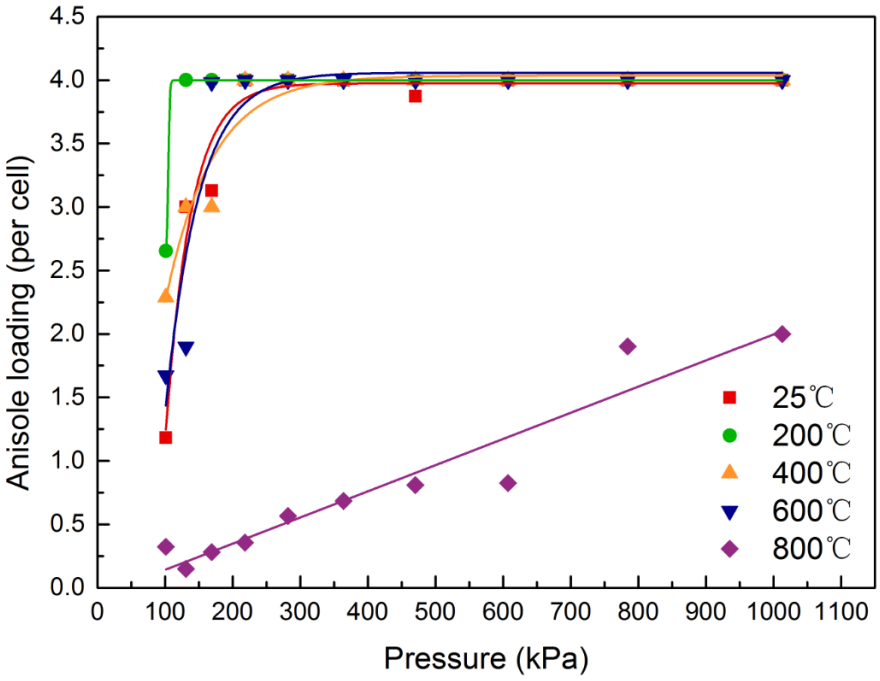

(b)

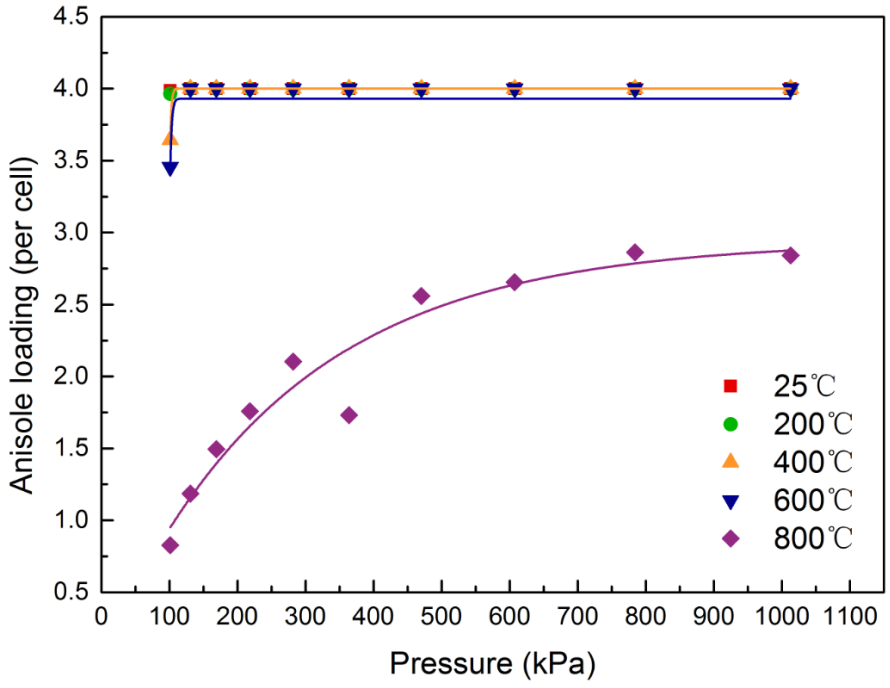

(c)

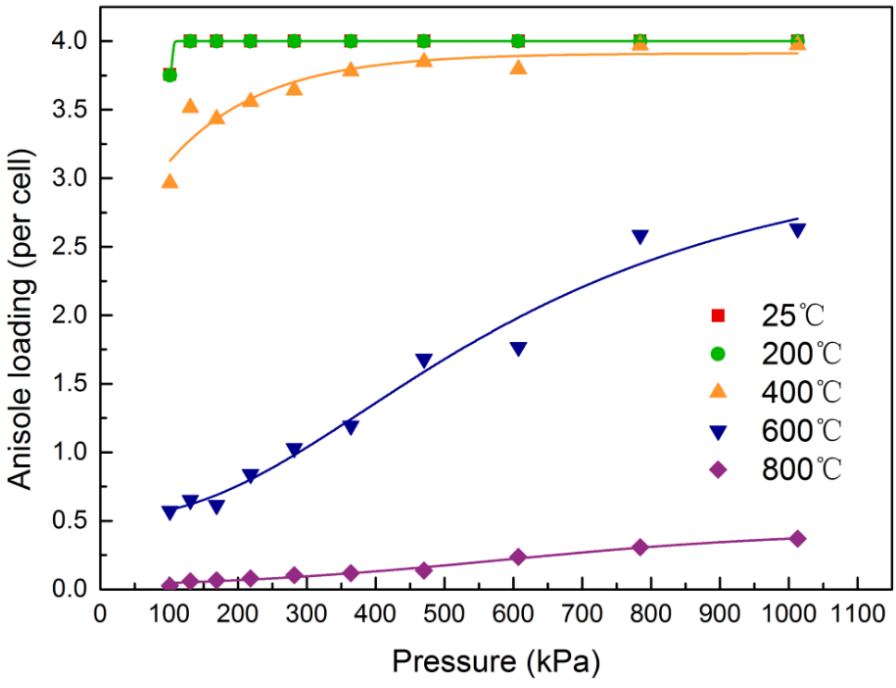

(d)

Fig. 5-4 Adsorption isotherms of anisole onto (a)Ni/HZ(23) (b)Co/HZ(23) (c)Mo/HZ(23) (d)Cu/HZ(23) (solid symbol: predicted by the model; line: fitting curve)

The result indicates that metal loading of the acid sites may decrease the adsorption capacity at relatively low temperatures (Gavrilov et al., 2010; Liu et

al., 2016; Zhao et al., 2013, 2014), nevertheless, their stronger chemical bond with the adsorbates compared to sole zeolite provides higher adsorption capacity (prevent significant desorption) at higher temperatures.

In the case based on Ni/HZ, average anisole loading became stable at 4 per cell even at 600°C, and showed significant rise at 800°C and reached 3.55 per cell eventually under high pressure. The isotherm based on Co/HZ exhibited that Co had negative effect in anisole adsorption only under atmospheric pressure at low and moderate temperatures, and it would promote the average loading of anisole up to 4.0 per cell at 600°C and to 2.0 per cell at 800°C respectively at high pressures. In the case based on Mo/HZ, relatively high average loading was observed at each temperature even under atmospheric pressures, and it became 2.9 per cell at 800°C under roughly 800kPa. The isotherm based on Cu/HZ showed the steady average loading of about 4.0 per cell at low temperatures and high pressures but a considerable declined at 600°C, and the loading on Cu/HZ at 800°C decreased significantly to be less than 0.4 per cell in the whole pressure range. The result implies Cu has lower adsorption capability to anisole and related molecules compared to Ni, Co, and Mo (Gavrilov et al., 2010; Zhao et al., 2013).

The average anisole loading values at 600°C under atmospheric pressure are highlighted in **Table 5-1**, as they are considered as criteria for the selection of the metal-based catalysts to be used in the experimental work included in this thesis. **Table 5-1** also shows the anisole loading on pure zeolite catalyst for comparison purposes.

Table 5-1 Average loading for catalysts at 600°C, 101kPa

Catalyst	HZ(23)	Ni/HZ	Co/HZ	Mo/HZ	Cu/HZ
Loading (molecules/cell)	0.26	3.28	1.67	3.45	0.57

The results reveal that each tested metal could promote the adsorption capacity compared to pure zeolite catalyst significantly. In real reactions of the catalytic decomposition of anisole, the strong adsorption capability of the metal based

zeolite catalyst may not only promote reactions, but also lead to high yield of carbonaceous deposit by the adsorption of reactants and intermediate compounds (Ghampson et al., 2017). It is also found that Ni/HZ(23) and Mo/HZ(23) exhibit larger capability for anisole adsorption compared to Co/HZ(23) and Cu/HZ(23), therefore, Ni and Mo are also selected to be investigated by modelling as components for bi-metal loadings consisted with iron in Section 5.3.

5.3 Reactants adsorption on bi-metal crystal surface

To alleviate the potential high yield of carbonaceous deposit over the metals with high adsorption capability, a second metal with weak adsorption capacity was introduced to form bi-metal loading catalyst. According to the results obtained in Section 5.1, Fe showed relatively weak anisole adsorption energy and was commonly applied in catalytic anisole decomposition (Li et al., 2017a). Therefore, Fe was selected to be alloyed with Ni and Mo respectively as the loadings for bi-metal based catalysts. The interaction between the parallelly adsorbed reactant molecule and bi-metal loaded HZ catalyst were predicted by modelling bi-metals crystals built based on Ni-Fe and Mo-Fe alloys. Bi-metal Ni-Mo was also modelled for comparison purposes. To solely investigate the effect of the bi-metals, the zeolite support was excluded in these models to eliminate its effect. As the reactant anisole and Phs (decomposition intermediates) were considered to be two most frequent types of compounds in interacting with the metal surface, before-adsorption and after-adsorption models were established both for the adsorption of anisole and phenol molecules. Since Phs as the actual reactants in the deoxygenation reaction, the detailed evaluation of the adsorption performance of phenol in terms of electron change inside the molecule has also been carried out. The models of phenol adsorption onto three alloys are shown in **Fig. 5-5**, **Fig. 5-6**, and **Fig. 5-7** respectively.

It is observed that the lattice appearance of the three alloys of Ni-Mo, Ni-Fe, and Mo-Fe was different; the Mo-Fe alloy had straight channels inside the crystal, while Ni-Mo and Ni-Fe did not exhibit obvious channels within the crystals. This results from different connections between two metal atoms of the alloys. The adsorption of the phenol molecule on the metal surface involved the reduction of

the distance between both species, with values normally below 2.5Å. Bonds were formed, which point to chemical interactions between the adsorbate and adsorbent. The adsorption energy for anisole and phenol adsorption onto each bi-metal alloy is shown in **Table 5-2**.

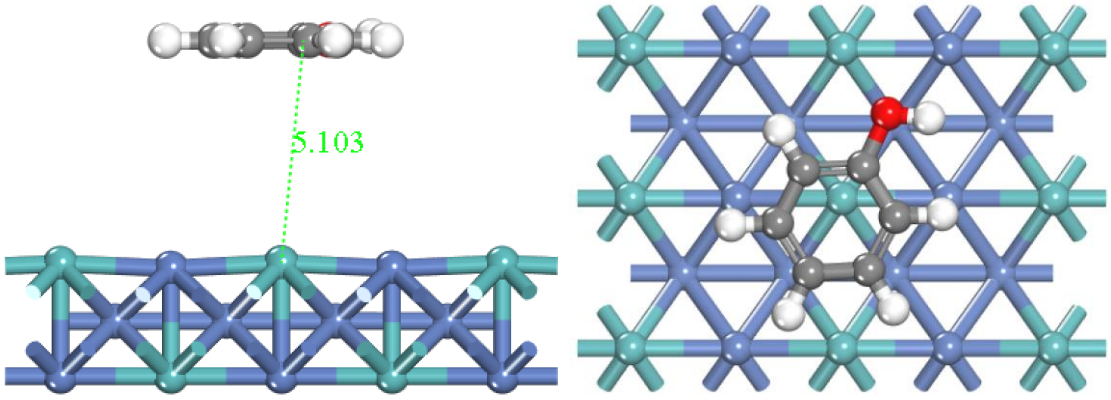

Front view Over view

(a)

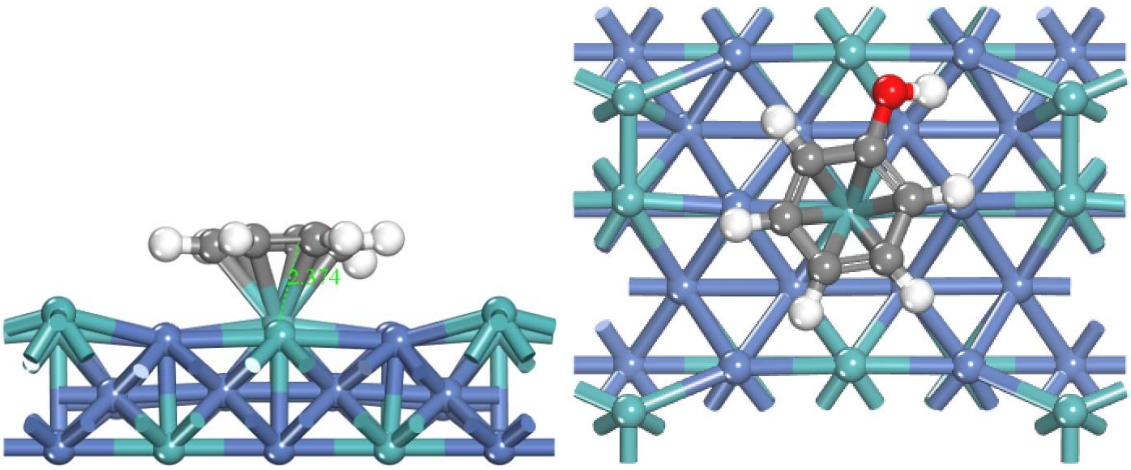

Front view Over view

(b)

Fig. 5-5 Adsorption model of phenol molecule onto bi-metal crystal surface (a) approach to Ni-Mo (b) adsorbed onto Ni-Mo. The distance between the adsorbate and the metal surface is given in Å

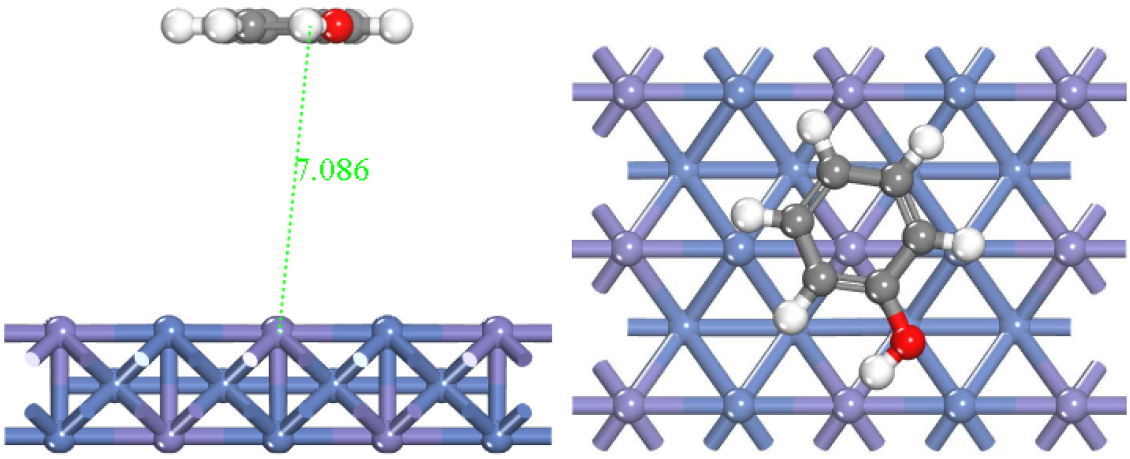

Front view Over view

(a)

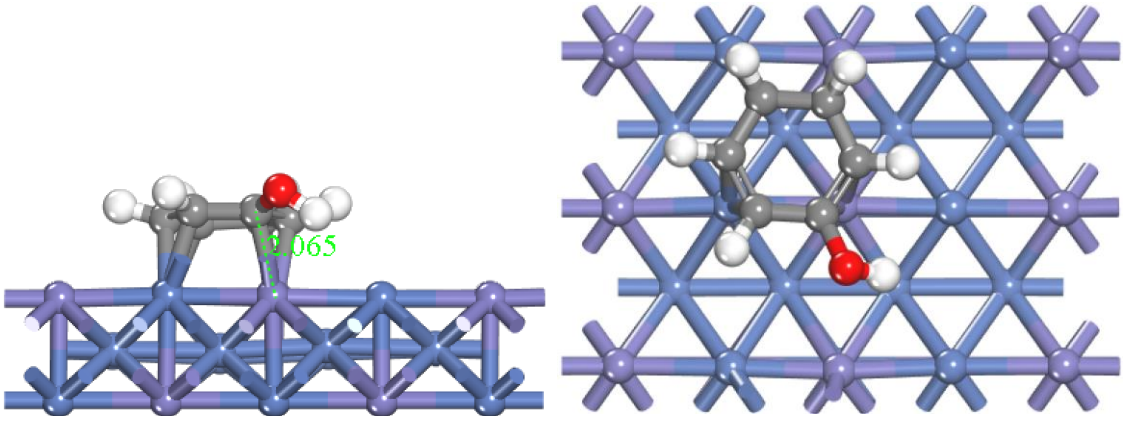

Front view Over view

(b)

Fig. 5-6 Adsorption model of phenol molecule onto bi-metal crystal surface (a) approach to Ni-Fe (b) adsorbed onto Ni-Fe. The distance between the adsorbate and the metal surface is given in Å

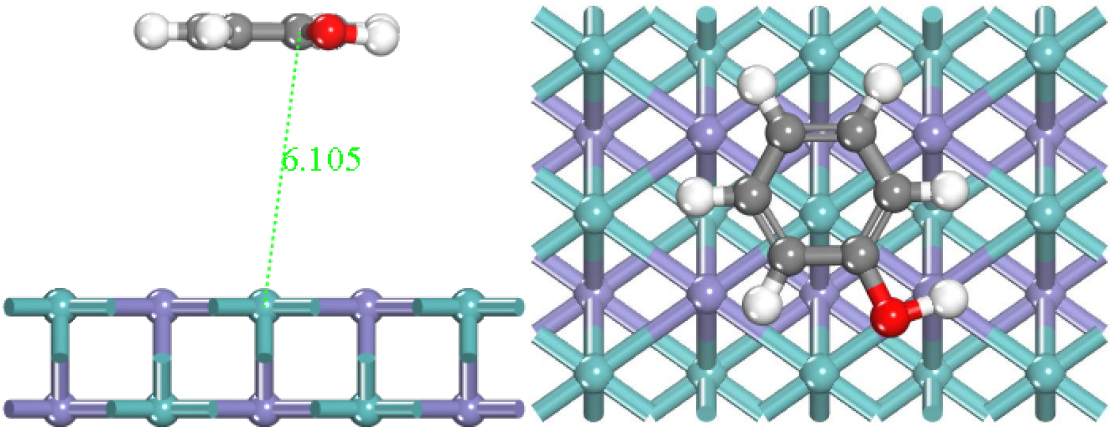

Front view Over view

(a)

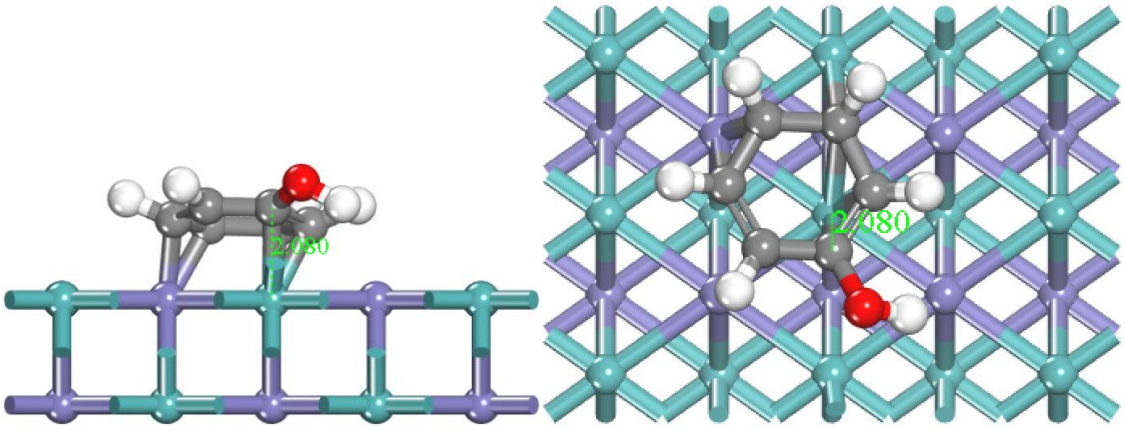

Front view Over view

(b)

Fig. 5-7 Adsorption model of phenol molecule onto bi-metal crystal surface (a) approach to Mo-Fe (b) adsorbed onto Mo-Fe. The distance between the adsorbate and the metal surface is given in Å

It is noted that Ni-Mo alloy showed the highest adsorption energy both to anisole and phenol molecules, and the addition of Fe decreased the adsorption energy for Ni-Fe and Mo-Fe alloys, herein Ni-Fe showed the lowest adsorption energy for both adsorbates, this could be ascribed to the lower adsorption energy of anisole on Ni than Mo as shown in **Fig. 5-2**. The predicted results meet bi-metal design concepts from a macroscopic view. The detailed interaction between alloy adsorbent and adsorbate was further illustrated by looking at the electrons change in the adsorbate molecule.

Table 5-2 Adsorption energy of anisole and phenol on three bi-metal alloy surfaces

Surface	Anisole	Phenol
	Adsorption energy (kcal/mol)	
Ni-Mo	72.67	79.88
Ni-Fe	43.08	45.41
Mo-Fe	63.99	60.67

Density of States (DOS) quantitatively addresses the electrons' states in each orbital of a system, a molecule and even a single atom in a molecule (Hernández

et al., 2012; Honkela, Björk and Persson, 2012; Wang, Zhang and Liu, 2017). The DOS change of a system usually reflects the interaction among each component within the system because these interactions give rise to electron displacement and transfer. Based on the mechanisms described in Chapter 4, Phs formed in the transmethylation of anisole were regarded as reactants for the deoxygenation reactions. DOS of the phenol molecule approaching and adsorbed onto the alloy surfaces are compared in **Fig. 5-8**, **Fig. 5-9** and **Fig. 5-10** respectively to evaluate the surface interaction with the adsorbate. The contribution of oxygen to the entire molecule DOS change was also determined. Electrons in s, p, d orbitals were considered for these cases.

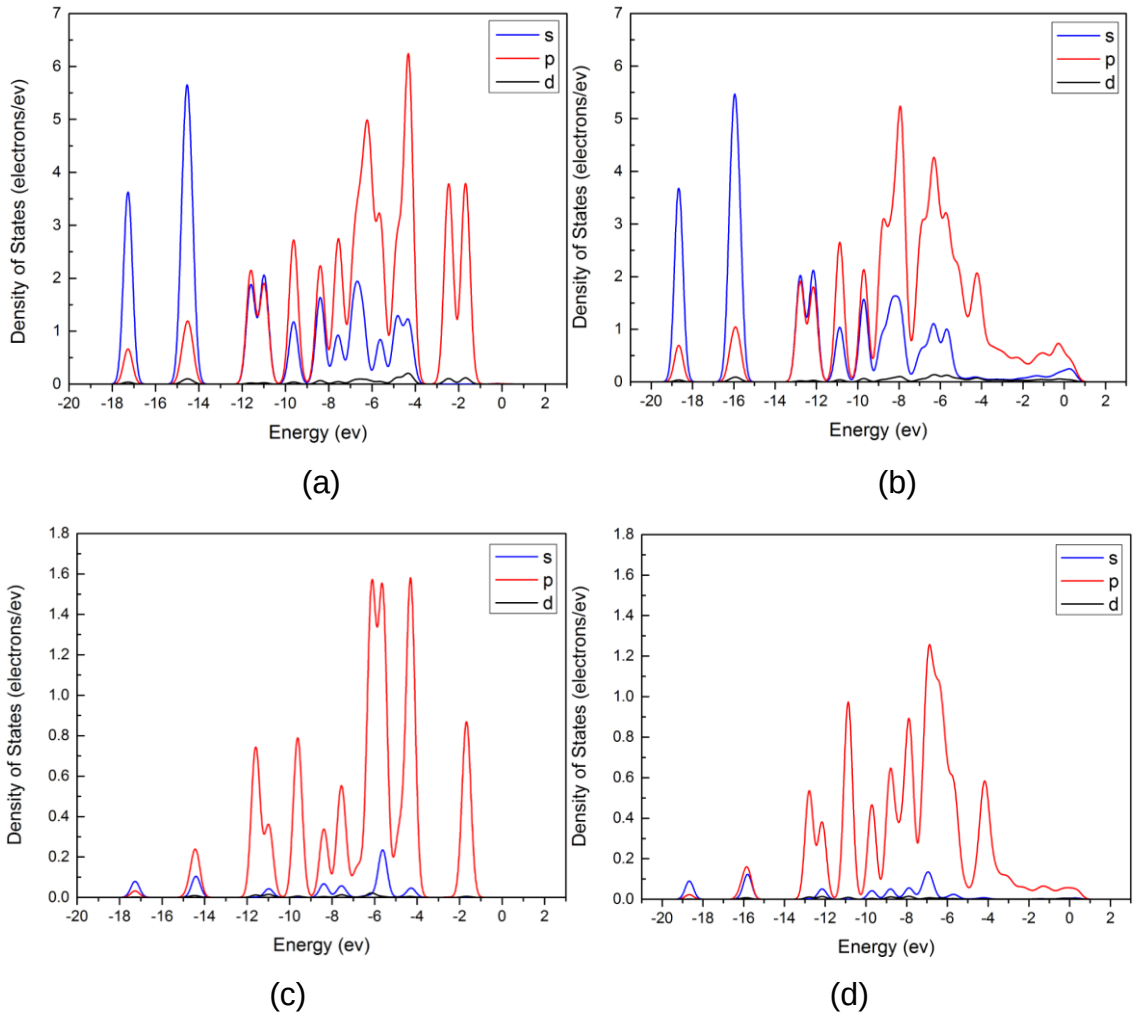

Fig. 5-8 Density of States (DOS) of Phenol: (a) approaching to Ni-Mo; (b) adsorbed on Ni-Mo. Oxygen contribution to DOS, Partial DOS (PDOS): (c) approaching to Ni-Mo; (d) adsorbed on Ni-Mo.

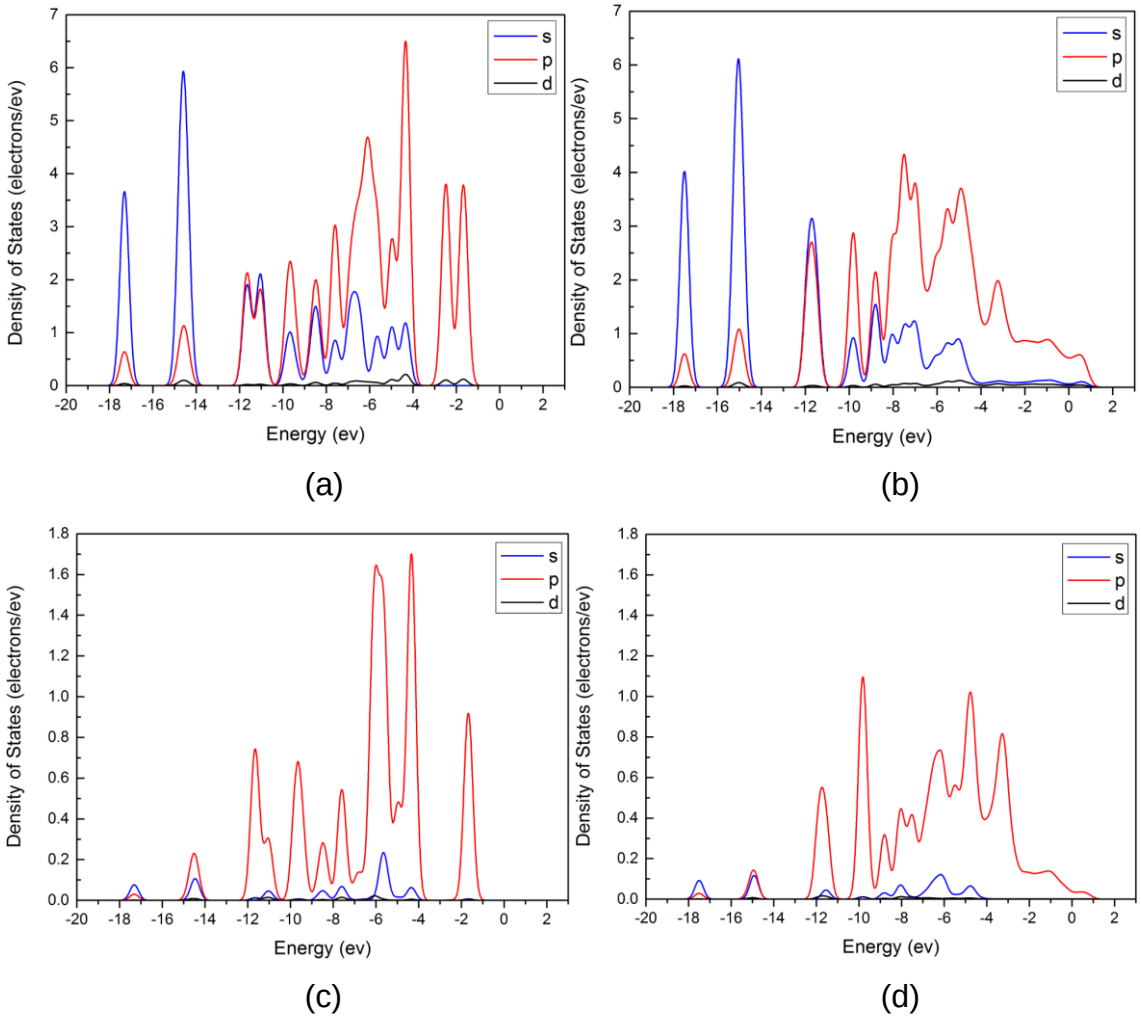

Fig. 5-9 Density of States (DOS) of Phenol: (a) approaching to Ni-Fe; (b) adsorbed on Ni-Fe. Oxygen contribution to DOS, Partial DOS (PDOS): (c) approaching to Ni-Fe; (d) adsorbed on Ni-Fe.

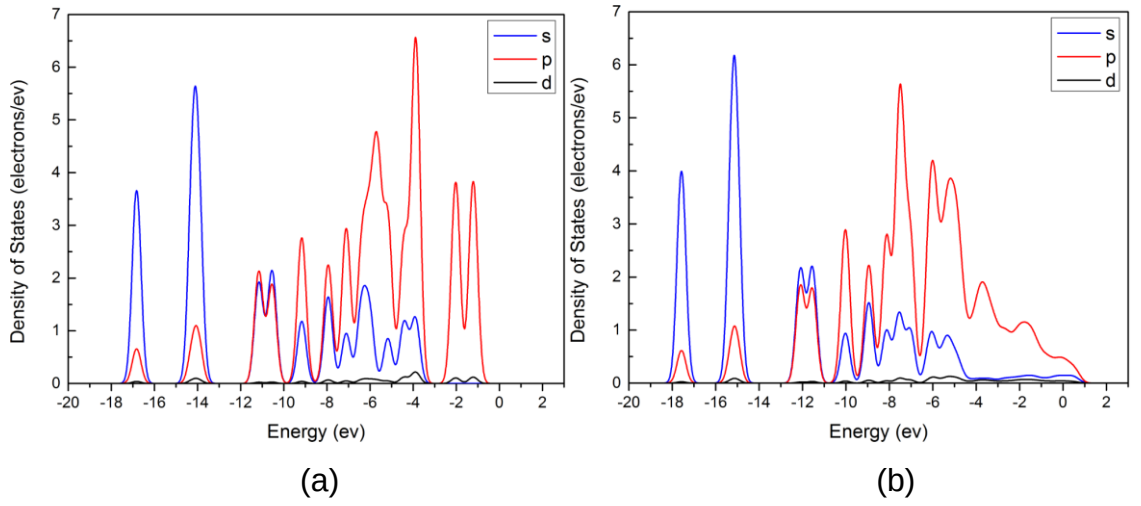

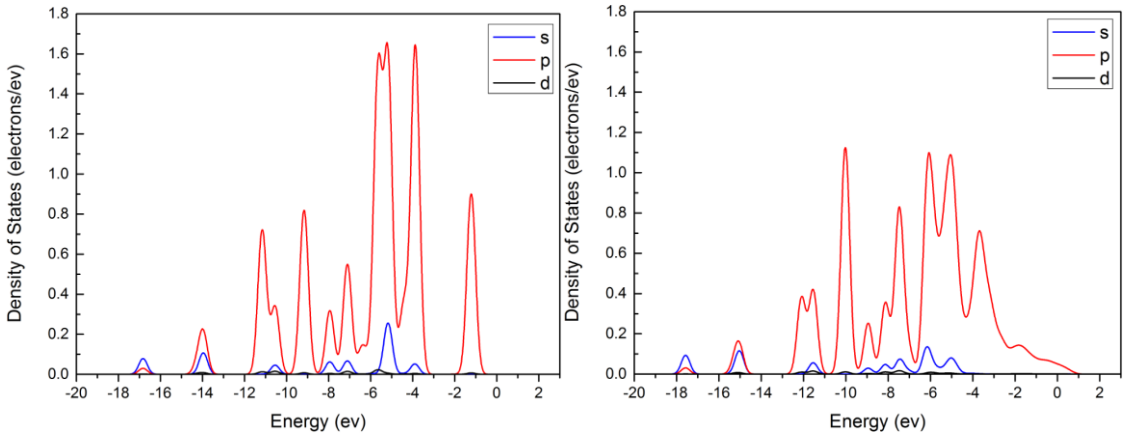

(c) (d)

Fig. 5-10 Density of States (DOS) of Phenol: (a) approaching to Mo-Fe; (b) adsorbed on Mo-Fe. Oxygen contribution to DOS, Partial DOS (PDOS): (c) approaching to Mo-Fe; (d) adsorbed on Mo-Fe.

Phenol molecule showed similar DOS profiles when approaching to all three alloys (shown in spectra (a) in **Fig. 5-8**, **Fig. 5-9** and **Fig. 5-10**), although the energy level of the electrons in phenol molecule was higher by 0.5eV when it was approaching to Mo-Fe alloy compared to Ni-Mo and Ni-Fe alloys. This result indicates that the alloys have little impact on the phenol molecule before the adsorption when the distance is larger than 5Å. Besides, it can be observed from the spectra that the electrons in s orbital of the phenol molecule were primarily located in lower energy levels (between -4 ~ -18 ev) before the adsorption, while the higher energy levels (between -12 ~ -1ev) were occupied by p electrons. Nevertheless, it is worth noting that some s orbital electrons were also present in higher energy levels (between -10 to -4 eV) before the adsorption, indicating the orbitals hybridization within phenol molecule. After phenol molecule was adsorbed onto alloys (as shown in spectra (b) in **Fig. 5-8**, **Fig. 5-9** and **Fig. 5-10**), the DOS spectra showed displacement of energy levels and changes in value of states (particularly at the high-energy levels range from -10 onwards) for both the s and p electrons, and these changes varied depending on the alloy. In the case of the phenol adsorbed on Ni-Mo alloy, the energy level of most electrons in s and p orbitals decreased about 1.5eV. This indicates the energy release in the contribution to the exothermic behavior of the whole system during the adsorption process. The change in energy also reveals a more stable structure of the

molecule compared to that prior to adsorption. Nevertheless, it should also be noticed that the value of DOS changed especially at the energy levels above -4 ev; electrons were gained at some of the energy levels during the adsorption process. This is related to the electron exchange between the phenol molecule and the adsorbent surface, and confirms the chemisorption between the phenol molecule and Ni-Mo alloy (Hensley, Wang and McEwen, 2014b). Similar change of DOS values was also observed for the adsorption of phenol onto Ni-Fe and Mo-Fe alloys, however, less displacement of the energy levels for each orbital were observed for them compared to the adsorption on Ni-Mo alloys; this is in accordance with previous prediction that Fe showed lower adsorption energy in Section 5.1. Regarding Ni-Fe, adsorbed phenol molecule showed little displacement of energy level but more gained electrons mainly in p orbital at energy levels above -2ev. This result is in line with the prediction that Ni-Fe showed the lowest adsorption energy (shown in **Table 5-2**), but also implies that Fe has more significant electron back-donation transfer to the absorbed phenol molecule, which may also give rise to strong interaction between Ni-Fe alloy surface and the adsorbate molecule (Hensley, Wang and McEwen, 2014b). In the case of Mo-Fe, larger displacement of energy level of the orbital electrons was observed compared to that of Ni-Fe, and this confirms the afore obtained result that Mo led to higher adsorption energy than Ni, simultaneously, the increased density of p orbital electrons at high energy levels also confirms that Fe is effective in interacting with the adsorbate by electron transfer. Indeed, the catalytic performance of each alloy on the deoxygenation process highly depends on their ability to disturb the oxygen in the phenol molecule. Spectra (c) and (d) in **Fig. 5-8**, **Fig. 5-9** and **Fig. 5-10** show the Partial DOS (PDOS) of the oxygen atom in a phenol molecule before and adsorbed onto each alloy.

The PDOS spectra of oxygen before the phenol adsorption were similar regardless the alloy difference, which indicates almost no effect from the alloys. In the three cases, it is found that most electrons in s orbital were located at high energy levels that ranged from -9 to -3ev, hybridizing with p electrons. After adsorption, the frontier orbitals within the oxygen atom on Ni-Mo system showed the largest decrease in the energy level (over 1ev). Simultaneously, a slight

decrease of the DOS values at most of the energy levels and an increase of the values mainly at high energy levels above -4ev were observed. The changes were more significant for Ni-Fe and Mo-Fe. The above results indicate the strong impact of the surfaces on the inner electron distribution of the oxygen atom. It is inferred that the changed p electrons may include the two non-hybridized 2p orbital electrons of oxygen atom that engage in π-p conjugation, so that making the hydroxyl group more reactive and consequently facilitating the deoxygenation reactions.

It can be also observed that the electron transition and change in energy level for the oxygen atom resemble those of phenol molecule, and analogous alloy influence can also be seen both to phenol molecule and oxygen atom; Ni and Mo would generate stronger binding with the adsorbate molecule by releasing more energy during the adsorption, while Fe gives rise to more electron exchange between the surface and the adsorbate (Hensley, Wang and McEwen, 2014b). However, which effect from the alloy could most benefit the deoxygenation reaction in the decomposition of anisole is still a question. All the bi-metal alloys mentioned in this section would be used to load on HZ catalyst and tested in the experiments in Chapter 8 to assess their contribution to the deoxygenation reaction towards desirable products.

5.4 Mechanism for deoxygenation of Phs in catalytic anisole decomposition

As described in the literature review, deoxygenation reaction is usually regarded as a second stage in the anisole decomposition process, and normally occurs at higher temperatures than the transmethylation reaction. The Phs produced from transmethylation as intermediates in the anisole catalytic decomposition are the main feedstock for the catalytic deoxygenation stage. Although large amount of the work focused on the investigation of the deoxygenation mechanism of Phs have been carried out, a unique mechanism has not been agreed yet (Hurff and Klein, 1983; Pichaikaran and Arumugam, 2016; Runnebaum et al., 2011b, 2011a, 2012; Thilakaratne, Tessonnier and Brown, 2016). However, it has been agreed that the occurrence of a straightforward hydrogenolysis reaction in the

deoxygenation of Phs is unlikely because of the π-p conjugation formed by the non-hybridized 2p orbital electrons of the oxygen atom and the benzene ring, as a consequence, the C_{sp}^2-O bond strength is reinforced and the cleavage of phenolic hydroxyl group becomes more difficult compared to aliphatic hydroxyl (Zhu et al., 2011). It has been reported when there is no acid catalyst engagement, the Phs is more likely to undergo a ring saturation and produce cyclohexanols before deoxygenation (Ohta et al., 2011; De Souza et al., 2014, 2015; Zhu et al., 2011), and the addition of acid catalyst could effectively inhibit ring saturation during the deoxygenation (Pichaikaran and Arumugam, 2016; Thilakaratne, Tessonnier and Brown, 2016; Zhu et al., 2011), but the mechanism is still not clear for the deoxygenation in the presence of both metal and acid catalysts, especially how the acid site affects mechanism.

Many studies confirmed that the Brønsted acid sites play an important role in enhancing the deoxygenation reaction (Thilakaratne, Tessonnier and Brown, 2016; Zhu et al., 2011), implying that the deoxygenation reactions of Phs are likely to commence through the electrophilic attack by protons from the Brønsted acid sites. According to the study performed in the Section 4.1 regarding the active sites in a phenol molecule (**Fig. 4-3**), the oxygen (Fukui (-) index = 0.152), para carbon (Fukui (-) index = 0.136), ortho carbon ((Fukui (-) index = 0.089)), and C1 ((Fukui (-) index = 0.089)) were identified as the most vulnerable sites to electrophilic attack on the phenol molecule. Two possible electrophilic attack (protonation) mechanisms for the deoxygenation reaction of Phs are thus proposed based on the carbon and oxygen atom respectively, as shown in **Fig. 5-11** and **Fig. 5-12**. The “carbon protonation mechanism” considers that the reaction is initiated through an electrophilic attack by proton to one of the ring carbons (**Fig. 5-11**), and the “hydroxyl protonation mechanism” is based on electrophilic attack to the hydroxyl group (**Fig. 5-12**).

Due to the fact that oxygen exhibits the highest Fukui index of 0.152, it is considered that the deoxygenation reaction is more likely to be initiated by the electrophilic attack to the oxygen by proton. To confirm the exact acting position of a proton on the Phs at the beginning of deoxygenation. The possible cations

under proton electrophilic attack based on both carbon and oxygen atoms that exhibit high Fukui index are compared in **Fig. 5-13**, and the bond orders of C_{sp}^2-O are assessed accordingly.

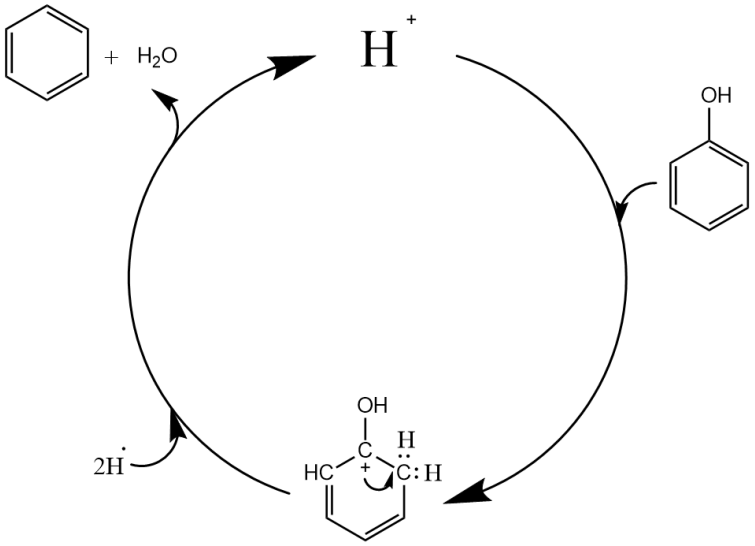

Fig. 5-11 Carbon protonation mechanism of deoxygenation of phenol

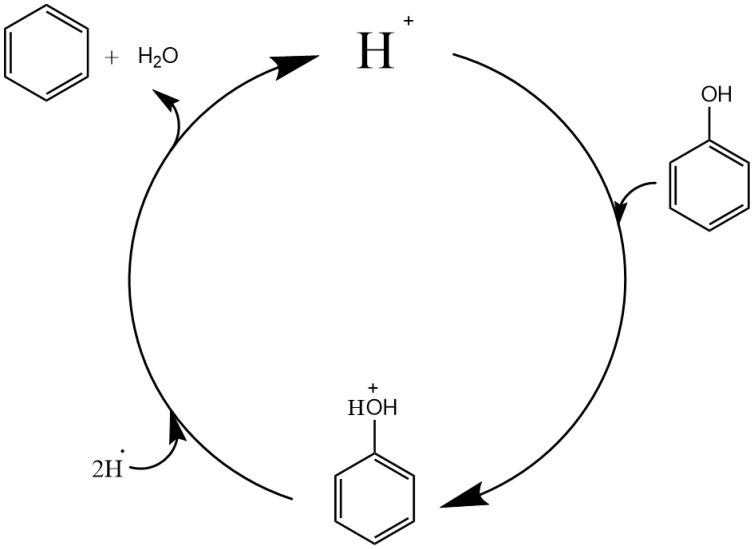

Fig. 5-12 Hydroxyl protonation mechanism of deoxygenation of phenol

Fig. 5-13 shows that the proton attack to different positions gave rise to significant change of the C_{SP}^2-O bond order. The bond orders of C_{sp}^2-O were 0.781 and 0.668 when the proton attacked C6 (**Fig. 5-13**(a)) and C1 (**Fig. 5-13**(b)), respectively. The electrophilic attack to the C4 atom resulted in the C_{sp}^2-O bond order of 0.783 (**Fig. 5-13**(d)). The lowest C_{sp}^2-O bond order (value of 0.332) was

attributed to oxygen atom under attack (**Fig. 5-13**(c)). The result reveals that the C_{sp}^2-O bond strength is significantly weakened when the proton attacks the phenol molecule at oxygen atom, confirming that the deoxygenation reaction is the most likely to commence following the oxygen atom being under electrophilic attack in the presence of the Brønsted acid catalyst.

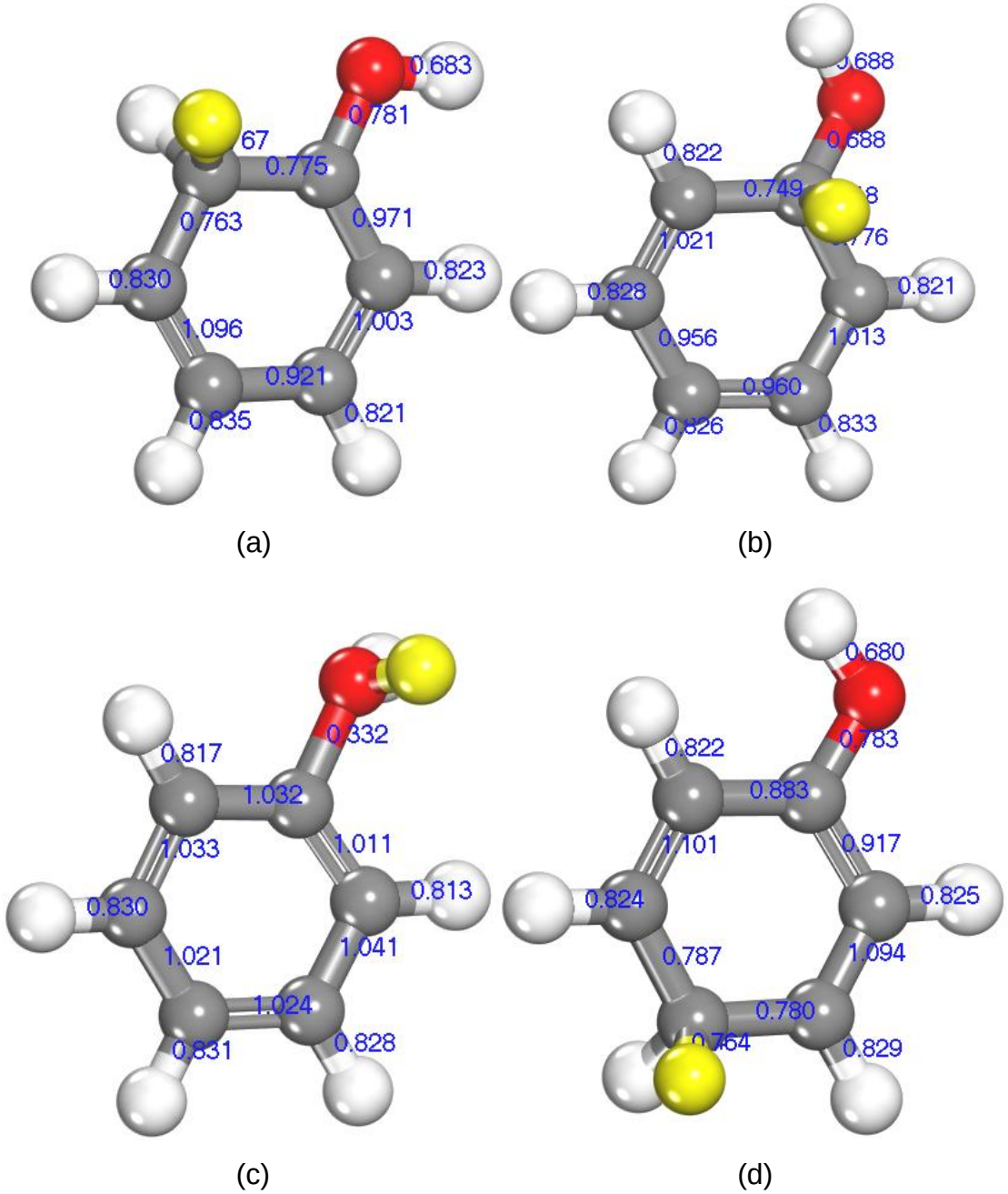

Fig. 5-13. Bond orders of possible cations under proton electrophilic attack. Atoms are coloured as follows: carbon atom (grey), hydrogen atom (light grey), oxygen atom (red), and proton (yellow).

According to above analysis, it is considered that the deoxygenation reaction of Phs in anisole catalytic decomposition is more likely to happen based on “hydroxyl protonation mechanism”, or such mechanism is predominating in the reactions. The “hydroxyl protonation mechanism” consists of an electrophilic attack reaction, a reduction reaction and a substitution reaction. The proton’s attack aims at the oxygen atom and enables the facile formation of an aromatic cation. The cation is then reduced by a hydrogen atom and then substituted by the other hydrogen atom to produce water molecule and an AH compound (a benzene molecule in **Fig. 5-12**). Meanwhile, one of the hydrogen atoms is oxidised into a proton, and the acid site is recovered. In all there are two additional hydrogen atoms engaging in the reaction, and the hydrogen source is supposed to be in-situ from other elemental reactions in the anisole decomposition. This will be further investigated and discussed in the experimental investigation in Chapter 7.

It is worth noticing that the presence of metal active sites may promote the catalysis effect of Brønsted acid sites by enhancing the reactivity of Phs for protonation (change the inner electron density by the adsorption of molecules) and by dissociating diatomic molecules, i.e. hydrogen (Cui et al., 2013; Florez et al., 2011; Klacar and Grönbeck, 2013). The integrated effect of metal/acid catalyst (bi-functional catalyst) on the deoxygenation reaction in anisole decomposition would be investigated through specific reaction modelling in Section 5.5.

5.5 Modelling of the deoxygenation reaction in the decomposition of anisole over bi-functional catalyst

The deoxygenation reactions of phenol, cresols, xylenols and trimethyl phenols over metal-supported HZ catalyst were modelled as second stage of the catalytic decomposition of anisole. Catalytic deoxygenation reactions over sole HZ (no metal loaded) were also modelled for comparison. Both HZ and metal/HZ catalytic deoxygenation models were built by locating equidistantly the reactant molecules (about 3Å) to minimize any possible position-related errors (**Fig. 5-14**). In all cases, the catalytic deoxygenation reaction was modelled based on the

proposed mechanism shown in **Fig. 5-12**. The deoxygenation reaction of phenol over HZ and over Ni/ HZ are shown in **Fig. 5-14** (a) and (b), respectively, as examples of the catalytic deoxygenation reactions of Phs. The transition state for each reaction is the state that has the highest energy throughout a reaction, and the unique imaginary frequency of the transition state structure is shown in Appendix **A6**.

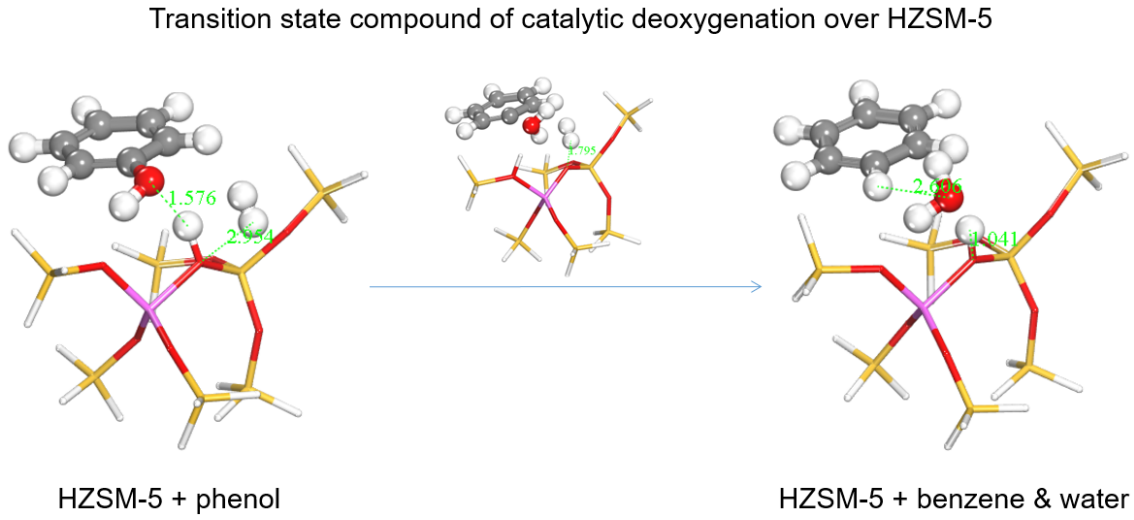

(a)

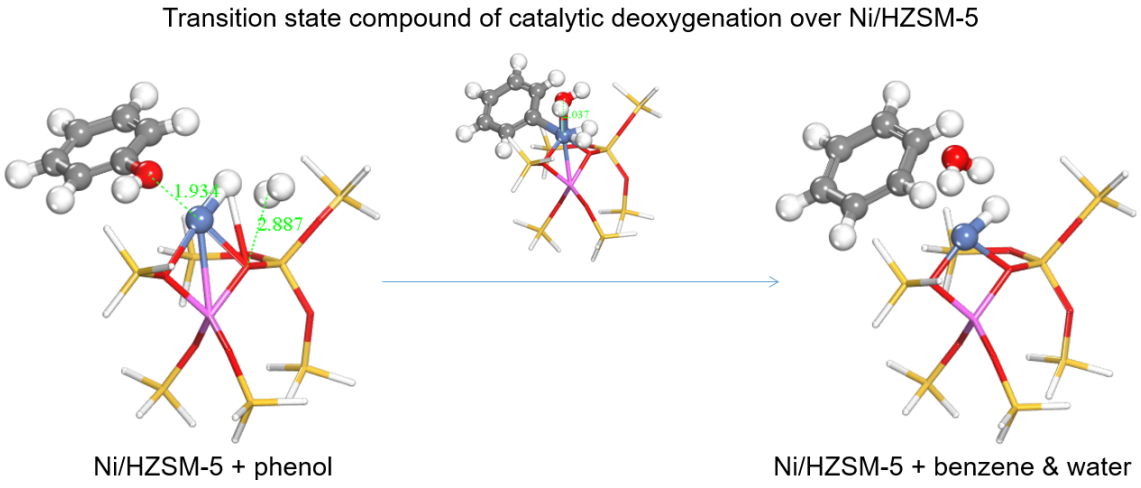

(b)

Fig. 5-14. Modelling of the deoxygenation reaction of phenol molecule over (a) HZ catalyst, and (b) Ni/HZ catalyst. Atoms are coloured as follows: carbon atom (grey), hydrogen atom (light grey), oxygen atom (red), silica atom (yellow) and aluminium atom (pink).

As shown in **Fig. 5-14**(a), the catalytic deoxygenation reaction over Ni/HZ had almost the same mechanism as non-metal catalytic reactions in the catalytic deoxygenation reaction, nevertheless, it is observed that a ligand was generated centred on the metal molecule that also connected reactant molecule and the support. The hydrogen molecule also connected to the metal atom and was dissociated into two atoms.

In addition to Ni, Co, Mo and Cu being evaluated as active site loaded on the HZ catalyst, the deoxygenation reactions of phenol, o-cresol, p-cresol, 2,4-xylenol, 2,6-xylenol, 3,5-xylenol, 2,4,6-trimethylphenol, 2,3,6- trimethylphenol and 3,4,5-trimethylphenol were modelled, and the intrinsic energy barriers at 0 K for the deoxygenation reactions of these Phs over HZ and metal/HZ catalysts were calculated (as shown in **Table 5-3**).

Table 5-3 Energy barrier for the deoxygenation of various phenolic compounds over HZ and metal/HZ catalysts as the second stage of the catalytic decomposition of anisole. Metal active sites: Ni, Co, Mo, and Cu

Phs (reactants)	Energy barrier (Kcal/mol)								
	HZ	Ni/HZ	Decline by (%)	Co/HZ	Decline by (%)	Mo/HZ	Decline by (%)	Cu/HZ	Decline by (%)
phenol	93.4	18.9	79.8	32.7	65.0	14.3	84.6	13.5	85.6
o-cresol	74.2	38.0	48.7	18.1	75.5	30.0	59.6	23.9	67.9
p-cresol	89.0	27.9	68.7	31.2	64.9	37.1	58.3	54.7	38.6
2,4-xylenol	77.1	13.3	82.8	15.7	79.6	12.5	83.8	56.0	27.4
2,6-xylenol	99.6	15.1	84.8	55.3	44.5	16.0	83.9	79.9	19.8
3,5-xylenol	81.8	58.7	28.2	26.1	68.1	14.0	82.9	26.1	68.1
2,4,6-tri-ph	95.7	43.8	54.2	39.3	59.0	26.5	72.3	30.5	68.1
2,3,6-tri-ph	97.0	13.5	86.1	34.4	64.5	33.9	65.1	63.8	34.3
3,4,5-tri-ph	86.5	20.0	76.9	10.5	87.8	26.9	68.9	70.3	18.7

In the case of non-metal HZ catalytic reactions, the energy barriers of deoxygenation changed significantly depending on the reactant molecules. This is related to the fact that the number and position of methyl groups in a molecule may affect the inner electron distribution of the aromatic rings (Lambert, 1958). Regarding the deoxygenation of phenol and cresol, the reaction of deoxygenation for phenol had the highest energy barrier for 93.4 kcal/mol, and the lower energy barriers of 74.2 kcal/mol and 89.0 kcal/mol existed for the deoxygenation reactions of o-cresol and p-cresol respectively. This result implies the positive

effect of the addition of single methyl group in the molecule on the Csp_2-O bond activation, especially when the methyl group was at 2-ortho position (o-cresol). Regarding multi-methyl Phs, reaction for 2,4-xylenol had the lowest energy of 77.1kcal/mol, confirming the positive effect of methyl group on ortho and para positions to the deoxygenation reaction, however, relative high energy barriers were found for the reactions for 2,6-xylenol, 2,4,6-trimethyl phenol and 2,3,6-trimethyl phenol. The results imply that dual methyl groups on both ortho positions of Phs decrease the molecule reactivity in the deoxygenation reactions, this might because of the steric hindrance effect caused by multi-methyl group closed to the hydroxyl (Rogers and Zheng, 2016).

Regarding metal/HZ catalytic deoxygenation reactions, the presence of metals notably decreased the energy barrier value of the deoxygenation reaction for each phenolic compound. For the case with Ni/HZ catalyst, all the energy barriers decreased to be below 60 kcal/mol, and the energy barriers for phenol, 2,4-xylenol, 2,6-xylenol, 2,3,6-trimethylphenol and 3,4,5-trimethylphenol decreased more significantly to be below 20kcal/mol. For the case with Co/HZ catalyst, the highest energy barrier was 55.3kcal/mol, and the energy barriers for o-cresol, 2,4-xylenol and 3,4,5-trimethylphenol decreased to be below 20 kcal/mol. Regarding Mo/HZ catalyst, most energy barriers are found to be no higher than 40 kcal/mol, especially those for phenol, 2,4-xylenol, 2,6-xylenol and 3,5-xylenol were less than 20 kcal/mol. Cu/HZ catalyst showed positive effect in decreasing the energy barrier for the reaction of phenol molecule to be 13.5 kcal/mol, but it is noticed that the energy barriers for the deoxygenation reactions of p-cresol and multi-methyl Phs did not significantly decrease compared to the cases for other metals, although they all decreased to be below 80 kcal/mol in the presence of Cu loading.

For each phenolic compound mentioned above, the “biggest drop” of energy barrier in the catalytic reactions based on the four metals is highlighted (in red, values are compared horizontally across four metals, difference within 1 kcal/mol are regarded to the same significance) in **Table 5-3**. It is found Mo/HZ achieved the most (five) “biggest drops” in energy barriers of the deoxygenation reaction

among the four tested metals. In the case of Ni/HZ, four “biggest drops” were observed. While the Co/HZ and Cu/HZ showed respectively two and one biggest drops.

The result predicts the most effective metal for the deoxygenation reaction of Phs should be Mo and Ni, followed by Co and Cu. This can be due to the intermediate adsorption energy shown by Ni and Mo; they adsorb the reactants strongly enough to hold and activate them compared to Cu, but moderately compared to Co, which allows the desorption of the products [48]. This result also coincides the adsorption capacity prediction in section 5.2, indicating a larger adsorption capacity with big binding energy is significant to facilitate the deoxygenation reaction. Furthermore, the big drops of the energy barrier also confirm that catalysis based on the hydroxyl protonation mechanism plays an important role in the catalytic deoxygenation of Phs over metal loaded acid sites. It has also been observed from the modelling results above that Mo/HZ catalyst has better effect on lowering the energy barrier for the most abundant compounds intermediate Phs in the reactions, like phenol and xylenols, and Ni/HZ exhibits excellent effect on the deoxygenation reactions for phenol, xylenols and trimethylphenols. Besides, Mo and Ni both are found could compensate the steric hindrance effectively in the reactant molecules, and facilitate deoxygenation reactions for the Phs that have dual ortho methyl groups.

5.6 Summary

Multi-scale modelling has been implemented in this chapter, for predicting appropriate designs of metal-supported HZSM-5 catalysts to be used for deoxygenation of Phs experiments. The modelling of anisole adsorption on common transition metal clusters revealed that Ni, Co, Mo and Cu exhibited relatively high adsorption energy values, while adsorption of anisole on Fe, Zn and other transition metals showed low adsorption energy values. Monte Carlo modelling was firstly implemented to assess the anisole adsorption capacity of the zeolite, which would be used as the support of bi-functional metal catalyst for the experiments of deoxygenation in anisole decomposition. The adsorption isotherms based on HZ with different Si/Al ratios pointed out that adsorption

capacity of zeolite increased with rising pressure and decreasing temperature. The results implied that the zeolites had good adsorption capability at low temperature range, but no significant difference was observed when Si/Al ratio changed. Further adsorption modelling based on Ni, Co, Mo, and Cu loaded HZ(23) confirmed that metals had significant effect in promoting adsorption capability compared to non-metal HZ especially at high temperatures. Ni/HZ(23) and Mo/HZ(23) were found to have relatively high adsorption capacities, for 3.28/cell and 3.45/cell at 600°C and 101kPa, respectively. DFT modelling of the adsorption of anisole and phenol onto bi-metal crystals was carried out; alloys of Ni-Mo, Ni-Fe, and Mo-Fe catalyst were considered. The comparison of adsorption energy for both anisole and phenol molecule revealed that Ni-Mo alloy exhibited the highest adsorption energy compared to Ni-Fe and Mo-Fe. Further analyses regarding the orbital electrons in phenol molecule during the adsorption process showed that the alloys all had significant impact on the electrons distribution of the oxygen atom. Ni and Mo promoted the decline in electrons energy levels consequently releasing more energy during the adsorption, while Fe was more effective in back-donating electrons between the surface and the frontier orbitals in the adsorbate. Mechanism investigation confirmed that the deoxygenation of Phs was initiated from hydroxyl protonation, and metals may facilitate this reaction, as well as dissociate hydrogen molecules. Reaction modelling revealed that a single methyl group on ortho or para position promoted the reactivity of deoxygenation over non-metal HZ catalyst, but dual ortho- methyl groups may inhibit the reaction due to steric hindrance effect. Active metals had significant effects in lowering energy barriers of the reactions for various Phs, and the most effective single metals are Mo and Ni, followed by Co and Cu.

6 Experimental study of transmethylation in the decomposition of anisole over zeolite catalyst

The aim of this chapter is to investigate experimentally the primary steps of the reaction mechanism of non-catalytic and catalytic decomposition of anisole, and to address the differences between both processes. The decomposition of anisole was carried out in a fluidised bed reactor, and HZSM-5 zeolite was used as catalyst. To address the effect of the acid sites on the catalytic decomposition, the performance of a series of HZSM-5 (HZ) zeolite catalysts with different Si/Al atomic ratio was studied. The distribution of products in the liquid fraction, with focus on the phenolic compounds (Phs), was evaluated to explain the catalytic activity of the HZSM-5 zeolite on the transmethylation process compared to the non-catalytic reaction. In addition, changes in carbonaceous deposition were investigated.

The results discussed in this Chapter have been published in the Journal of Analytical and Applied Pyrolysis (Zhang et al., 2016), and complement the DFT modelling results presented in Chapter 4.

6.1 Characterization of zeolite catalysts

The catalytic activity of zeolites on the conversion of lignin-related compounds from biomass to aromatic hydrocarbons (AHs) and Phs during pyrolysis has been reported (Blatnik, 2013; Foster et al., 2012; Guisnet and Gilson, 2002; Huber et al., 2012; Ivanova et al., 2007; Wang, Johnston and Brown, 2014; Wang, Kim and Brown, 2014; Zhang et al., 2011), and the combined function of Brønsted and Lewis acid sites is usually considered to promote the transmethylation process (Meng et al., 2015; Sad, Padró and Apesteguía, 2008, 2010). In particular, HZSM-5 has been described as one of the best zeolite catalysts in order to achieve high conversion and selectivity to AHs, due to its structure and content of acid sites (Guisnet and Gilson, 2002; Ivanova et al., 2007; Thilakaratne, Tessonnier and Brown, 2016). To properly address the effect of the surface acidity of the zeolite on its catalytic performance, pyridine-FTIR analysis was carried to HZSM-5 with different Si/Al ratios: 25 (denoted as HZ(25)), 50

(denoted as HZ(50)), 80 (denoted as HZ(80)), and 200 (denoted as HZ(200)). The acid density distribution of Brønsted and Lewis sites was identified, as shown in **Table 6-1**.

Table 6-1: Surface acidity of HZSM-5 zeolites with different Si/Al ratio as determined by Pyridine-FTIR analysis

	Acid density (mmol of pyridine/g of zeolite)					
	Brønsted			Lewis		
Si/Al ratio	total	weak	strong	total	weak	strong
25	0.280	0.181	0.099	0.139	0.099	0.040
50	0.237	0.148	0.089	0.076	0.056	0.020
80	0.038	0.029	0.009	0.081	0.053	0.028
200	0.041	0.033	0.008	0.051	0.037	0.014

As can be seen, the acid density of the zeolite decreased when the Si/Al ratio increased, which corresponds to the decline of acid sites due to the aluminium dispersion in the silica framework. It is also observed that the amount of Brønsted acid sites was higher than the Lewis acid sites for HZ(25) and HZ(50). However, the density of the Brønsted acid sites decreased faster with the Si/Al ratio than that of Lewis acid sites, and consequently Lewis acid sites predominated at high Si/Al ratio (HZ(80) and HZ(200)).

6.2 Effect of temperature on non-catalytic and catalytic decomposition of anisole

The conversion in non-catalytic and catalytic decomposition of anisole at different temperatures is shown in **Fig. 6-1**, and HZ(25) was used in the catalytic experiment because it has the largest amount of Brønsted and Lewis acid sites. In both sets of experiments, the anisole conversion values increased with temperature. In the case of non-catalytic experiments, the conversion increased from approximately 30.54% at 200°C up to 99.8% at 650°C, and remained constant for higher temperatures. It is noticed that relatively low anisole conversion was observed at temperatures lower than 400°C when no catalysts

was used. In the case of catalytic experiments with catalyst HZ(25), conversion increased from 73.6% at 200°C to around 99.4% at 400°C, which was maintained at higher temperatures. In the presence of the HZ(25) catalyst, the complete conversion of anisole was achieved at lower temperature than in the case of non-catalytic decomposition. This reflects the catalyst effect in lowering activation energy of reactions, and it agrees with the results obtained from DFT modelling shown in Chapter 4.

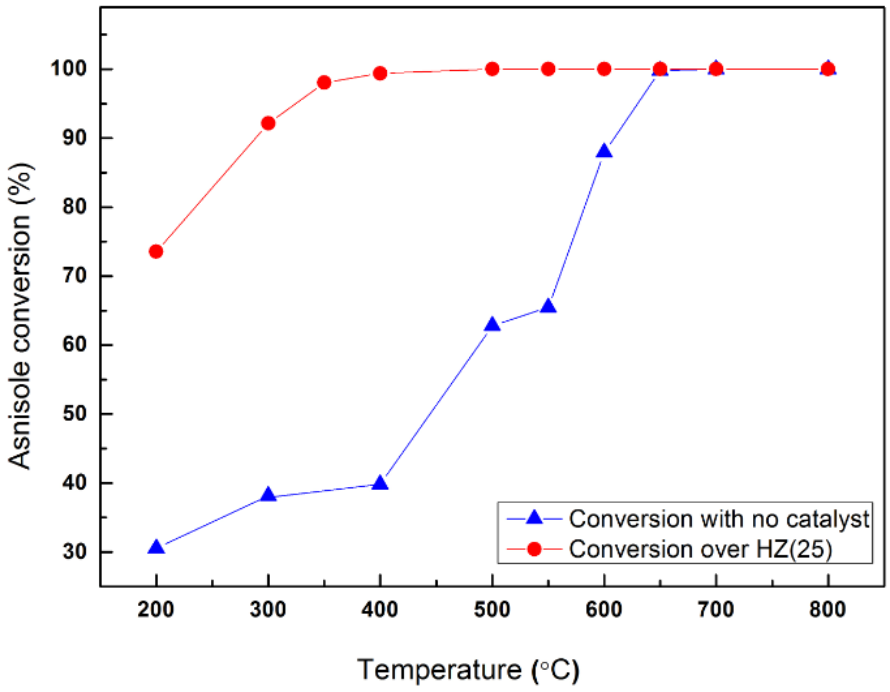

Fig. 6-1 Influence of zeolite catalyst on the conversion of anisole at different reaction temperatures

Fig. 6-2 and **Fig. 6-3** presents the yields of products in the liquid fraction at different temperatures in non-catalytic and catalytic decomposition of anisole. Details regarding xylenol and trimethyl-phenols are specified in **Fig. 6-4** and **Fig. 6-5** respectively. **Table 6-2** shows the grouped yields of the AHs and Phs for each experiment. Yields of specific Phs, i.e. phenol and methyl phenols (mono-, di- and trimethyl-phenols) are also summarized.

Both for non-catalytic and catalytic reactions, maximum yield of liquid products was observed at the minimum temperature required for achieving the complete conversion; i.e. 650°C for non-catalytic decomposition and 400°C for catalytic

decomposition. These temperature values are referred as “key temperatures” in this thesis.

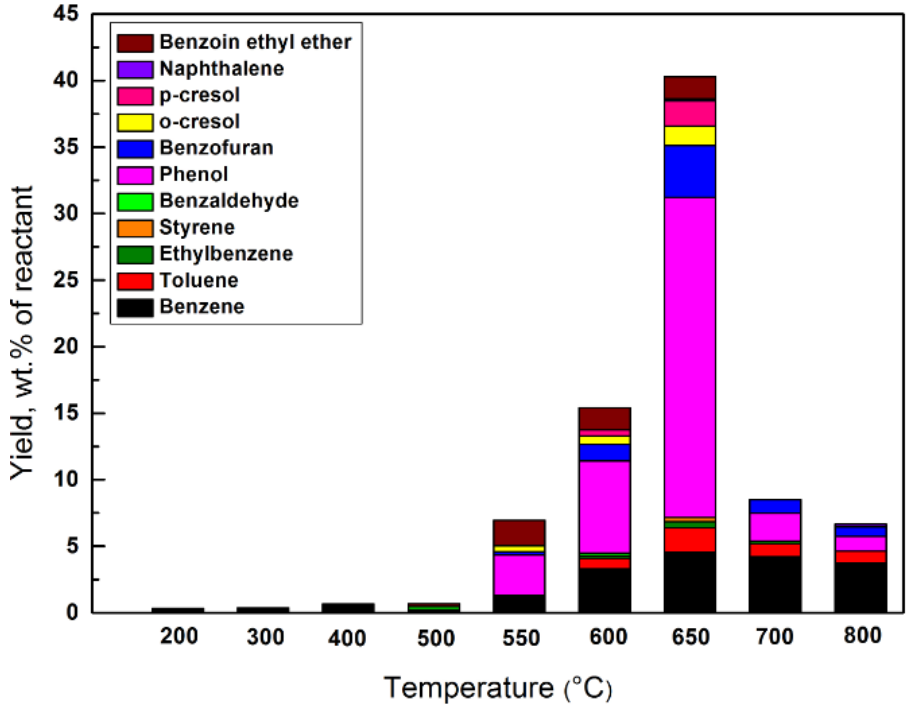

Fig. 6-2: Products distribution in the liquid fraction at different temperatures in non-catalytic decomposition

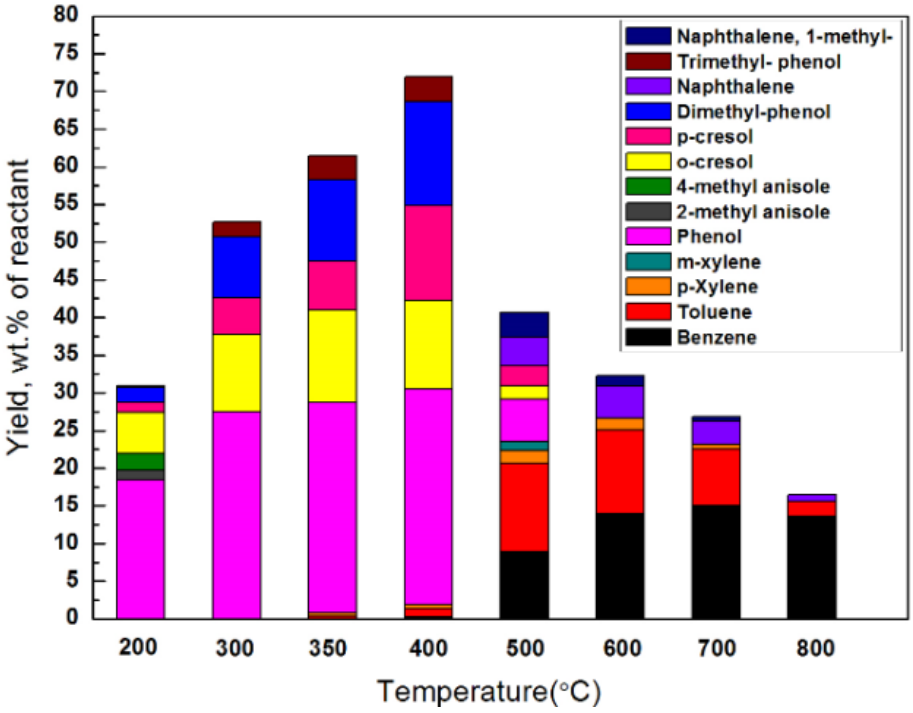

Fig. 6-3 Products distribution in the liquid fraction at different temperatures in catalytic decomposition over HZ(25) of anisole

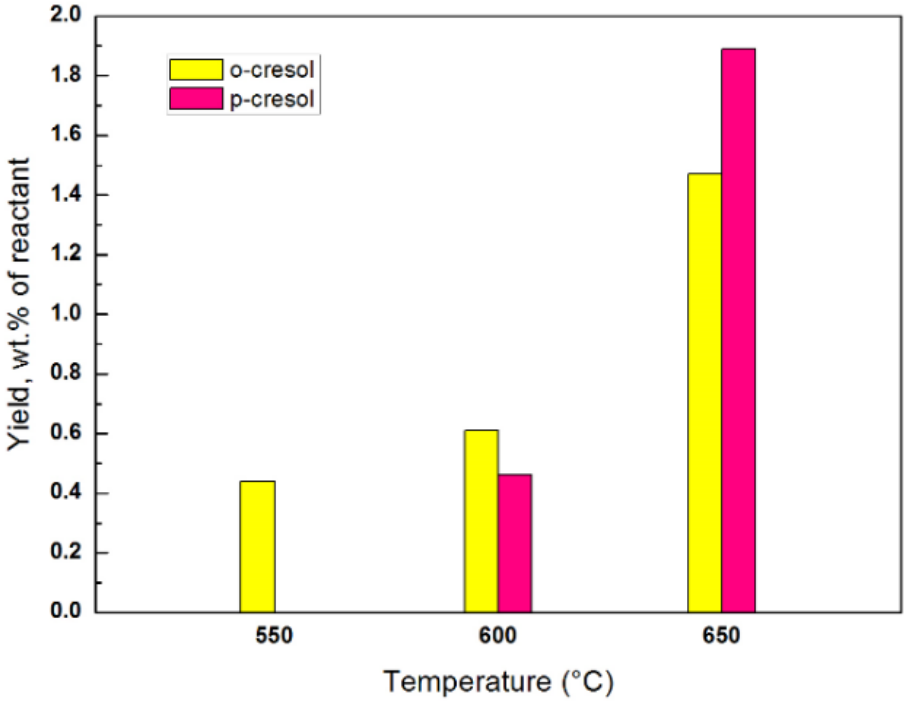

Fig. 6-4 Yield of methyl-phenols at different temperatures in non-catalytic decomposition

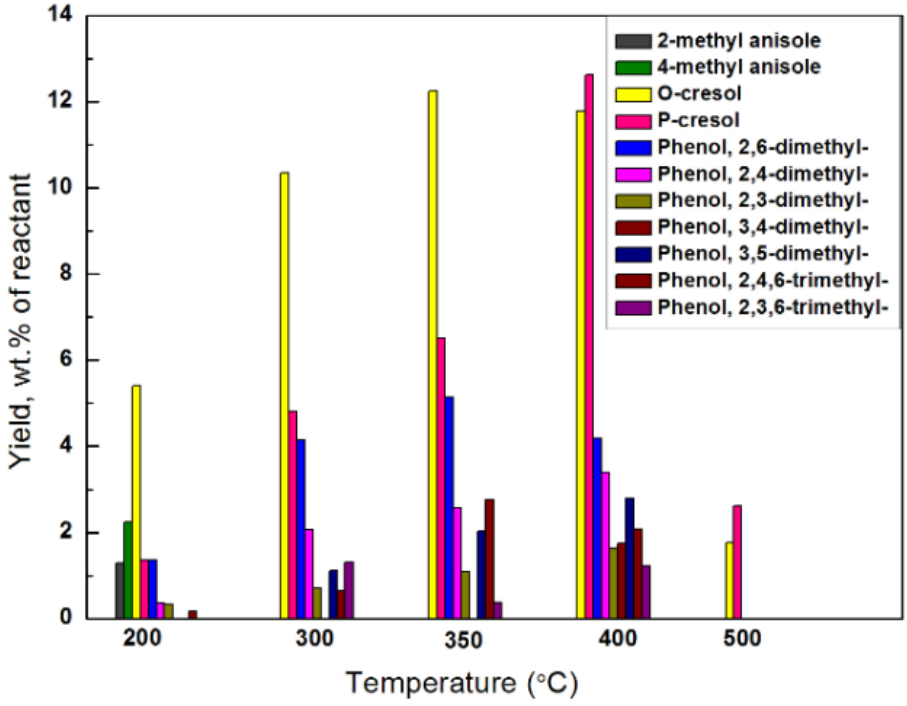

Fig. 6-5 Yield of methyl-phenols at different temperatures in catalytic decomposition over HZ(25)

Table 6-2: Grouped yields of AHs and Phs in the decomposition of anisole (wt. % of reactant)

Set	T (°C)	Catalyst	Anisole Conversion (%)	AHs	Phs				
					Total	Phenol	o- & p-cresol	Xylenols	Trimethyl phenols
T1	200	No catalyst	30.5	0.3	0.0	0.0	0.0	0.0	0.0
T2		HZ(25)	73.6	0.0	27.4	18.3	6.8	2.1	0.2
T3	300	No catalyst	38.2	0.4	0.0	0.0	0.0	0.0	0.0
T4		HZ(25)	92.2	0.0	52.6	27.5	15.1	8.0	2.0
T5	350	HZ(25)	98.0	0.8	60.6	27.9	18.7	10.8	3.2
T6	400	No catalyst	39.8	0.7	0.0	0.0	0.0	0.0	0.0
T7		HZ(25)	99.4	1.9	70.0	28.6	24.3	13.8	3.3
T8		HZ(50)	99.7	2.4	73.4	29.1	25.7	14.5	4.1
T9		HZ(80)	99.5	0.3	78.9	30.1	27.2	17.1	4.5
T10		HZ(200)	99.5	0.0	67.8	26.7	22.2	14.6	4.3
T11	500	No catalyst	62.8	0.3	0.0	0.0	0.0	0.0	0.0
T12		HZ(25)	100.0	31.2	10.0	5.7	4.3	0.0	0.0
T13	550	No catalysts	65.5	1.2	3.5	3.1	0.4	0.0	0.0
T14	600	No catalyst	77.0	4.3	8.0	6.9	1.1	0.0	0.0
T15		HZ(25)	100.0	33.5	0.0	0.0	0.0	0.0	0.0
T16	650	No catalyst	99.8	7.3	27.4	24.0	3.4	0.0	0.0
T17	700	No catalyst	100.0	5.2	2.1	2.1	0.0	0.0	0.0
T18		HZ(25)	100.0	27.6	0.0	0.0	0.0	0.0	0.0
T19	800	No catalyst	100.0	4.9	1.1	1.1	0.0	0.0	0.0
T20		HZ(25)	100.0	16.5	0.0	0.0	0.0	0.0	0.0

Phs were the primary products at the key temperature and below. The maximum yield of Phs was 27.4 wt. % at 650°C in non-catalytic decomposition process (shown in **Table 6-2**). The yield increased up to 70.0 wt.% when the HZ(25) was used while the temperature at which this maximum value was obtained decreased in 150°C (maximum at 400°C). This reflects the decreased activation energy of the reactions producing Phs when adding the catalyst, in line with the prediction in Chapter 4. Regarding Phs, only phenol and n-methyl phenols (ortho-

cresol and para-cresol) were produced during the non-catalytic decomposition of anisole. O-cresol was first formed at 550°C, while p-cresol appeared at 600°C. Yields of both compounds increased with temperature and peaked at 650°C. Moreover, o-cresol yield was higher than p-cresol yield at 600°C, while the opposite was observed at 650°C. In the case of anisole catalytic decomposition, o- and p-cresols were also the main compounds in the methyl phenolic fraction. The yield of o-cresol and p-cresol was promoted by approximately 8 and 7 times respectively when HZ(25) was used as catalyst. Like non-catalytic decomposition, o-cresol yield was higher than that of p-cresol at low temperatures (between 200 and 350°C), while p-cresol yield was larger at 400°C and 500°C. In addition, multi-methyl phenols, such as 2,6-dimethylphenol, 3,4-dimethylphenol and 2,4,6-trimethylphenol, were abundantly produced over HZ(25) at temperatures below the key temperature.

Aromatic hydrocarbons dominated over phenolics at temperatures higher than the key temperature. In non-catalytic decomposition process, AHs were present in the whole range of tested temperatures, but the maximum yield of 7.3 wt. % was observed at the key temperature of 650°C. The yield then decreased to 4.9 wt.% at 800°C, following the decrease in the liquid product fraction, as high temperatures usually result in increasing gaseous products yield (Shen et al., 2010). A significant increment of AHs yields was observed at temperatures higher than the key temperature when catalytic decomposition over HZ(25) was performed (1.9 wt.% at 400°C and 33.5 wt.% at 600°C). In this case, the maximum AHs yield was not observed at the key temperature but at a higher temperature of 600°C. Moreover, maximum AHs yield improved by almost 5 times compared to that obtained from non-catalytic experiments. The temperature at which the maximum AHs yield was obtained decreased 50°C when using a catalyst.

Fig. 6-6 shows the influence of temperature on the deposition of carbonaceous species in both non-catalytic decomposition and catalytic decomposition of anisole. Carbonaceous deposits yields were higher when catalytic decomposition was conducted because the acid sites on HZSM-5 promote the absorption of

anisole and accelerate the reaction rates which in turn results in more carbon deposition (Zhou et al., 2016). For non-catalytic decomposition, the yield of carbonaceous deposits was found to increase fast with temperature. Interestingly, in the case of catalytic decomposition, the carbon deposits increased up to a maximum at 600°C, and then decreased at higher temperature. This trend is similar to that of the AHs, and has been previously reported (Wang, Johnston and Brown, 2014; Wang, Kim and Brown, 2014; Zhou et al., 2016; Zhu, Mallinson and Resasco, 2010).

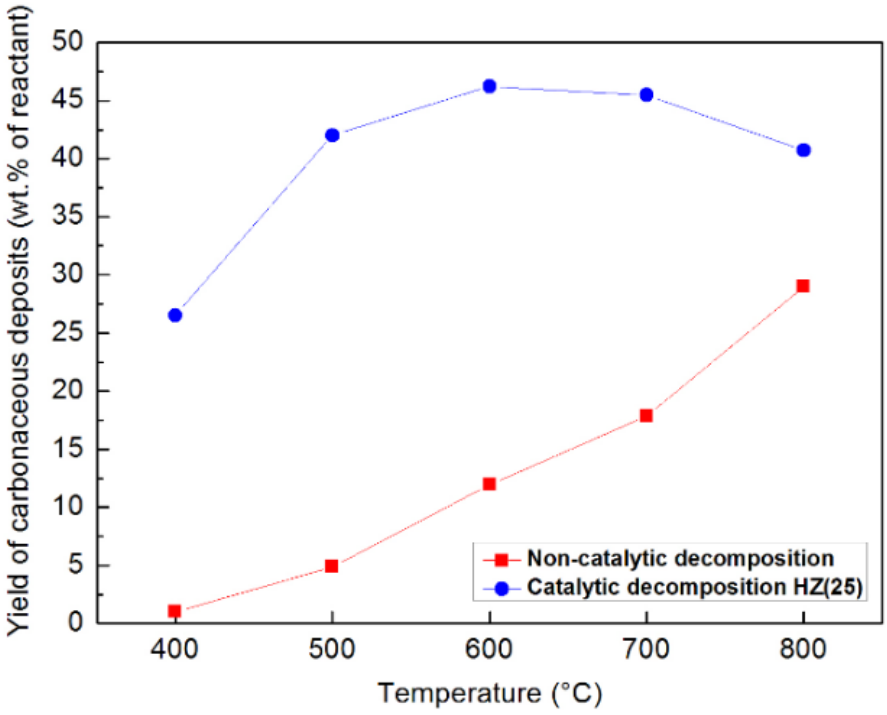

Fig. 6-6 Change of yields of carbonaceous deposit with temperature in non-catalytic decomposition and catalytic decomposition over HZ (25)

The above results on liquid and solid yields and liquid product distribution suggest that transmethylation occurs as the main reaction at the range of low temperatures when anisole conversion is not complete either with or without catalyst. Moreover, the formation of AHs as non-primary products depends both on temperature and acid catalytic effect, and deoxygenation as secondary step during anisole decomposition requires higher energy to take place, this would be further discussed in both Chapter 7 and 8. As explained above, complete anisole conversion and maximum yield of Phs were simultaneously reached at 400°C

over zeolite HZ(25). Maximum yield of AHs compounds was observed at 600°C. In the case of non-catalytic decomposition, the complete conversion of anisole and maximum yields of both Phs and AHs compounds were obtained at 650°C. In other words, the presence of the catalyst lowered the temperature at which Phs yield peaked by approximately 150°C, while in the case of maximum yield of AHs compounds the temperature decreased by only approximately 50°C. This result indicates that HZSM-5 is better at promoting the transmethylation reaction than the deoxygenation process, implying that acid catalyst has effect primarily in isomerization. Notably, in the catalytic decomposition process, the steep decrease of Phs yields coincided with the sharp increase of AHs yields, which implies that phenolics are precursor compounds for the formation of AHs. At high temperatures (around 600°C and higher), the yield of carbonaceous deposit is favoured at the expense of AHs. Simultaneously, further cracking of molecules over the zeolite is enhanced, increasing gas yields and decreasing solid and liquid yield (Shen et al., 2010).

6.3 Effect of the catalyst Si/Al ratio on the catalytic decomposition of anisole

HZSM-5 catalysts with four different Si/Al ratio were tested in order to evaluate the effect of catalyst properties on transmethylation in terms of its acidic properties, i.e. the density, strength, and type of acid sites (Wu Jianbing, 2015). Decomposition of anisole over HZSM-5 with Si/Al ratios of 25, 50, 80 and 200 was studied at the key temperature of 400°C, based on the results obtained over HZ(25) related to the transmethylation reaction. The anisole conversion was approximately 99.5% in all cases, which exhibits the limited effect of the change in Si/Al ratio on the total conversion. However, slight changes on liquid product yield and distribution are observed at different Si/Al ratios (see **Table 6-2**, **Fig.6-7** and **Fig. 6-8**). As observed, in the case of HZ(25), phenol and n-cresol were major products in the Phs fraction for all the tested Si/Al ratios. Formation of xylenols (or dimethyl phenols) was also significant. Increasing of Si/Al ratio to 80 promoted Phs products yield from 70 wt.% to about 79 wt.%. Nevertheless, further increment of Si/Al ratio to 200 resulted in a decrease of the Phs compound yields

to approximately 68 wt.%, with the main decrease for phenol and n-cresol. In the case of n-cresol, p-cresol yield was slightly higher than that of o-cresol over HZ(25). However, the opposite was observed when Si/Al ratio increased. This result points that a decrease in the acid density of the zeolite favoured the preferential attack of ortho-positions because of the lower energy requirement. At 400°C, AHs were not major products from anisole catalytic decomposition for any of the tested zeolites. In fact, in the case of HZ(80) and HZ(200), AHs yields were negligible.

Fig. 6-9 shows the yield of carbonaceous deposits at different Si/Al ratios. As can be seen, carbon deposition was also influenced by the acidity of the surface catalyst with a minimum value reached over HZ(80). The trend observed for the yield of carbon deposits was opposite to that observed for the yield of Phs. Thus, the lowest and highest yield of carbonaceous deposits and Phs respectively were obtained over the zeolite with Si/Al ratio of 80. Similar result was observed by Du et al. when producing AHs by catalytic pyrolysis of microalgae with zeolites (Du et al., 2013).

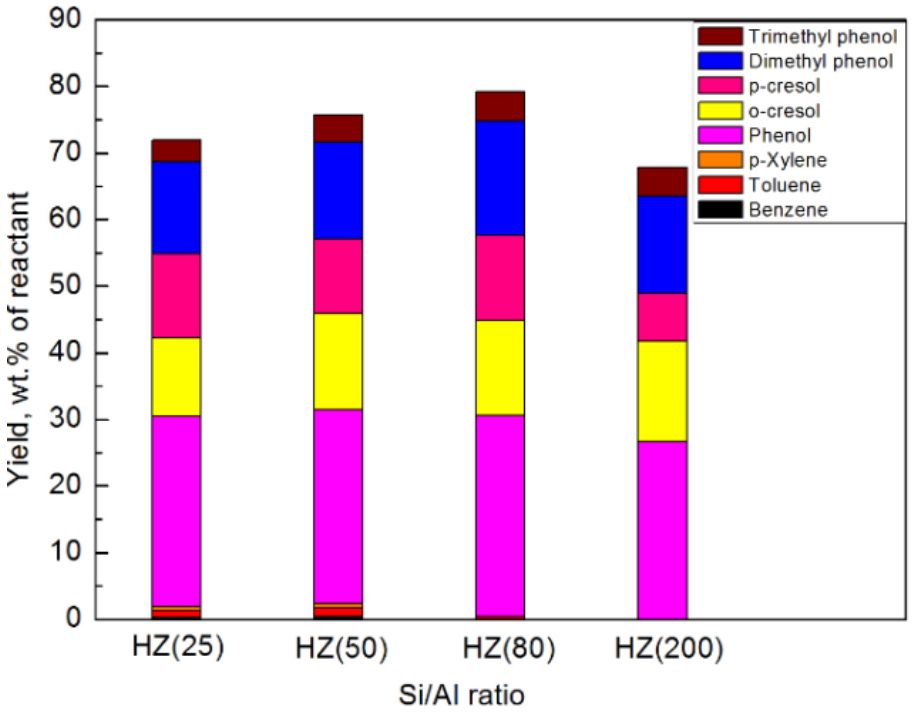

Fig.6-7: Yield of main products in the liquid fraction

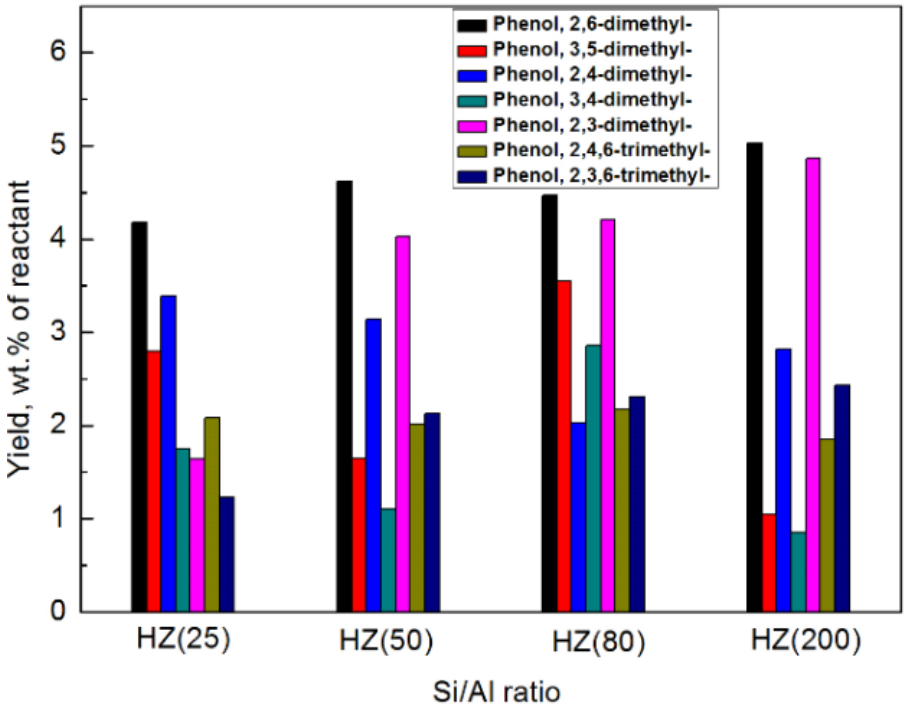

Fig. 6-8 Yield of main products of multi-methyl phenols obtained over HZSM-5 with Si/Al ratios of 25, 50, 80 and 200

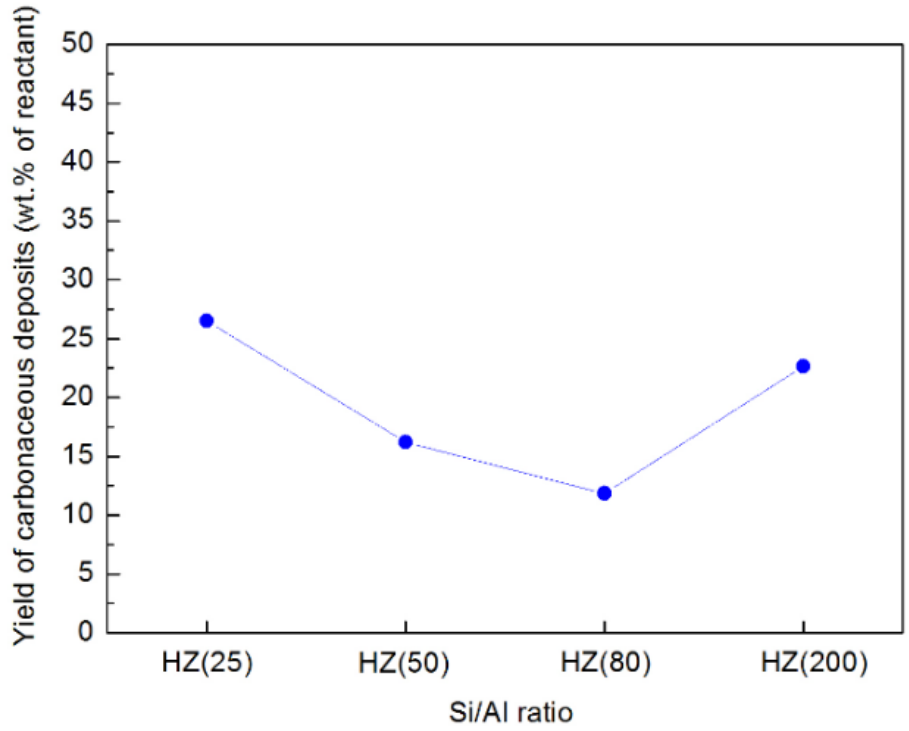

Fig. 6-9: Change of yields of carbonaceous deposit with the Si/Al ratio in the zeolite for catalytic decomposition at 400°C

It has been reported that the activity and stability of zeolites as catalysts depend on the amount and proportion between Brønsted and Lewis acid sites (Qu et al., 2011). As observed in Chapter 4, Brønsted acids are known to play a vital role in the catalytic transmethylation because of easier group exchange compared to Lewis acid (Meng et al., 2015). At the same time, Lewis acid sites have been found to aid catalytic stability due to lower coking rates (Qu et al., 2011).

Similar to results previously obtained for the catalytic pyrolysis of microalgae and glucose (Du et al., 2013; Foster et al., 2012), the experiments in this chapter showed higher Phs yields over HZ(80) than those over HZ(25) and HZ(50). Zeolites with low Si/Al ratios present enhanced initial catalytic performance because of the high surface acid density (Wu Jianbing, 2015). However, the presence of large amount of acid sites, particularly strong acid sites as in the case of HZ(25), also favours the rapid deposition of carbon and subsequent catalyst deactivation due to the blockage of the pore mouth and limited access of reactant and intermediate molecules to the active sites (Foster et al., 2012; Qu et al., 2011). The high Phs yield obtained over HZ(80) can be related to its improved catalytic stability. Coking rate for HZ(80) dropped compared to that of HZ(25) and HZ(50) because of the reduced amount of Brønsted acid sites (Qu et al., 2011). Moreover, S. Qu et al (Qu et al., 2011) reported that when Si/Al increased, carbon deposits were more likely to build uniformly in the pore walls instead of plugging the pore-mouth, the rapid deactivation of the catalyst being prevented. On the other hand, the higher Phs yield obtained over HZ(80) compared to HZ(200) may be related to the Lewis to Brønsted acid sites ratio. Although both HZ(80) and HZ(200) present low amount of Brønsted acid sites, the former exhibits significantly higher Lewis to Brønsted acid sites ratio. The relatively larger amount of Lewis acid sites in HZ(80) compared to that in HZ(200) seems to better promote the formation of the Phs (Qu et al., 2011). Therefore it can be concluded that acid sites with relatively low density and medium strength are preferred for enhancing liquid production and reducing carbon deposition (Qu et al., 2011; Wang et al., 2014; Wu Jianbing, 2015). Analogous conclusions from investigations of the catalytic activity of zeolites with different Si/Al ratios have been previously reported (Chang, 1984; Gayubo et al., 1996; Luk'yanov, 1992).

6.4 Reaction pathways of anisole decomposition at “key temperature”

Fig. 6-10 and **Fig. 6-11** show the proposed plausible reaction pathways for the catalytic decomposition and non-catalytic decomposition of anisole at the key temperatures, which are based both on the experimental results shown in this chapter and the modelling results discussed in Chapter 4. Transmethylation is the main reaction occurring during the process of anisole decomposition at this range of temperatures, as observed from the experimental results on the liquid fraction compositions. Just as it was predicted in Chapter4, anisole decomposition is initiated via the transmethylation reaction.

In the case of catalytic decomposition (**Fig. 6-10**), anisole is first converted into phenol (reaction 1) followed by the relocation of the methyl radical to form o-cresol (reaction 2) and p-cresol (reaction 3). At temperatures between 200°C and 350°C, the ortho-position transfer is predominant. However, at 400°C, both ortho- and para-position transfers are promoted. O-cresol is formed at lower temperatures, because the transfer of methyl groups to ortho-position has lower energy costs than that to para-positions based on the prediction in Chapter 4. Moreover, the slight decrease of relative yield of o-cresol to p-cresol at the key temperature may be attributed to the formation of o-toluene via deoxygenation of o-cresol. Interestingly, formation of methyl anisole is observed at the lowest tested temperature, i.e. 200°C, which indicates that transfer of methyl groups to the anisole molecule is possible before it is largely converted. The addition of another methyl radical to the n-cresol molecule gives rise to the formation of xylenols (Reaction 4). This reaction occurs at temperatures of 300°C or higher. Ortho-position transfer (positions 2 and 6 of the aromatic ring) is favoured over para-position (position 4 of the aromatic ring). Meta-position transfer also occurs although to a small extent. In addition, the rearrangement to trimethyl phenols (Reaction 5) is observed to a lesser extent. The larger yields of xylenols indicate that these compounds act as the precursors of the transmethylation transfers for trimethyl-phenol formation. As to cresols and xylenols, the major orientations for transmethylation are the ortho- and para-positions, and are favoured by the increase in temperature.

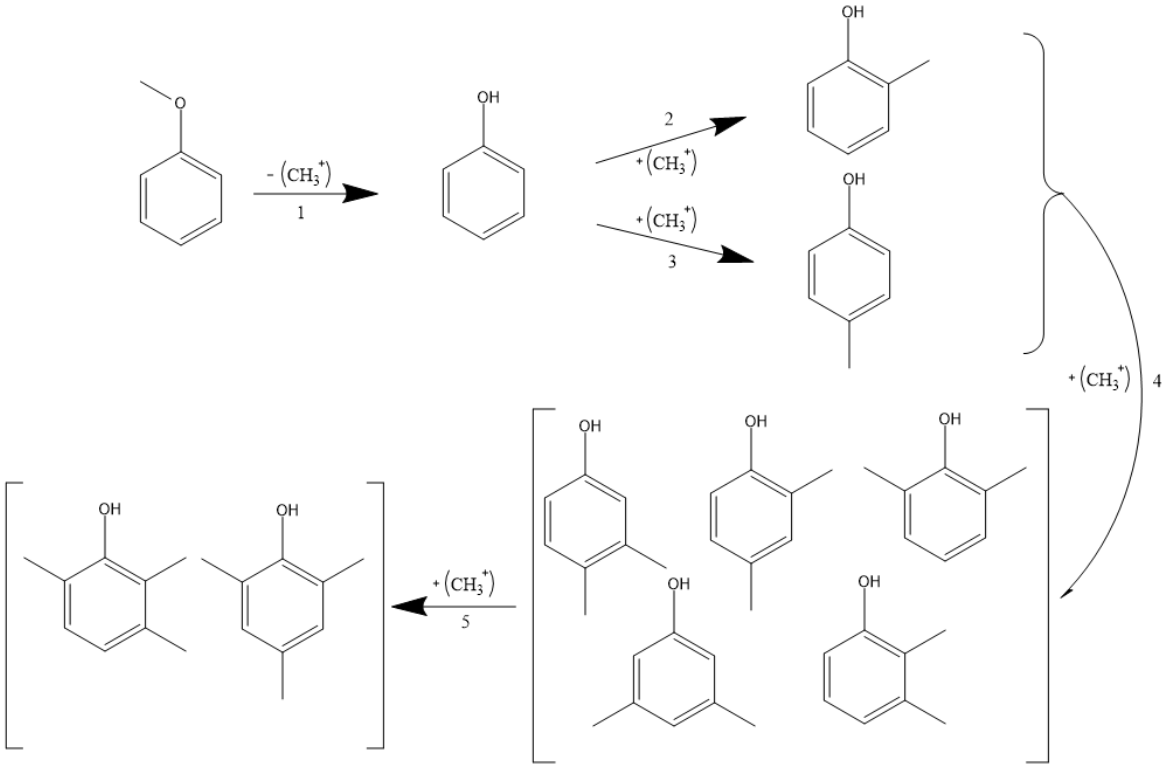

Fig. 6-10 Reaction pathways for catalytic transmethylation in anisole decomposition over HZSM-5

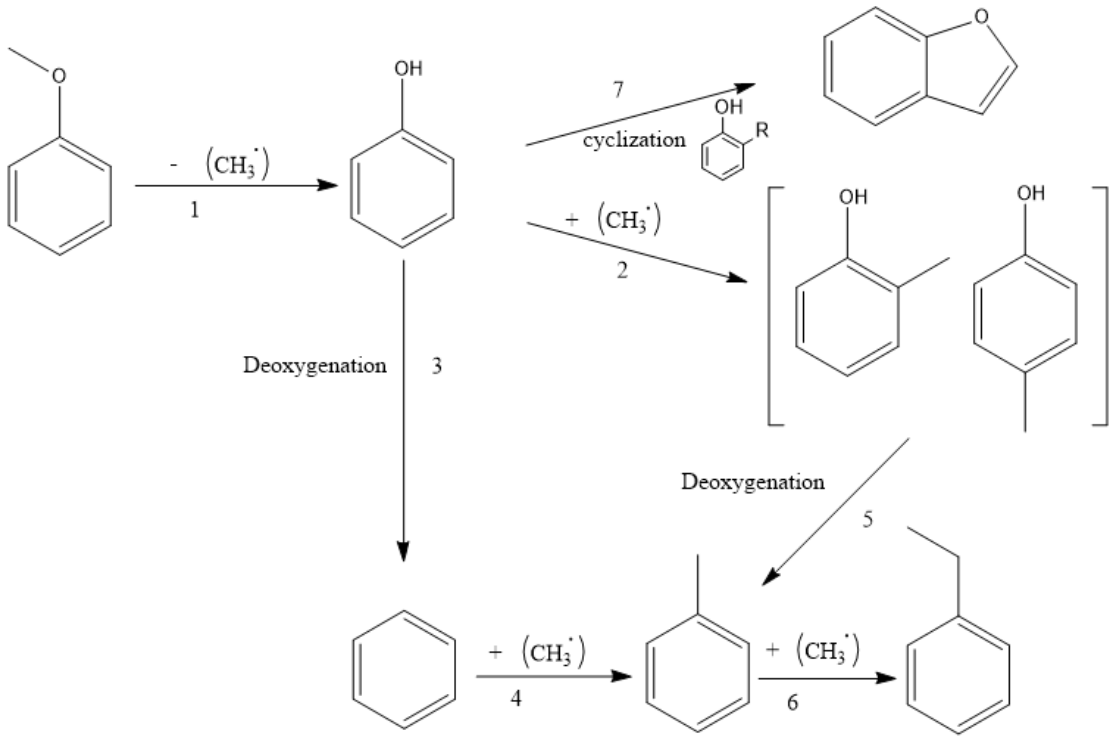

Fig. 6-11: Reaction pathways for non-catalytic transmethylation in anisole decomposition

In the case of the non-catalytic decomposition of anisole (**Fig. 6-11**), the most probable conversion route also involves the formation of phenol (reaction 1). Contrary to the catalytic decomposition, the transfer of the methyl radical to form n-cresols (reaction 2) is not a significant conversion route. Moreover, the relocation of other methyl radicals to form xylenol and trimethyl phenols does not occur under the non-catalytic thermal decomposition conditions. This implies that methyl groups are preserved and transmethylation is favoured in the case of catalytic decomposition due to the acid environment provided by the presence of the catalyst. At temperatures below the key temperature, when thermal decomposition of anisole is not complete, the yield of AHs is in the same order as that for Phs compounds. This points to the conversion of phenol into benzene (Reaction 3), followed by the formation of toluene (Reaction 4) and ethylbenzene (Reaction 6), which increase with temperature. It is also possible that toluene is produced by cresols through deoxygenation (Reaction5). In addition, as temperature increases, formation of benzofuran may occur through cyclization with the junction of C-O bond (reaction 7) (Pan et al., 2006).

6.5 Summary

In this chapter, the non-catalytic and catalytic decomposition of anisole in a fluidized bed was investigated. A series of zeolite HZSM-5 with different Si/Al atomic ratios was tested as catalyst. Transmethylation was found to be primary reaction in the decomposition of anisole at low-to-moderate temperatures, leading to the formation of Phs. Ortho-cresol and para-cresol were the most abundant substances containing a methyl group in the products. Experimental results indicated that complete conversion of anisole is achieved at 650°C in the absence of a catalyst and at 400°C in the presence of HZSM-5. The presence of the catalysts reduced the energy cost by aiding a decrease in the temperature for transmethylation of 150°C, promoting the transmethylation process, and increasing the most yield of Phs by 2.5 times. Reaction pathways for non-catalytic and catalytic decomposition at key temperatures were proposed to explain the main conversion pathways of anisole and other intermediate products. In the case of the catalytic decomposition of anisole, acidity of the catalyst contributed to

preserve methyl groups and resulted in larger selectivity towards compounds containing methyl functionality. This was particularly remarkable in the case of multi-methyl phenolic products whose formation was only observed in the presence the zeolite catalyst. In the case of catalytic decomposition of anisole, the highest yield of Phs was observed over HZSM-5 with a Si/Al ratio of 80. The enhanced anisole conversion and reduced coking rate exhibited by HZ(80) was related to the balanced proportion between Brønsted and Lewis acid sites, which resulted in improved catalytic stability.

7 Experimental study of deoxygenation in the decomposition of anisole over single metal-based zeolite catalyst

In this chapter, the conversion of anisole over single metal-based zeolite catalysts without external hydrogen supply was studied to assess the deoxygenation stage as second stage of the anisole decomposition process. Following the modelling results discussed in Chapter 5, Ni, Co, Mo and Cu loaded on HZSM-5 (Si/Al=25, metal/HZ(25)) were selected as catalysts for the deoxygenation experiments. Fresh and spent catalysts were characterized by H_2-TPR, TEM, EDS, XPS and TGA to assess their catalytic activity and figure out reaction mechanism.

7.1 Characterization of fresh single-metal/HZ(25) catalyst

To gain insights in the morphology, state and amounts of active metals, a few measurements (TEM, EDS, XPS) were performed on fresh catalysts after reduction by hydrogen.

7.1.1 H_2-TPR analyses

H_2-TPR analyses were performed to determine the reduction temperature for each metal oxide loaded on HZSM-5. **Fig. 7-1** shows the H_2-TPR profiles of Ni/HZ(25), Co/HZ(25), Mo/HZ(25) and Cu/HZ(25) catalyst samples, which were reduced in hydrogen atmosphere at a constant increasing temperature from room temperature up to 800°C.

In the case of Ni based catalyst, two distinct peaks at around 423°C and 535°C were observed. The larger peak at 423°C indicates a higher consumption of hydrogen, which usually points to the principal reduction of NiO to Ni at this temperature. The second peak at 535°C relates to the metal oxides in the channels of zeolite that are difficult to be reduced and the stronger interaction between metal sites and the support, which is probably attributed to the presence of acidic sites in the zeolite support (Jin et al., 2014; Pichaikaran and Arumugam, 2016; Sankaranarayanan et al., 2015; Zakaria, Linnekoski and Amin, 2012). The reduction profile of Co/HZ(25) also showed two peaks at around 516°C and

672°C respectively. The major peak is assigned to the transition of Co oxide to Co, and the small peak seen at high temperature suggests the existence of nanosize Co oxide species in the zeolite channels and the stronger metal-support interaction (Ochoa-Hernández et al., 2013; Sankaranarayanan et al., 2015). In the case of Mo/HZ(25) catalyst, a main H_2 consumption that peaked at around 424°C with a shoulder at 453°C was observed, indicating the reduction of MoO_3 to MoO_2. Besides, another peak at 710°C is attributed to further reduction of MoO_2 to metal Mo^0 (Liu and Xu, 2006; Martínez and Peris, 2016). Two clearly distinctive reduction peaks were observed in the case of Cu/HZ(25) at 201°C and 425°C respectively. The first peak is assigned to the reduction of introzeolite Cu^{2+} to Cu^{1+}, while the peak at higher temperature corresponds to the further reduction to Cu^0 (Li et al., 2004; Torreabreu et al., 1997; Zakaria, Linnekoski and Amin, 2012). Besides, additional H_2 consumption was also observed at 600°C, which is ascribed to the Cu oxide particles in zeolite channels that are difficult to be reduced.

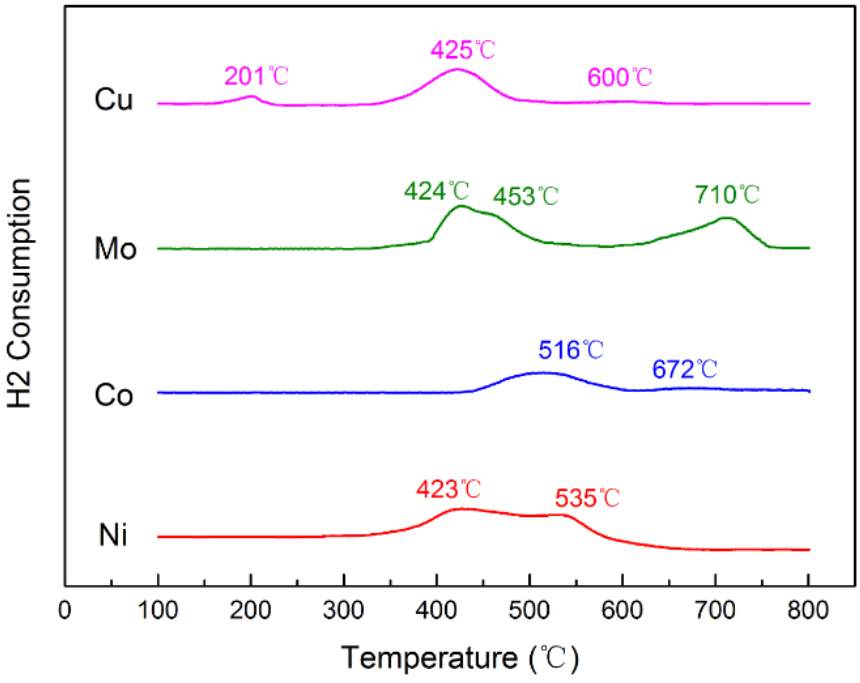

Fig. 7-1 H_2-TPR profiles of single Ni, Co, Mo, Cu supported HZSM-5 catalysts. 10vol.%H_2/Ar flow rate = 20mL/min; Heating rate = 10°C/min

Based on above results, Ni/HZ(25), and Cu/HZ(25) were in-situ reduced at 600°C, Co/HZ(25) was reduced at 700°C, and Mo/HZ(25) was reduced at 800°C

respectively in a mixed hydrogen stream as mentioned in Section 3.3.5 prior to each characterization and experiment.

7.1.2 TEM and EDS analyses

TEM analyses with various magnifications (200nm, 100nm, 50nm, and 20nm) were performed on sample of the fresh 1 wt.% single metal based catalyst: 1%Ni/HZ(25), 1%Co/HZ(25), 1%Mo/HZ(25), 1%Cu/HZ(25). Representative TEM micrographs are shown in **Fig. 7-2** to **Fig. 7-5**. For all the catalysts, the metal particles were observed to be highly dispersed on the zeolite surface in the form of primarily micro polycrystal structure (González et al., 2009; Martínez et al., 2003), and the crystal nature could be confirmed by the diffraction rings observed in the selected area electron diffraction (SAED) patterns as shown in **Fig. 7-2** to **Fig. 7-5**. In section c of each figure, average sizes of the crystals are highlighted, which were found range between 4 and 10 nm for all metals. As it shown in **Fig. 7-2**(c), the microcrystal particles of Ni exhibited irregular shape, and were difficult to be distinguished (Sankaranarayanan et al., 2015). The particles of Mo and Cu also consisted of microcrystals with blurry boundaries, as shown in **Fig. 7-4**(c) and **Fig. 7-5**(c). But the microcrystals of Co showed polygon shapes with clear boundaries, as shown in **Fig. 7-3**(c).

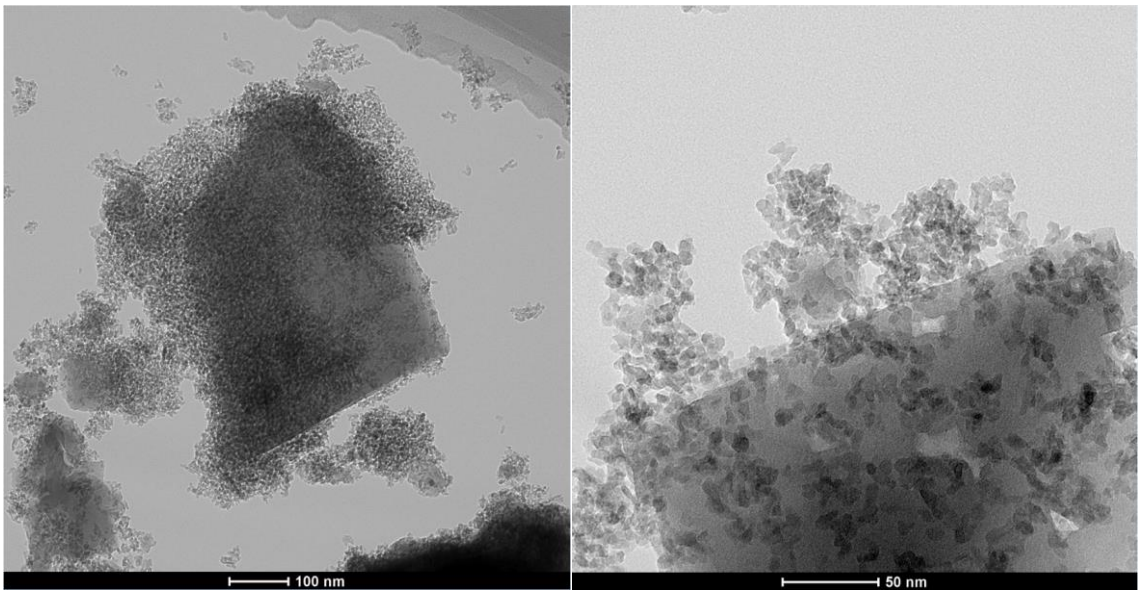

(a) (b)

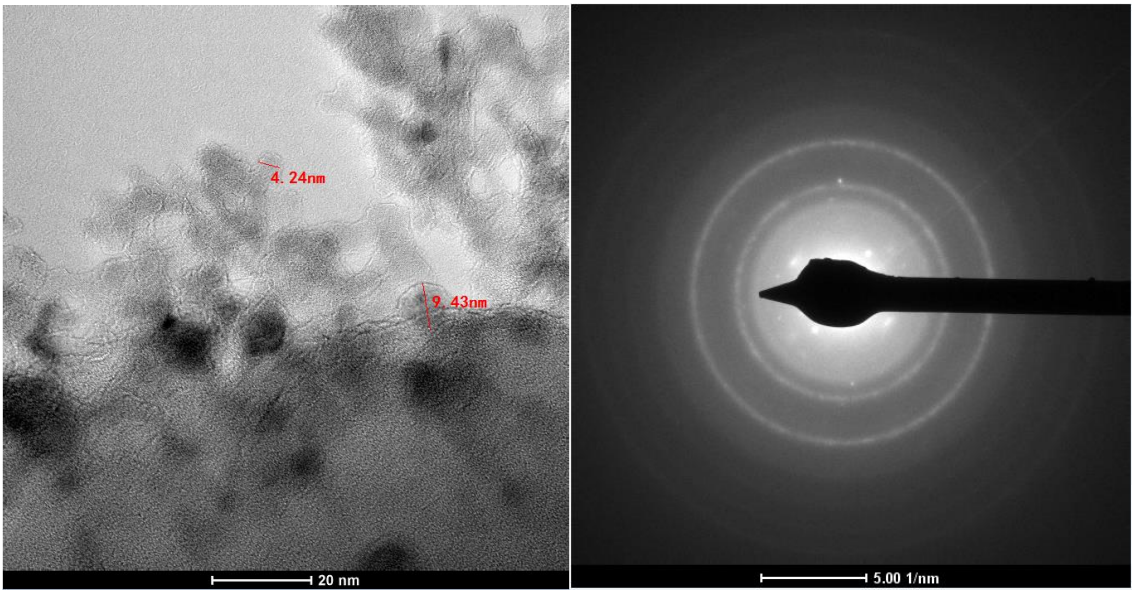

(c) (d)

Fig. 7-2 TEM micrographs of the fresh 1%Ni/HZ(25) catalyst at different resolutions: (a) 100 nm; (b) 50 nm; (c) 20 nm and (d) SAED pattern

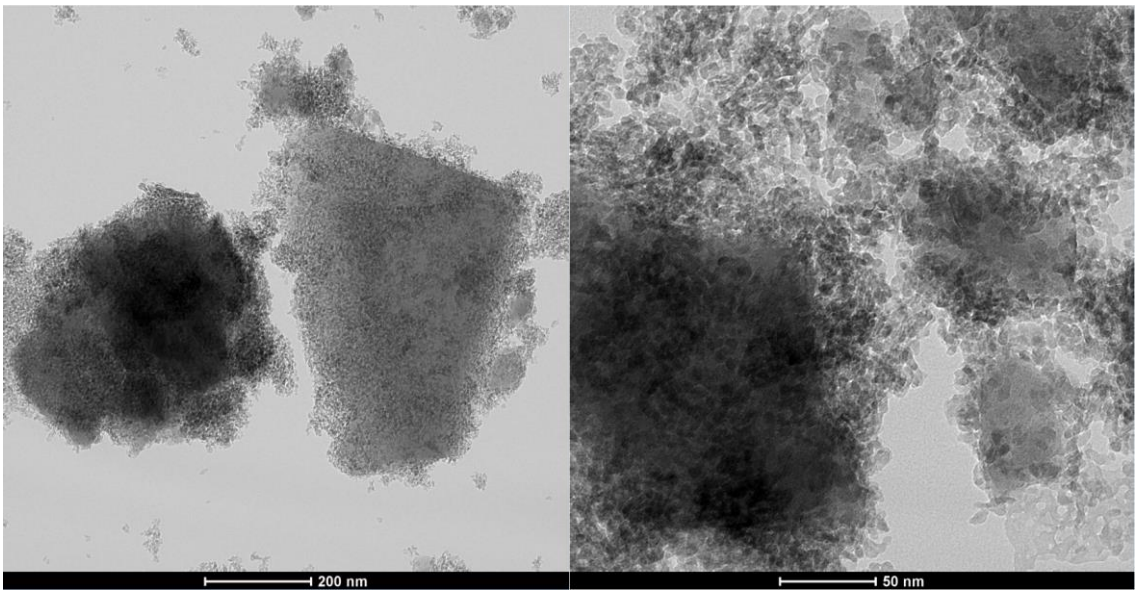

(a) (b)

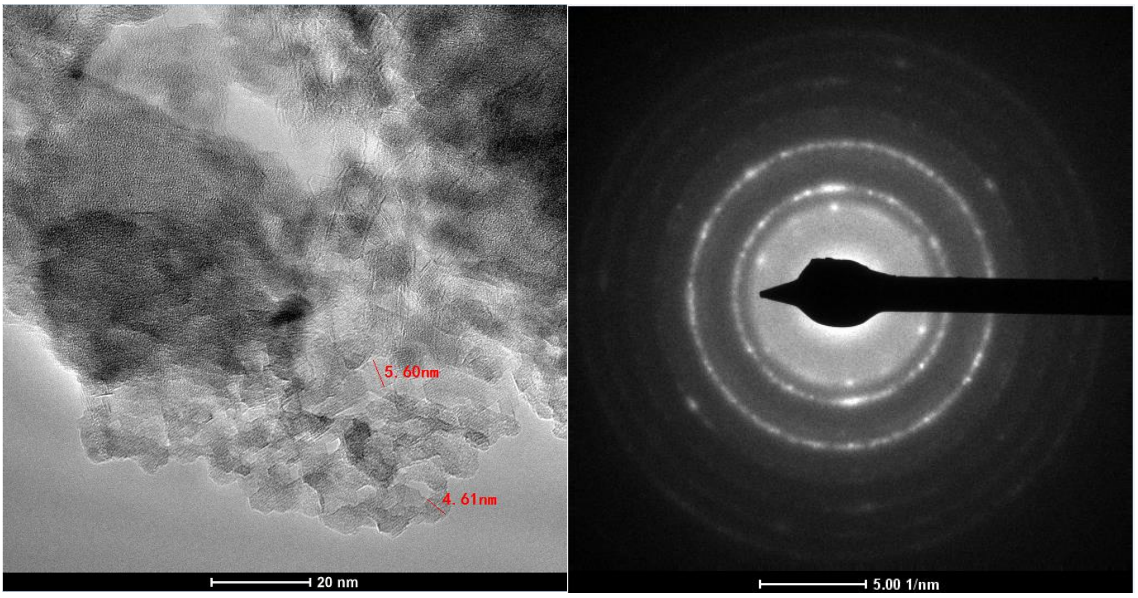

(c) (d)

Fig. 7-3 TEM micrographs of the fresh 1%Co/HZ(25) catalyst at different magnifications: (a) 200 nm; (b) 50 nm; (c) 20 nm and (d) SAED pattern

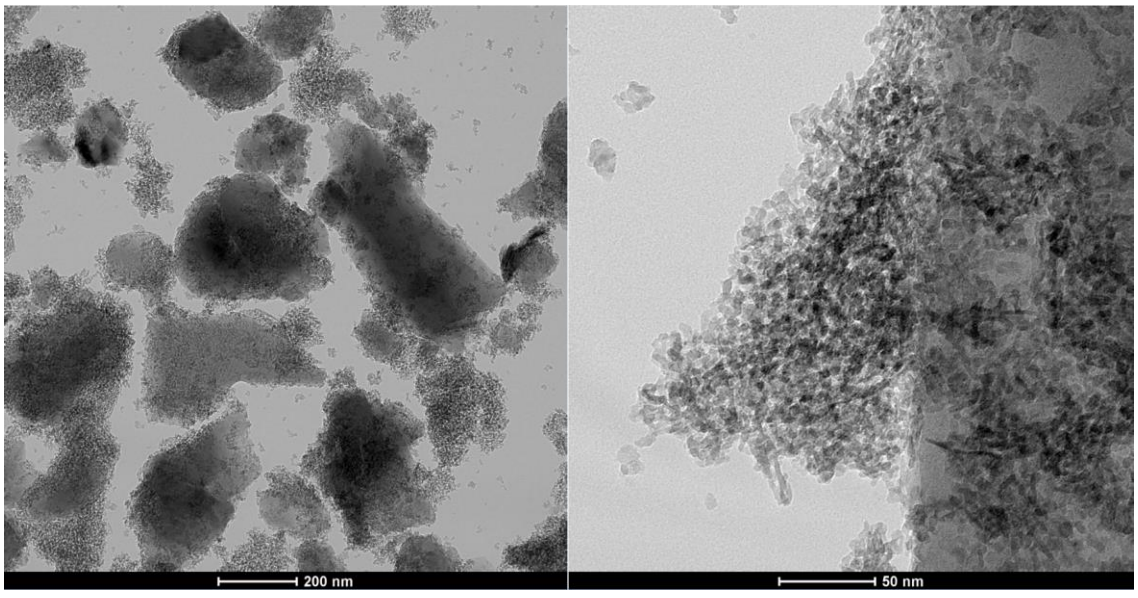

(a) (b)

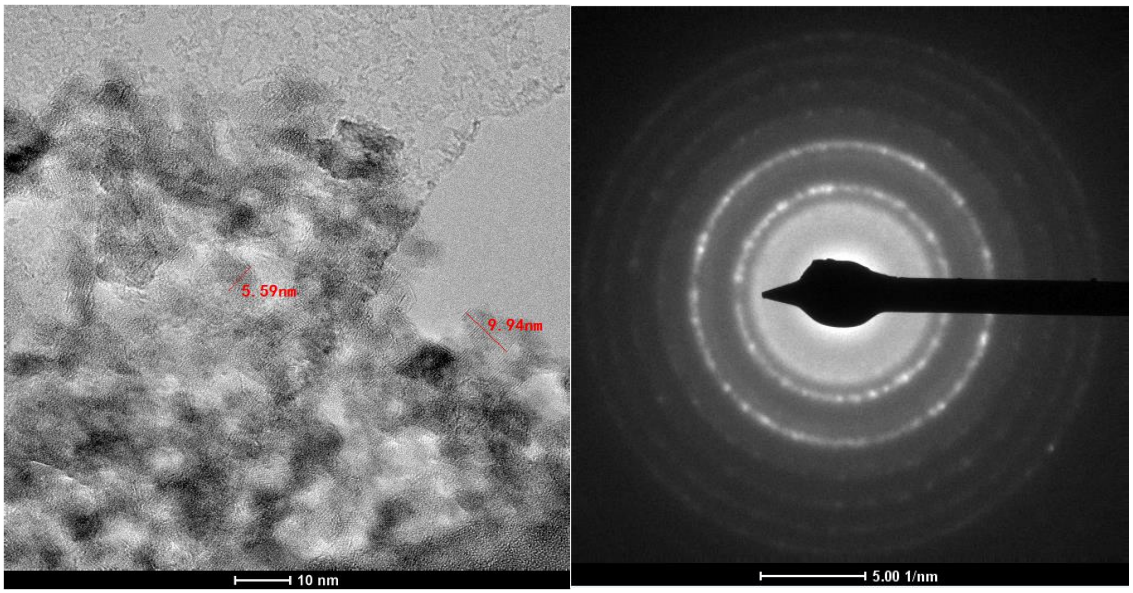

(c) (d)

Fig. 7-4 TEM micrographs of the fresh 1%Mo/HZ(25) catalyst at different magnifications: (a) 200 nm; (b) 50 nm; (c) 20 nm and (d) SAED pattern

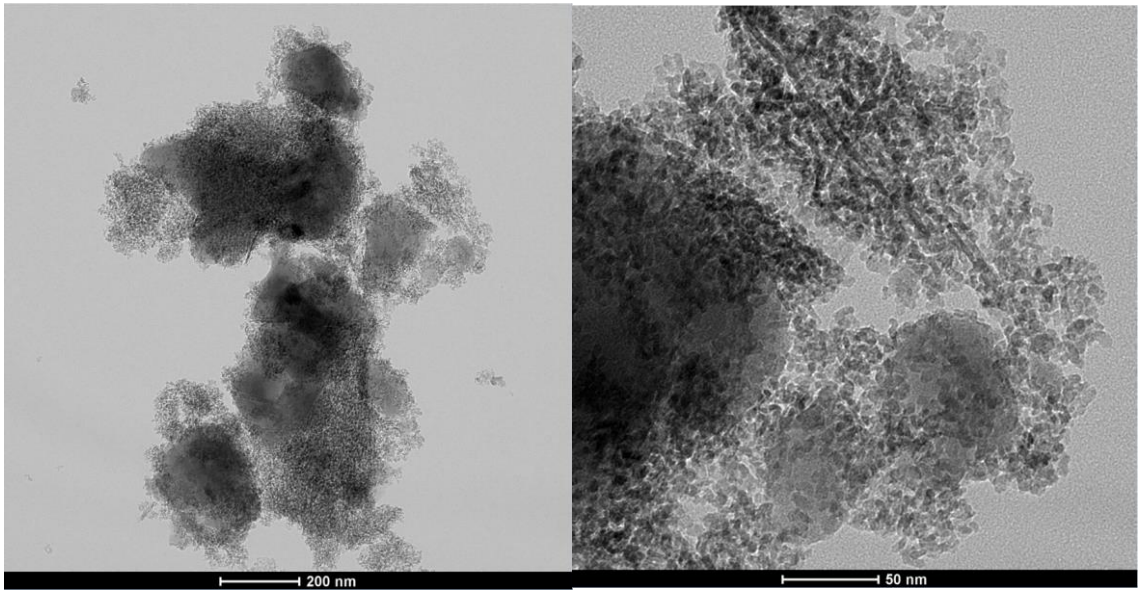

(a) (b)

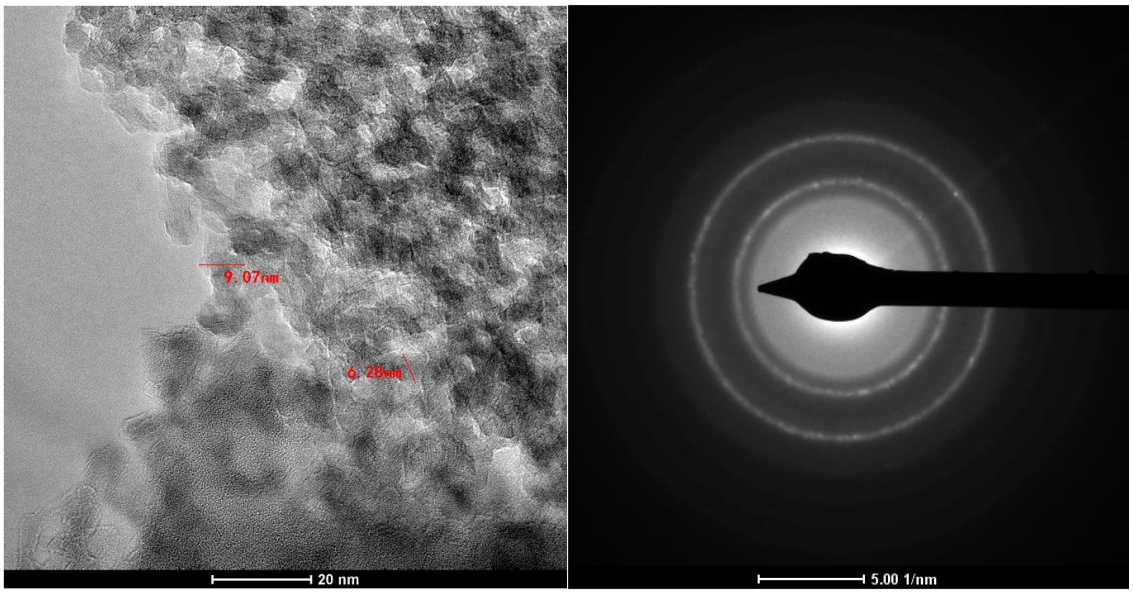

(c) (d)

Fig. 7-5 TEM micrographs of the fresh 1%Cu/HZ(25) catalyst at different magnifications: (a) 200 nm; (b) 50 nm; (c) 20 nm and (d) SAED pattern

EDS tests were implemented to confirm the main elements present in the surface of the four fresh catalysts and estimate their quantities, as shown in **Table 7-1** and Appendix **A7**[2].

Table 7-1 Metals loading on single metal loaded catalysts detected by EDS

Catalyst	Elem	Weight%	Atomic%
1%Ni/HZ(25)	Ni	1.0	0.3
1%Co/HZ(25)	Co	1.3	0.4
1%Mo/HZ(25)	Mo	1.1	0.2
1%Cu/HZ(25)	Cu	1.4	0.4

The signals of O (45.6 – 59.7 wt.%), Al (12.5 – 20.5 wt.%) and Si (22.3 – 40.9 wt.%) are assigned to the support HZSM-5 zeolite. For each of the catalysts, the

[2] Copper support grid was used for testing the Ni, Co, and Mo catalysts in the tests of TEM-EDS, and nickel support grid was used for testing the Cu catalysts. The net grid metals were also identified in the tests but have been excluded in the quantitative analysis.

active metal species were found to be in a concentration around 1wt.% (based on the whole catalyst sample) as shown in **Table 7-1**.

The detected loading ratio for each sample agrees with the designed value. It should note that EDS is a surface technique, and for the prepared samples with wet impregnation method, much metal particles are deposited on the surface and accessible to the reactants.

7.1.3 XPS analyses

XPS was used to identify the state (i.e. valence) of metal elements on the surface of the fresh catalyst and evaluate the interaction between metals and the support. The spectra for fresh 1%Ni/HZ(25), 1%Co/HZ(25), 1%Mo/HZ(25) and 1%Cu/HZ(25) were based on Ni(2p), Co(2p), Mo(3d) and Cu(2p) respectively and shown in **Fig. 7-6**.

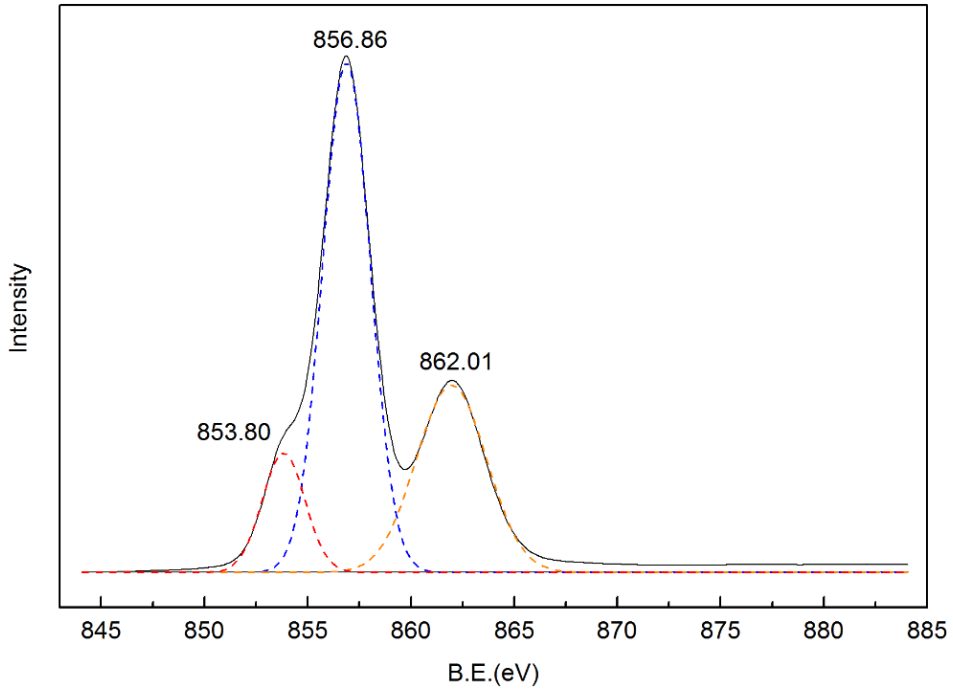

(a)

Fig. 7-6 XPS spectra of (a) Ni(2p) on Ni/HZ(25), (b) Co(2p) on Co/HZ(25), (c) Mo(3d) on Mo/HZ(25), (d) Cu(2p) on Cu/HZ(25)

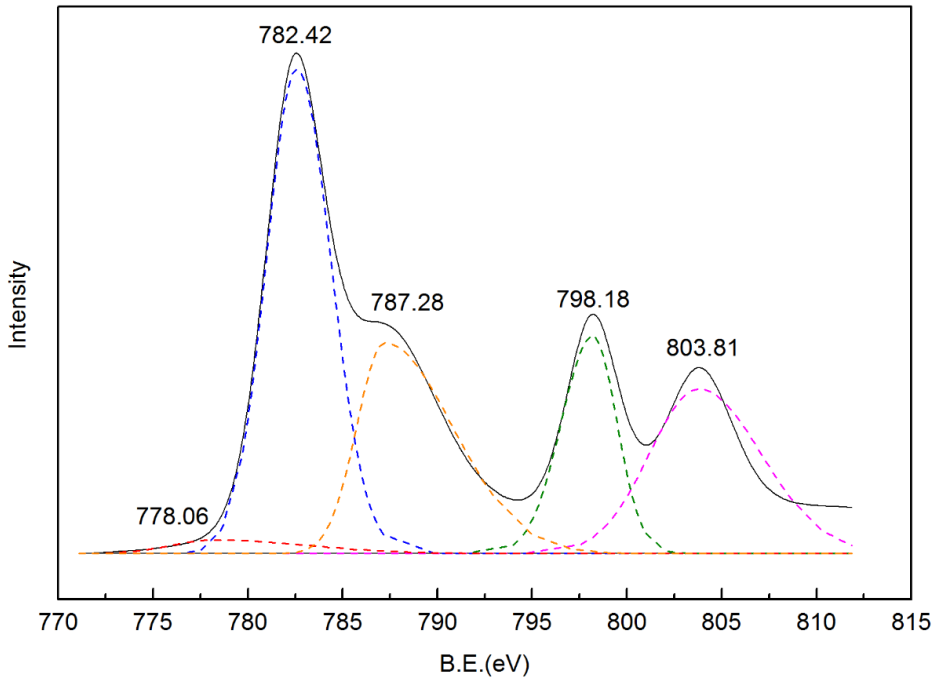

(b)

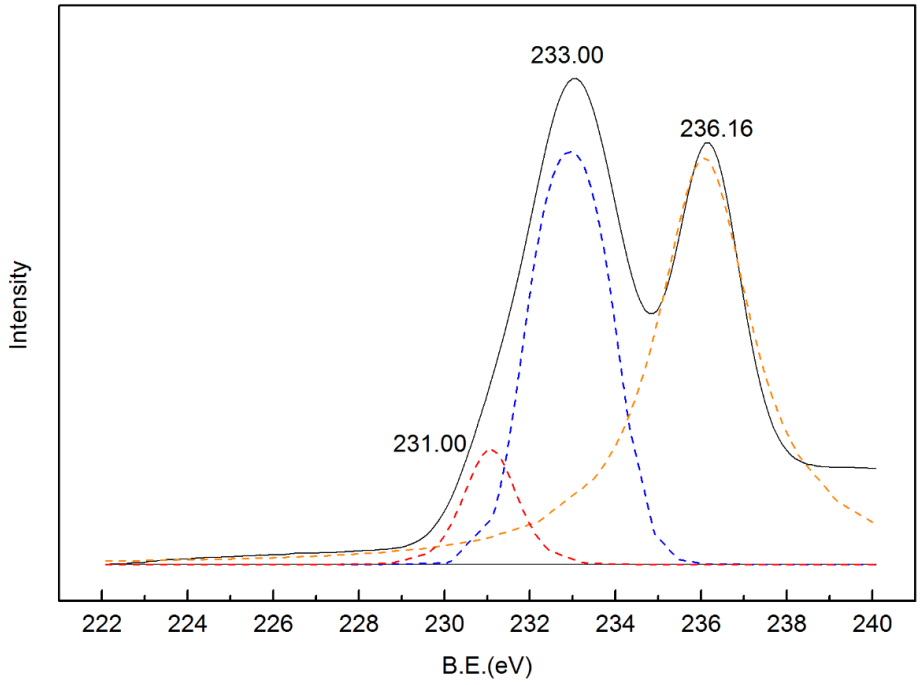

(c)

Fig. 7-6 XPS spectra of (a) Ni(2p) on Ni/HZ(25), (b) Co(2p) on Co/HZ(25), (c) Mo(3d) on Mo/HZ(25), (d) Cu(2p) on Cu/HZ(25)

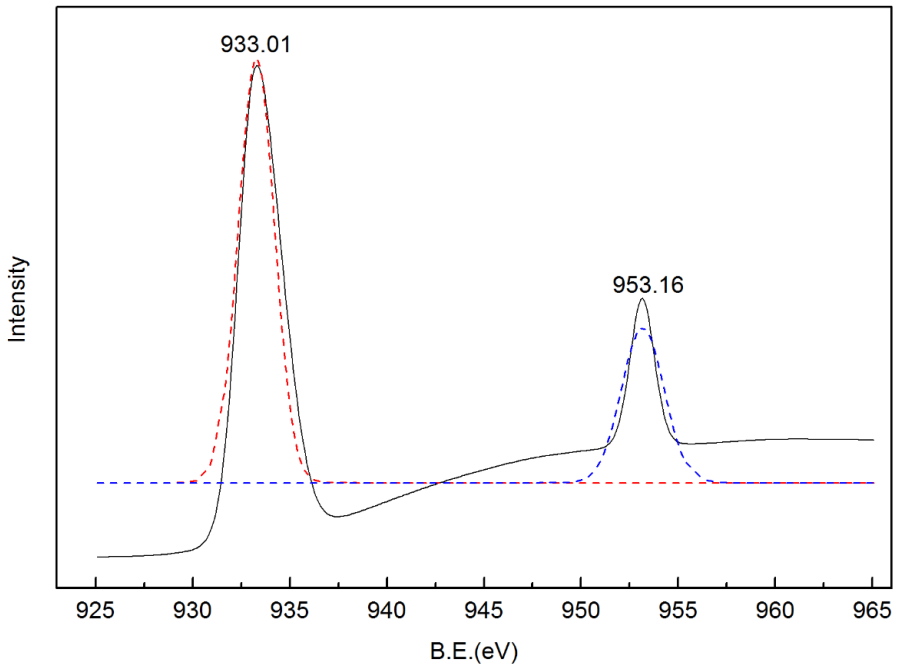

(d)

Fig. 7-6 XPS spectra of (a) Ni(2p) on Ni/HZ(25), (b) Co(2p) on Co/HZ(25), (c) Mo(3d) on Mo/HZ(25), (d) Cu(2p) on Cu/HZ(25)

For Ni/HZ(25), the peaks at 862.01 ev and 856.86 ev are ascribed to Ni^{2+}, which can be either $Ni(OH)_2$ or NiO , and the peak at 853.80ev is assigned to Ni^0. In the case of Co/HZ(25), there were five peaks identified; the first peak at 787.28ev is assigned to CoO, and the peaks at 803.82ev, 798.18ev and 782.42ev could all be assigned to $Co(OH)_2$. The small peak at 778.06 is attributed to Co^0. In the case of Mo/HZ(25), the peaks at 236.16ev and 233.00ev are ascribed to MoOx, and the peak at 231.00ev may attribute to either Mo^0 or $Mo(OH)_x$/Mo. For Cu/HZ(25), there were two peaks, the peak at 953.16ev can be assigned to either CuO or $Cu(OH)_2$, and the other peak at 933.01ev is attributed to Cu^0. It is found that even though the metals have been reduced in the hydrogen stream, they all showed oxidization state to different extents. This can be ascribed to both unreduced metals and metals acting as active sites that have interactions with the HZSM-5 zeolite support, especially their connections to the structure oxygen. Considering that XPS is a surface technique and the surface metal would be readily reduced at the corresponding temperatures, the metal support interaction would be the dominating reason. A similar phenomenon was also observed in the literature (Cheng et al., 2017). The metal hydroxides i.e. $Ni(OH)_2$, $Co(OH)_2$,

$Mo(OH)_x$ and $Cu(OH)_2$ are regarded as the evidence for the interactions between metals and the acid sites. The above results also agree with the prediction explained in Chapter 5 that the formation of ligand was found over the Brønsted acid site centred at the metal atom. The results in **Fig. 7-6** also show that the oxidation state metals were dominating in the catalysts of Ni/HZ(25), Co/HZ(25), and Mo/HZ(25), especially only a small portion of Co^0 has been observed in Co/HZ(25) (Chai et al., 2005; Domínguez et al., 2010; Watanabe et al., 2013), however, relatively large amount of Cu^0 existed in Cu/HZ(25), implying Cu may have less interaction with the HZSM-5 support compared to other metals. This is in line with the H_2-TPR results that the reduction peak of Cu/HZ(25) was at lower temperatures compared to other metals, and there was no obvious interaction peak observed at high temperature for Cu/HZ(25) reduction.

7.2 Catalytic deoxygenation of anisole over single-metal/HZ(25) catalysts

7.2.1 Effect of temperature on deoxygenation reaction over single-metal/HZ(25) catalysts

Anisole deoxygenation over 1%Ni/HZ(25) was carried out in a temperature range from 400°C to 600°C. The anisole conversion and grouped yields of liquid, gaseous and solid (carbonaceous deposits) products are shown in **Table 7-2** (experiments D1, D2 and D3). In general, the conversion of anisole was 90.0% at 400°C and 100% at both 500°C and 600°C. The bulk liquid product yield decreased with temperature from 41.6 wt.% at 400°C (excluding undecomposed anisole) to 19.9 wt.% at 600°C, and the carbonaceous deposit yield increased from 45.2 wt.% at 400°C to 77.3 wt.% at 600°C. Gaseous products yield was lower than 0.5 wt.% in all cases. It is observed that gaseous fraction mainly contained alkanes and olefins at all the temperatures (as shown in Appendix **A8**). These compounds are supposed to be produced by the methyl groups.

Fig. 7-7 shows the composition of the liquid products obtained over 1%Ni/HZ(25) at the different tested temperatures. The composition of the liquid products over HZ(25) is also shown for comparison purposes. The liquid produced at 400°C consisted mainly of undecomposed anisole and Phs. It should be noticed that the

conversion of anisole over Ni based catalyst was even lower than that of non-metal loading catalyst (~99.4%, Chapter 6), this may attribute to the loss of acid site by metal loading, and the metal is not active at 400°C. The amount of Phs significantly decreased to 2.4 wt.% at 500°C, while no Phs were detected at 600°C. On the contrary to Phs yield, the yield of AHs was as low as 3.8 wt.% of the reactant at 400°C, with a maximum of 28.8 wt.% at 500°C and it dropped to 19.9 wt.% at 600°C. AHs consisted mainly of BTX, and small proportion of polycyclic aromatic hydrocarbon (PAH) including naphthalene, and methyl naphthalene at all tested temperatures. Similar to the change of AHs yield with temperature, the maximum BTX yield was also observed at 500°C (for 25.6 wt.%).

Table 7-2 Grouped product yields and product recovery (wt. % of reactant)

No.	Cat	T (°C)	Conv (%)	Product recovery (%)	Liquid product					Gas	Solid
					Bulk	AHs	BTX	BTX selectivity (%)	Phs		
D1		400	90	96.8	51.6[a]	3.8	3.0	7.3	37.8	0.1	45.2
D2	1%Ni /HZ(25)	500		99.4	31.3	28.8	25.6	81.9	2.4	0.2	68.0
D3		600		97.6	19.9	19.9	19.4	97.6	0.0	0.4	77.3
D4	0.5%Ni /HZ(25)	500		99.3	33.8	27.2	23.9	70.6	6.7	0.1	65.4
D5	5%Ni /HZ(25)	500		95.0	4.3	4.3	4.3	98.7	0.0	1.2	89.5
D6	1%Co /HZ(25)	500	100	95.9	37.6	28.8	25.9	68.8	8.8	0.1	58.2
D7	1%Mo /HZ(25)	500		100.0	38.8	35.2	30.0	77.4	3.6	0.5	60.7
D8	0.5%Mo /HZ(25)	500		96.0	35.7	30.4	25.6	71.7	5.3	0.6	59.7
D9	5%Mo /HZ(25)	500		99.9	35.4	27.3	25.2	71.2	8.0	0.3	64.2
D10	1%Cu /HZ(25)	500		98.2	40.8	33.7	28.3	69.3	7.1	0.5	56.9

[a] The value considers unreacted anisole

The results reveal that the increase in temperature favours the production of BTX through the deoxygenation reactions of Phs, which are intermediates abundantly produced at the “key temperature” (400°C as observed in Chapter 6) in the anisole decomposition, and that the deoxygenation over 1%Ni/HZ(25) mainly takes place from 500°C onwards. On the other hand, the observed significant increase in carbonaceous deposit yield and decrease in total liquid yield also indicates that temperature rise would also promote the solid products formation. Deoxygenation reactions and carbonaceous deposit formation are found to be competitive reactions over Ni based catalysts both favour high temperature (Li et al., 2017b). A compromise between these two reactions is better achieved at 500°C, giving rise to the highest BTX. Additionally, it is worth noting that multi-methyl Phs (xylenols and trimethyl-methyl Phs) were only detected in the liquid products at 400°C, this points that they are more readily to be consumed at higher temperatures compared to phenol and cresols.

In comparison with the decomposition of anisole over HZ(25), even though the conversion of anisole and the bulk liquid yield from 1%Ni/HZ(25) based experiment was lower compared to non-metal based experiment at each temperature due to the increase of carbonaceous deposit caused by 1%Ni loading, the BTX yield and selectivity has been both improved. The BTX yield was respectively improved from 1.9 wt.% to 3.0 wt.% at 400°C, and from 23.6 wt.% to 25.6 wt.% at 500°C; simultaneously, the BTX selectivity was enhanced from 2.6% to 7.3% at 400°C, from 57.1% to 81.9% at 500°C, and from 81.5% to 97.6% at 600°C. The results are attributed to more Phs being converted to BTX through deoxygenation and less polycyclic aromatic hydrocarbon (PAH) being yielded in the liquid in the presence of Ni especially at high temperatures. At respect 400°C and 500°C, the dramatic decrease in the Phs yield compared to non-metal catalysis does not correspond to the same much promotion of AHs yield, revealing that apart from the conversion to AHs in liquid products through deoxygenation, portion of Phs turns directly or indirectly (turns to be AHs first) to be carbonaceous deposit in the presence of 1%Ni (Thilakaratne, Tessonnier and Brown, 2016), so that gives rise to a significant increase of solid product (increased by respect 18.6wt.% at 400°C and 26.0 wt.% at 500°C). However, it

is also found that the distribution of Phs products showed little change (cresols, xylenols and trimethyl-phenols) regardless of the 1%Ni loading at 400°C and 500°C respectively, this implies Ni loading may not inhibit the transmethylation reactions, but phenol, cresols and multi-methyl Phs formed in the transmethylation are probably further consumed as the precursors for both AHs and carbonaceous deposit at these temperatures. It is also worth noting that there was not any Phs detected in the liquid product at 600°C in both cases, but the BTX yield was even much lowered at such temperature when 1%Ni was loaded to the catalyst, this result confirms that the severe formation of carbonaceous deposit on the Ni based catalyst surface also occurs at the expense of AHs (indirect way of Phs conversion). Nevertheless, the dramatic enhancement of BTX selectivity at 600°C after 1%Ni addition confirms that Ni is still favourable to produce monomer AHs by deoxygenation even at the high temperature.

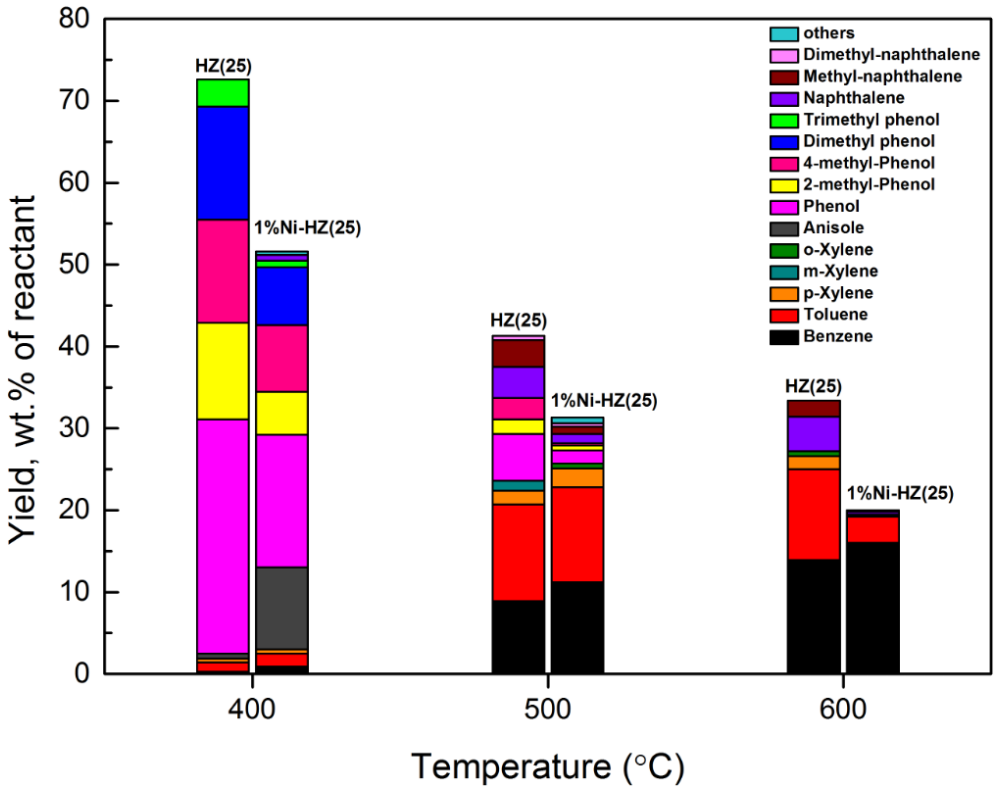

Fig. 7-7 Liquid product yields obtained from anisole decomposition over HZ(25) (Zhang et al., 2016) **and 1%Ni/HZ(25). Reaction temperature at respective 400, 500 and 600°C**

Furthermore, as aforementioned, the BTX yield peaked at 500°C in the present of 1%Ni/HZ(25). This is analogous with the results for non-metal loading catalysts in Chapter 6, where the peak yield for BTX in non-metal loading experiment happened at 600°C. This 100°C difference in peak temperature reflects the effect of Ni in lowering the activation energy required for the deoxygenation reaction in anisole decomposition. Nevertheless, it should also be noted that Ni addition may simultaneously lower the activation energy of carbonaceous deposit formation so that enhances solid product yield.

7.2.2 Effect of type of metal on deoxygenation reaction over single-metal/HZ(25) catalysts

The anisole conversion and grouped yields of liquid product, gaseous product and carbonaceous product for the experiments D2, D6, D7 and D10 based on respect 1%Ni, 1%Co, 1%Mo and 1%Cu loaded HZ(25) catalysts are shown in **Table 7-2**. **Fig. 7-8** exhibits the liquid yield distribution obtained from the experiments over metal based catalysts at 500°C in comparison with the liquid products over HZ(25). Gaseous species are specified in Appendix **A8**. Generally, metal based catalysts lead to lower liquid yield and higher carbonaceous yield compared to non-metal based case. Among the four experiments with metal based catalysts, the lowest liquid yield of 31.3 wt.% and highest carbonaceous deposit yield of 68.0 wt.% were obtained over 1%Ni/HZ(25), while the highest liquid yield of 40.8 wt.% and the lowest carbonaceous deposit yield of 56.9 wt.% are obtained over 1%Cu/HZ(25). The results indicate that, with similar loading rates, Ni active site presents higher activity towards carbonaceous formation than other metals.

Liquid products obtained from the experiments at 500°C based on 1%Ni/HZ(25), 1%Co/HZ(25), 1%Mo/HZ(25) and 1%Cu/HZ(25) presented similar product distribution as that for non-metal HZ(25). However, the Phs yield decreased significantly when the metal active site was added. The most decrease (to 2.4 wt.% and 3.6% respectively) was observed over 1%Ni/HZ(25) and 1%Mo/HZ(25). Regarding AHs, 1%Mo/HZ(25) improved its yield from 31.2 wt.% to 35.2 wt.%, and 1%Cu/HZ(25) promoted the yield to 33.7 wt.%. 1%Ni/HZ(25) and

1%Co/HZ(25) showed the same AHs yield of 28.8 wt.%. Alike the products distribution over 1%Ni/HZ(25), BTX constituted the main component in the AHs species produced over other metal based catalysts. The BTX yield in the experiment with 1%Mo/HZ(25) based catalyst was found to be the highest for 30.0 wt.%, which accounted for 77.4% of the liquid products, and other proportion mainly consisted of the PAH (yield of 5.2 wt.%) and Phs (yield of 3.6 wt.%). 1%Ni/HZ(25) based catalyst did not produce the most BTX, but it led to the highest BTX selectivity of 81% as aforementioned. 1%Co/HZ(25) gave rise to a BTX yield of 25.9 wt.% similar to that from 1%Ni/HZ(25), but the BTX selectivity was only 68.8%. Even though 1%Co also led to less PAH for only 2.92 wt.%, it showed less conversion of Phs. The liquid products over 1%Cu/HZ(25) comprised 28.3 wt.% BTX with a selectivity of 69.3% in the liquid products. It showed the lowest BTX selectivity because of a large proportion of both Phs (for 7.1 wt.%) and PAH (for 5.4 wt.%).

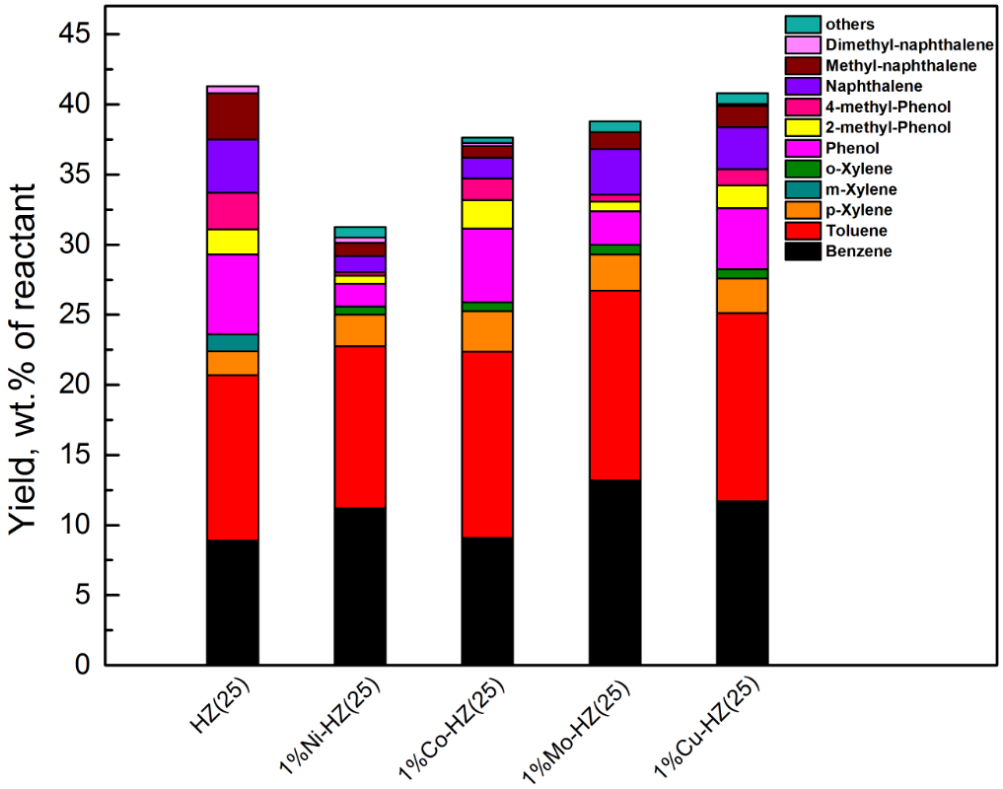

Fig. 7-8 liquid product yields obtained from anisole decomposition over different metals loaded HZ(25) catalysts. Reaction temperature = 500°C

Ni could convert the Phs efficiently with very high BTX selectivity in the liquid products of the decomposition of anisole, but it could also cause severe formation of carbonaceous deposit that decreasing the total liquid yield. Mo would give rise to more yield of AHs and reserve more liquid products by relieving severe carbonaceous formation over the catalyst compared to Ni, but it shows less conversion of Phs, and more PAH would be produced.

7.2.3 Effect of metal loading ratio on deoxygenation reaction over single-metal/HZ(25) catalysts

The catalysts of Ni/HZ(25) and Mo/HZ(25) with the metal loading ratios of 0.5wt.%, 1.0wt.% and 5.0wt.% were tested for the decomposition of anisole at 500°C respectively (experiments series D2, D4, D5 and D7, D8, D9). These two metals were selected based on their positive results shown in Section 7.2.2. The anisole conversion and grouped yields of liquid product, gaseous product and carbonaceous product are shown in **Table 7-2**, and the liquid yield distribution is specified in **Fig. 7-9** (a) and (b).

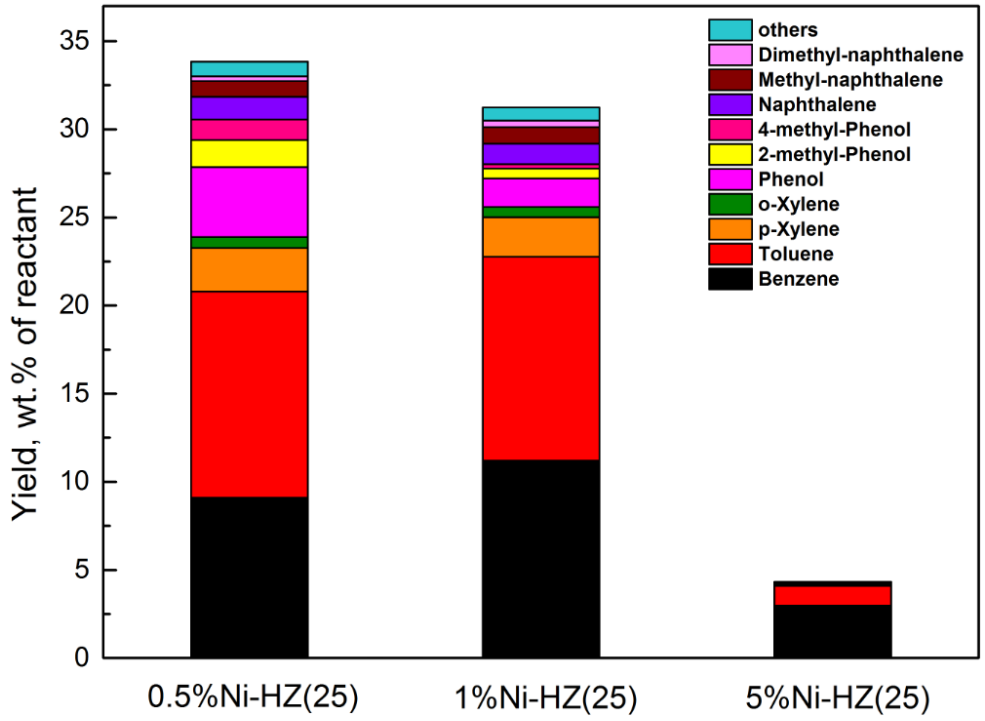

(a)

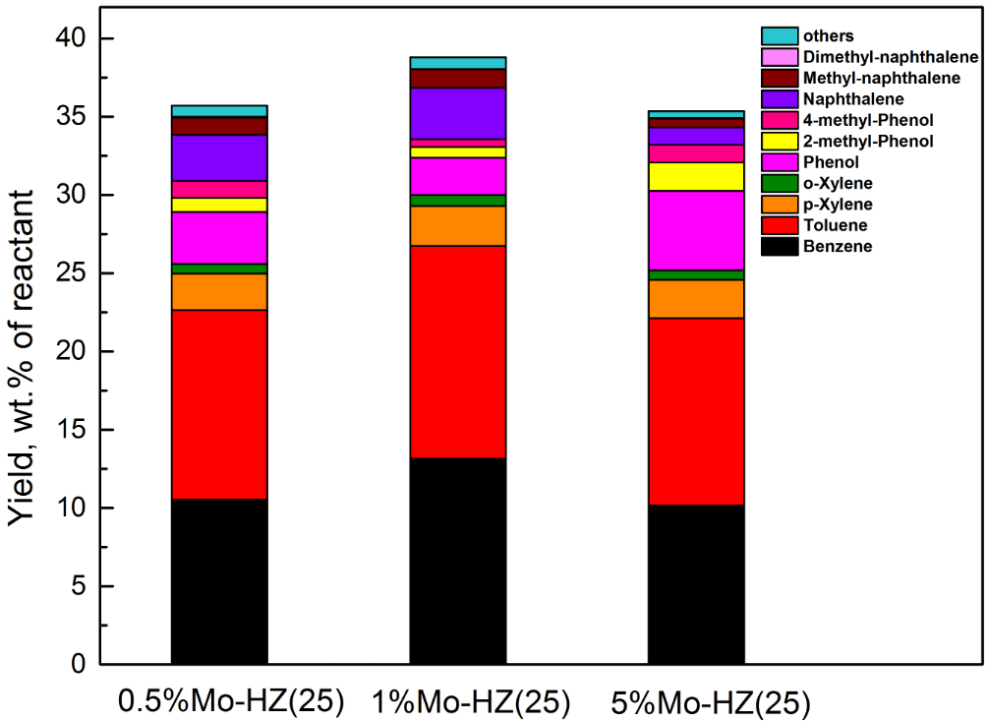

(b)

Fig. 7-9 liquid product yields obtained from anisole decomposition over (a) Ni/HZ(25) and (b) Mo/HZ (25) catalysts with metal loading ratios of 0.5 wt.%, 1 wt.% and 5 wt.% respectively. Reaction temperature = 500°C

In the case of Ni/HZ(25), when the loading ratio increased, the yield of bulk liquid products decreased significantly from 33.8 wt.% for 0.5%Ni/HZ(25) to 4.3 wt.% for 5%Ni/HZ(25); accordingly, carbonaceous deposit increased from 65.4 wt.% to 89.5 wt.%. Negligible gaseous products were produced during the reactions (as shown in Appendix **A8**).

Specifically, Phs yield was 6.7 wt.% when 0.5%Ni/HZ(25) was used, and decreased when the loading ratio increased, till no Phs were obtained in the experiment with 5%Ni/based catalyst. The yields of AHs and BTX both experienced a slight rise when the loading ratio increased from 0.5 to 1wt.%, although they sharply deceased over 5%Ni/HZ(25) catalyst. Regarding BTX selectivity, it kept increasing with the loading ratio till 98.7% corresponding to the 5%Ni loading.

The results indicate that 0.5%Ni and 1%Ni loadings have similar catalytic activity towards the conversion of anisole into liquids. However, it seems that the

conversion pathway of Phs into BTX is relatively impaired when using 0.5%Ni/HZ(25), as a result the BTX selectivity for 1%Ni loading was higher than that for 0.5%Ni loading by 11.3%. The complete conversion of Phs into BTX was observed over 5%Ni/HZ(25) with almost 100% selectivity. This result confirms the high efficiency of Ni in production of mono AHs. On the other hand, more solid products were found at the expense of liquid product when the loading ratio raised to 5%, this proves that Ni loading is also the key factor leading to the formation of carbonaceous deposit. Among the tested catalysts, 1%Ni loading gives rise to the best results in terms of both BTX yield and selectivity, and carbonaceous deposits formation.

In the case of Mo/HZ(25) series, the differences in liquid yield and distribution due to increase of metal loading are not as significant as those observed with the Ni/HZ(25) series, particularly when referring to 5% loading. The maximum AHs yield, BTX yield and BTX selectivity were 35.2 wt.%, 30.0 wt.% and 77.4% respectively when using 1%Mo/HZ(25) as catalyst. At the same time, this catalyst exhibited a minimum for the Phs yield. This result indicates the increase of Mo loading may give rise to better conversion of Phs, but 5%Mo loading may be so high that the metal blocks the micro-pores of HZSM-5 (atomic radius of Mo is ~2.0Å) and deactivates the catalyst to some extent before the reaction (Rahzani et al., 2017). Contrary to Ni/HZ(25) series, the increment of Mo loading did not enhance significantly the production of carbonaceous deposits; this implies that Mo active sites promote liquid formation even at high metal loading ratio. 1 wt.% loading of Mo gave rise to higher BTX yields than the other loading ratios, and the yield was also higher than that obtained over 1%Ni/HZ(25). However, none of the x%Mo/HZ(25) catalysts led to a BTX selectivity as high as that achieved over 1%Ni/HZ(25).

7.3 Characterization of spent single-metal/HZ(25) catalysts

Apart from that the amount of carbonaceous deposit has been determined by thermogravimetry (TG) tests, TEM, EDS, and XPS tests were used to investigate the morphology and composition of the carbonaceous deposit in the spent catalyst.

7.3.1 TEM and EDS analyses

TEM tests were carried out to characterize the spent catalyst samples of 1%Ni/HZ(25) and 1%Mo/HZ(25) (see in **Fig. 7-10** and **Fig. 7-11**, from experiments D2 and D7).

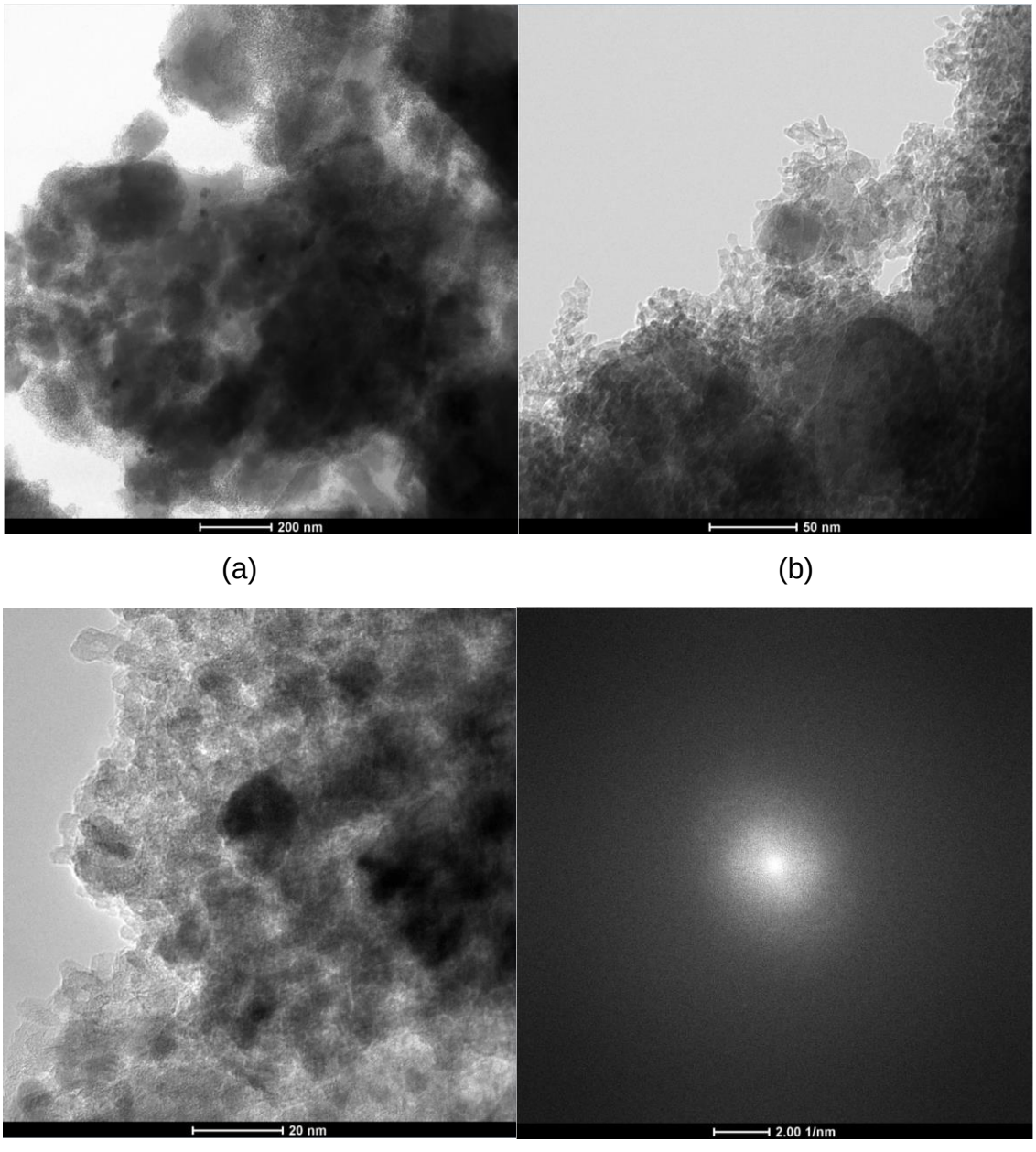

(a) (b)

(c) (d)

Fig. 7-10 TEM micrographs for the spent catalysts of 1%Ni/HZ(25) after experiment D2: (a) 200 nm; (b) 50 nm; (c) 20 nm and (d) FFT image

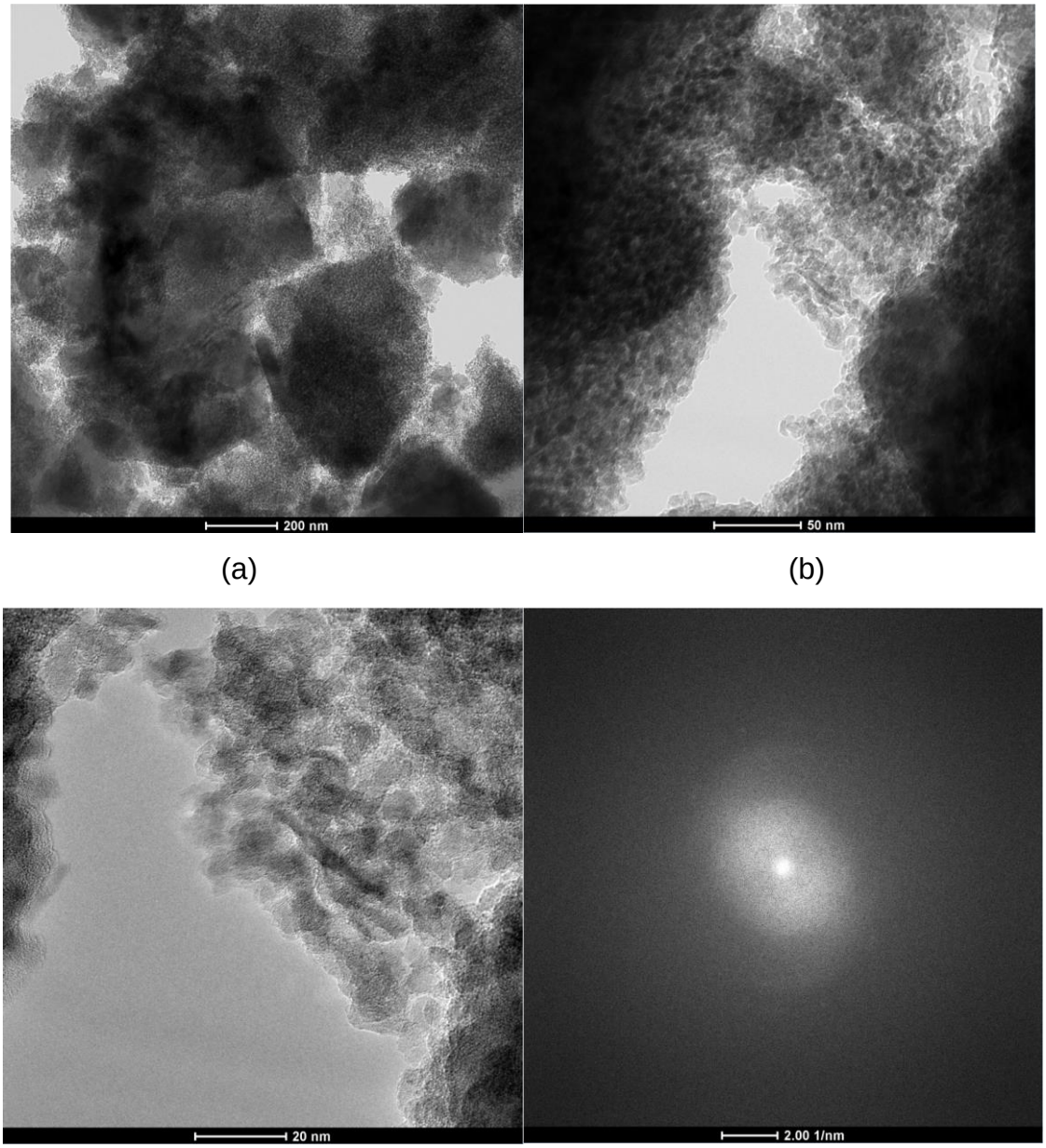

(a) (b)

(c) (d)

Fig. 7-11 TEM micrographs for the spent catalysts of 1%Mo/HZ(25) after experiment D7: (a) 200 nm; (b) 50 nm; (c) 20 nm and (d) FFT image

It is found carbonaceous deposits covered the surface of the catalyst in comparison to the fresh catalyst, such that the metal particles were almost non-visible in most areas. The absence of diffraction rings in Fast Fourier Transform (FFT) images of the spent catalyst confirms the amorphous nature of the carbon deposit.

EDS tests were used to identify the main elements present in the surface of the spent catalysts and to estimate the amount of carbonaceous deposits, as shown in Appendix **A9** and **Table 7-3**.

Table 7-3 Carbon deposit on spent 1%Ni/HZ(25) and 1%Mo/HZ(25) catalyst detected by EDS

	Spent 1%Ni/HZ(25)		Spent 1%Mo/HZ(25)	
Elem	Weight%	Atomic%	Weight%	Atomic%
C	6.6	10.7	5.0	8.7
Ni	1.0	0.3	-	-
Mo	-	-	1.6	0.4

As can be seen, carbon element in the spent catalysts was roughly 6.6 wt.% for the unit spent 1%Ni/HZ(25) catalyst and 5.0 wt.% of the spent unit 1%Mo/HZ(25) catalyst. This agrees with the experimental results that Ni based catalysts gave rise to more carbonaceous products. It should be noted that part of the oxygen element identified in these analyses may also come from the carbonaceous deposit, but EDS technique does not allow to distinguish them from the zeolite structure oxygen.

7.3.2 XPS analyses

XPS spectra based on C(1s) for spent catalyst are shown in **Fig. 7-12** and **Fig. 7-13**. The samples were obtained after experiments run over Ni/HZ(25) at 400°C (D1), Ni/HZ(25) at 500°C (D2), Ni/HZ(25) at 600°C (D3), Co/HZ(25) at 500°C (D6), Mo/HZ(25) at 500°C (D7), and Cu/HZ(25) at 500°C (D10). In general, carbon on all spent catalysts exhibited three peaks, except Mo/HZ(25) that exhibited only two obvious peaks.

The peaks around 289.10ev, 288.90ev and 288.70ev are assigned to periodic chain compounds containing carbonyl groups i.e.-CH_2-$C(CH_3)(C(O)O$-CH_2-$CH_3)$-$)_n$ and (-$CH_2CH(C(O)OH)$-$)_n$ (Zou et al., 2016). The carbonyl compounds could be formed by the adsorption of CO and CO_2 on the catalyst surface (Liu et al., 2007). The peaks around 286.00ev, 285.90ev, 285.80ev and 285.90ev are

attributed to periodic chain compounds primarily consisting of C-O bond for phenol ethers or alcohols (Li et al., 2017b). The peak around 284.40ev, 284.50ev and 284.70ev are considered ascribed to either graphitic carbon (Weckhuysen, Rosynek and Lunsford, 1998) or aliphatic and aromatic carbon polymers (Albers et al., 1998; Hantsche, 1993). Considering the samples in this work, amorphous aliphatic and aromatic carbon polymers are more likely to be formed based on previous analyses.

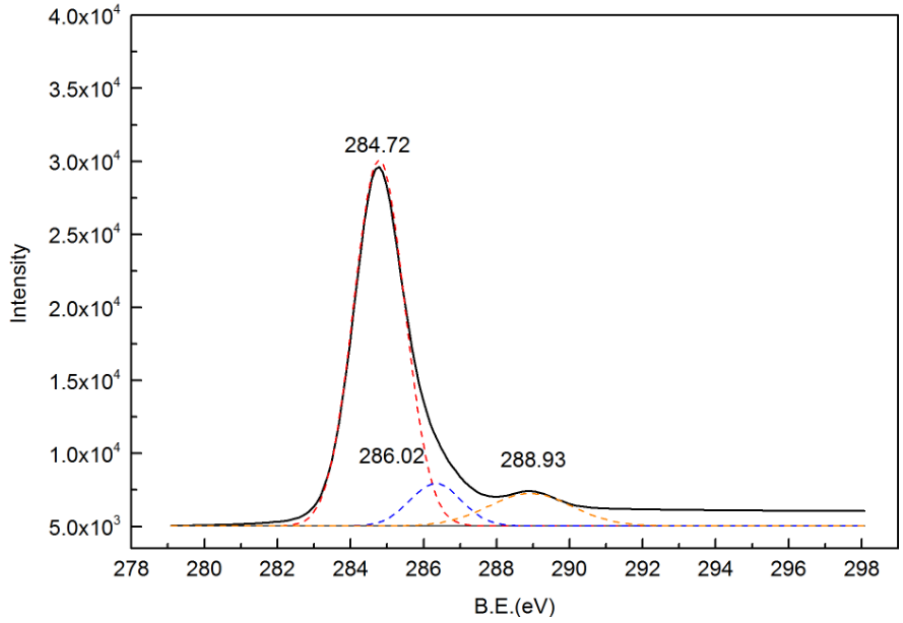

(a)

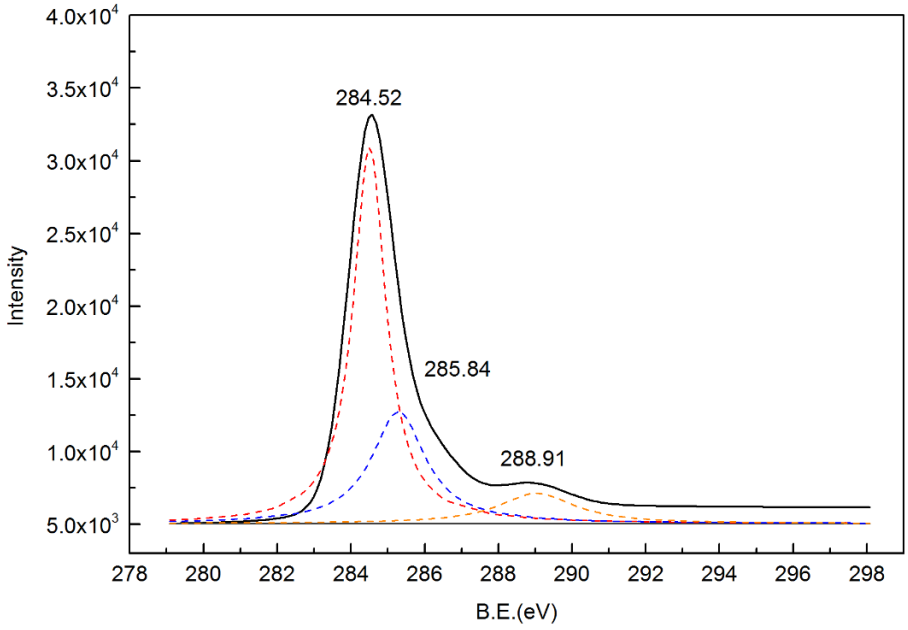

(b)

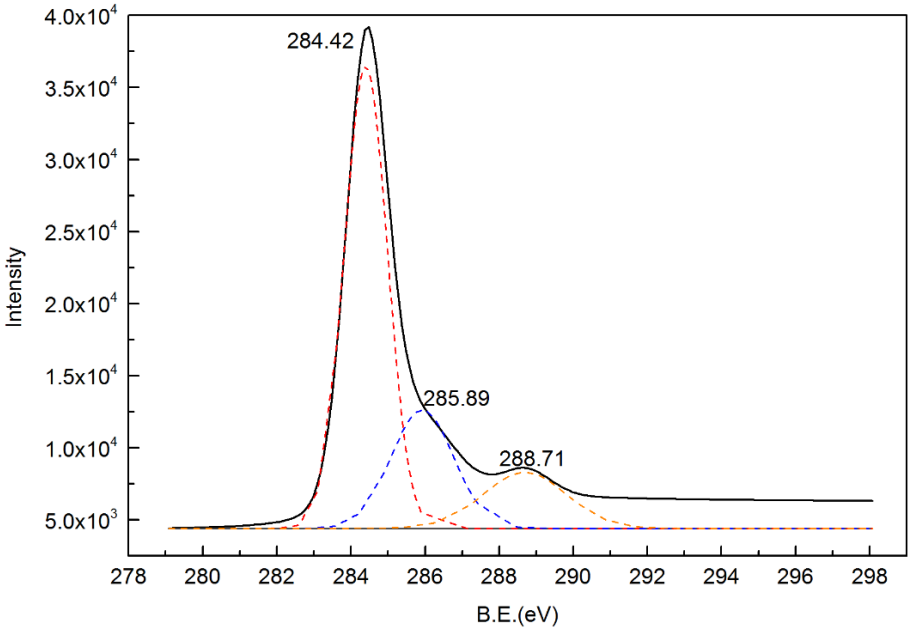

(c)

Fig. 7-12 XPS spectra of C(s1) for the spent catalyst of (a) Ni/HZ(25) at 400°C, (b) Ni/HZ(25) at 500°C, (c) Ni/HZ(25) at 600°C

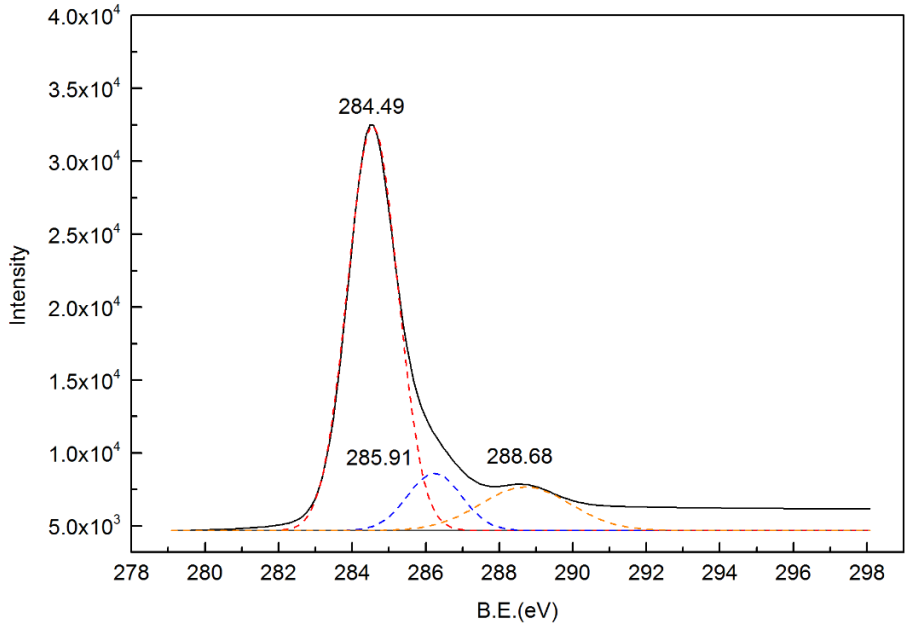

(a)

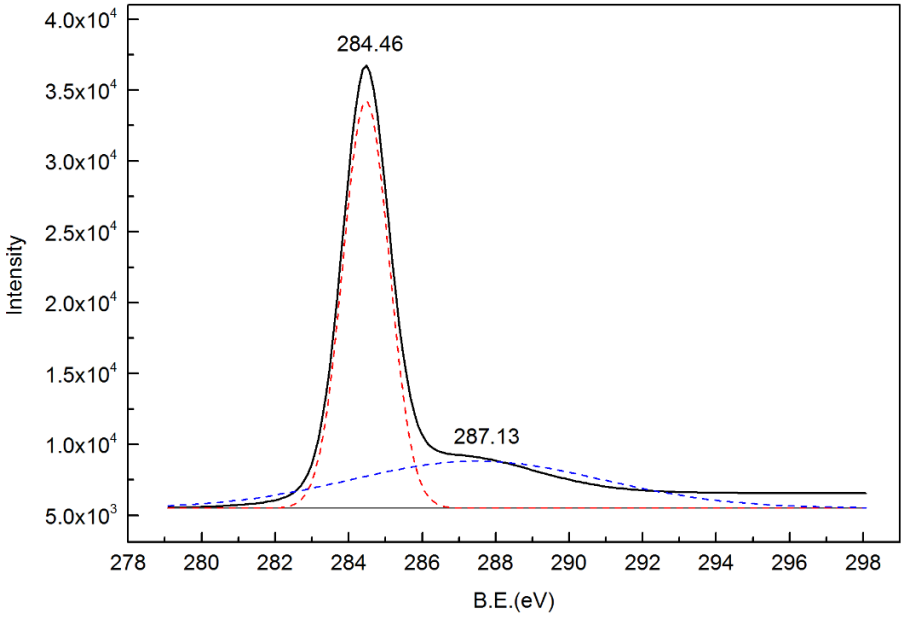

(b)

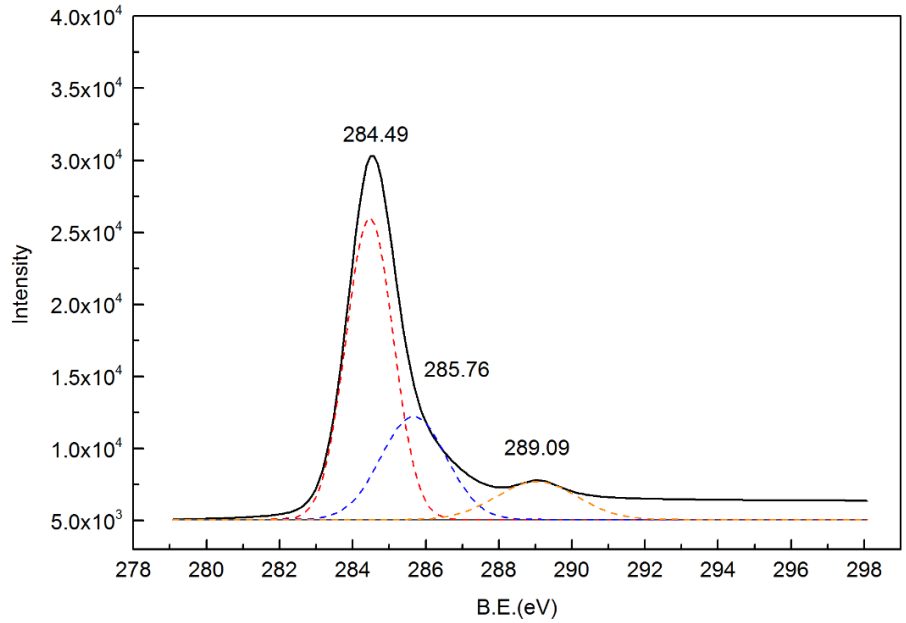

(c)

Fig. 7-13 XPS spectra of C(s1) for the spent catalyst of (a) Co/HZ(25) at 500°C, (b) Mo/HZ(25) at 500°C, (c) Cu/HZ(25) at 500°C

Regarding the spent Mo/HZ(25), apart from the peak at 284.46ev being assigned to be aliphatic and aromatic carbon, the other peak at 287.13ev is attributed to chain compounds containing metal carbide (Willemen et al., 1977). The signal for metal carbides compounds may also be involved in the peaks at around 284ev for spent Ni/HZ(25) (Karweik and Winograd, 1976) and spent Co/HZ(25)(Barber

et al., 1973), 288ev for Co/HZ(25) (Hoof, Tisley and Walton, 1973), and 289ev for Cu/HZ(25) (Moretti et al., 1989). The metal carbides are known to be important intermediates for the formation of carbonaceous deposit (Cooper and Trimm, 1980).

The results shown in **Fig. 7-12** and **Fig. 7-13** reveal that the carbonaceous substance deposited on each spent metal/HZ(25) catalyst mainly consists of chain compounds of aliphatic carbon, aromatics and carbonyl groups, which can be attributed to the polycondensation of the methyl groups and aromatic compounds during the decomposition of anisole. Considering the experimental results in Section 7.2, Phs and AHs can be the main precursors for the polycondensation reactions that originate from the metal carbides.

The intensity of the three peaks for spent 1%Ni/HZ(25) increased with temperature, confirming the increment of temperature in the range of 400 to 600°C may result in larger carbon deposition. Regarding the four spent catalysts of different metals based HZ(25) at 500^{o}C, the spent 1%Ni/HZ(25) and spent 1%Mo/HZ(25) showed the highest intensities, implying these two metals based catalysts are more prone to give rise to the formation of carbonaceous deposit compared to Co and Cu. This agrees with the model prediction in Chapter 5 that Ni/HZ(25) and Mo/HZ(25) have larger adsorption capacity to the reactant compounds, and also the experimental results that Ni and Mo showed higher activity compared to Co and Cu.

7.4 Reaction pathways of catalytic deoxygenation in anisole decomposition over metal/HZ(25)

Based on the experimental investigation in above sections and the investigation of deoxygenation mechanism in Chapter 5, reaction pathways for the deoxygenation in the decomposition of anisole over metal/HZ(25) catalyst at 500°C are proposed, as shown in **Fig. 7-14**.

The deoxygenation reactions follow transmethylation reactions as the second stage of anisole decomposition, and the products primarily consist of BTX compounds. As aforementioned in Chapter 5, the deoxygenation is regarded to

happen with the engagement of hydrogen. Since no hydrogen stream is used during the experiments, the hydrogen is assumed to be transferred in situ during for the reactions, therefore the process could be called hydrodeoxygenation. Based on the analyses of gaseous products and XPS analyses of spent catalyst, besides the products of alkanes, olefins generated from methyl group polycondensation, carbonaceous deposit of periodic chain aliphatic and aromatic polymers were also yielded from the polycondensation reactions of aromatic compounds (Phs and AHs). The polycondensation may simultaneously produce abundant hydrogen so that becomes the potential hydrogen source for the “hydrodeoxygenation”. There are primarily three different reaction pathways proposed for the deoxygenation reactions in the decomposition of anisole over metal/HZ(25) catalyst.

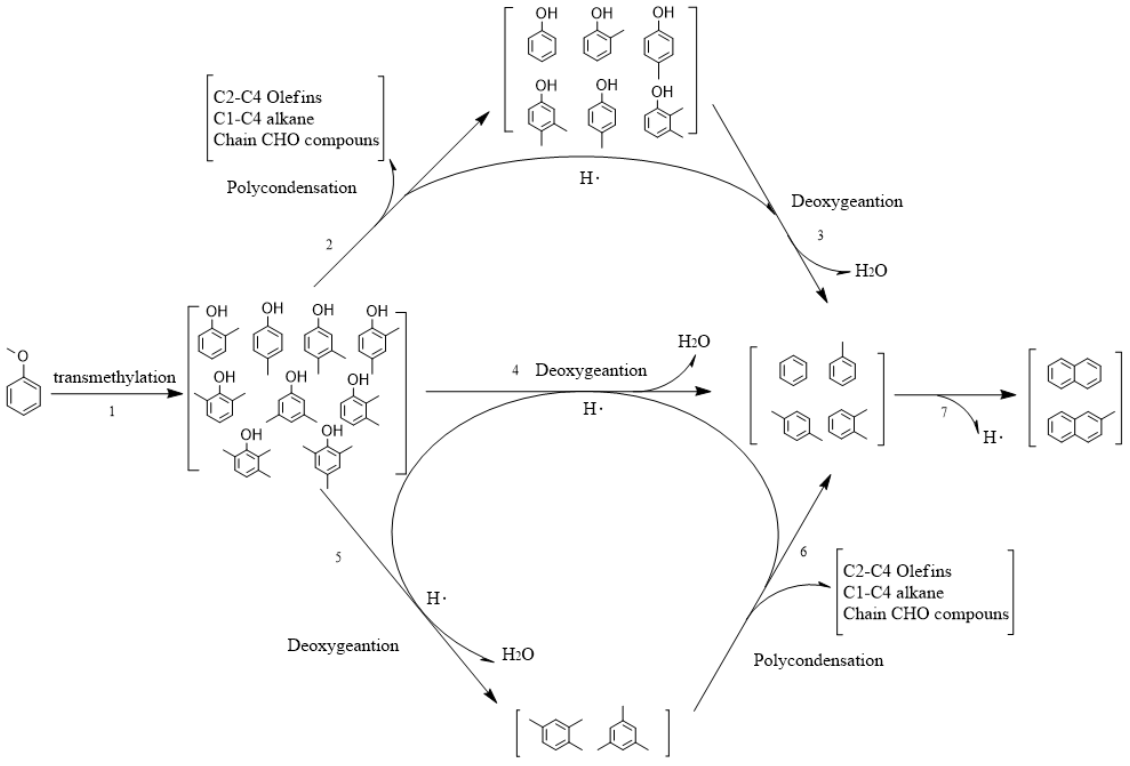

Fig. 7-14 Reaction pathways for deoxygenation in the decomposition of anisole

A phenolic compound could either undergo polycondensation prior to deoxygenation (pathway 2-3 in **Fig. 7-14**), or experience firstly deoxygenation followed by polycondensation (pathways 4 and 5-6). It should be noticed that xylenols and trimethyl phenols were obtained as low temperature products and

only a little xylene and no trimethylbenzene were found in the products at 500°C. This implies that multi-methyl phenols may easily undergo demethylation reaction before deoxygenation or be more readily consumed in the polycondensation over the surface of metal/HZ(25).

All the three pathways lead to the products of BTX, part of which could further be converted to PAH (naphthalene and methyl naphthalene, pathway 7), which were also observed in the liquid fraction along with the BTX products in most of the experiments.

7.5 Summary

Experiments of the anisole catalytic decomposition were performed over the catalysts of respect Ni, Co, Mo and Cu loaded HZSM-5 zeolites. TEM tests for the fresh catalysts revealed that metals were loaded on the zeolite surface primarily as micro polycrystalline ranging in 4-10nm, and further EDS spectra confirmed that the loading rate for each metal was about 1 wt.%, in line with the designed ratio. XPS tests for the fresh catalyst samples indicated that the metal atoms on the zeolite surface primarily exhibited oxidized state, and a small portion of them existed in metallic state. This reflected the strong interaction between metals and the structure oxygen and acid sites on HZSM-5 zeolite. Experimental investigation results showed that temperature rise was effective in the promotion of the BTX yield and selectivity, but it also increased the yield of undesirable carbonaceous deposit, which would be at the expense of both Phs and AHs. The type of metal active site supported on HZSM-5 was found to have an influence on the BTX yield and selectivity. Ni/HZ(25) presented the best selectivity towards the formation of BTX by converting more Phs to mono-AHs, while Mo/HZ(25) presented the best catalytic activity towards BTX formation with the highest AHs production by impairing the formation of carbonaceous deposits. Change of metal loading ratio had significant influence in the case of Ni/HZ(25) series. Experiments based on 5%Ni/HZ(25) exhibited 98.7% BTX selectivity but with only 4.3 wt.% liquid yield, while 0.5%Ni/HZ(25) showed worse catalytic effect in the conversion of intermediates Phs into AHs. In the case of Mo/HZ(25), the loading ratio had less influence in the BTX yield and selectivity. The optimal loading ratio,

in terms of BTX formation, was 1 wt.% both for the Ni and Mo catalyst series. TEM-EDS and XPS tests for spent catalysts of Ni/HZ(25) and Mo/HZ(25) indicated an amorphous nature of the carbonaceous deposits, primarily consisting of aliphatic and aromatic carbon produced by the polycondensation during the decomposition of anisole, and Phs and AHs were important precursor compounds. The enhanced yield of carbonaceous deposits at high temperatures was also detected by XPS tests in the case of Ni/HZ(25) series. Based on the experimental investigation, three possible reaction pathways were proposed for the catalytic deoxygenation reactions, which follows the transmethylation reaction as the second stage in the catalytic anisole decomposition. The deoxygenation was considered primarily with the engagement of hydrogen, which was supplied in-situ as product resulting from the polycondensation reactions.

8 Experimental study of anisole deoxygenation over bi-metal based zeolite catalyst

This chapter describes anisole decomposition experiments carried out over bi-metal loaded zeolite catalyst with the aim to investigate the effects of the two metals on the deoxygenation reactions without external hydrogen supply. The results in Chapter 7 showed that the yield and selectivity of BTX were influenced by temperature and metal loading of the catalysts, and Ni and Mo were observed to be the most active catalyst as single metal loadings in the deoxygenation reactions during the catalytic decomposition of anisole. However, severe polycondensation was also caused by the metal loading on the catalysts. It is deemed that the introduction of a second metal as a promoter to the catalyst may be helpful for maximizing the selectivity and yields of desired products and relieving the polycondensation reactions (Alonso, Wettstein and Dumesic, 2012). According to the modelling investigation on the reactants adsorption onto various transition metals presented in Chapter 5, Fe exhibited low adsorption energy, and it was considered as second metal to affect the strong adsorption capability of Ni or Mo based catalysts. The bi-metal catalysts of Ni-Mo, Ni-Fe and Mo-Fe loaded HZSM-5 (Si/Al=25, labelled as bi-metal/HZ(25)) were then selected to experimentally evaluate their catalytic performance for the deoxygenation reaction in the anisole decomposition; results are presented in this chapter.

8.1 Characterization of fresh bi-metal/HZ(25) catalysts

Fresh catalysts were analysed by TEM-EDS to evaluate their surface morphology of the active metals. TEM tests at four resolutions (500nm, 100nm, 50nm and 20nm) were carried out respectively on the catalysts of 1%Ni-1%Mo/HZ(25), 1%Ni-1%Fe/HZ(25), 1%Mo-1%Fe/HZ(25). Representative TEM micrographs of each catalyst are shown in **Fig. 8-1**, **Fig. 8-2** and **Fig. 8-3**, respectively.

All the bi-metaled metal (bi-metal) particles were found to be highly dispersed on the zeolite surface and in the form of microcrystal structure, the crystal nature was pointed by the SEAD patterns shown in the section d of respect **Fig. 8-1**, **Fig. 8-2** and **Fig. 8-3** (González et al., 2009; Martínez et al., 2003). This is like

the single metal-based HZ(25) reported in Section 7.1.2. However, compared to the single metal loading, it is found that support was more densely covered by the metal loading. The individual particles of the bi-metal loading showed similar diameters (within 10nm) as single metal particle (Nie et al., 2014), but with unclear boundaries, so that the individual particle was more difficult to be distinguished.

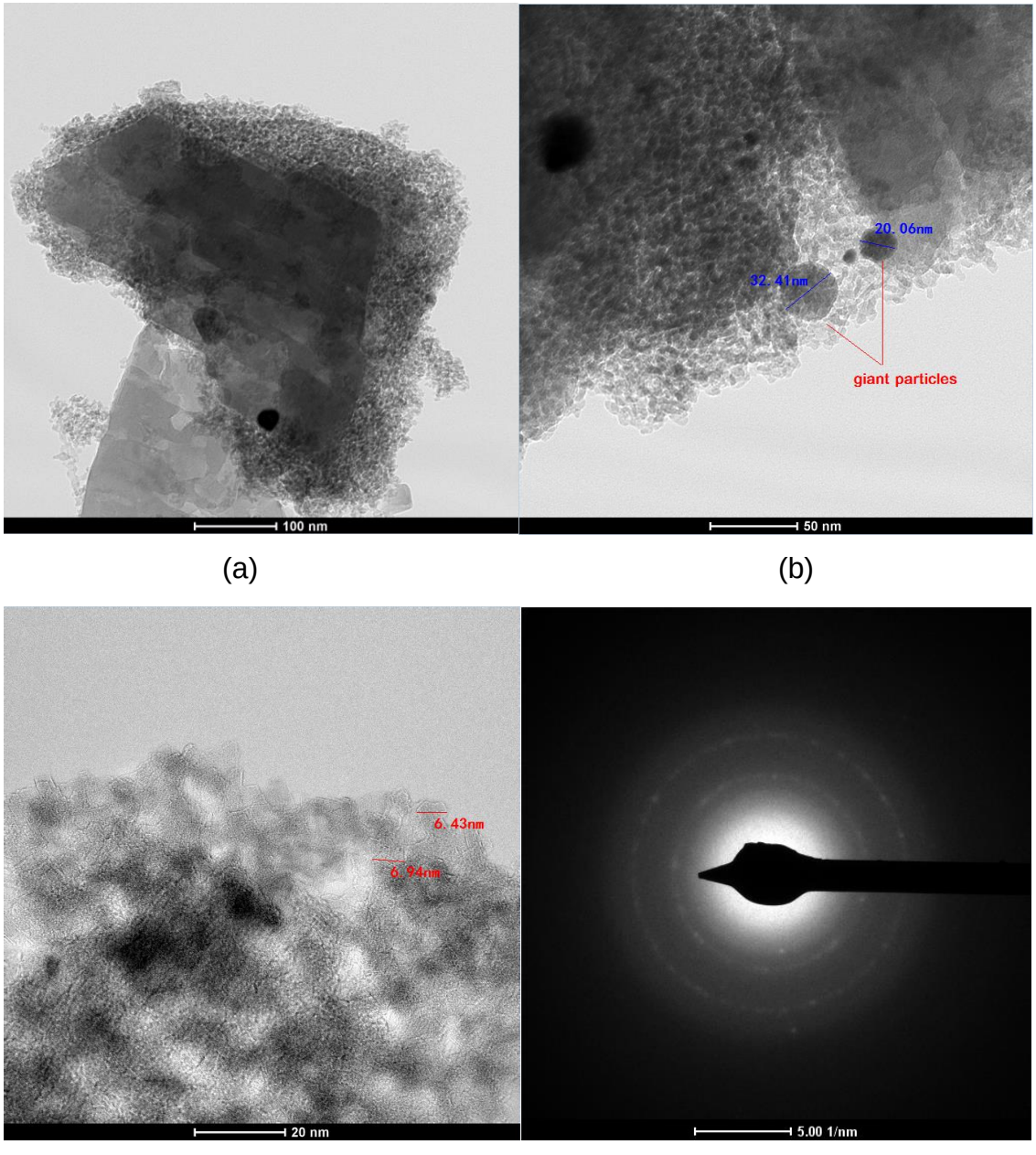

Fig. 8-1 TEM micrographs for the fresh 1%Ni-1%Mo/HZ(25) catalyst at different magnifications: (a) 100 nm; (b) 50 nm; (c) 20 nm and (d) SAED pattern

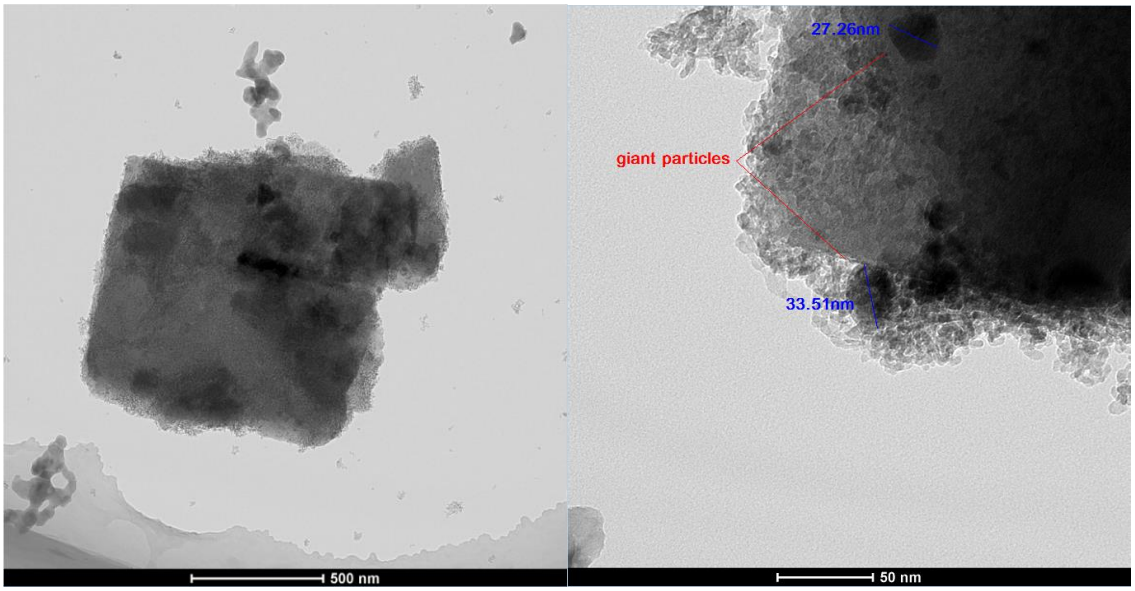

(a) (b)

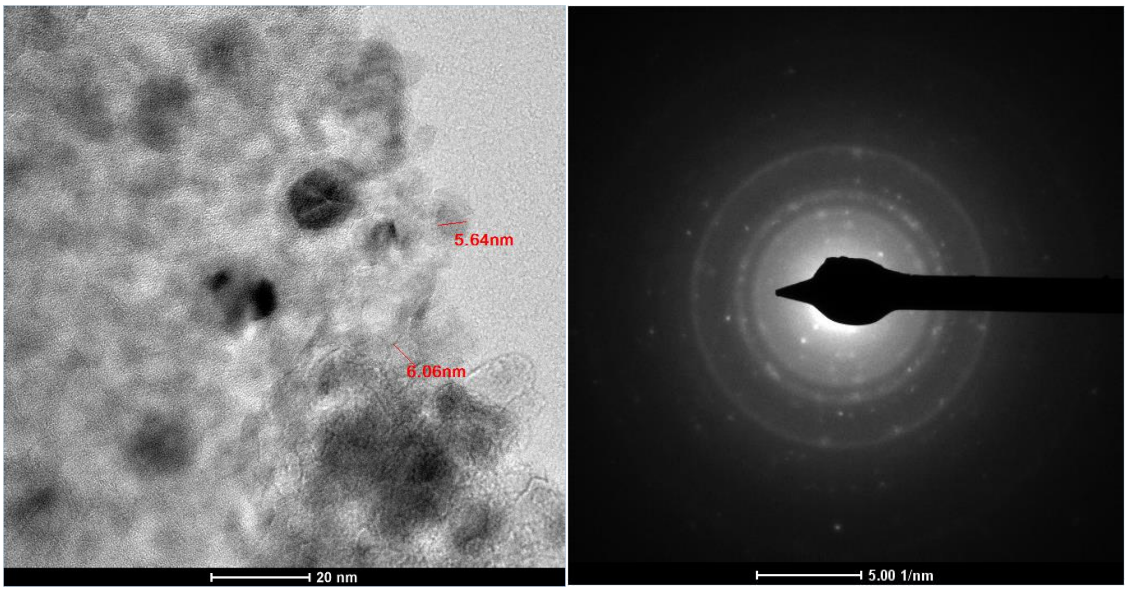

(c) (d)

Fig. 8-2 TEM micrographs for the fresh 1%Ni-1%Fe/HZ(25) catalyst at different magnifications: (a) 500 nm; (b) 50 nm; (c) 20 nm and (d) SAED pattern

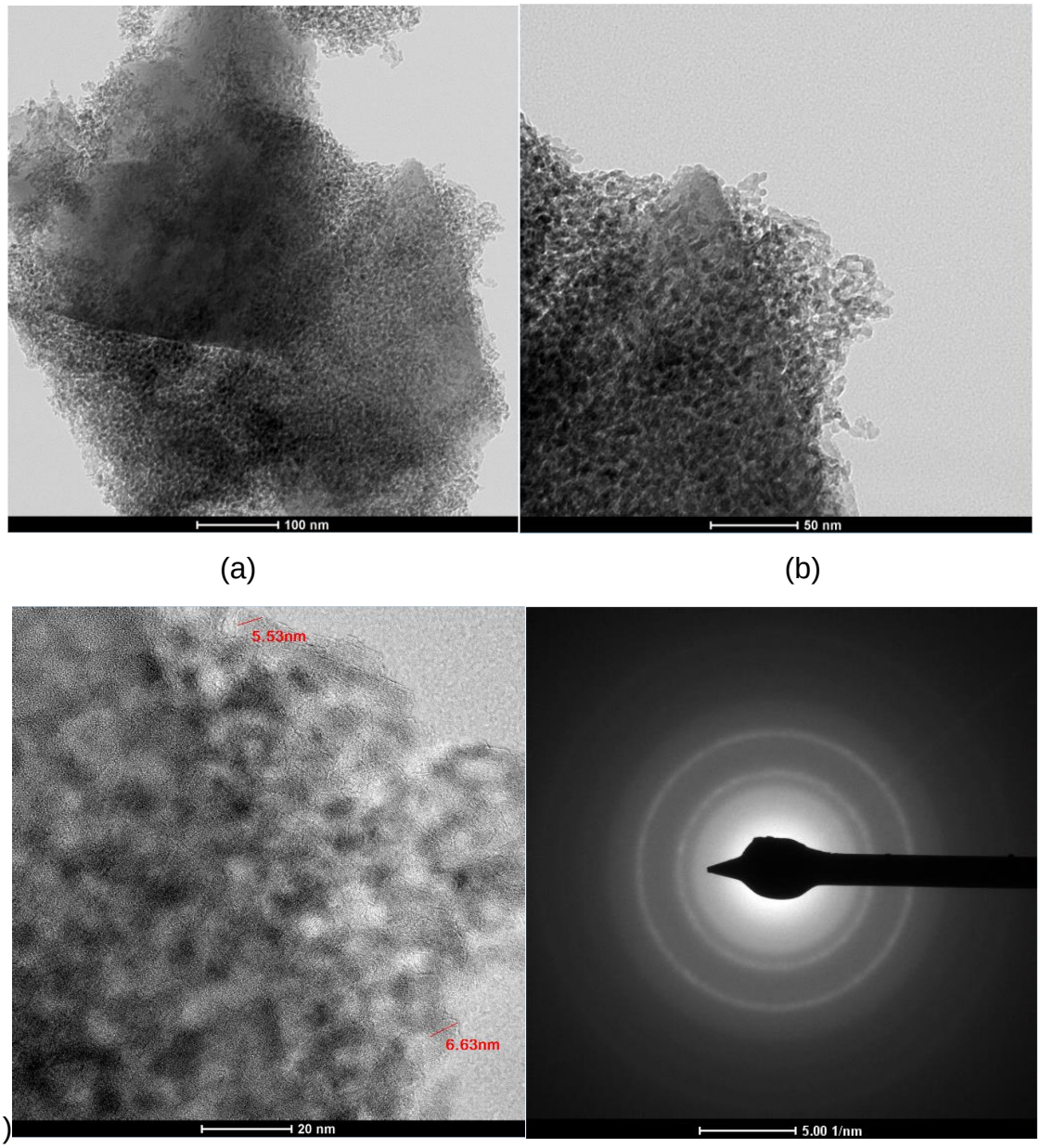

(a) (b)

(c) (d)

Fig. 8-3 TEM micrographs for the fresh 1%Mo-1%Fe/HZ(25) catalyst at different magnifications: (a) 100 nm; (b) 50 nm; (c) 20 nm and (d) SAED pattern

The result reveals that the crystallinity of bi-metal catalysts is less than single metal loading, and this is also confirmed by the weaker diffraction rings in the SEAD patterns. In addition, giant particles (over 20nm) were observed in the fresh catalysts of Ni-Mo and Ni-Fe loaded HZ(25) as shown in the section b of respect **Fig. 8-1** and **Fig. 8-2**, whose formation is probably attributed to the occurrence of

bi-metal agglomeration caused by the high adsorption ability of Ni during the catalyst reduction (Ardiyanti et al., 2012).

EDS tests were used to identify and quantify the main elements present in the surface of the three fresh catalysts (as shown in Appendix **A10** and **Table 8-1**). The signals of O (38.7 - 51.5 wt.%), Al (14.9 - 15.5 wt.%) and Si (30.9 - 43.2 wt.%) are assigned to the support HZSM-5 zeolite.

Table 8-1 Metals loadings on bimetal loaded catalysts detected by EDS

	1%Ni-1%Mo/HZ(25)		1%Ni-1%Fe/HZ(25)		1%Mo-1%Fe/HZ(25)	
Elem	Weight%	Atomic%	Weight%	Atomic%	Weight%	Atomic%
Ni	1.1	0.4	1.3	0.5	-	-
Mo	1.0	0.2	-	-	0.8	0.2
Fe	-	-	1.4	0.5	1.3	0.5

For each of the catalysts, the active metal species of bi-metals were found to be in a concentration around 1wt.% (based on the whole catalyst sample) as shown in **Table 8-1**. This is in close agreement with the designed bulk loading rate.

8.2 Effect of the type of bi-metal on deoxygenation reaction

Experiments with 1%Ni-1%Mo/HZ(25), 1%Ni-1%Fe/HZ(25) and 1%Mo-1%Fe/HZ(25) catalysts were carried out at 500°C (Experiments D12, D16 and D17 respectively) to investigate the effect of the bi-metal type on the deoxygenation stage of the decomposition of anisole. The anisole conversion and grouped yields of liquid, gas and solid (carbonaceous deposits) products are shown in **Table 8-2**. The mass of carbonaceous deposit in the spent catalyst was determined by Thermogravimetry (TG) tests. Anisole conversion was 100% for all the three experiments. Products for the experiments primarily consisted of liquid products and carbonaceous deposit, and trace of gaseous products were produced (mainly contained alkanes and olefins, as shown in Appendix **A11**). Regardless of the different bi-metal catalysts used, similar yields of the liquid products (range from 34.5 wt.% to 38.7 wt.%) and the carbonaceous deposit (range from 61.0 wt.% to 63.9 wt.%) were obtained.

Table 8-2 Grouped product yields and product recovery (wt. % of reactant)

No.	Cat /HZ(25)	T (°C)	Conv (%)	Product recovery (%)	Liquid product					Gas	Solid
					Bulk	AHs	BTX	BTX selectivity (%)	Phs		
D11	1%Ni-1%Mo-	400	99.6	100.0	38.8	5.8	4.7	12.3	32.7	0.0	61.1
D12		500		99.8	35.8	33.0	30.0	83.7	2.8	0.1	63.9
D13		600		98.0	21.0	21.0	20.5	97.5	0.0	0.3	76.7
D14	1%Ni-0.5%Mo	500		97.7	31.6	28.8	25.4	80.3	2.8	0.1	66.0
D15	0.5%Ni-1%Mo-	500	100	100.3	33.5	29.9	26.0	77.6	3.6	0.1	66.7
D16	1%Ni-1%Fe-	500		97.6	34.5	27.4	24.3	70.3	7.1	0.3	62.8
D17	1%Mo-1%Fe-	500		100.0	38.7	33.9	30.5	78.9	4.7	0.4	61.0

Fig. 8-4 shows the liquid product distribution obtained from the deoxygenation of anisole over bi-metal/HZ(25) catalysts. Liquid products comprised AHs and Phs. In all cases, AHs mainly consisted of BTX, and Phs included primarily phenol and cresols, in agreement with previously reported results (Bredenberg et al., 1982). Experiment D12 showed high BTX yield of 30.0 wt.% and selectivity of 83.7%; with only 2.8 wt.% of the products being Phs. The experiment D16 led to the lowest AH yield of 27.4 wt.%, with also the lowest BTX yield and selectivity (24.3 wt.% and 70.3% respectively). On the contrary, D16 gave rise to the highest Phs yield of 7.1 wt.%, which was dominantly composed of phenol. D17 yielded the highest amount of AHs (33.9 wt.%), with the BTX yield of 30.5 wt.%. However, it showed a lower BTX selectivity of 78.9 wt.% compared to that obtained in D12.

The yield and selectivity of BTX for experiments D12, D16 and D17 all have been considerably promoted if compared to the results obtained over the non-metal catalyst (see experiment T12 as reported in chapter 6) (Zhang et al., 2016). This result is attributed to an increment in the conversion of Phs towards BTX, and indicates the bi-metals used in the experiments may promote the deoxygenation reactions of Phs. In addition, it is also found that the selectivity of BTX is higher with the Mo-Fe/HZ(25) than that based on non-supported Mo-Fe catalyst in the literature (Rensel et al., 2013), this reflects the important role of acid support in the deoxygenation reaction of anisole decomposition.

When comparing the liquid product distribution obtained over 1%Ni-1%Mo/HZ(25) with those obtained over single metal-based catalysts (experiments of D2 and D7 in Chapter 7), it is observed that the bi-metal catalyst not only retains the high BTX yield achieved over 1%Mo/HZ(25) (experiment D7), but also enhances the BTX selectivity compared that obtained from 1%Ni/HZ(25) (experiment D2). The high yield of BTX results from less formation of carbonaceous deposit (63.9%) compared to the case with sole 1%Ni catalyst (68.0%), and the high BTX selectively led by Ni-Mo bi-metal catalyst compared to the case with sole 1%Mo catalyst is attributed to the less yield of PAH (3.05 wt.% to 5.22 wt.%) in the liquid product besides the improved conversion of Phs. This result confirms the good catalytic activity of Ni-Mo/catalyst resulting from synergistic effect between both active metals in the deoxygenation stage of the decomposition of anisole.

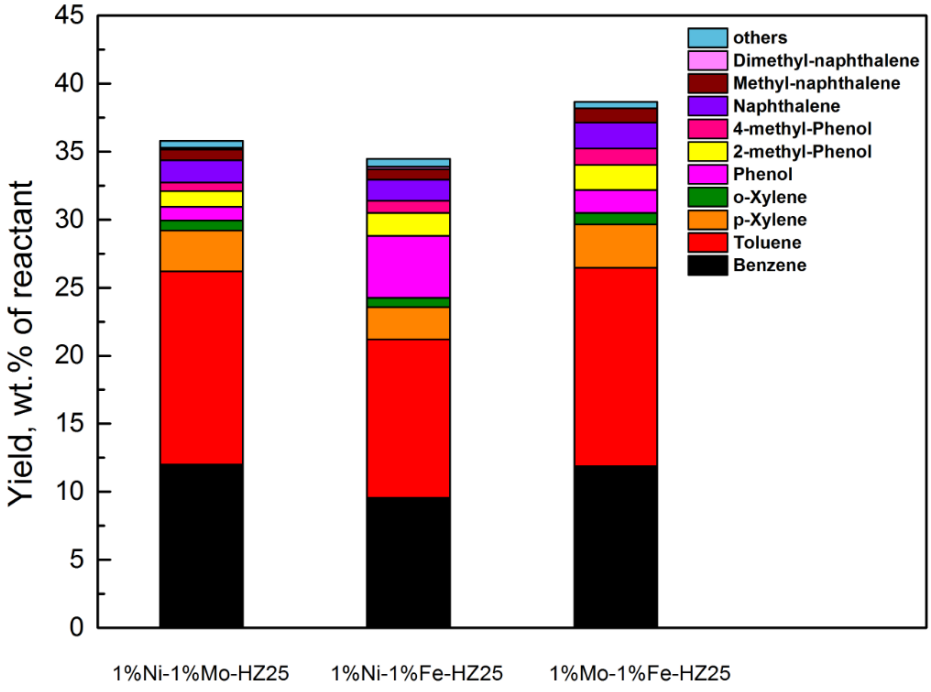

Fig. 8-4 Influence of the type of bi-metal/HZ(25) catalysts on the liquid product yields obtained from deoxygenation reaction. Reaction temperature = 500°C

The addition of Fe to 1%Ni/HZ(25) (results from D16 compared to results from D2) resulted in a decrease in carbonaceous deposits from 68.0 wt.% to 62.8 wt.%. This result implies that Fe may moderate the deactivation of the catalyst by

weakening the high adsorption capability of Ni loading, which agrees with the prediction in respect of adsorption capability in Chapter 5. However, the combination of Fe and Ni (1%Ni-1%Fe/HZ(25), experiment D16) also reduced the BTX yield and selectivity because of the lower conversion of Phs. In the case of D17, the introduction of 1%Fe to 1%Mo loading showed negligible impact on BTX yield and carbonaceous deposit yield and a slight promotion on BTX selectivity compared to D7. The results reveal that 1%Fe would astrict the catalysis activity of Ni and have little improvement effect to 1%Mo.

Among three bi-metals loaded catalyst, 1%Ni-1%Mo exhibits better catalytic activity towards the production of BTX, giving rise to both high yield and selectivity. Consequently, this catalyst has been selected for further investigation on the effect of temperature and metal loadings.

8.3 Effect of temperature on deoxygenation reaction over bi-metal/HZ(25) catalysts

Anisole decomposition over the catalyst of 1%Ni-1%Mo/HZ(25) was performed at 400°C, 500°C, and 600°C (D11, D12, and D13 in **Table 8-2** respectively) to investigate the effect of temperature on the deoxygenation stage. Total conversion of anisole occurred at 400°C, 500°C and 600°C. Liquid and carbonaceous deposits were found to be the main products in this temperature range. The total liquid products yield decreased significantly with temperature from 38.4 wt.% (excluding undecomposed anisole) at 400°C to 21.0 wt.% at 600°C, while the yield of carbonaceous deposits increased correspondingly from 61.1 wt.% at 400°C to 76.7 wt.% at 600°C. Trace gaseous products were produced, and the details are shown in Appendix **A11**.

The change in the liquid product distribution with temperature is specified in **Fig. 8-5**. At 400°C, Phs in the liquid fraction accounted for 32.7 wt.% of the total products and consisted mainly of phenol, ortho-cresol and para-cresol. At the same temperature, the AHs fraction only constituted 5.8 wt.% of the total products, which mainly contained BTX (selectivity of 12.3% in the liquid products), and naphthalene and its derivatives. On the contrary, as explained in Section 8.2, the Phs yield was only 2.8 wt.% and the AHs yield was 33.0 wt.% of the total

product at 500°C, of which BTX accounted for 83.7% in the liquid fraction. In the case of 600°C, no Phs were observed, and the AHs yield was 21.0 wt.%. The AHs fraction contained extremely large proportion of BTX (selectivity of 97.5%), with benzene being the main product. It is observed that mainly transmethylation happened at 400°C and deoxygenation occurred since 500°C, this confirms that the "key temperature" in the decomposition of anisole over the bi-metal based catalysts is the same as that observed in the decomposition over the catalysts of sole HZ(25) (Chapter 6) and single metal/HZ(25) (Chapter 7).

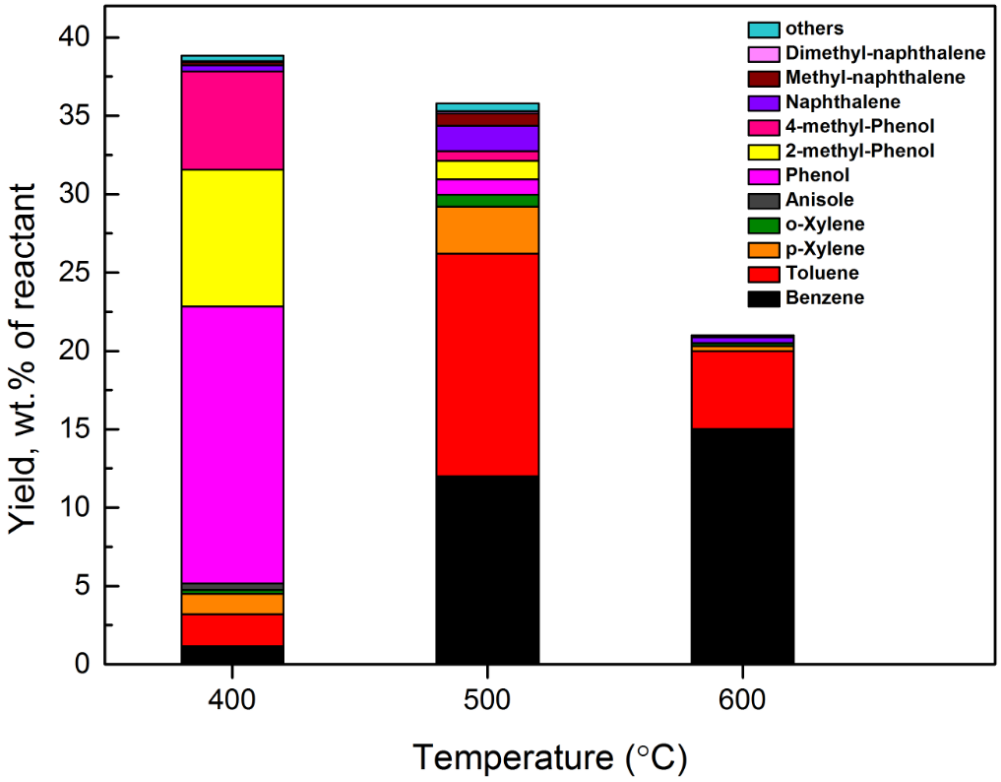

Fig. 8-5 Influence of temperature on the liquid product yields obtained from deoxygenation reaction over 1%Ni-1%Mo/HZ(25).

The results show that an increase in temperature from 400°C to 600°C enhanced carbonaceous deposition, with a simultaneous reduction in the liquid products. This tendency is like that observed during the experiments performed over the single metal based catalysts D1, D2, and D3 (see Chapter 7). It is worth noting that, at 400°C, the conversion of anisole for D11 was higher than that for D1, and more carbonaceous deposits were also produced, 15.9 wt.% higher in the case of D11. However, a different trend is observed at 500°C and 600°C; the yields of

carbonaceous deposit obtained over bi-metal catalysts (D12 and D13) were no more than those obtained over single metal catalyst (D2 and D3). This result implies that the addition of Mo to the Ni-based catalyst not only promotes the overall activity of the catalyst at lower temperatures, it also alleviates the polycondensation reactions leading to carbonaceous deposit at high temperature. In other words, at temperatures higher than the “key temperature”, the use of Ni-Mo based catalyst does not particularly promote polycondensation reactions while giving rise to slightly higher liquid products compared to Ni-based catalyst (by around 4.5 wt.% at 500°C).

As can be seen in **Fig. 8-5**, the effect of temperature on the distribution of liquid products from the catalytic decomposition of anisole is noticeable. The increase in temperature resulted in a rapid decrease of Phs compounds since they are intermediate compounds in the anisole decomposition and are consumed by the deoxygenation reactions and polycondensation reactions (as illustrated in Chapter7). Indeed, no Phs were detected at 600°C. These results are like those obtained from the single metal based experiments (D1-D3). Temperature does have obverse effect on the carbonaceous yield also for bi-metal experiments. The occurrence of polycondensation reactions at higher temperatures also resulted in over 70 wt.% of carbonaceous deposit by the sacrificing liquid yield, meanwhile released hydrogen. At higher temperatures, AHs, particularly PAHs seem to be involved in polycondensation reactions to form carbonaceous deposits. The preferential decrease in PAH from 500 to 600°C simultaneously contributes to a noticeable decrease of the AHs yield of around 10 wt.% and an increase in BTX selectivity (from 83.7% at 500ºC up to 97.5% at 600ºC). This agrees with the observations in Chapter 7. Considering the BTX yield and selectivity values obtained at different temperatures, 500°C is a compromise operating temperature as high Phs conversion is achieved while polycondensation is moderate.

Additionally, the results also confirm the Ni-Mo bi-metal is more favourable in the production of AHs and BTX at the temperature range compared the single 1%Ni based experiments (D1-D3). Even though entire liquid products are decreased at 400°C when 1%Mo introduction, the yields of AHs and BTX show slightly rise due

to the higher conversion of Phs, and the BTX selectivity for D11 is 5% more than that for D1. At 500°C, both AHs and BTX yields of D12 are higher compared to D2 by 4.2 wt.% and 4.4 wt.% respectively, and the BTX selectivity of D12 is even higher than that of D2 as aforementioned. There is not much difference in respect to the liquid products distributions at 600°C except a slight increase of the yields of BTX, this result implies the effect of the introduction of 1%Mo has been completely hindered by the severe polycondensation at such temperature, which is evidenced by the dominant selectivity of benzene at 600°C.

8.4 Effect of metal loading ratio on deoxygenation reaction over bi-metal/HZ(25) catalysts

Experiments of anisole decomposition over the catalysts of 1%Ni-1%Mo/HZ(25) (D12), 1%Ni-0.5%Mo/HZ/25 (D14) and 0.5%Ni-1%Mo/HZ(25) (D15) at 500°C to investigate the effect of metal loading ratio on the deoxygenation reaction. As shown in **Table 8-2**, anisole was completely converted in all the cases, and the three catalysts exhibited similar grouped product yields (from 63.9 wt.% to 66.7 wt.% for carbonaceous deposits, and from 31.6 wt.% to 35.8 wt.% for liquid products). Gaseous products were negligible (as shown in Appendix **A11**). The influence of the metal loading on the liquid product distribution is depicted in **Fig. 8-6**.

The composition of liquid fraction exhibited little variation for the three experiments, and mainly consisted of BTX, phenol, cresols, naphthalene, methyl naphthalene and trace of phenanthrene. In the cases of D14 and D15, the yields of AHs and BTX were lower than those obtained from D12. When the loading of Mo was reduced from 1% to 0.5% (experiment D14), both AHs and BTX yields exhibited a decrease around 4.5 wt.% while the yield of carbonaceous deposit increased in 2.1 wt.%. However, no change was observed in the yield of Phs. This result confirms the ability of Mo to retain liquid products especially AHs by relieving polycondensation reactions, in line with the conclusion obtained in Chapter 7. It is also observed that BTX selectivity only had a slight decrease when the Mo loading was reduced, implying 0.5%Mo may still have good synergistic

effect with Ni in assisting promoting the BTX selectivity. The synergistic effect of Mo was discussed in Section 8.2 when comparing experiments D12 and D2.

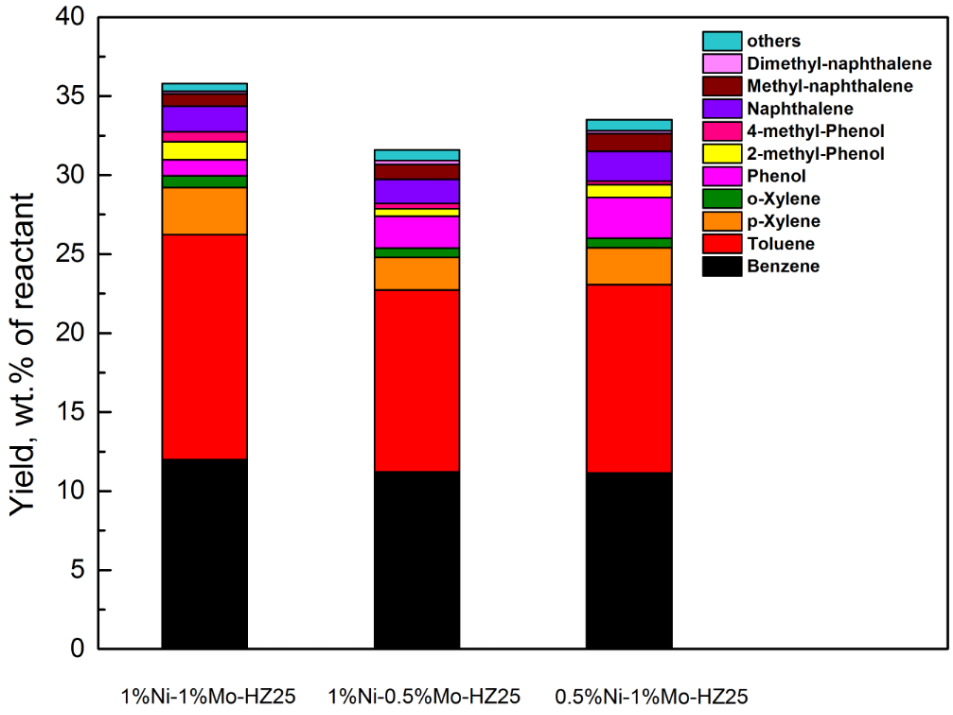

Fig. 8-6 Influence of metal loading ratio on the liquid product yields obtained from deoxygenation reaction over Ni-Mo/HZ(25) catalysts. Reaction temperature = 500°C

When the loading of Ni was decreased from 1%Ni to 0.5%Ni (experiments D12 and D15, respectively), the yield of AHs was slightly decreased by around 3 wt.%, and the yield and selectivity of BTX showed a moderate decrease of around respective 4 wt.% and 6 wt.%, which is due to the rise of the yields for both Phs and PAH compounds, as well as more yield of carbonaceous deposit. The results reflect the key role of Ni in promoting BTX selectivity by converting more Phs to mono AHs in the deoxygenation reactions. Besides, the decrease of BTX yield in D15 compared to D12 also implies the synergistic effect of 1%Ni in assisting Mo to promote the yield of BTX. When comparing the distribution of products obtained from D15 and D7 (1%Mo/HZ(25), **Table 7-2** in chapter7), it can be found that the addition of 0.5%Ni almost did not promote the BTX selectivity by converting more Phs; although, the yields of AHs and BTX decreased in favour of more carbonaceous deposits. The results indicate that the addition of 0.5%Ni

to 1%Mo/HZ(25) is actually detrimental to the performance of the catalyst because polycondensation is promoted by the addition of Ni. However, with the addition of 1%Ni to 1%Mo/HZ(25), despite the fact that the amount of carbonaceous deposit is also higher than that obtained over single Mo (D12 compared to D7), the presence of 1%Ni promoted the deoxygenation of Phs and the BTX selectivity. This result implies that the Ni/Mo ratio of the catalyst is not trivial but determines the synergistic effect between both active metals.

8.5 Characterization of spent bimetal catalyst

Carbonaceous deposit on the surface of the spent 1%Ni-1%Mo/HZ(25) catalyst from experiment D12 were characterized by TEM-EDS. TEM micrographs are shown in **Fig. 8-7**.

Cloud-shaped carbonaceous deposits were observed in **Fig 8.7**(a) and (b), covering the metal particles, which were almost non-visible in most area. Nevertheless, it is found that no further agglomeration of particles was observed compared to the fresh catalyst. High magnification micrograph of the spent catalyst is shown in **Fig. 8-7**(c); like what was observed in the case of the spent catalyst of single metal based HZ(25) (see **Fig. 7-10** and **Fig. 7-11** in Chapter 7), the carbonaceous deposit exhibited amorphous nature, which is further confirmed by the absence of diffraction rings in the FFT image in **Fig. 8-7**(d).

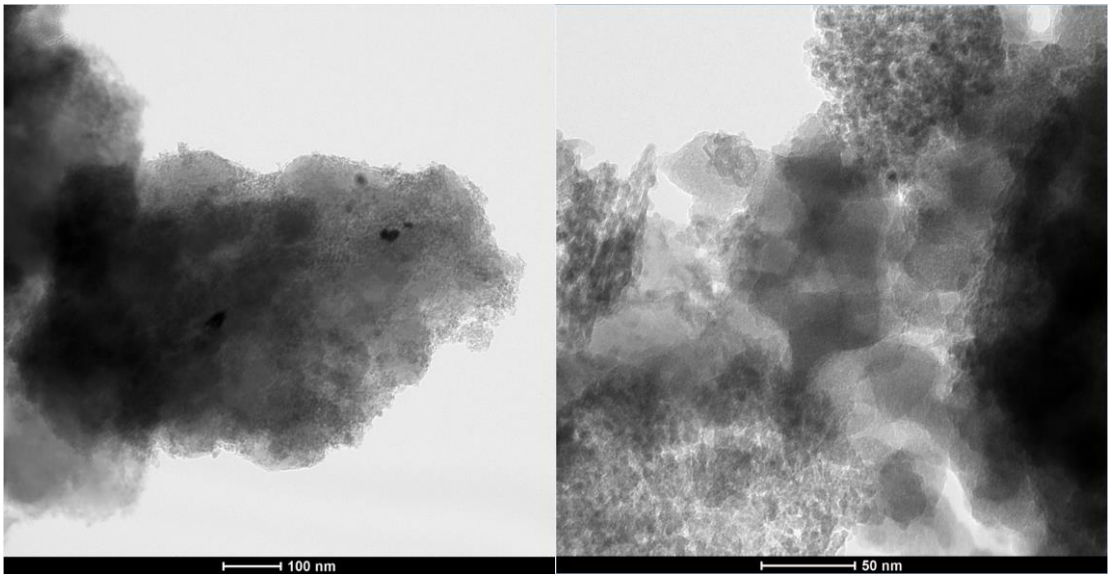

(a) (b)

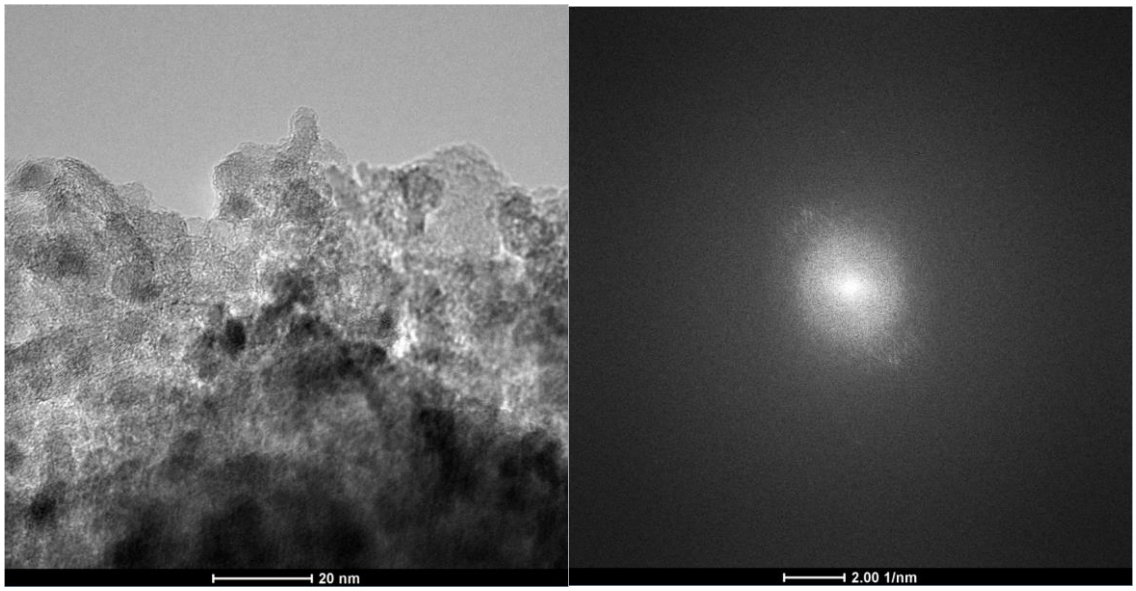

(c) (d)

Fig. 8-7 TEM micrographs for the spent catalysts of 1%Ni-1%Mo/HZ(25) after experiment D12: (a) 100 nm; (b) 50 nm; (c) 20 nm and (d) FFT image

EDS was used to identify the main elements present in the surface of the spent catalyst, as shown in Appendix **A12**. The key elements including the carbonaceous deposit are shown in **Table 8-3**.

Table 8-3 Carbon deposit on spent 1%Ni-1%Mo/HZ(25) catalyst detected by EDS

	Spent 1%Ni-1%Mo/HZ(25)	
Elem	Weight%	Atomic%
C	10.2	15.9
O	48.1	56.5
Ni	0.6	0.2
Mo	1.0	0.2

The signals of Al (14.7 wt.%) and Si (25.5 wt.%) assigned to the support HZSM-5 zeolite are excluded in **Table 8-3**. As can be seen, carbon element in the spent catalysts corresponded to around 10 wt.% accounting for the weight of unit catalyst. It should be noticed that part of the oxygen element identified in the analyses might be involved in the carbonaceous deposit, and the technique is not able to distinguish them from the zeolite structure oxygen.

The results of TEM-EDS show that the bimetal based catalyst is significantly deactivated after the reaction, and most surface area is covered by the species that mainly consists of amorphous carbonaceous deposit.

8.6 Summary

In this chapter, experiments of anisole decomposition were carried out over bi-metal bi-metals loaded HZ(25). The experimental results showed that Ni-Mo bi-metal could combine the positive effects of respective Ni and Mo by maintaining the high yield of BTX for 30 wt.% while promoting the its selectivity to 83.7%. Fe showed negative effect as part of the bi-metal in promoting the BTX yield and selectivity in the decomposition of anisole, even though it was active in relieving the deactivation of catalyst by weakening polycondensation effect caused by Ni loading. Temperature exhibited significant promotion effect in the deoxygenation reactions over Ni-Mo bi-metal based catalyst, giving rise to higher selectivity of BTX with temperature increase. However, much severer polycondensation of both Phs and AHs could also be caused at higher temperature. 500°C was found to be a compromise temperature for the BTX production in the deoxygenation reactions attributed to a balance between achieving good catalyst performance and moderate polycondensation. Experiments on loading ratio variation of respective Ni and Mo to the bi-metal of Ni-Mo further confirmed Ni promoted the conversion towards BTX, hence increasing its selectivity, and Mo enhanced the total yield of liquid products especially AHs by relieving polycondensation. Besides, 1%Ni and 1%Mo showed synergistic effect in achieving both the highest yield and selectivity of BTX in the deoxygenation reactions. The TEM tests to fresh catalysts showed the microcrystal particles of the bi-metal loadings had fuzzy boundaries and readily agglomerated during the reduction. Further EDS tests confirmed the bi-metal loadings were in accord with the designed loading ratio of 1 wt.%. TEM-EDS test of the spent 1%Ni-%Mo/HZ(25) showed evidence of amorphous carbon deposited after the reaction.

9 Conclusion

This chapter includes the conclusions drawn from the key results obtained in this thesis, and provides recommendations and outlooks for future work.

9.1 Summary of key results

The scope of the research in this thesis is within the catalytic decomposition of anisole, and it primarily comprised investigations on transmethylation reactions, deoxygenation reactions over both single metal based bi-functional catalyst and bi-metal based bi-functional catalyst. Methodology included DFT modelling, molecular modelling and experiments.

9.1.1 Transmethylation

For the study on transmethylation, the molecule analysis results indicated that methyl free radical transfer happened in the absence of catalyst, and the catalytic transmethylation over Brønsted acid sites was considered based on the dual electrophilic attack mechanism with protonation and carbocation substitution respectively. Molecule analysis also showed that the ortho- and para- positions of the acceptor phenolic compounds exhibited greater reactivity in both the non-catalytic and catalytic transmethylation. Reactions modelling for the formation of methyl containing compounds in both non-catalytic and catalytic anisole decomposition indicated that the energy barriers were significantly decreased in the presence of catalyst by most 60 kcal/mol in the case of o-cresol. The results also revealed that the intrinsic transmethylation orientation preferred the ortho- and para-positions on the acceptor compounds contained oxygen-rich substituents due to its large electronegativity, and the lowest energy barrier was observed in the case of transmethylation towards the para-position of the cresol molecule (54.1 kcal/mol).

Experimental results confirmed that methyl phenols were the main products for both non-catalytic and acid catalytic transmethylation, with the yield of o-cresol being higher than that of p-cresol at the temperatures below 600°C. The transmethylation reaction over HZSM-5 zeolite catalyst was found to occur at

temperatures 150°C lower than those for non-catalytic reaction, with the yield of the phenolic compounds being promoted by 2.5 times. Production of the main phenolic compounds during the catalytic decomposition of anisole was enhanced to different extents depending on the Si/Al ratio. The highest yield of 79 wt.% was achieved over the zeolite catalyst with a Si/Al ratio of 80. The Brønsted acid sites of the catalyst played a significant role in both the preferential formation of phenolic compounds and preservation of the methyl group.

9.1.2 Deoxygenation reactions over single metal based bi-functional catalyst

For the study on deoxygenation, modelling results revealed that Ni and Mo loaded HZ(25) showed adsorption capacities for respect 3.28/cell and 3.45/cell at 600°C and 101kPa in the adsorption of anisole molecule, which were larger compared to Co and Cu. Mechanism analysis results showed that deoxygenation over bi-functional catalysts was dominated by the protonation on the hydroxyl group of Phs, and metals active sites facilitated the protonation by developing strong interaction with the adsorbed reactant, and they also promoted reactants adsorption and dissociated hydrogen. Reactions modelling revealed that active metals had significant effects in lowering energy barriers of the reactions for all the Phs, and Ni/HZ and Mo/HZ catalysts showed the best catalytic effect on the deoxygenation for most Phs.

Characterization of fresh bi-functional catalysts showed that each metal loading existed as micro polycrystalline ranging in 4-10 nm on the fresh catalyst, and showing strong interaction with the HZ(25) support. Experimental results revealed that both temperature rise and addition of metal loading promoted the production of BTX in the decomposition of anisole, but they also increased the yield of carbonaceous deposit at the expense of both Phs and AHs. Compared to non-metal loading HZ(25), Ni loading converted more Phs to mono AHs and promoted BTX selectivity most by 43.4%, and Mo presented the best catalytic activity towards total AHs yield and promoted the BTX yield most by 27.1%. Experiments results also showed that 1 wt.% was the optimum loading ratio for both Ni and Mo to obtain the highest BTX yield and selectivity values.

Characterization of the spent catalysts indicated that carbonaceous deposit exhibited amorphous state, and was formed mainly through polycondensation of aromatic compounds during the reaction. The deoxygenation may be completed with the in-situ hydrogen donation from the polycondensation reactions.

9.1.3 Deoxygenation reactions over bi-metal based bi-functional catalyst

Modelling on bi-metal loadings showed that Ni-Mo bi-metal loading declined electrons energy levels most by around 1.5ev in the adsorbate molecule and released the highest adsorption energy, while Ni-Fe and Mo-Fe loadings would lead to more electrons exchange with the adsorbate. All the bi-metals exhibited strong interactions with phenol molecule during the adsorption.

Experimental results showed that 1%Ni-1%Mo/HZ(25) led to both the highest BTX yield for 30.0 wt.% and selectivity for 83.7% respectively, while Fe was less effective as part of the bi-metal in promoting the BTX production. 500°C was the optimum temperature for BTX production over 1%Ni-1%Mo/HZ(25) catalysts. Experiments with various loading ratios of bi-metal based catalysts confirmed the distinct characteristic of respective Ni and Mo loading, and 1 wt.% loading of both Ni and Mo exhibited the best synergistic effect of the bi-metals on deoxygenation in the decomposition of anisole.

9.2 Contributions to knowledge

The research in this thesis provided detailed mechanism and reaction pathways for the catalytic methoxyl group decomposition, and linked the characteristics of various types of catalysts to the desirable products formation. Besides, a systematic method with multi-approaches has been established for the investigation of analogues reactions.

9.3 Recommendations and Future work

Even though numerous previous research as well as the study in this thesis have been implemented for gaining understanding of the thermal decomposition of lignin-derived methoxy compounds, their catalytic conversion for fuel production

is still at the early stage of investigation, and more efforts should be made in the future towards following scientific challenges and questions:

(1) Polycondensation as a potential hydrogen donor in the reactions also gives rise to high yield of carbonaceous deposit, so that severely inhibits the liquid production especially in the presence of metal based catalysts. Further investigation regarding its formation mechanism is essential to regulate and design novel catalyst for higher liquid production. Besides, co-feeding with water or hydrogen donors should be considered for alleviating the polycondensation.

(2) More metals especially bi-metal loadings and acid zeolites with proper pore size and acidity should be investigated for the catalytic reforming of methoxy compounds.

(3) The investigation of anisole decomposition in this thesis could be expanded to more complex model compounds that have additional functional groups other than the unique methoxy group in the molecule (e.g. guaiacol and syringol etc.), and gradually to a mixture of the complex compounds for gaining more understanding to the methoxyl group decomposition in real catalytic reforming of lignin derived bio-oil.

(4) Full process modelling of methoxy compounds decomposition including adsorption, reaction and desorption at quantum level in large catalyst systems should be considered when adequate computing power is developed.

(5) Finally, it would also be interesting to investigate the effects of a wide range of reaction conditions, for example pressure, on the catalyst performance in the decomposition of methoxy compounds.

REFERENCES

Abdullah, A. et al. (2004) ‘Modeling of the deactivation kinetics for the combustion of ethyl acetate and benzene present in the air stream over ZSM-5 catalyst loaded with chromium’, *Chemical Engineering Journal*, 99(2), pp. 161–168.

Adam, J. et al. (2006) ‘In situ catalytic upgrading of biomass derived fast pyrolysis vapours in a fixed bed reactor using mesoporous materials’, *Microporous and Mesoporous Materials*, 96(1–3), pp. 93–101.

Adjaye, J.D. and Bakhshi, N.N. (1995) ‘Catalytic conversion of a biomass-derived oil to fuels and chemicals I: Model compound studies and reaction pathways’, *Biomass & bioenergy*, 8(3), pp. 131–149.

Albers, P. et al. (1998) ‘SIMS/XPS Study on the Deactivation and Reactivation of B-MFI Catalysts Used in the Vapour-Phase Beckmann Rearrangement’, *Journal of Catalysis*, 176(2), pp. 561–568.

Alonso, D.M. et al. (2010) ‘Catalytic conversion of biomass to biofuels’, *Green Chemistry*, 12(October), pp. 1493–1513.

Alonso, D.M. et al. (2012) ‘Bimetallic catalysts for upgrading of biomass to fuels and chemicals’, *Chemical Society Reviews*, 41(24), p. 8075.

Andzelm, J. et al. (1989) ‘Spin Density Functional Approach to the Chemistry of Transition Metal Clusters’, in *Gaussian-Type Orbital Implementation*. American Chemical Society, pp. 228–245.

Anex, R.P. et al. (2010) ‘Techno-economic comparison of biomass-to-transportation fuels via pyrolysis, gasification, and biochemical pathways’, *Fuel*, 89(0), pp. S29–S35.

Ardiyanti, A.R. et al. (2012) ‘Catalytic hydrotreatment of fast-pyrolysis oil using non-sulfided bimetallic Ni-Cu catalysts on a δ-Al2O3 support’, *Applied Catalysis B: Environmental*, 117–118, pp. 105–117.

Ashcroft, N.W. and N D Mermin (1976) *Solid state physics*. Philadelphia.

Ballarini, N. et al. (2007) ‘The transformations involving methanol in the acid- and base-catalyzed gas-phase methylation of phenol’, *Journal of Catalysis*, 251(2), pp. 423–436.

Baraban, J.H. et al. (2015) ‘Spectroscopic characterization of isomerization transition states’, *Science*, 350(6266), pp. 1338–1342.

Barber, M. et al. (1973) ‘High energy photoelectron spectroscopy of transition metal complexes. Part 2.—Metallocenes’, *Journal of the Chemical Society, Faraday Transactions 2: Molecular and Chemical Physics*, 69, pp. 559–562.

Barry, E.F. and Grob, R.L. (2004) *Modern practice of gas chromatography*. New York: Wiley-Interscience.

Barta, K. et al. (2010) ‘Catalytic disassembly of an organosolv lignin via hydrogen transfer from supercritical methanol’, *Green Chemistry*, 12(9), p. 1640.

Beckhoff et al. (2006) *Handbook of Practical X-Ray Fluorescence Analysis*. Springer.

Bhattacharyya, K.G. et al. (2003) ‘Al-MCM-41 catalysed alkylation of phenol with methanol’, *Journal of Molecular Catalysis A: Chemical*, 197(1–2), pp. 255–262.

Blatnik, M.T. (2013) *Optimization of mixing in a simulated biomass bed reactor with a center feeding tube*. US: University of Massachusetts Amherst.

Boerjan, W. et al. (2003) ‘Lignin Biosynthesis’, *Annual Review of Plant Biology*, 54(1), pp. 519–546.

Van den Bosch, S. et al. (2015) ‘Reductive lignocellulose fractionation into soluble lignin-derived phenolic monomers and dimers and processable carbohydrate pulps’, *Energy Environvironment scicense*, 8(6), pp. 1748–1763.

Bredenberg, J.B.-S. et al. (1982) ‘Hydrogenolysis and hydrocracking of the carbon-oxygen’, *Journal of Catalysis*, 77, pp. 242–247.

Bregolato, M. et al. (2007) ‘Methylation of phenol over high-silica beta zeolite: Effect of zeolite acidity and crystal size on catalyst behaviour’, *Journal of Catalysis*, 245(2), pp. 285–300.

Bridgwater, A.V. (2012) ‘Review of fast pyrolysis of biomass and product upgrading’, *Biomass and Bioenergy*, 38, pp. 68–94.

Bridgwater, A.V. and Cottam, M.-L. (1992) ‘Opportunities for biomass pyrolysis liquids production and upgrading’, *Energy & Fuels*, 6(2), pp. 113–120.

Bridgwater, A.V. and Peacocke, G.V.C. (2000) ‘Fast pyrolysis processes for biomass’, *Renewable & sustainable energy reviews*, 4(1), pp. 1–73.

Broclawik, E. et al. (2006) ‘DFT quantum chemical modeling of the interaction of alkenes with Cu+ sites in zeolites’, *Catalysis Today*, 114(2–3), pp. 162–168.

Broglie, L. De (1924) *Researches on the quantum theory*. Université de Paris (Sorbonne).

Brunauer, S. et al. (1938) ‘Adsorption of Gases in Multimolecular Layers’, *Journal of the American Chemical Society*, 60(2), pp. 309–319.

Budiman, H. et al. (2015) ‘Comparison between GC-TCD and GC-FID for the determination of propane in gas mixture’, *Procedia Chemistry*, 16, pp. 465–472.

Calais, J.L. (1993) ‘Density-functional theory of atoms and molecules. R.G. Parr and W. Yang, Oxford University Press, New York, Oxford, 1989. IX + 333 pp. Price £45.00’, *International Journal of Quantum Chemistry*, 47(1), pp. 101–101.

Carlson, T.R. et al. (2008) ‘Green gasoline by catalytic fast pyrolysis of solid biomass derived compounds.’, *ChemSusChem*, 1(5), pp. 397–400.

Ceperley, D.M. and Alder, B.J. (1980) ‘Ground State of the Electron Gas by a Stochastic Method’, *Physical Review Letters*, 45(7), pp. 566–569.

Chai, J.W. et al. (2005) ‘Thermal behaviour of ultra-thin Co overlayers on rutile TiO2(100) surface’, *Surface Science*, 589(1–3), pp. 32–41.

Chang, C.D. (1984) ‘Methanol Conversion to Light Olefins’, *Catalysis Reviews*, 26(3–4), pp. 323–345.

Chantal, P. et al. (1984) ‘Production of hydrocarbons from aspen poplar pyrolytic oils over H-ZSM5’, *Applied Catalysis*, 10(3), pp. 317–332.

Chantal, P.D. et al. (1985) ‘Reactions of phenolic compounds over HZSM-5’, *Applied Catalysis*, 18(1), pp. 133–145.

Chen, p (1994) *Unimolecular and bimolecular reaction dynamics*.Ng CY et al. (eds.) New York.

Cheng, C. et al. (2017) ‘Methanation of syngas (H2/CO) over the different Ni-based catalysts’, *Fuel*, 189, pp. 419–427.

Chiaramonti, D. et al. (2003) ‘Development of emulsions from biomass pyrolysis liquid and diesel and their use in engines - Part 2: Tests in diesel engines’, *Biomass and Bioenergy*, 25(1), pp. 101–111.

Ciambelli, P. et al. (1995) ‘Lean NOx reduction on Cu-NaY and Cu-HZSM5 zeolites at the spark ignition engine exhaust’, in *Studies in Surface Science and Catalysis*. , pp. 605–617.

Cooper, B.J. and Trimm, D.L. (1980) ‘Carbon Deposition from Propylene on Polycrystalline and Single-Crystal Iron’, *Journal of Catalysis*, 62(1), pp. 35–43.

Corbari, L. et al. (2008) ‘Iron oxide deposits associated with the ectosymbiotic bacteria in the hydrothermal vent shrimp Rimicaris exoculata’, *Biogeosciences*, 5(5), pp. 1295–1310.

Corma, A. et al. (1989) ‘Design of synthetic zeolites as catalysts in organic reactions’, *Applied Catalysis*, 49(1), pp. 109–123.

Cornella, J. et al. (2013) ‘Combined Experimental and Theoretical Study on the Reductive Cleavage of Inert C–O Bonds with Silanes: Ruling out a Classical Ni(0)/Ni(II) Catalytic Couple and Evidence for Ni(I) Intermediates’, *Journal of the American Chemical Society*, 135(5), pp. 1997–2009.

Cornella, J. and Martin, R. (2014) ‘Metal-catalyzed activation of ethers via C – O bond cleavage : a new strategy for molecular diversity’, *Chemical Society Reviews*, 43(July 2013), pp. 8081–8097.

Cui, S. et al. (2013) ‘Effect of Hydrogen Molecule Dissociation on Hydrogen Storage Capacity of Graphene with Metal Atom Decorated’, *Journal of Physical*

Chemistry C, 118, pp. 8–13.

Dagaut, P. (1998) ‘A Comparative Study of the Kinetics of Benzene Formation from Unsaturated C2 to C4 Hydrocarbons’, *Combustion and Flame*, 113(4), pp. 620–623.

Davis, M.E. and Davis, R.J. (2003) ‘Heterogeneous Catalysis’, in *Fundamentals of chemical reaction engineering*. McGraw-Hil. New York, pp. 133–183.

Delley, B. (1990) ‘An all- electron numerical method for solving the local density functional for polyatomic molecules’, *The Journal of Chemical Physics*, 92(1), pp. 508–517.

Delley, B. (2000) ‘From molecules to solids with the DMol3 approach’, *The Journal of Chemical Physics*, 113(18), p. 7756.

Demirbaş, A. (2001) ‘Biomass resource facilities and biomass conversion processing for fuels and chemicals’, *Energy Conversion and Management*, 42(11), pp. 1357–1378.

Domínguez, M. et al. (2010) ‘Fast and efficient hydrogen generation catalyzed by cobalt talc nanolayers dispersed in silica aerogel’, *Journal of Materials Chemistry*, 20(23), p. 4875.

Du, Z. et al. (2013) ‘Production of aromatic hydrocarbons by catalytic pyrolysis of microalgae with zeolites: Catalyst screening in a pyroprobe’, *Bioresource Technology*, 139, pp. 397–401.

Dubnikova, F. and Lifshitz, A. (2002) ‘Ring Expansion in Methylcyclopentadiene Radicals. Quantum Chemical and Kinetics Calculations’, *The Journal of Physical Chemistry A*, 106(35), pp. 8173–8183.

Eigenberger, G. and Ruppel, W. (2012) ‘Catalytic Fixed-Bed Reactors’, in *Ullmann’s Encyclopedia of Industrial Chemistry*. Weinheim, Germany: Wiley-VCH Verlag GmbH & Co. KGaA.

Elanany, M. et al. (2004) ‘Periodic density functional investigation of Bronsted acidity in isomorphously substituted chabazite and AlPO-34 molecular sieves’,

Microporous and mesoporous materials, 71, pp. 51–56.

Ewald, P.P. (1921) 'Die Berechnung optischer und elektrostatischer Gitterpotentiale', *Annalen der Physik*, 369(3), pp. 253–287.

Fermi, E. (1927) 'Un Metodo Statistico per la Determinazione di alcune Prioprietà dell'Atomo', *Rend. Accad. Naz. Lincei*, 6, pp. 602–607.

Ferrari, M. et al. (2001) 'Influences of the Hydrogen Sulfide Partial Pressure and of a Nitrogen Compound on the Hydrodeoxygenation Activity of a CoMo/Carbon Catalyst', *Journal of Catalysis*, 198(1), pp. 47–55.

Florez, E. et al. (2011) 'On the dissociation of molecular hydrogen by Au supported on transition metal carbides: choice of the most active support', *Physical Chemistry Chemical Physics*, 13(15), p. 6865.

Fogler, H.S. (1981) 'Chemical reactors', in *Chemical reactors*. Washington, D.C. : American Chemical Society.

Foster, A.J. et al. (2012) 'Optimizing the aromatic yield and distribution from catalytic fast pyrolysis of biomass over ZSM-5', *Applied Catalysis A: General*, 423–424(0), pp. 154–161.

Friderichsen, A. V. et al. (2001) 'The pyrolysis of anisole (C6H5OCH3) using a hyperthermal nozzle', *Fuel*, 80(12), pp. 1747–1755.

Gao, J. et al. (2014) 'Structure of Mo 2 C x and Mo 4 C x Molybdenum Carbide Nanoparticles and Their Anchoring Sites on ZSM-5 Zeolites', *The Journal of Physical Chemistry C*, 118(9), pp. 4670–4679.

Gao, Y. et al. (2016) 'Effect of the Si/Al ratio on the performance of hierarchical ZSM-5 zeolites for methanol aromatization', *RSC Advances*, 6(87), pp. 83581–83588.

Gavrilov, V.Y. et al. (2010) 'Distribution of copper- and nickel-containing modifier components in the pore space of HZSM-5 zeolite', *Kinetics and Catalysis*, 51(1), pp. 88–97.

Gayubo, A.G. et al. (2004) 'Transformation of Oxygenate Components of

Biomass Pyrolysis Oil on a HZSM-5 Zeolite. II. Aldehydes, Ketones, and Acids', *Industrial & Engineering Chemistry Research*, 43(11), pp. 2619–2626.

Gayubo, A.G. et al. (2010) 'Selective production of olefins from bioethanol on HZSM-5 zeolite catalysts treated with NaOH', *Applied Catalysis B: Environmental*, 97(1–2), pp. 299–306.

Gayubo, A.G. et al. (1996) 'Relationship between Surface Aciditv and Activity of catalysts in the Transforhation of Methanol into Hydrocarbons', *Journal of Chemical Technology and Biotechnology*, 65(2), pp. 186–192.

Geng, Z. et al. (2012) 'Theoretical investigation on pyrolysis mechanism of glycerol', *Fuel*, 93, pp. 92–98.

Gera, D. et al. (1998) 'Computer simulation of bubbles in large-particle fluidized beds', *Powder Technology*, 98, pp. 38–47.

Gevert, B.S. et al. (1987) 'Kinetics of the HDO of methyl-substituted phenols', *Applied Catalysis*, 31(1), pp. 119–131.

Ghampson, I.T. et al. (2017) 'Catalytic hydrodeoxygenation of anisole over Re-MoO x /TiO 2 and Re-VO x /TiO 2 catalysts', *Applied Catalysis B: Environmental*, 208, pp. 60–74.

González-Borja, M.A. and Resasco, D.E. (2011) 'Anisole and Guaiacol Hydrodeoxygenation over Monolithic Pt–Sn Catalysts', *Energy & Fuels*, 25(9), pp. 4155–4162.

González, O. et al. (2009) 'Use of different mesostructured materials based on silica as cobalt supports for the Fischer–Tropsch synthesis', *Catalysis Today*, 148(1–2), pp. 140–147.

Grimme, S. (2006) 'Semiempirical GGA-type density functional constructed with a long-range dispersion correction', *Journal of Computational Chemistry*, 27(15), pp. 1787–1799.

Guisnet, M. and Gilson, J.P. (2002) *Zeolites for Cleaner Technologies*. Imperial College Press.

Hantsche, H. (1993) ‘High resolution XPS of organic polymers, the scienta ESCA300 database. By G. Beamson and D. Briggs, Wiley, Chichester 1992, 295 pp., hardcover, £ 65.00, ISBN 0-471-93592-1’, *Advanced Materials*, 5(10), pp. 778–778.

Haw, J.F. et al. (1989) ‘Reactions of propene on zeolite HY catalyst studied by in situ variable temperature solid-state nuclear magnetic resonance spectroscopy’, *Journal of the American Chemical Society*, 111(6), pp. 2052–2058.

He, J. et al. (2012) ‘Ni-catalyzed cleavage of aryl ethers in the aqueous phase’, *Journal of the American Chemical Society*, 134(51), pp. 20768–20775.

He, M. et al. (2013) ‘Green Carbon Science: Scientific Basis for Integrating Carbon Resource Processing, Utilization, and Recycling’, *Angewandte Chemie International Edition*, 52(37), pp. 9620–9633.

Heisenberg, W. (1927) ‘Über den anschaulichen Inhalt der quantentheoretischen Kinematik und Mechanik’, *Zeitschrift für Physik*, 43(3–4), pp. 172–198.

Hellmann, H.G.A. (1999) ‘*Hans G.A. Hellmann (1903-1938)*’, 1999(1), pp. 10–21.

Hensley, A.J.R. et al. (2014a) ‘Adsorption of guaiacol on Fe (110) and Pd (111) from first principles’, *Surface Science*, 648, pp. 227–235.

Hensley, A.J.R. et al. (2014b) ‘Adsorption of phenol on Fe (110) and Pd (111) from first principles’, *Surface Science*, 630, pp. 244–253.

Hernández, J.M.G. et al. (2012) ‘First principles studies of the graphene-phenol interactions’, *Journal of Molecular Modeling*, 18(8), pp. 3857–3866.

Hirshfeld, F.L. (1977) ‘Bonded-atom fragments for describing molecular charge densities’, *Theoretica Chimica Acta*, 44(2), pp. 129–138.

Hohenberg, P. and Kohn, W. (1964) ‘Inhomogeneous Electron Gas’, *Physical Review*, 136(3B), pp. B864–B871.

Honkela, M.L. et al. (2012) ‘Computational study of the adsorption and dissociation of phenol on Pt and Rh surfaces’, *Physical Chemistry Chemical Physics*, 14(16), p. 5849.

Hoof, D.L. et al. (1973) ‘Studies on metal carboxylates. Part III. Pyridine-2,6-dicarboxylates of the lanthanides. Synthesis and spectral studies and the X-ray photoelectron spectra of several pyridine carboxylate complexes’, *Journal of the Chemical Society, Dalton Transactions*, (2), p. 200.

Horáček, J. et al. (2012) ‘Lignin to liquids over sulfided catalysts’, *Catalysis Today*, 179(1), pp. 191–198.

Horne, P.A. and Williams, P.T. (1996) ‘Reaction of oxygenated biomass pyrolysis model compounds over a ZSM-5 catalyst’, *Renewable Energy*, 7(2), pp. 131–144.

Hua, L. et al. (2014) ‘CFD simulation of solids residence time distribution in a CFB riser’, *Chemical Engineering Science*, 117(0), pp. 264–282.

Huang, Y. et al. (2015) ‘A density functional theory study on ethylene formation and conversion over P modified ZSM-5’, *Catalytic Science Technology*, 5(2), pp. 1093–1105.

Huang, Y. et al. (2014) ‘Density Functional Theory study of the structural and electronic properties of H3PO4/ZSM-5’, *RSC Advances*, 4(28), p. 14573.

Huber, G.W. et al. (2012) ‘Catalytic Fast Pyrolysis of Lignocellulosic Biomass with Bifunctional Ga / ZSM-5 Catalysts Catalysts’, *Angewandte*

Hurff, S.J. and Klein, M.T. (1983) ‘Reaction pathway analysis of thermal and catalytic lignin fragmentation by use of model compounds’, *Industrial & Engineering Chemistry Fundamentals*, 22(1981), pp. 426–430.

Isahak, W.N.R.W. et al. (2012) ‘A review on bio-oil production from biomass by using pyrolysis method’, *Renewable and Sustainable Energy Reviews*, 16(8), pp. 5910–5923.

Ivanova, S. et al. (2007) ‘ZSM-5 coatings on-SiC monoliths: Possible new structured catalyst for the methanol-to-olefins process’, *Journal of Physical Chemistry C*, 111(11), pp. 4368–4374.

J.F.Watts and J.Wolstenholme (2003) *An Introduction to Surface Analysis by*

XPS and AES. Chichester: Wiley & Sons.

Jin, S. et al. (2014) 'Catalytic hydrodeoxygenation of anisole as lignin model compound over supported nickel catalysts', *Catalysis Today*, 234, pp. 125–132.

Johnston, K. et al. (2010) 'Adsorption structures of phenol on the Si(001)-(2*1) surface calculated using density functional theory', *Physical Review B*, 81(23), p. 235428.

Jongerius, A.L. et al. (2012) 'CoMo sulfide-catalyzed hydrodeoxygenation of lignin model compounds: An extended reaction network for the conversion of monomeric and dimeric substrates', *Journal of Catalysis*, 285(1), pp. 315–323.

Jung, K.A. et al. (2015) 'Pyrolytic production of phenolic compounds from the lignin residues of bioethanol processes', *Chemical Engineering Journal*, 259, pp. 107–116.

Kalita, B. and Deka, R.C. (2009) 'DFT study of CO adsorption on neutral and charged Pdn(n = 1-7) clusters', *European Physical Journal D*, 53, pp. 51–58.

Kallury, R. (1985) 'Hydrodeoxygenation of hydroxy, methoxy and methyl phenols with molybdenum oxide/nickel oxide/alumina catalyst', *Journal of Catalysis*, 96(2), pp. 535–543.

Karanjkar, P.U. et al. (2014) 'Production of aromatics by catalytic fast pyrolysis of cellulose in a bubbling fluidized bed reactor', *AIChE Journal*, 60(4), pp. 1320–1335.

Karweik, D.H. and Winograd, N. (1976) 'Nitrogen Charge Distribution in Free-Base Porphyrins, Metalloporphyrins, and their reduced analogues observed by X-ray Photoelectron Spectroscopy', *Inorganic Chemistry*, 15(10), pp. 2336–2342.

Khromova, S.A. et al. (2014) 'Anisole hydrodeoxygenation over Ni–Cu bimetallic catalysts: The effect of Ni/Cu ratio on selectivity', *Applied Catalysis A: General*, 470, pp. 261–270.

Kislitsyn, A. et al. (1972) 'Thermal decomposition of anisole', *Zhurnal Prikladnoi Khimii*, 45(2), p. 384.

Klacar, S. and Grönbeck, H. (2013) ‘H2 dissociation over Ag/Al2O3 : the first step in hydrogen assisted selective catalytic reduction of NOx’, *Catalytic Science Technology*, 3(1), pp. 183–190.

Klein, I. et al. (2015) ‘Lignin depolymerization over Ni/C catalyst in methanol, a continuation: effect of substrate and catalyst loading’, *Catalytic Science Technology*, 5(6), pp. 3242–3245.

Kohn, W. and Sham, L.J. (1965) ‘Self-Consistent Equations Including Exchange and Correlation Effects’, *Physical Review*, 140(4A), pp. A1133–A1138.

Lambert, F.L. (1958) ‘Substituent effects on the benzene ring: A demonstration’, *JOURNAL OF CHEMICAL EDUCATION*, 35(7), pp. 342–343.

Lamprecht, A. et al. (2000) ‘Fuel-rich flame chemistry in low-pressure cyclopentene flames’, *Proceedings of the Combustion Institute*, 28(2), pp. 1817–1824.

Lancefield, C.S. and Westwood, N.J. (2015) ‘The synthesis and analysis of advanced lignin model polymers’, *Green Chemistry*, 17(11), pp. 4980–4990.

Laurent, E. and Delmon, B. (1994) ‘Study of the hydrodeoxygenation of carbonyl, carboxylic and guaiacyl groups over sulfided CoMo/γ-Al2O3 and NiMo/γ-Al2O3 catalyst’, *Applied Catalysis A: General*, 109(1), pp. 97–115.

Leibbrandt, N.H. et al. (2011) ‘Comparing biological and thermochemical processing of sugarcane bagasse: An energy balance perspective’, *Biomass and Bioenergy*, 35(5), pp. 2117–2126.

Levy, M. (1979) ‘Universal variational functionals of electron densities, first-order density matrices, and natural spin-orbitals and solution of the v-representability problem’, *Proceedings of the National Academy of Sciences*, 76(12), pp. 6062–6065.

Li, G. et al. (2014a) ‘Experimental and Theoretical Study on the Pyrolysis Mechanism of Three Coal-Based Model Compounds’, *Energy & Fuels*, 28(2), pp. 980–986.

Li, L. et al. (2004) ‘Study on metal-MFI/cordierite as promising catalysts for selective catalytic reduction of nitric oxide by propane in excess oxygen’, *Journal of Catalysis*, 228(1), pp. 12–22.

Li, X. et al. (2017a) ‘Hydrodeoxygenation of lignin-derived bio-oil using molecular sieves supported metal catalysts: A critical review’, *Renewable and Sustainable Energy Reviews*, 71, pp. 296–308.

Li, X. et al. (2012) ‘Catalytic fast pyrolysis of Kraft lignin with HZSM-5 zeolite for producing aromatic hydrocarbons’, *Frontiers of Environmental Science & Engineering*, 6(3), pp. 295–303.

Li, Y. et al. (2017b) ‘Coke formation on the surface of Ni/HZSM-5 and Ni-Cu/HZSM-5 catalysts during bio-oil hydrodeoxygenation’, *Fuel*, 189, pp. 23–31.

Li, Z.K. et al. (2014b) ‘Alkanolysis simulation of lignite-related model compounds using density functional theory’, *Fuel*, 120, pp. 158–162.

Lifshitz, A. et al. (2005) ‘Decomposition and ring expansion in methylcyclopentadiene: single-pulse shock tube and modeling study’, *Proceedings of the Combustion Institute*, 30(1), pp. 1039–1047.

Lin, C.-Y. and Lin, M.C. (1986) ‘Thermal decomposition of methyl phenyl ether in shock waves: the kinetics of phenoxy radical reactions’, *The Journal of Physical Chemistry*, 90(3), pp. 425–431.

Liu, B.S. et al. (2007) ‘XPS, XAES, and TG/DTA characterization of deposited carbon in methane dehydroaromatization over Ga–Mo/ZSM-5 catalyst’, *Applied Surface Science*, 253(11), pp. 5092–5100.

Liu, C. et al. (2014) ‘Catalytic fast pyrolysis of lignocellulosic biomass’, *Chemical Society Reviews*, 43(9), pp. 7594–7623.

Liu, H. and Xu, Y. (2006) ‘H2-TPR Study on Mo/HZSM-5 Catalyst for CH4 Dehydroaromatization’, *Chinese Journal of Catalysis*, 27(4), pp. 319–323.

Liu, J. et al. (2016) ‘NiO-PTA supported on ZIF-8 as a highly effective catalyst for hydrocracking of Jatropha oil’, *Scientific Reports*, 6, p. 23667.

Liu, W.J. et al. (2015) ‘Thermochemical conversion of lignin to functional materials: a review and future directions’, *Green Chemistry*, 17(11), pp. 4888–4907.

Luk’yanov, D.B. (1992) ‘Effect of SiO2/Al2O3 ratio on the activity of HZSM-5 zeolites in the different steps of methanol conversion to hydrocarbons’, *Zeolites*, 12(3), pp. 287–291.

Lyu, G. et al. (2015) ‘Estimation and Comparison of Bio-Oil Components from Different Pyrolysis Conditions’, *Frontiers in Energy Research*, 3, pp. 1–11.

Ma, Z. et al. (2012) ‘Controlling the selectivity to chemicals from lignin via catalytic fast pyrolysis’, *Applied Catalysis A: General*, 423–424, pp. 130–136.

Mackie, C. et al. (1989) ‘Kinetics of the thermal decomposition of methoxybenzene(anisole)’, *Journal of Physical Chemistry C*, 93(2) Cambridge, pp. 664–670.

Martínez, A. and Peris, E. (2016) ‘Non-oxidative methane dehydroaromatization on Mo/HZSM-5 catalysts: Tuning the acidic and catalytic properties through partial exchange of zeolite protons with alkali and alkaline-earth cations’, *Applied Catalysis A: General*, 515, pp. 32–44.

Martínez, A. et al. (2003) ‘Fischer–Tropsch synthesis of hydrocarbons over mesoporous Co/SBA-15 catalysts: the influence of metal loading, cobalt precursor, and promoters’, *Journal of Catalysis*, 220(2), pp. 486–499.

Marx, D. and Hutter, J. (2000) *Ab initio molecular dynamics: Theory and implementation*.

Massoth, F.E. et al. (2006) ‘Catalytic Hydrodeoxygenation of Methyl-Substituted Phenols: Correlations of Kinetic Parameters with Molecular Properties’, *The Journal of Physical Chemistry B*, 110(29), pp. 14283–14291.

Max Born (1954) *The Nobel Prize in Physics 1954*.

Mellin, P. et al. (2015) ‘Comprehensive Secondary Pyrolysis in Fluidized-bed Fast Pyrolysis of Biomass, a Fluid Dynamics Based Modelling Effort’, *Energy*

Procedia, 66, pp. 281–284.

Meng, Q. et al. (2015) 'Efficient Transformation of Anisole into Methylated Phenols over High-Silica HY Zeolites under Mild Conditions', *ChemCatChem*, 7(18), pp. 2831–2835.

Metropolis, N. et al. (1953) 'Equation of State Calculations by Fast Computing Machines', *The Journal of Chemical Physics*, 21(6), pp. 1087–1092.

Miller, J.A. and Melius, C.F. (1992) 'Kinetic and thermodynamic issues in the formation of aromatic compounds in flames of aliphatic fuels', *Combustion and Flame*, 91(1), pp. 21–39.

Mo, J.J. et al. (2013) 'Quantum chemical studies on adsorption of CO2 on nitrogen-containing molecular segment models of coal', *Surface Science*, 616, pp. 85–92.

Moretti, G. et al. (1989) 'Characterization of CuO-ZnO catalysts by X-ray photoelectron spectroscopy: Precursors, calcined and reduced samples', *Surface and Interface Analysis*, 14(6–7), pp. 325–336.

Mu, W. et al. (2013) 'Lignin Pyrolysis Components and Upgrading-Technology Review', *Bioenergy Research*, 6(4), pp. 1183–1204.

Mukarakate, C. et al. (2015) 'Catalytic fast pyrolysis of biomass: the reactions of water and aromatic intermediates produces phenols', *Green Chemistry*, 17(8), pp. 4217–4227.

Mukarakate, C. et al. (2014) 'Real-time monitoring of the deactivation of HZSM-5 during upgrading of pine pyrolysis vapors', *Green Chemistry*, 16(3), p. 1444.

Mukundan, S. et al. (2015) 'Guaiacol hydrodeoxygenation reaction catalyzed by highly dispersed, single layered MoS 2/C', *Catalytic Science Technology*, 5(9), pp. 4422–4432.

Mulcahy, M.F.R. et al. (1967) 'Reactions of free radicals with aromatic compounds in the gaseous phase. III. Kinetics of the reaction of methyl radicals with anisole (methoxybenzene)', *Australian Journal of Chemistry*, 20(6), pp.

1155–1171.

Mulcahy, M.F.R. and Williams, D.J. (1965) ‘Reactions of free radicals with aromatic compounds in the gaseous phase. II. Kinetics of the reaction of methyl radicals with phenol’, *Australian Journal of Chemistry*, 18(1), pp. 20–38.

Munson, E.J. et al. (1993) ‘In situ nuclear magnetic resonance study of allyl alcohol conversion on zeolites: evidence for an allyl cation intermediate’, *Journal of the Chemical Society, Chemical Communications*, (6 66), pp. 75–76.

Nie, L. et al. (2014) ‘Selective conversion of m-cresol to toluene over bimetallic Ni-Fe catalysts’, *Journal of Molecular Catalysis A: Chemical*, 388–389, pp. 47–55.

Nie, R. et al. (2012) ‘Core–shell structured CuO–ZnO@H-ZSM-5 catalysts for CO hydrogenation to dimethyl ether’, *Fuel*, 96, pp. 419–425.

Ochoa-Hernández, C. et al. (2013) ‘Hydrocarbons production through hydrotreating of methyl esters over Ni and Co supported on SBA-15 and Al-SBA-15’, *Catalysis Today*, 210, pp. 81–88.

Odebunmi, E. (1983) ‘Catalytic hydrodeoxygenation I. Conversions of o-, p-, and m-cresols’, *Journal of Catalysis*, 80(1), pp. 56–64.

Ohta, H. et al. (2011) ‘Hydrodeoxygenation of phenols as lignin models under acid-free conditions with carbon-supported platinum catalysts’, *Chemical Communications*, 47(44), p. 12209.

Özdemir, E. et al. (2014) ‘Catalytic Conversion of a Mesitylene and n -Decane Mixture in the Presence of Hydrogen Over ZSM-5 Based Catalysts’, *Petroleum Science and Technology*, 32(13), pp. 1598–1606.

Paasikallio, V. et al. (2013) ‘Catalytic pyrolysis of forest thinnings with ZSM-5 catalysts: Effect of reaction temperature on bio-oil physical properties and chemical composition’, *Energy and Fuels*, 27, pp. 7587–7601.

Pan, C. et al. (2006) ‘An efficient method to synthesize benzofurans and naphthofurans’, *Synlett*, 3(11), pp. 1657–1662.

Papadikis, K. et al. (2009) ‘CFD modelling of the fast pyrolysis of biomass in fluidised bed reactors. Part B. Heat, momentum and mass transport in bubbling fluidised beds’, *Chemical Engineering Science*, 64(5), pp. 1036–1045.

Parrott, E.P.J. et al. (2009) ‘Understanding the Dielectric Properties of Heat-Treated Carbon Nanofibers at Terahertz Frequencies: a New Perspective on the Catalytic Activity of Structured Carbonaceous Materials’, *The Journal of Physical Chemistry C*, 113(24), pp. 10554–10559.

Payne, M.C. et al. (1992) ‘Iterative minimization techniques for ab initio total-energy calculations: molecular dynamics and conjugate gradients’, *Reviews of Modern Physics*, 64(4), pp. 1045–1097.

Peköz, R. and Donadio, D. (2016) ‘Effect of van der Waals interactions on the chemisorption and physisorption of phenol and phenoxy on metal surfaces’, *The Journal of Chemical Physics*, 145(10), p. 104701.

Perdew, J.P. et al. (1996) ‘Generalized Gradient Approximation Made Simple’, *Physical Review Letters*, 77(18), pp. 3865–3868.

Perdew, J.P. et al. (1992) ‘Atoms, molecules, solids, and surfaces: Applications of the generalized gradient approximation for exchange and correlation’, *Physical Review B*, 46(11), pp. 6671–6687.

Phuong, T. (1986) ‘Competitive hydrogenation of benzene and toluene on group VIII metals: Correlation with the electronic structure’, *Journal of Catalysis*, 102(2), pp. 456–459.

Pichaikaran, S. and Arumugam, P. (2016) ‘Vapour phase hydrodeoxygenation of anisole over ruthenium and nickel supported mesoporous aluminosilicate’, *Green Chemistry*, 18(9), pp. 2888–2899.

Prasomsri, T. et al. (2011) ‘Catalytic conversion of anisole over HY and HZSM-5 zeolites in the presence of different hydrocarbon mixtures’, *Applied Catalysis B: Environmental*, 106(1–2), pp. 204–211.

De Proft, F. et al. (1993) ‘Ab initio determination of substituent constants in a

density functional theory formalism: calculation of intrinsic group electronegativity, hardness, and softness', *The Journal of Physical Chemistry*, 97(9), pp. 1826–1831.

Qu, S. et al. (2011) 'Catalytic Cracking of Supercritical n -Dodecane over Wall-Coated HZSM-5 with Different Si/Al Ratios', *Energy & Fuels*, 25(7), pp. 2808–2814.

Rahmati, M. and Modarress, H. (2009) 'Nitrogen adsorption on nanoporous zeolites studied by Grand Canonical Monte Carlo simulation', *Journal of Molecular Structure: THEOCHEM*, 901(1–3), pp. 110–116.

Rahzani, B. et al. (2017) 'Experimental investigation of upgrading of lignin-derived bio-oil component anisole catalyzed by carbon nanotube-supported molybdenum', *RSC Advances*, 7(17), pp. 10545–10556.

Rensel, D.J. et al. (2013) 'Highly selective bimetallic FeMoP catalyst for C-O bond cleavage of aryl ethers', *Journal of Catalysis*, 305, pp. 256–263.

Réocreux, R. et al. (2016) 'Decomposition Mechanism of Anisole on Pt(111): Combining Single-Crystal Experiments and First-Principles Calculations', *ACS Catalysis*, 6(12), pp. 8166–8178.

Richardson, B.R. et al. (1990) 'Reactions of butadiene in zeolite catalysts by in situ variable-temperature solid-state nuclear magnetic resonance spectrometry', *Journal of the American Chemical Society*, 112(8), pp. 2886–2891.

Richardson, F. et al. (2002) *Particle Technology and Separation Processes*.5th Editio. Elsevier.

Rimarcík, J. et al. (2008) 'Theoretical study of structure and electronic properties of cyano-substituted pyrroles', *Chemical Physics*, 353(1–3), pp. 177–184.

Rogers, K.A. and Zheng, Y. (2016) 'Selective Deoxygenation of Biomass-Derived Bio-oils within Hydrogen-Modest Environments: A Review and New Insights', *ChemSusChem*, 9(14), pp. 1750–1772.

Romero, Y. et al. (2010) 'Hydrodeoxygenation of 2-ethylphenol as a model

compound of bio-crude over sulfided Mo-based catalysts: Promoting effect and reaction mechanism', *Applied Catalysis B: Environmental*, 98(3–4), pp. 213–223.

Ruddy, D.A. et al. (2014) 'Recent advances in heterogeneous catalysts for bio-oil upgrading via "ex situ catalytic fast pyrolysis": catalyst development through the study of model compounds', *Green Chemistry*, 16(2), pp. 454–490.

Runnebaum, R.C. et al. (2011a) 'Conversion of Anisole Catalyzed by Platinum Supported on Alumina: The Reaction Network', *Energy & Fuels*, 25(10), pp. 4776–4785.

Runnebaum, R.C. et al. (2011b) 'Catalytic Conversion of Anisole: Evidence of Oxygen Removal in Reactions with Hydrogen', *Catalysis Letters*, 141(6), pp. 817–820.

Runnebaum, R.C. et al. (2012) 'Catalytic conversion of compounds representative of lignin-derived bio-oils: a reaction network for guaiacol, anisole, 4-methylanisole, and cyclohexanone conversion catalysed by Pt/γ-Al2O3', *Catalytic Science Technology*, 2(1), pp. 113–118.

Sad, M.E. et al. (2010) 'Study of the phenol methylation mechanism on zeolites HBEA, HZSM5 and HMCM22', *Journal of Molecular Catalysis A: Chemical*, 327(1–2), pp. 63–72.

Sad, M.E. et al. (2008) 'Synthesis of cresols by alkylation of phenol with methanol on solid acids', *Catalysis Today*, 133–135(1–4), pp. 720–728.

Saidi, M. et al. (2014) 'Upgrading of lignin-derived bio-oils by catalytic hydrodeoxygenation', *Energy Environvironment scicense*, 7(1), pp. 103–129.

Samolada, M.C. et al. (2000) 'Catalyst evaluation for catalytic biomass pyrolysis', *Energy and Fuels*, 14(6), pp. 1161–1167.

Sankaranarayanan, T.M. et al. (2015) 'Hydrodeoxygenation of anisole as bio-oil model compound over supported Ni and Co catalysts: Effect of metal and support properties', *Catalysis Today*, 243(C), pp. 163–172.

Scheer, A.M. et al. (2010) 'Radical Chemistry in the Thermal Decomposition of

Anisole and Deuterated Anisoles: An Investigation of Aromatic Growth', *The Journal of Physical Chemistry A*, 114(34), pp. 9043–9056.

Schrödinger, E. (1926) 'An Undulatory Theory of the Mechanics of Atoms and Molecules', *Physical Review*, 28(6), pp. 1049–1070.

Segall, M.D. et al. (2002) 'First-principles simulation: ideas, illustrations and the CASTEP code', *Journal of Physics: Condensed Matter*, 14(11), pp. 2717–2744.

Shen, D.K. et al. (2010) 'The pyrolytic degradation of wood-derived lignin from pulping process', *Bioresource Technology*, 101(15), pp. 6136–6146.

Shu, R. et al. (2017) 'Synergistic effects of highly active Ni and acid site on the hydrodeoxygenation of syringol', *Catalysis Communications*, 91, pp. 1–5.

Smets, K. et al. (2014) 'Valorization of raspberry seed cake by flash and slow pyrolysis: Product yield and characterization of the liquid and solid fraction', *Journal of Analytical and Applied Pyrolysis*, 107, pp. 289–297.

Smirnov, A. et al. (2014) 'Effect of the Ni/Cu ratio on the composition and catalytic properties of nickel-copper alloy in anisole hydrodeoxygenation', *Kinetics and Catalysis*, 55(1), pp. 69–78.

Smirnov, A. et al. (2016) 'The composition of Ni-Mo phases obtained by NiMoOx-SiO2 reduction and their catalytic properties in anisole hydrogenation', *Applied Catalysis A: General*, 514, pp. 224–234.

Song, Q. et al. (2013a) 'Hydrogenation and cleavage of the C-O bonds in the lignin model compound phenethyl phenyl ether over a nickel-based catalyst', *Chinese Journal of Catalysis*, 34(4), pp. 651–658.

Song, Q. et al. (2013b) 'Lignin depolymerization (LDP) in alcohol over nickel-based catalysts via a fragmentation–hydrogenolysis process', *Energy & Environmental Science*, 6(3), p. 994.

De Souza, P.M. et al. (2014) 'Role of Oxophilic Supports in the Selective Hydrodeoxygenation of m-Cresol on Pd Catalysts', *Catalysis Letters*, 144(12), pp. 2005–2011.

De Souza, P.M. et al. (2015) ‘Role of Keto Intermediates in the Hydrodeoxygenation of Phenol over Pd on Oxophilic Supports’, *ACS Catalysis*, 5(2), pp. 1318–1329.

Steven Mufson (2009) Papermakers Dig Deep in Highway Bill To Hit Gold, *Washington Post*,

Sukrat, K. et al. (2012) ‘Proton exchange reactions of C2–C4 alkanes sorbed in ZSM-5 zeolite’, *Theoretical Chemistry Accounts*, 131(6), p. 1232.

Szabo, A. and Ostlund N, S. (1989) *Modern Quantum Chemistry: Introduction to Advanced Electronic Structure Theory*. New York: McGraw-Hill.

Taghvaei, H. et al. (2014) ‘Upgrading of Anisole in a Dielectric Barrier Discharge Plasma Reactor’, *Energy & Fuels*, 28(7), pp. 4545–4553.

Takagi, Y. (1967) ‘The hydrogenation of o-, m-, and p-cresols with a rhodium catalyst’, *Journal of Catalysis*, 8(1), pp. 100–103.

Tan, Q. et al. (2017) ‘Mechanistic analysis of the role of metal oxophilicity in the hydrodeoxygenation of anisole’, *Journal of Catalysis*, 347, pp. 102–115.

Teng Xu, Jinhua Zhang, E.J.M. and J.F.H. (1994) ‘A report of a persistent allyl cation on H-ZSM-5 zeolite was due to propanal’, *Chemical Communications*, (23), pp. 2733–2735.

Tessonnier, J.-P. et al. (2006) ‘Quantitative Measurement of the Brönsted Acid Sites in Solid Acids: Toward a Single-Site Design of Mo-Modified ZSM-5 Zeolite’, *The Journal of Physical Chemistry B*, 110(21), pp. 10390–10395.

Thilakaratne, R. et al. (2016) ‘Conversion of methoxy and hydroxyl functionalities of phenolic monomers over zeolites’, *Green Chemistry*, 18(7), pp. 2231–2239.

Thomas, L.H. (1927) ‘The calculation of atomic fields’, *Mathematical Proceedings of the Cambridge Philosophical Society*, 23(5), p. 542.

Toledano, A. et al. (2013) ‘Heterogeneously Catalysed Mild Hydrogenolytic Depolymerisation of Lignin Under Microwave Irradiation with Hydrogen-Donating Solvents’, *ChemCatChem*, 5(4), pp. 977–985.

Torreabreu, C. et al. (1997) ‘NO TPD and H2-TPR studies for characterisation of CuMOR catalysts The role of Si/Al ratio, copper content and cocation’, *Applied Catalysis B: Environmental*, 14(3–4), pp. 261–272.

Vichaphund, S. et al. (2014) ‘Catalytic upgrading pyrolysis vapors of Jatropha waste using metal promoted ZSM-5 catalysts: An analytical PY-GC/MS’, *Renewable Energy*, 65(0), pp. 70–77.

Viljava, T. (2000) ‘Effect of H2S on the stability of CoMo/Al2O3 catalysts during hydrodeoxygenation’, *Catalysis Today*, 60(1–2), pp. 83–92.

Wang, K. et al. (2014) ‘Highly selective synthesis of para-cresol by conversion of anisole on ZSM-5 zeolites’, *Microporous and Mesoporous Materials*, 185, pp. 61–65.

Wang, K. et al. (2014) ‘Bioresource Technology Comparison of in-situ and ex-situ catalytic pyrolysis in a micro-reactor system’, *Bioresource Technology*, 173, pp. 124–131.

Wang, K. et al. (2014) ‘Catalytic pyrolysis of individual components of lignocellulosic biomass’, *Green Chemistry*, 16(2), p. 727.

Wang, R. et al. (2017) ‘DFT study of the adsorption of 2,3,7,8-tetrachlorodibenzo-p-dioxin on pristine and Ni-doped boron nitride nanotubes’, *Chemosphere*, 168, pp. 18–24.

Wang, W. et al. (2004) ‘Methylation of phenol by methanol on acidic zeolite H–Y investigated by in situ CF MAS NMR spectroscopy’, *Catalysis Communications*, 94(3), pp. 119–123.

Watanabe, R. et al. (2013) ‘Stable and selective perovskite catalyst for dehydrogenation of propane working with redox mechanism’, *Journal of Molecular Catalysis A: Chemical*, 377, pp. 74–84.

Watkinson, I. (2014) *IEA bioenergy-Task 34 Pyrolysis*.

Weckhuysen, B.M. et al. (1998) ‘Characterization of surface carbon formed during the conversion of methane to benzene over Mo/H-ZSM-5 catalysts’,

Catalysis Letters, 52(1/2), pp. 31–36.

Wei, Y. et al. (2014) 'Catalyst-free transformation of levulinic acid into pyrrolidinones with formic acid', *Green Chemistry*, 16(3 mL), pp. 1093–1096.

Weigold, H. (1982) 'Behaviour of Co-Mo-Al2O3 catalysts in the hydrodeoxygenation of phenols', *Fuel*, 61(10), pp. 1021–1026.

Whiffen, V.M.L. et al. (2012) 'The influence of citric acid on the synthesis and activity of high surface area MoP for the hydrodeoxygenation of 4-methylphenol', *Applied Catalysis A: General*, 419–420, pp. 111–125.

Willemen, H. et al. (1977) 'ESCA and IR study of cyclopentadienyl tungsten and molybdenum carbonyl compounds', *Journal of Electron Spectroscopy and Related Phenomena*, 11(3), pp. 245–250.

Wu, X. et al. (2013) 'Kinetics and Mechanism of Hydrothermal Decomposition of Lignin Model Compounds', *Industrial & Engineering Chemistry Research*, 52(14), pp. 5016–5022.

Wu Jianbing (2015) 'High Si/Al ratio HZSM-5 zeolite: an efficient catalyst for the synthesis of polyoxymethylene dimethyl ethers from dimethoxymethane and trioxymethylene', *Green Chemistry*, 17, pp. 2353–2357.

Xiong, J. et al. (2010) 'Effects of Current upon Electrochemical Catalytic Reforming of Anisole', *Chinese Journal of Chemical Physics*, 23(6), pp. 693–700.

Xu, J. et al. (1999) 'Alkylation of Phenol with Methanol over Basic X Zeolites', *Applied Catalysis*, 10(12), pp. 983–986.

Xu, T. et al. (1994) 'A Report of a Persistent Ally Cation on H-ZSM-5 Zeolite was due to Propanal', *Chemical Communications*, 5(6), pp. 2733–2735.

Xue, Q. et al. (2012) 'Experimental validation and CFD modeling study of biomass fast pyrolysis in fluidized-bed reactors', *Fuel*, 97(0), pp. 757–769.

Yang, J. et al. (2016) 'Hydrogen production via catalytic steam reforming of m-cresol over Ni-Fe/HZSM-5 catalyst', *Modern Chemical Industry*, 36(8), pp. 146–149.

Yang, M.L. et al. (2011) ‘DFT study of propane dehydrogenation on Pt catalyst: effects of step sites.’, *Physical chemistry chemical physics*, 13, pp. 3257–3267.

Yildiz, G. et al. (2014) ‘Catalytic fast pyrolysis of pine wood: Effect of successive catalyst regeneration’, *Energy and Fuels*, 28(7), pp. 4560–4572.

Yildiz, G. et al. (2013) ‘Validation of a new set-up for continuous catalytic fast pyrolysis of biomass coupled with vapour phase upgrading’, *Journal of Analytical and Applied Pyrolysis*, 103, pp. 343–351.

Zakaria, Z.Y. et al. (2012) ‘Catalyst screening for conversion of glycerol to light olefins’, *Chemical Engineering Journal*, 207–208, pp. 803–813.

Zhai, X. et al. (2005) *New Energy Technology*.Chinese Ed. Beijing: Chemical Industry Press.

Zhang, H. et al. (2011) ‘Catalytic conversion of biomass-derived feedstocks into olefins and aromatics with ZSM-5: the hydrogen to carbon effective ratio’, *Energy & Environmental Science*, 4(6), p. 2297.

Zhang, J. et al. (2016) ‘Mechanism of transmethylation in anisole decomposition over HZSM-5: Experimental study’, *Journal of Analytical and Applied Pyrolysis*, 122, pp. 323–331.

Zhang, L. et al. (2013) ‘Upgrading of bio-oil from biomass fast pyrolysis in China: A review’, *Renewable and Sustainable Energy Reviews*, 24, pp. 66–72.

Zhao, C. et al. (2013) ‘Understanding the impact of aluminum oxide binder on Ni/HZSM-5 for phenol hydrodeoxygenation’, *Applied Catalysis B: Environmental*, 132–133, pp. 282–292.

Zhao, Y. et al. (2014) ‘Pd nanoparticles supported on ZIF-8 as an efficient heterogeneous catalyst for the selective hydrogenation of cinnamaldehyde’, *Catalysis Communications*, 57(5), pp. 119–123.

Zhou, C. et al. (2011) ‘Catalytic conversion of lignocellulosic biomass to fine chemicals and fuels’, *Chemical Society Reviews*, 40(11), p. 5588.

Zhou, G. et al. (2016) ‘Direct upgrading of fast pyrolysis lignin vapor over the

HZSM-5 catalyst', *Green Chemistry*, 18(7), pp. 1965–1975.

Zhu, X. et al. (2011) 'Bifunctional transalkylation and hydrodeoxygenation of anisole over a Pt/HBeta catalyst', *Journal of Catalysis*, 281(1), pp. 21–29.

Zhu, X. et al. (2010) 'Role of transalkylation reactions in the conversion of anisole over HZSM-5', *Applied Catalysis A: General*, 379(1–2), pp. 172–181.

Zou, X. et al. (2016) 'Catalytic cracking of toluene over hematite derived from thermally treated natural limonite', *Fuel*, 177, pp. 180–189.

APPENDICES

A1 Determination of the minimum fluidization flowrate (U_{mf}) for silica sand

Calculation of minimum fluidization flowrate (U_{mf})	Particle diameter dp (m)	2.00E-04
	Viscosity of gas μ (kg/(m·s))	3.69E-05
	True density of sand ρc (kg/m^3)	2.20E+03
	True density of gas ρg (kg/m^3)	3.91E-01
	Porosity at minimum fluidization ε	5.60E-01
	V_{mf} (m/s)	6.23E-02
	U_{mf} (L/min)	3.00
Multi times of U_{mf}	U_{mf} (L/h)	180.21
	$2U_{mf}$ (L/h)	360.42
	$3U_{mf}$ (L/h)	540.63
	$4U_{mf}$ (L/h)	720.83
	$5U_{mf}$ (L/h)	901.04

A2 Determination of the minimum fluidization flowrate (U_{mf}) for HZ catalyst

Calculation of minimum fluidization flowrate (U_{mf})	Particle diameter dp (m)	2.00E-04
	Viscosity of gas μ (kg/(m·s))	3.69E-05
	True density of catalysts ρc (kg/m^3)	1.50E+03
	True density of gas ρg (kg/m^3)	3.91E-01
	Porosity at minimum fluidization ε	5.00E-01
	V_{mf} (m/s)	2.66E-02
	U_{mf} (L/min)	1.28
Multi times of U_{mf}	U_{mf} (L/h)	76.96
	$2U_{mf}$ (L/h)	153.91

A3 Dosage of metal precursors for the preparation of metal/HZ(25) catalysts

Dosage for every 50g of impregnating HZ(25)	Metal precursors	Dosage (g)
0.5%Ni		1.24
1%Ni	$Ni(NO_3)_2 \cdot 6H_2O$	2.50
5%Ni		13.04
1%Co	$Co(NO_3)_2 \cdot 6H_2O$	2.49
0.5%Mo		0.46
1%Mo	$(NH_4)_6Mo_7O_{24}.4H_2O$	0.93
5%Mo		4.84
1%Cu	$Cu(NO_3)_2 \cdot 3H_2O$	1.92
1%Fe	$Fe(NO_3)_3 \cdot 9H_2O$	3.65

A4 Quench traps for the collection of liquid products

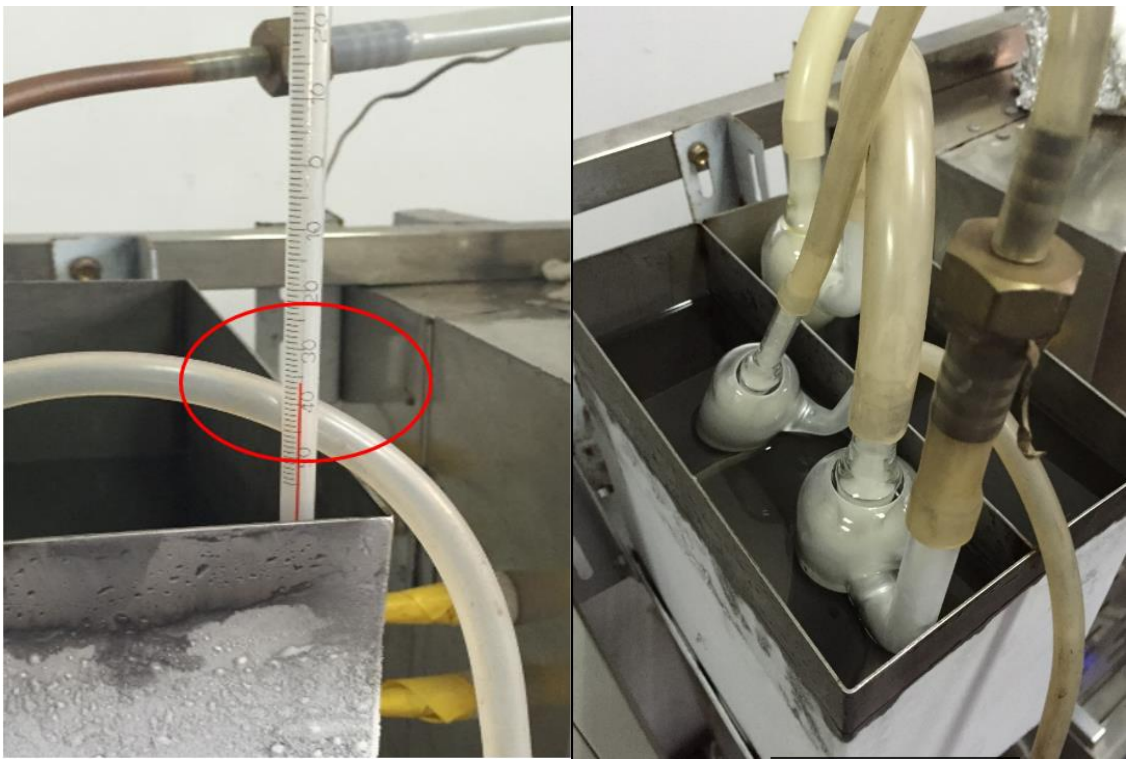

A5 Unique imaginary frequency identified for each transition state of the reactions for both non-catalytic and catalytic transmethylation

Reactant	Via	Product	Orientation	Imaginary frequency (Frequency(1/cm); Intensity(km/mol))		
				Non-catalytic (TS)	Catalytic	
					Cleavage (TS1)	Methyl cation transfer (TS2)
anisole	phenol	Cresol	Ortho	-15.49/0.03	-331.54/99.74	-352.36/6.86
			Meta	-11.96/0.14		-285.63/7.12
			Para	-10.15/0.11		-435.58/5.90
	o-cresol	Xylenol	Ortho	-304.25/658.68		-345.63/7.72
			Meta	-144.6/1.40		-311.78/158.17
			Para	-270.32/163.89		-343.56/192.81
	2,4-xylenol	2,4,6-phenol	Ortho	-237.38/453.09		-171.58/6.64
	2,6-xylenol	2,3,6-phenol	Meta	-229.42/129.61		-511.45/499.08
	benzene	Toluene	-	-686.39/37.85		-233.06/16.67
	toluene	Xylene	Ortho	-244.71/129.42		-138.44/101.67
			Meta	-240.01/87.44		-320.08/188.36
			Para	-36.49/27.64		-302.45/185.02
	anisole	methyl-anisole	Ortho	-283.22/185.03		-98.98/4.73
			Meta	-6823.26/7.10		-313.60/67.33
			Para	-267.68/159.39		-309.34/2.79

A6 Unique imaginary frequency identified for each transition state of the reactions for deoxygenation

Imaginary frequency (frequency(1/cm)/intensity(km/mol))					
Compounds	HZ(25)	Ni/HZ(25)	Co/HZ(25)	Mo/HZ(25)	Cu/HZ(25)
Phenol	-1131.65/2493.37	-1089.83/162.11	-961.56/-2072.35	-539.55/776.18	-826.52/1400.91
o-cresol	-877.93/2844.54	-327.85/803.61	-202.08/518.55	-312.81/1908.45	-912.94/2159.29
p-cresol	-211.94/34.23	-281.17/249.70	-298.38/306.61	-369.51/99.94	-823.03/153.84
2,4-cresol	-245.01/16.18	-119.83/56.82	-601.40/124.30	-143.64/78.82	-524.08/87.99
2,6-cresol	-1292.90/3716.42	-250.41/271.62	-631.78/120.33	-998.06/176.48	-449.30/321.85
3,5-cresol	-520.19/22.89	-910.77/246.19	-816.79/509.01	-472.51/68.22	-323.91/51.42
2,4,6-cresol	-849.32/4856.68	-522.54/709.25	-1171.59/2309.02	-779.97/106.50	-614.73/682.06
2,3,6-cresol	-325.72/590.78	-976.68/393.13	-116.06/54.58	-691.87/828.10	-819.66/73.01
3,4,5-cresol	-583.97/924.76	-140.35/96.99	-1230.93/31.56	-305.04/155.10	-232.10/27.10

A7 EDS spectra for the fresh catalysts of (a)1%Ni/HZ(25), (b)1%Co/HZ(25), (c)1%Mo/HZ(25), and (d)1%Cu/HZ(25)

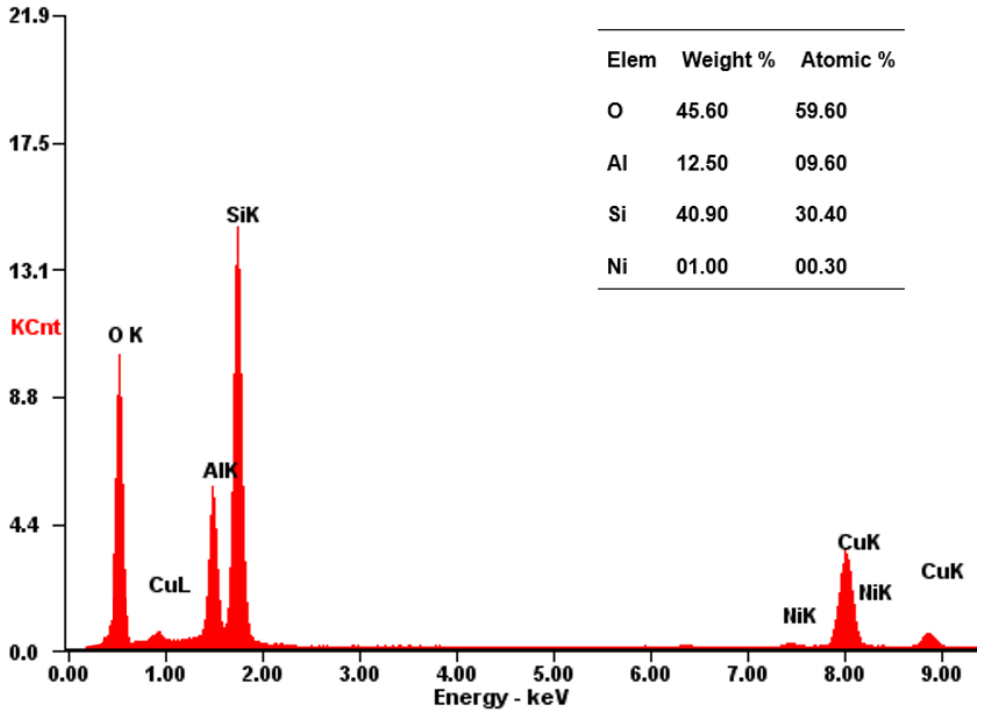

Elem	Weight %	Atomic %
O	45.60	59.60
Al	12.50	09.60
Si	40.90	30.40
Ni	01.00	00.30

(a)

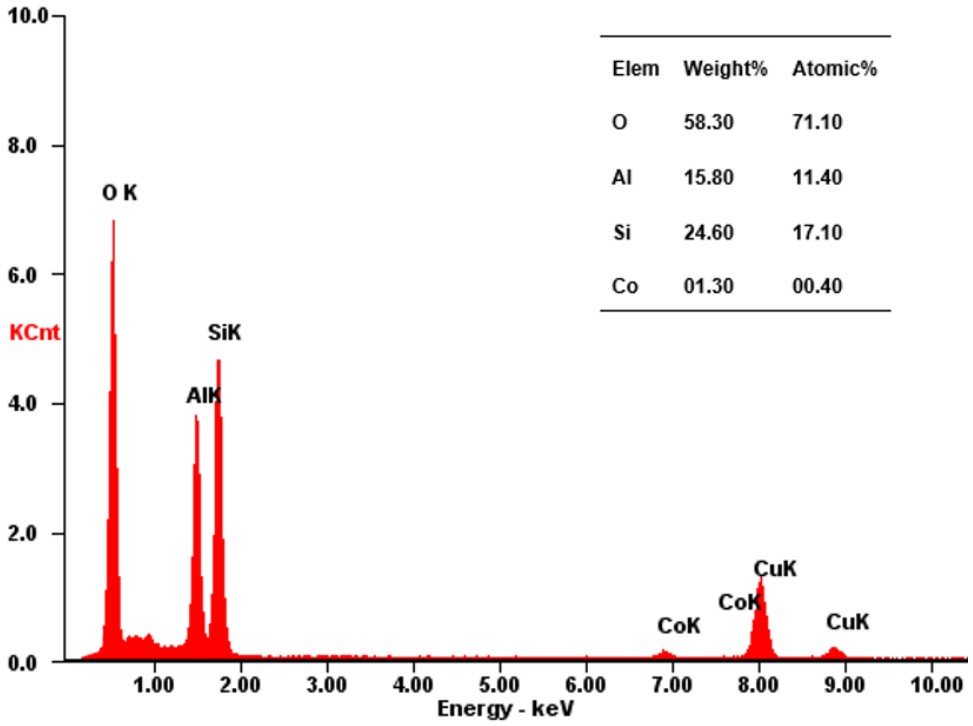

Elem	Weight%	Atomic%
O	58.30	71.10
Al	15.80	11.40
Si	24.60	17.10
Co	01.30	00.40

(b)

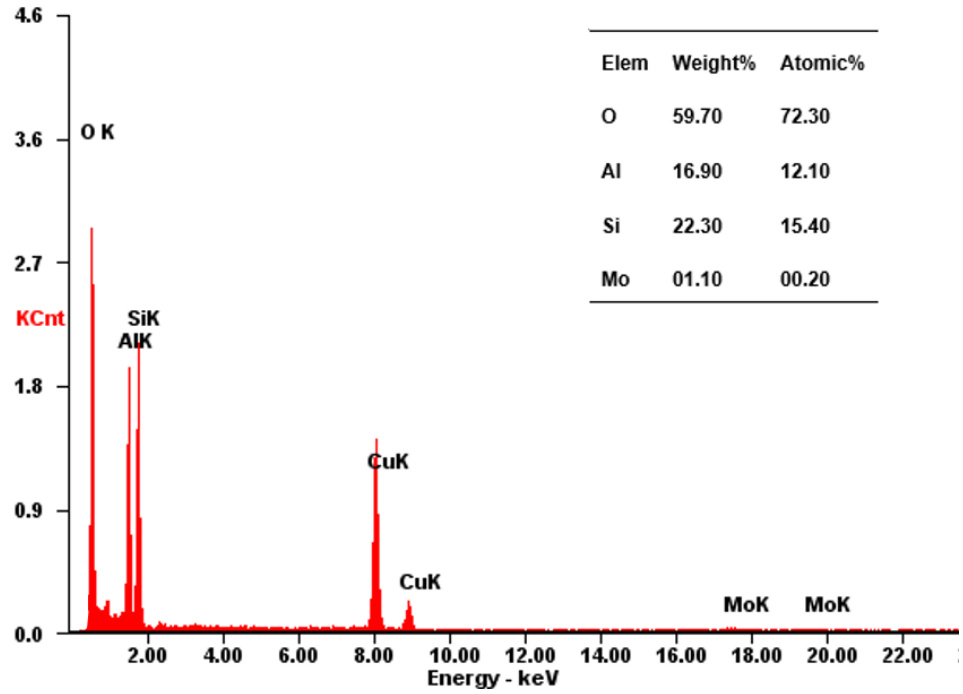

Elem	Weight%	Atomic%
O	59.70	72.30
Al	16.90	12.10
Si	22.30	15.40
Mo	01.10	00.20

(c)

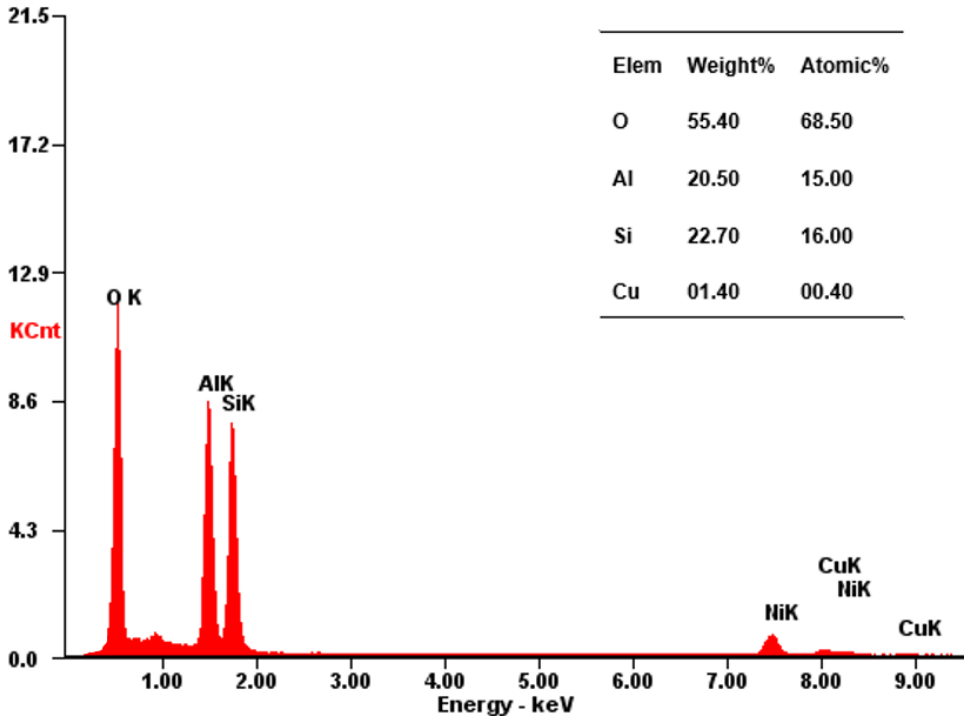
21.5
17.2
12.9
8.6
4.3
0.0
KCnt
O K
AlK
SiK
NiK
CuK
NiK
CuK
1.00
2.00
3.00
4.00
5.00
6.00
7.00
8.00
9.00
Energy - keV
Elem Weight% Atomic%
O 55.40 68.50
Al 20.50 15.00
Si 22.70 16.00
Cu 01.40 00.40

(d)

A8 Yields of gaseous products in single metal based experiments

Absolute yield (mass, mg)			
Substance	D1	D2	D3
CH_4	2.95	11.49	31.09
C_2H_6	0.00	0.00	0.68
C_3H_8	0.00	0.00	0.00
C_4H_{10}	0.00	0.00	0.00
C_2H_4	1.30	3.13	1.20
C_3H_6	0.00	0.00	0.00
C_4H_8	0.00	0.00	0.00

Absolute yield (mass, mg)				
Substance	D2	D6	D7	D10
CH_4	11.49	7.45	10.20	9.02
C_2H_6	0.00	0.00	5.75	4.91
C_3H_8	0.00	0.00	2.65	4.07
C_4H_{10}	0.00	0.00	0.00	0.00
C_2H_4	3.13	0.00	22.14	18.39
C_3H_6	0.00	0.00	3.20	3.63
C_4H_8	0.00	0.00	0.00	0.00

Absolute yield (mass, mg)						
Substance	D4	D2	D5	D8	D7	D9
CH_4	5.36	11.49	96.49	9.96	10.20	9.47
C_2H_6	0.45	0.00	2.35	5.02	5.75	1.08
C_3H_8	0.00	0.00	0.00	3.23	2.65	0.00
C_4H_{10}	0.00	0.00	0.00	0.00	0.00	0.00
C_2H_4	2.98	3.13	0.00	23.69	22.14	14.61
C_3H_6	0.00	0.00	0.00	4.65	3.20	0.00
C_4H_8	0.00	0.00	0.00	0.00	0.00	0.00

A9 EDS spectra for the spent catalysts of (a)1%Ni/HZ(25) after experiment D2, (b) 1%Mo/HZ(25) after experiment D7

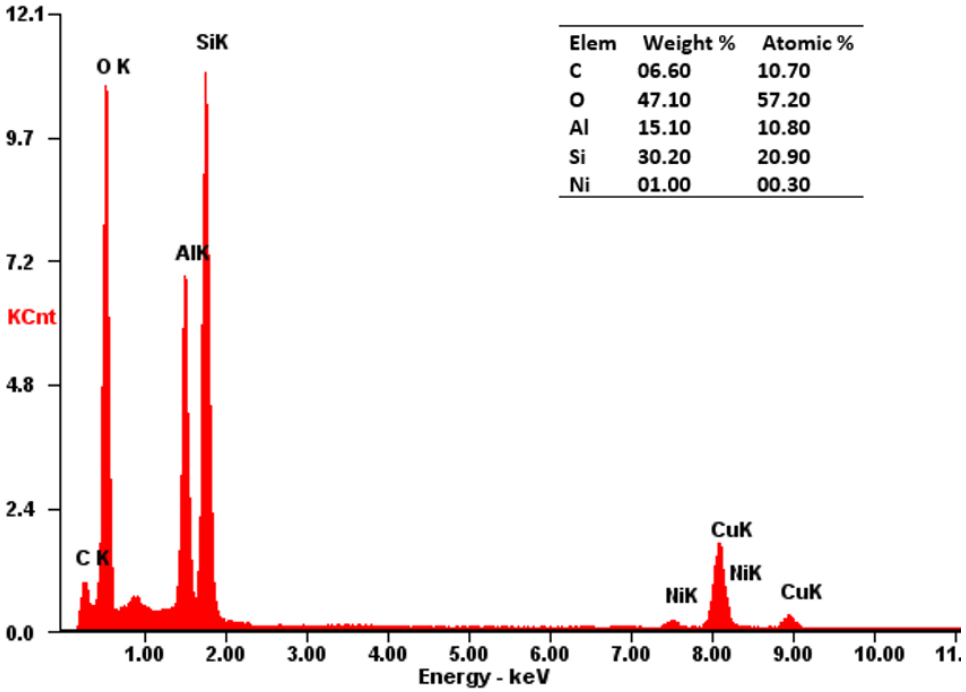

Elem	Weight %	Atomic %
C	06.60	10.70
O	47.10	57.20
Al	15.10	10.80
Si	30.20	20.90
Ni	01.00	00.30

(a)

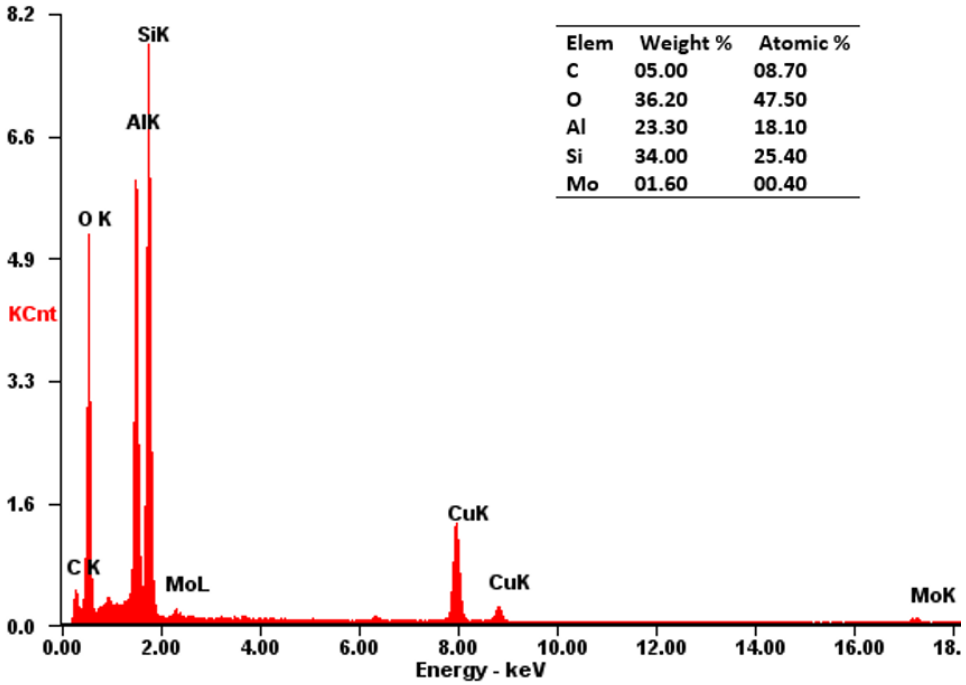

Elem	Weight %	Atomic %
C	05.00	08.70
O	36.20	47.50
Al	23.30	18.10
Si	34.00	25.40
Mo	01.60	00.40

(b)

A10 EDS spectra for the fresh catalysts of (a)1%Ni-1%Mo/HZ(25), (b)1%Ni-1%Fe/HZ(25), (c)1%Mo-1%Fe/HZ(25)

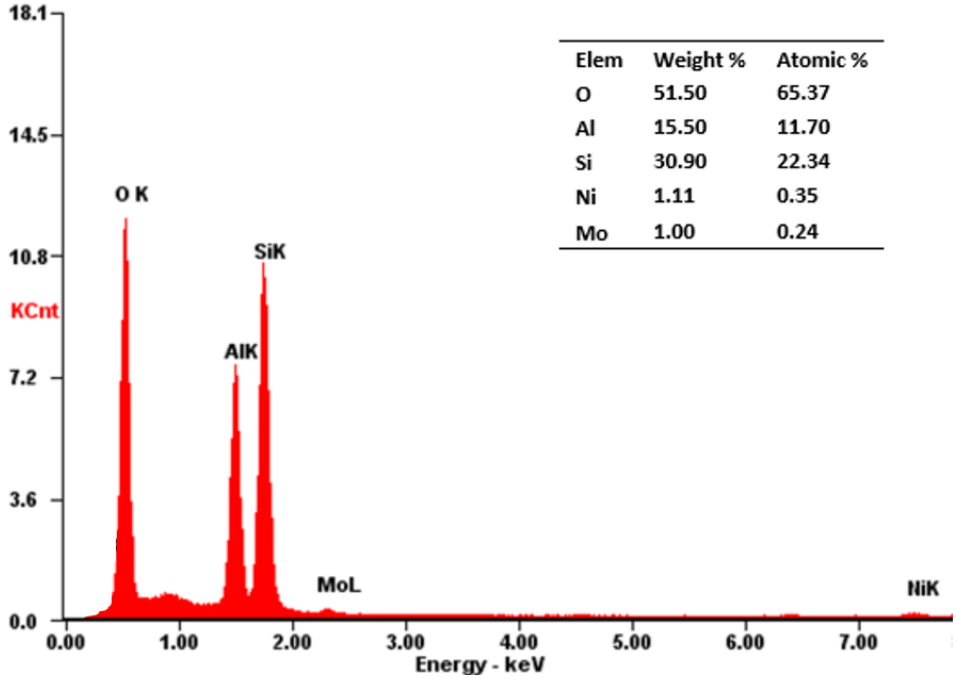

Elem	Weight %	Atomic %
O	51.50	65.37
Al	15.50	11.70
Si	30.90	22.34
Ni	1.11	0.35
Mo	1.00	0.24

(a)

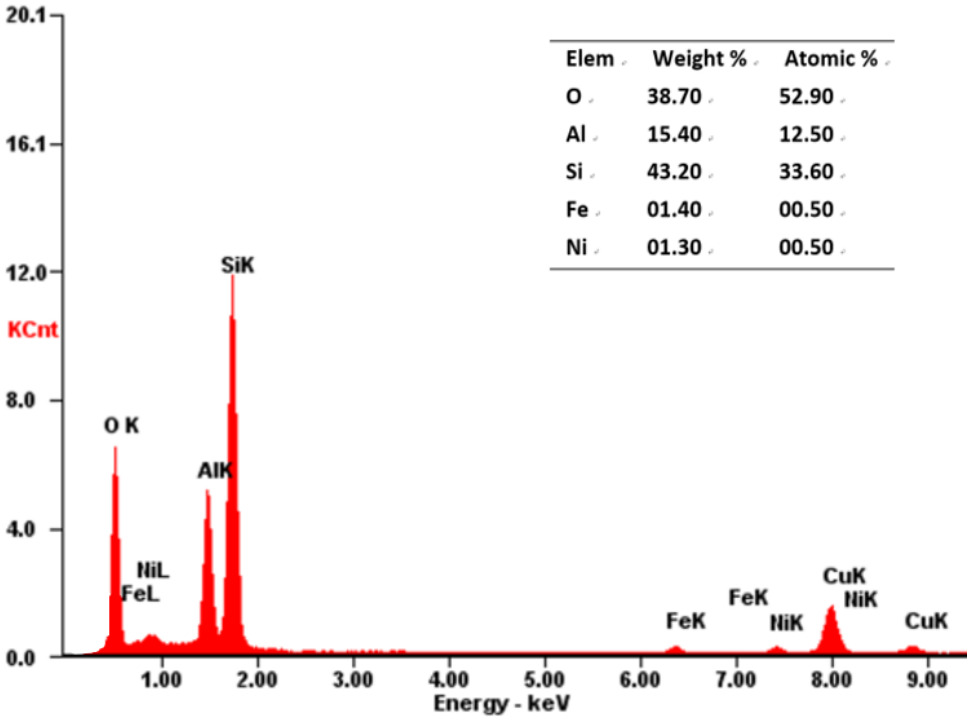

Elem	Weight %	Atomic %
O	38.70	52.90
Al	15.40	12.50
Si	43.20	33.60
Fe	01.40	00.50
Ni	01.30	00.50

(b)

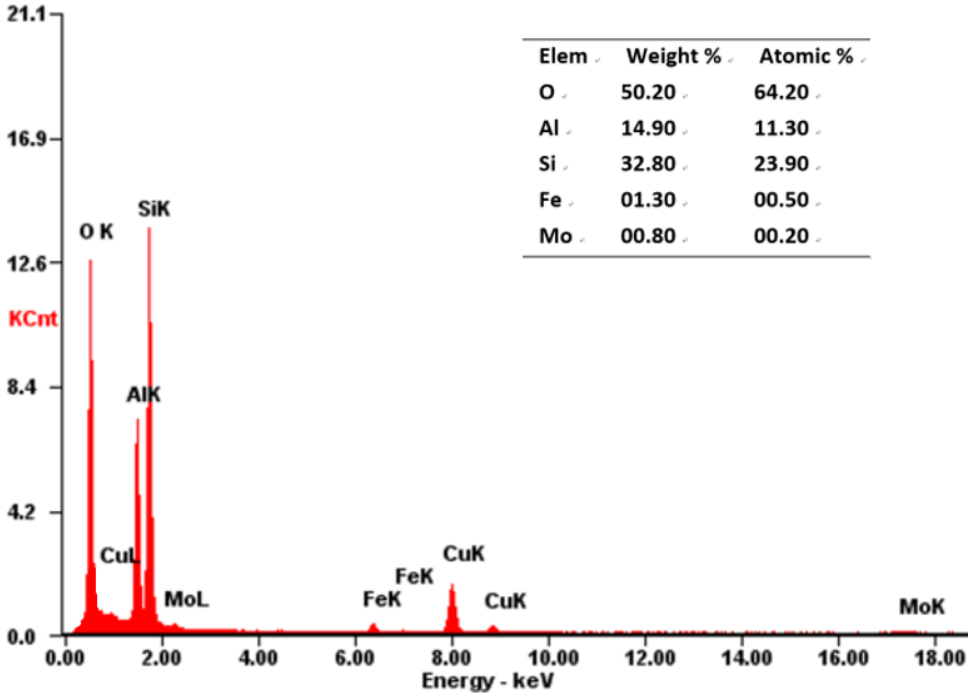
21.1
16.9
12.6
KCnt
8.4
4.2
0.0
O K
SiK
AlK
CuL
MoL
FeK
FeK
CuK
CuK
MoK
0.00
2.00
4.00
6.00
8.00
10.00
12.00
14.00
16.00
18.00
Energy - keV
Elem Weight % Atomic %
O 50.20 64.20
Al 14.90 11.30
Si 32.80 23.90
Fe 01.30 00.50
Mo 00.80 00.20

(c)

A11 Yields of gaseous products in bi-metal based experiments

Absolute yield (mass, g)			
Substances	D12	D16	D17
CH_4	2.52	10.69	9.88
C_2H_6	0.00	1.54	2.32
C_3H_8	0.00	0.00	1.66
C_4H_{10}	0.00	0.00	0.00
C_2H_4	2.76	11.83	18.00
C_3H_6	0.00	0.00	2.78
C_4H_8	0.00	0.00	0.00

Absolute yield (mass, mg)			
Substances	D11	D12	D13
CH_4	0.83	2.52	27.62
C_2H_6	0.00	0.00	0.00
C_3H_8	0.00	0.00	0.00
C_4H_{10}	0.00	0.00	0.00
C_2H_4	2.74	2.76	0.00
C_3H_6	0.00	0.00	0.00
C_4H_8	0.00	0.00	0.00

Absolute yield (mass, mg)			
Substances	D12	D14	D15
CH_4	2.52	2.66	4.93
C_2H_6	0.00	0.27	0.81
C_3H_8	0.00	0.00	0.00
C_4H_{10}	0.00	0.00	0.00
C_2H_4	2.76	2.04	0.00
C_3H_6	0.00	0.00	0.00
C_4H_8	0.00	0.00	0.00

A12 EDS spectrum for the spent catalyst of 1%Ni-1%Mo/HZ(25) after experiment D12

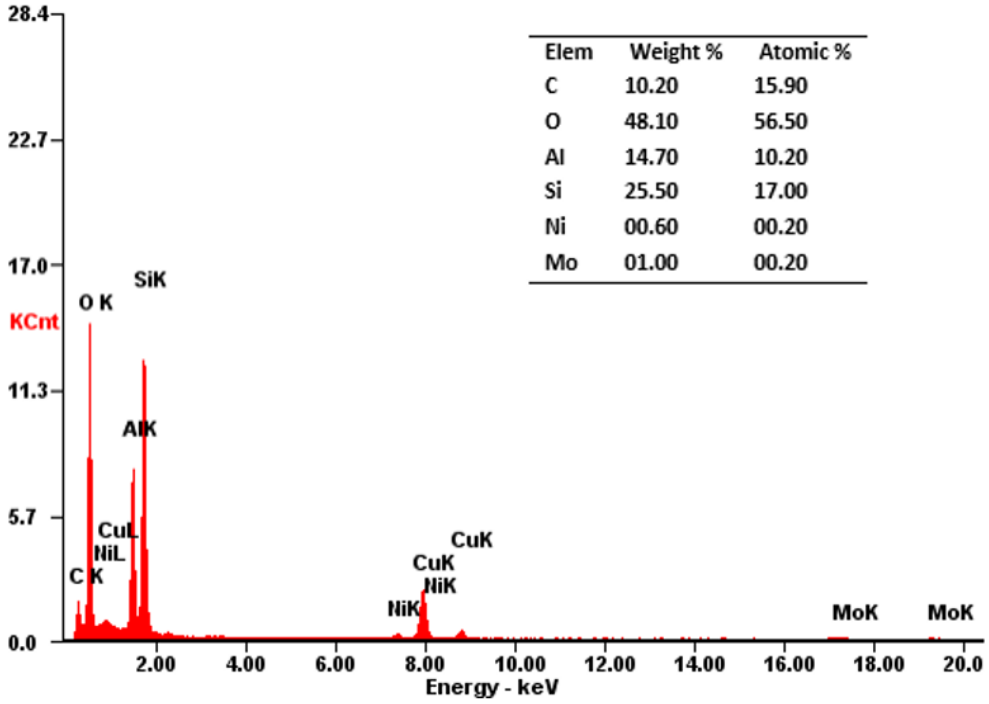

Elem	Weight %	Atomic %
C	10.20	15.90
O	48.10	56.50
Al	14.70	10.20
Si	25.50	17.00
Ni	00.60	00.20
Mo	01.00	00.20